TECHNISCHE UNIVERSITÄT MÜNCHEN
Lehrstuhl für Regelungstechnik

Adaptive Control of Mechatronic Vehicle Suspension Systems

Guido P. A. Koch

Vollständiger Abdruck der von der Fakultät für Maschinenwesen
der Technischen Universität München zur Erlangung
des akademischen Grades eines

Doktor-Ingenieurs

genehmigten Dissertation.

Vorsitzender:	Univ.-Prof. Dr.-Ing. Markus Lienkamp
Prüfer der Dissertation:	1. Univ.-Prof. Dr.-Ing. habil. Boris Lohmann
	2. Univ.-Prof. Dr.-Ing. habil. Ansgar Trächtler, (Universität Paderborn)

Die Dissertation wurde am 15.11.2010 bei der Technischen Universität München eingereicht und durch die Fakultät für Maschinenwesen am 21.02.2011 angenommen.

For my family and for Kathrin.

ABSTRACT

The Thesis presents two new adaptive vehicle suspension control methods, which significantly improve the performance of mechatronic suspension systems by adjusting the controller parametrization to the current driving state. Thereby, ride comfort is enhanced while the dynamic wheel load and the suspension deflection remain uncritical. The first concept is an adaptive switching controller structure, which dynamically interpolates between differently tuned linear quadratic regulators. The required estimates of the state vector and the dynamic wheel load are provided by a new estimator concept based on parallel Kalman filters. The stability of the switching controller structure is analyzed employing a common Lyapunov function approach, that takes into account arbitrary fast controller parameter variations and the nonlinear damper characteristic. The performance of the concept is successfully validated in experiments on a quarter-vehicle test rig for a fully active suspension. To overcome the drawbacks of fully active systems, i.e. primarily their high power demand and complex actuators, a new suspension concept called *hybrid suspension system* is presented. It involves a continuously variable semi-active damper and a low bandwidth actuator integrated in series to the primary spring. The potential of the hybrid concept is shown in an optimization-based analysis. To experimentally validate its performance potential, a hybrid suspension strut is constructed based on stock components from production vehicles and it is integrated in an appropriately designed automotive quarter-car test rig. The second control approach (adaptive reference model based suspension control) emulates the dynamic behavior of a passive suspension system, which is optimally tuned to improve ride comfort for the current driving state while keeping constraints on the dynamic wheel load and the suspension deflection. Its stability is proven by a physically motivated Lyapunov function approach and a switching restriction for the adaptation of the spring stiffness. The adaptive controller structure employs the well-known tuning parameters of passive suspensions, natural frequency and damping ratio of the sprung mass, which fosters transparency and tuneability of the control approach. The new suspension control concept is implemented on the automotive quarter-car test rig for the hybrid suspension employing a new filter-based estimator. Simulations and experiments show that the hybrid suspension system in combination with the adaptive reference model based control achieves performance improvements that are similar to the adaptive switching controller structure for the fully active suspension, however, with a lower power demand.

ACKNOWLEDGMENTS

First, I would like to deeply thank my Thesis advisor Prof. Boris Lohmann for the freedom he gave me to develop and explore the presented suspension control techniques. Especially his sponsoring for the realization of the test rigs has been greatly appreciated. His invaluable support and insights during my time at the Institute of Automatic Control have laid the groundwork for the next steps of my career.

I would like to thank Prof. Ansgar Trächtler for his interest in my work and for being the co-referee for this Thesis. I would also like to thank Prof. Markus Lienkamp for chairing the board of examiners for the Thesis.

Special thanks go to Prof. Günther Roppenecker, PD Dr. Christoph Wurmthaler and Dr. Karl-Peter Jäker for the many fruitful discussions and helpful hints, which have been indispensable for the success of my work.

Moreover, I would like to deeply thank all my students, whose excellent works have contributed significantly to the quality of the research project's results. Especially my former students and today's colleagues Klaus Diepold, Oliver Fritsch, Tobias Kloiber, Enrico Pellegrini, Nils Pletschen and Sebastian Spirk deserve my deepest gratitude for being extraordinarily supportive.

I am very grateful to all my old and new colleagues for providing an excellent working atmosphere. You have been a source of motivation, support and joy at the Institute and beyond. Without the know-how and great skills of Thomas Huber, the realization of the test rigs would not have been possible. The quality and readability of the Thesis have been greatly improved by considering the comments of my aforementioned colleagues as well as especially Dr. Michael Buhl, Dr. Rudy Eid, Dr. Paul Kotyczka and Andreas Unger.

Furthermore, I would like to thank Carsten Bischoff, Dr. Marcus Jautze, Dr. Markus Nyenhuis and Karsten Röski at *BMW AG* for providing suspension components and helpful hints to realize the hybrid suspension test rig and for being admitted to use a damper test rig of the company. I am also very thankful for the funding support for the realization of the hybrid suspension test rig provided by the DFG (German Research Foundation).

A very special acknowledgment goes to my family for their care and support throughout all my years of education and for finding the right words to keep me on track. I am also extremely thankful to all my friends for their moral support and motivation. The help of Matthias Windhorst with image formatting has been greatly appreciated.

Finally, my deepest thanks go to Kathrin Ortmann, whose immense support, understanding, encouragement and love helped me to accomplish this and many other tasks during the last years.

TABLE OF CONTENTS

Chapter 4: Estimator design 61

Chapter 5: Adaptive switching control of active suspension systems 83

LIST OF FIGURES

LIST OF TABLES

GLOSSARY

Abbreviations

3KF	Three parallel Kalman filters with nonlinear damper force estimation
ABC	Active Body Control
AKTAKON	“Aktive Aufbaukontrolle” (Active Body Control)
ASCA	Active suspension system with integrated body control and variable wheel damping
CAD	Computer aided design
EKF	Extended Kalman filter
ER	Electrorheological
FB	Filter based estimation
FEM	Finite element method
HBAS	High bandwidth active suspension / fully active suspension
ISO	International Organization for Standardization
LBAS	Low bandwidth active suspension
LMI	Linear matrix inequality
LPV	Linear parameter-varying
LQR	Linear quadratic regulator
LTI	Linear time-invariant
MPC	Model predictive control
MR	Magnetorheological
MRAC	Model reference adaptive control
PSD	Power spectral density
SAC	Slow active (suspension) control
SISO	Single input single output (system)
WRAPT	Wire rope actuated position transducer

Notation

$\mathrm{diag}(\mathbf{A})$	$(1 \times n)$-vector including the diagonal elements of the $(n \times n)$-matrix $\mathbf{A}$
$\hat{x}(t)$	Estimate of variable $x(t)$
$\|\|x\|\|_{\mathrm{rms}}$	Root mean square (rms) value of $x(t)$
$\|\|x\|\|_{\mathrm{std}}$	Standard deviation of $x(t)$
$\|\|x\|\|$	Any p-norm of $x(t)$
x^*	Optimal value of x / reference value for $x(t)$

Chapter 1

INTRODUCTION

More than one million people per year loose their lives worldwide in traffic fatalities and approx. 50 million people suffer non-fatal injuries from road accidents [166]. Ride safety and the handling capabilities of an automobile are mainly determined by its suspension system, which transmits the forces between the vehicle and the road [106, 125]. The suspension system should not only enable the driver to keep authority over the vehicle in critical situations but also should provide a high level of ride comfort to prevent physical fatigue of the driver. Moreover, since the suspension system significantly influences the subjective impression of the vehicle, the customer demands regarding safety and ride comfort of modern automobiles are constantly increasing. These aspects represent a challenge for the design of automotive suspension systems.

The main parts of conventional (passive) suspension systems are the wheels with the tires, the wheel carrier systems, spring and damper elements, the steering and the brakes [11]. The dynamic behavior of passive automotive suspension systems is primarily determined by the choice of the spring (stiffness c_c) and the damper (damping coefficient d_c)[1]. For the choice of the spring and damper setting, different aspects are taken into account: On the one hand, the suspension should provide excellent ride comfort by a soft spring and damper setup isolating the chassis from the road induced vibrations. On the other hand, the vehicle should be controllable by the driver to ensure ride safety, which requires a stiff, well damped coupling between the vehicle and the road, especially for non-stationary driving maneuvers, e.g. driving a rough road or cornering [11]. Consequently, the requirements regarding comfort and safety are conflicting.

---

[1] To simplify the following illustrations, linear suspension component characteristics are assumed.

Mechatronic suspensions can ease this conflict by employing controlled force-generating actuators between the wheels and the chassis (active suspension systems) or adjustable dampers (semi-active suspension configurations) to improve the dynamic behavior of the suspension. Figure 1.1 shows a modern mechatronic suspension system, which is equipped with continuously variable dampers and active anti-roll bars to improve the suspension performance and enable the driver to select between differently tuned suspension settings. However, all active suspension systems require an external power-supply, which especially obviates the integration of high bandwidth actuators in todays efficiency focussed production vehicles.

Figure 1.1: Mechatronic suspension system of *BMW 7 series* (model year 2009) [160]. Image is reproduced with kind permission of *BMW AG*.

A simple measure for ride comfort is the root mean square (rms) value of the vertical chassis acceleration $||\ddot{x}_c||_{\mathrm{rms}}$, which should be low to bring forward a comfortable impression of the vehicle suspension. To provide ride safety, the tires must be able to transfer vertical and lateral forces between the vehicle and the road, which is only possible if the so called dynamic wheel load F_{dyn} is bounded, i.e. the wheel stays in contact with the road. This requirement can also be formulated in terms of a bound on the rms-value $||F_{dyn}||_{\mathrm{rms}}$ [55, 106].

Figure 1.2 visualizes the performance potential of different mechatronic vehicle suspension types compared to the passive system in a conflict diagram (or *carpet plot*) by means of the quantities introduced above. The depicted conflict diagram is obtained from a simulation that excites a suspension system by an exemplary road profile and evaluates the quantities $||\ddot{x}_c||_{\text{rms}}$ and $||F_{dyn}||_{\text{rms}}$ for different suspension settings. Both quantities should be as low as possible to provide ride comfort and ride safety.

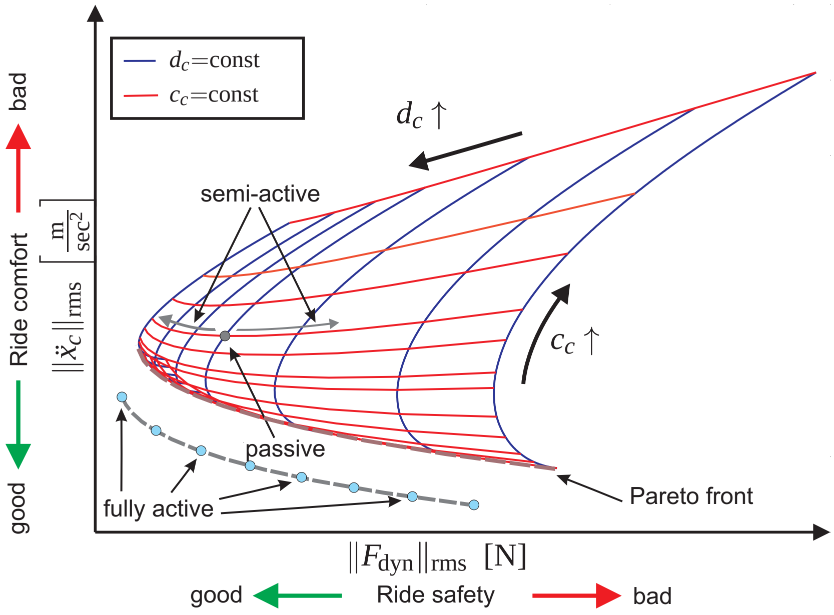

Figure 1.2: Conflict diagram of different vehicle suspension configurations.

It can be seen that the spring and damper settings have a significant influence on the suspension performance. The passive suspension system represents a standard choice for the stiffness and damping. Although better ride comfort could be achieved if the stiffness c_c of the passive configuration is lowered, this is frequently obviated by limits on the suspension deflection. The semi-active system can adjust the damping and thus improve either ride comfort or ride safety compared to the passive system. In the part of the Figure that represents the variations of stiffness and damping, a Pareto front is present, i.e. even if the stiffness could be significantly lowered, the designer would have to choose if the car should exhibit a comfort or a safety oriented suspension setting since improving one objective leads to a deterioration of the other.

As Figure 1.2 shows, ride comfort and ride safety can be significantly enhanced by mechatronic suspension systems, especially by the so called “fully active” configurations, which include actuators with high bandwidths to actively damp chassis and wheel vibrations. However, although the Pareto front can be shifted towards the origin by the fully active suspension (grey curve), the new Pareto front consists of differently tuned suspension controllers (depicted as cyan bullets) for a fully active system.

Hence, an important fact is that the required trade-off between ride comfort and ride safety is also persistent for mechatronic suspension systems although the tuning parameters for the adjustment of the suspension setting change from the choice of the passive suspension elements (c_c and d_c) to the choice of the parametrization of the suspension controller.

The most important benefit of mechatronic suspension systems is the flexibility provided by the actuator components. If this flexibility is not utilized, i.e. if a time-invariant suspension control law is employed, the tuning of the mechatronic suspension cannot deliver optimal results for every driving state. Thus, the full performance potential of the systems cannot be exploited since the requirement to keep the safety limits for different kinds of road profiles introduces conservatism in the controller design. From this observation the idea to develop a driving state adaptive control concept has evolved.

1.1 Scope of the Thesis

In order to maximize the performance of a vehicle suspension system while considering the nonstationary environment (changing excitations by different road surfaces, variety of driving states of the vehicle), several *adaptive control* approaches are presented in this Thesis. The term *adaptive* in this context refers to self-optimization of the controller parameters (see e.g. [155, 167]) in order to maximize ride comfort as long as the driving state is uncritical regarding ride safety and maximum suspension deflection. Therefore, adaptation strategies are developed to detect the driving state and to schedule the controller parametrization accordingly. As a result, conservatism in the controller design can be reduced and ride safety is still guaranteed since a safety-oriented controller parametrization is activated immediately if the driving state becomes more critical.

The contributions of the Thesis can be summarized as follows:

- **Design of new estimator concepts for suspension control:** To enhance the suspension performance by modern state feedback based control methods, the vehicle states must be inferred from measurement signals. In this Thesis three different estimation approaches with different levels of complexity are presented, compared and evaluated.

- **A new adaptive switching control approach:** To fully take advantage of the potential of mechatronic suspension systems, an adaptive controller structure is presented, that adapts its parametrizations according to the current driving state in order to maximize ride comfort while preserving ride safety and the suspension deflection limits. The stability of the closed-loop system is analyzed and the method is applied to a fully active suspension system.

- **A new mechatronic suspension configuration - The *hybrid suspension*:** To overcome significant drawbacks of fully active suspension systems, a new suspension configuration including the combination of a fast semi-active damper and a low bandwidth actuator is motivated and realized from stock components of production vehicles. It is shown that the performance potential of an adaptively controlled *hybrid suspension* is comparable to that of a fully active suspension configuration while promising significant advantages regarding power demand and realizability.

- **A new, transparent suspension control approach - Adaptive reference model based control:** By this suspension control method, the dynamic behavior of a passive suspension configuration, that is optimally tuned for the current driving state to maximize ride comfort while keeping the safety limits, is emulated by the mechatronic suspension system. Thereby the well-known tuning parameters for passive suspension systems, natural frequency and damping ratio of the sprung mass, are dynamically adjusted to exploit the advantages of adaptive suspension control. The concept is validated in simulations and experiments for the hybrid suspension as well as the fully active system and offers significant performance improvements compared to benchmark concepts.

Many works on suspension control have been published over the last decades. Their scope reaches from very theoretical works neglecting important properties of the suspension to practical applications of mechatronic suspension systems, which focus on implementability aspects of rather simple control concepts. Thus, the suspension control concepts presented in this Thesis try to consider aspects, which are rarely found in combination in the literature on suspension controller design:

1. **A realistic framework** for the controller design and the performance evaluation. To this end, two quarter-vehicle suspension test rigs have been designed to derive realistic

nonlinear models and to validate the performance of the adaptive control and estimation algorithms experimentally. The sensor architecture and considered actuator specifications are similar to those, either realized in production vehicles, or - in the case of the fully active suspension system - in industrial automotive suspension studies. Moreover, measurements of real road profiles are used as road excitation signals for the simulations as well as for the experiments and benchmark controller structures are employed to permit an appropriate evaluation of the performance of the new mechatronic suspension control concepts.

2. The application of **advanced control concepts** for the controller and estimator design to exploit the performance potential of mechatronic suspension systems from a control engineering point of view. This includes the important analysis of stability of the adaptive control concepts, which is frequently neglected in the literature.

3. Although the performance of adaptively controlled suspension systems is exploited with a focus on the control algorithms, the **transparency and feasibility of the concepts** is thoroughly discussed. These aspects have primarily motivated the development of the *hybrid suspension* concept and the adaptive reference model-based control approach.

1.2 Structure of the Thesis

An overview on modern vehicle suspension systems is given in Chapter 2. Based on a simple model (*quarter-vehicle model*) of the suspension system, performance criteria for ride comfort and safety as well as constraints, e.g. for the suspension deflection, that have to be met by suspension systems, are introduced. Moreover, an overview on the state of the art regarding the hardware of mechatronic suspension systems and their control techniques is presented including a literature survey on adaptive control approaches for mechatronic suspension systems.

In order to provide a realistic framework for the design and validation of the suspension control methods presented in this Thesis, Chapter 3 describes an experimental setup, that has been designed to study the potential of a fully active suspension configuration. The test rig is based on a quadricycle suspension and is equipped with a high bandwidth linear motor to realize the fully active suspension system. The Chapter also highlights the main nonlinearities of the considered suspension elements. The results are accurate models of the considered passive and active suspension configurations, which are used for the estimator and controller designs in the next two Chapters.

For the implementation of state feedback control techniques and the determination of the current driving state, information about the state variables of the vehicle is needed. However, measuring all state variables is economically not feasible and for some state variables like the tire deflection it is even difficult to be technically realized. Therefore, Chapter 4 describes estimator structures, that reconstruct the state vector from measurement signals, which are obtained from a realistic sensor configuration of modern production vehicles. A comparison of different new estimator concepts with varying complexity is presented and supported by simulation and measurement results.

In Chapter 5 the performance potential of a new adaptive switching controller structure for a fully active suspension system is analyzed. The controller structure interpolates between differently tuned state feedback controllers depending on the driving state. The adaptation is scheduled by an adaptation logic derived from the performance requirements for the suspension system. A stability analysis that takes into account the nonlinear damper characteristic and arbitrary fast switching between the controller settings is conducted. The performance of the proposed adaptive control approach is shown in simulations and measurements at the active suspension test rig and a comparison to benchmark controllers is presented.

Chapter 6 introduces an optimization based approach to evaluate the potential of different actuator configurations in suspension control with the aim to overcome the power demand drawback of a fully active suspension system. The combination of a low bandwidth actuator and a continuously variable semi-active damper (*hybrid suspension system*) is analyzed and it is shown that this suspension configuration has the potential to provide a performance similar to the fully active suspension system, if a suitable adaptive control approach is developed for the actuator combination.

The realization of this *hybrid suspension* configuration is demonstrated in Chapter 7 based on stock actuator components from production vehicles, i.e. a continuously variable hydraulic semi-active damper and a slow hydraulic actuator. Furthermore, a nonlinear model and suitable actuator controllers are developed for this new suspension configuration. Moreover, an appropriate automotive quarter-car test rig is presented, which has been designed to experimentally validate the performance potential of the *hybrid suspension* system.

Chapter 8 introduces a new adaptive reference model based controller structure that emulates the optimal passive suspension configuration for the current driving state. In combination with the hybrid suspension system, this control approach can provide lower actuator power demand compared to fully active systems although it is demonstrated in simulations and experiments that its performance in terms of comfort and ride safety is remarkable. The approach is compared to benchmark systems and aspects on the realizability of the concept are discussed.

A summary of the results and an outline of possible future work conclude the Dissertation in Chapter 9.

Furthermore, in Appendix A some theoretical preliminaries for linear quadratic regulator design, stability concepts and signal processing are given. The parameters of the considered suspension configurations as well as further simulation results are summarized in Appendix B.

Chapter 2

VEHICLE SUSPENSION SYSTEMS

In this Chapter, an overview on the relevant conceptual basics for vehicle suspension systems is given. First, the structure of a commonly used model for vehicle suspension systems, the quarter-vehicle model, is presented in Section 2.1. This model structure is employed in different contexts (e.g. nonlinear simulation models, test rig models with different actuator configurations) throughout this Thesis. In Section 2.2, two classes of road excitation signals are introduced and appropriate disturbance models, which are utilized in the Chapters 4, 6 and 8, are presented. The performance requirements for suspension systems and an approach for the vertical dynamic performance evaluation are given in Section 2.3.

Section 2.4 gives an overview on the state of the art of mechatronic suspension systems. Especially, semi-active and active suspension systems, which are either already available in production vehicles or have been studied as concepts by the automotive industry. Moreover, a survey on the state of the art of mechatronic suspension control is presented in Section 2.5. Since the vertical dynamic suspension control problem is a frequently used example in control engineering, in the given literature overview the focus is on control concepts for semi-active and active suspension systems. Control concepts that adapt their parametrization according to the driving state or the road excitation are presented in more detail.

Based on this overview, benchmark controllers are presented in Section 2.7, which are used to realistically evaluate the performance of the new adaptive suspension control concepts introduced in this Thesis.

2.1 Quarter-vehicle models

The vertical dynamic primary degrees of freedom of a vehicle are the heave, roll and pitch movements of the chassis [11]. In the literature, different models exist to describe the vertical dynamic behavior: Full-car models that take into account the dynamic behavior of the complete vehicle, half-car models to analyse pitch or roll movements and the simplest form, the quarter-vehicle[1] model, that describes only the heave motions of an equivalent sprung mass and one wheel [106]. If the motions of the four wheels are assumed to be decoupled, the quarter-vehicle model is a suitable model in the frequency range of interest for suspension control, i.e. $0-25\,\mathrm{Hz}$ [129].

Figure 2.1 depicts the quarter-vehicle models for three different suspension types, which are presented in more detail in this Chapter, i.e. passive, semi-active and fully active suspension systems (see Section 2.4 for a detailed classification of suspension types). In general, a quarter-vehicle model consists of the unsprung mass m_w (representing the tire, the wheel, the brake and parts of the masses of the wheel carrier and suspension system), the sprung mass m_c (representing a quarter of the mass of the chassis including passengers and loading), the suspension system to connect the two masses and a tire model represented by a parallel spring and damper configuration. In the semi-active suspension (middle), the damping $d_c = d_c(t)$ is adjustable (see also Section 2.4) and in the fully active suspension system, a force $F(t)$ can be applied by an actuator (e.g. an electrical linear motor) between the sprung and the unsprung mass. In order to get first insights regarding the vertical dynamic behavior of a suspension system and for the performance evaluation of vertical dynamic suspension control concepts for the vertical translatory motions (see e.g. [30, 55, 66, 76, 138]), the quarter-vehicle model structure is well suited due to its simple structure and sufficient accuracy if nonlinear suspension components are considered [106].

To present the structure of the quarter-vehicle model and describe its fundamental properties, linear characteristics of the tire and the damper are assumed. The equations of motions are derived for the fully active system including a passive damper, since the other two suspension models result from this model if the control force vanishes, i.e. $F(t) = 0$ (passive system), and

---

[1] It is noted that due to the quadricycle suspension system considered in Chapter 3, the term “quarter-vehicle” instead of “quarter-car” is used for general models in this Thesis, except when it is actually referred to an automotive suspension (Chapters 7 and 8).

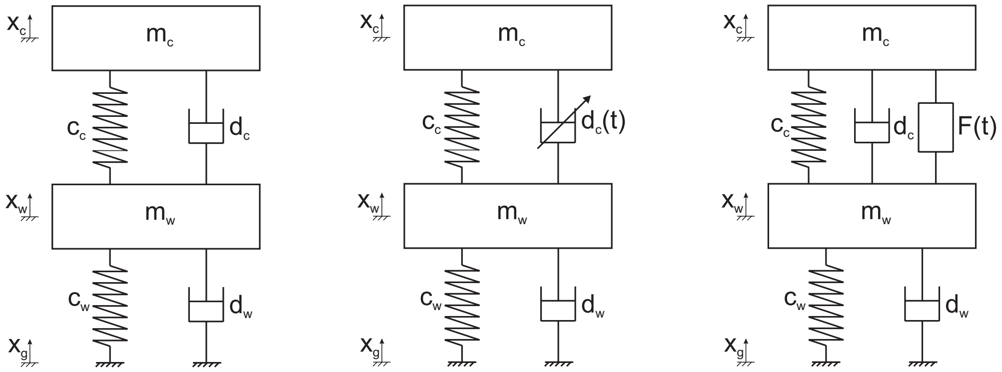

Figure 2.1: Quarter-vehicle models of a passive, semi-active and fully active suspension system.

the damping is adjustable, i.e. $d_c = d_c(t)$ (semi-active system). The equations of motion are

$$m_c\ddot{x}_c = -c_c\left(x_c - x_w\right) - d_c\left(\dot{x}_c - \dot{x}_w\right) + F\left(t\right), \tag{2.1}$$

$$m_w\ddot{x}_w = c_c\left(x_c - x_w\right) + d_c\left(\dot{x}_c - \dot{x}_w\right) - c_w\left(x_w - x_g\right) - d_w\left(\dot{x}_w - \dot{x}_g\right) - F\left(t\right). \tag{2.2}$$

Let

$$\mathbf{x} = \begin{bmatrix} x_1 \\ x_2 \\ x_3 \\ x_4 \end{bmatrix} = \begin{bmatrix} x_c - x_w \\ \dot{x}_c \\ x_w - x_g \\ \dot{x}_w \end{bmatrix} \tag{2.3}$$

be the state-vector and

$$u = F\left(t\right), \tag{2.4}$$

$$u_d = \dot{x}_g \tag{2.5}$$

be the control input u and the disturbance input u_d of the quarter-vehicle model, respectively. The output vector **y** includes the variables of interest for the suspension performance as

$$\mathbf{y} = \begin{bmatrix} \ddot{x}_c \\ F_{dyn} \\ x_c - x_w \end{bmatrix}, \tag{2.6}$$

where $F_{dyn} = c_w(x_g - x_w) + d_w(\dot{x}_g - \dot{x}_w)$ denotes the dynamic wheel load. Then, the quarter-vehicle model can be expressed as a linear state space model in the form

$$\begin{aligned} \dot{\mathbf{x}} &= \mathbf{A}\mathbf{x} + \mathbf{b}u + \mathbf{e}u_d\,, \qquad (2.7) \\ \mathbf{y} &= \mathbf{C}\mathbf{x} + \mathbf{d}u + \mathbf{f}u_d \qquad (2.8) \end{aligned}$$

as

$$\begin{bmatrix} \dot{x}_1 \\ \dot{x}_2 \\ \dot{x}_3 \\ \dot{x}_4 \end{bmatrix} = \begin{bmatrix} 0 & 1 & 0 & -1 \\ -\frac{c_c}{m_c} & -\frac{d_c}{m_c} & 0 & \frac{d_c}{m_c} \\ 0 & 0 & 0 & 1 \\ \frac{c_c}{m_w} & \frac{d_c}{m_w} & -\frac{c_w}{m_w} & -\frac{d_c+d_w}{m_w} \end{bmatrix} \begin{bmatrix} x_1 \\ x_2 \\ x_3 \\ x_4 \end{bmatrix} + \begin{bmatrix} 0 \\ \frac{1}{m_c} \\ 0 \\ -\frac{1}{m_w} \end{bmatrix} u + \begin{bmatrix} 0 \\ 0 \\ -1 \\ \frac{d_w}{m_w} \end{bmatrix} u_d\,, \tag{2.9}$$

$$\begin{bmatrix} \ddot{x}_c \\ F_{dyn} \\ x_c - x_w \end{bmatrix} = \begin{bmatrix} -\frac{c_c}{m_c} & -\frac{d_c}{m_c} & 0 & \frac{d_c}{m_c} \\ 0 & 0 & -c_w & -d_w \\ 1 & 0 & 0 & 0 \end{bmatrix} \mathbf{x} + \begin{bmatrix} \frac{1}{m_c} \\ 0 \\ 0 \end{bmatrix} u + \begin{bmatrix} 0 \\ d_w \\ 0 \end{bmatrix} u_d\,. \tag{2.10}$$

Thus, the model is improper regarding both input signals due to the direct feedthrough terms in (2.10). Exemplary parameters for the quarter-vehicle model of a compact-car are given in Table 2.1 and formulas for the calculation of the natural frequencies and damping ratios are given in Table B.5 in the Appendix. Detailed discussions on the influence of the suspension parameters on the dynamic behavior of the suspension are presented in [50, 106, 170]. Figure 2.2 shows the Bode diagrams of the corresponding passive suspension system ($x_{cw} = x_c - x_w$ denotes the suspension deflection), where the resonance peaks of the unsprung and sprung mass can be seen clearly (see also Section 2.3.1).

It is noted that the tire damping d_w is small and thus it is frequently neglected in the literature (see Table 2.1) [106]. In this case, an invariant point occurs in the transfer function $G_{\ddot{x}_c \dot{x}_g}(s)$ (from the road excitation $\dot{x}_g$ to the chassis acceleration $\ddot{x}_c$) at the “tirehop frequency” $\omega_1 = \sqrt{\frac{c_w}{m_w}}$ [31, 49]. Invariant points can limit the achievable performance of a mechatronic suspension system if the system is analyzed in a linear framework [67]. Since tire damping is taken into account for most of the control approaches presented in the following Chapters and the simulations are conducted with nonlinear quarter-vehicle models, the invariant point at the “tirehop frequency” vanishes. For detailed discussions on invariant points of linear quarter-vehicle models the reader is referred to [49, 67, 128].

Table 2.1: Quarter-vehicle model parameters of an exemplary compact-car [106, 170].

Model parameter	Symbol	Value	Unit
Quarter-car chassis mass (sprung mass)	m_c	256	[kg]
Wheel assembly mass (unsprung mass)	m_w	31	[kg]
Suspension spring stiffness	c_c	20200	[N/m]
Tire stiffness	c_w	128000	[N/m]
Tire damping	d_w	0	[Nsec/m]
Sprung mass damping coefficient	d_c	1140	[Nsec/m]
Undamped uncoupled natural frequency of the sprung mass	$f_c = \frac{1}{2\pi}\sqrt{\frac{c_c}{m_c}}$	1.41	[Hz]
Damping ratio sprung mass	$D_c = \frac{d_c}{2\sqrt{m_c c_c}}$	0.25	[−]
Uncoupled natural frequency of the unsprung mass	$f_w = \frac{1}{2\pi}\sqrt{\frac{c_c+c_w}{m_w}}$	11.00	[Hz]
Damping ratio unsprung mass	$D_w = \frac{d_c+d_w}{\sqrt{m_c(c_c+c_w)}}$	0.09	[−]

2.2 Disturbance types and models

The vehicle is subject to vibrations induced by different sources (see [106]). While vehicle induced vibrations (e.g. by the motor or unbalanced masses) are periodic, road induced vibrations are in general of stochastic type e.g. [106]. In this Section, the road induced disturbance is considered. Therefore, in Section 2.2.1 stochastic road profiles and two types of models for stochastic road induced vibrations are presented. Since for the design of any suspension system also singular disturbance events (also called discrete-event disturbances) like bumps or potholes have to be taken into account, e.g. to determine if the suspension deflection limits are sufficient, in Section 2.2.2 a widely used model for singular disturbance events is presented.

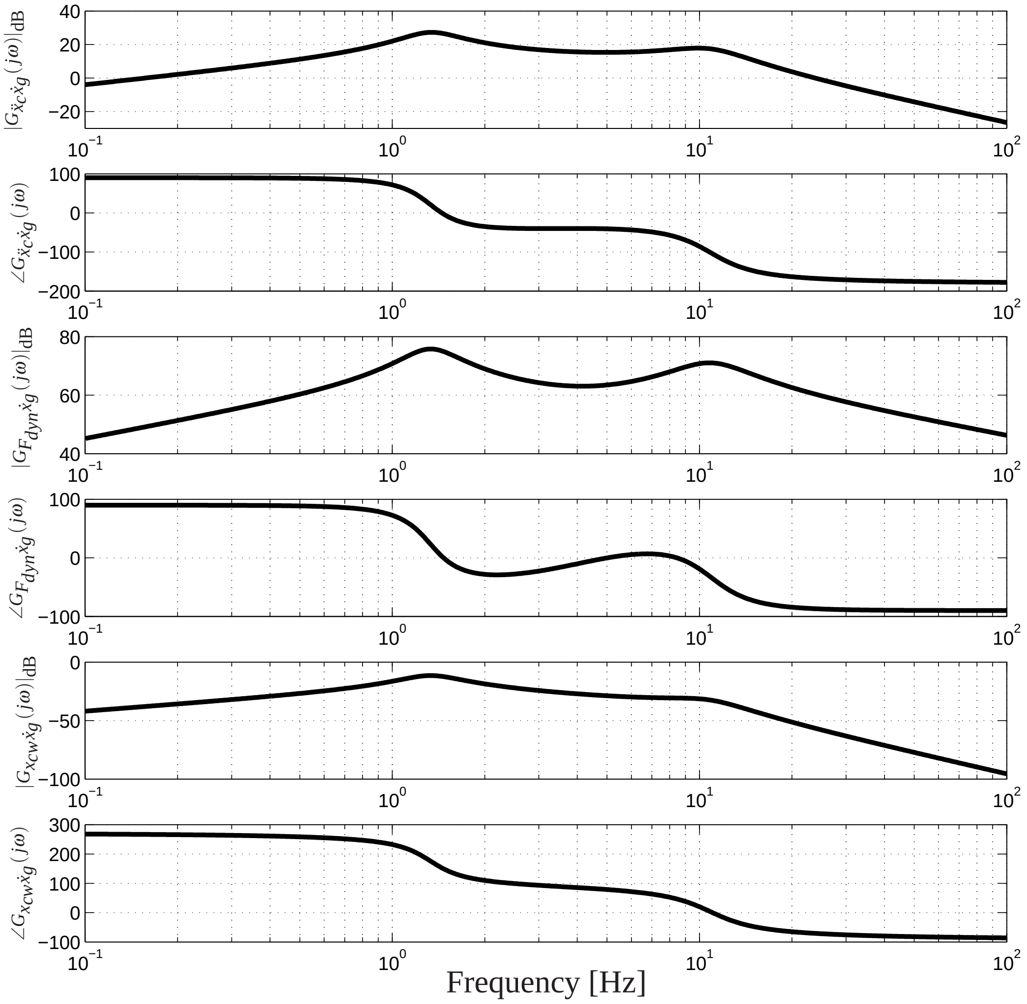

Figure 2.2: Bode diagrams of the passive suspension system (2.9)-(2.10) with parameters according to Table 2.1 (phases are given in degrees).

2.2.1 Stochastic road profiles

In general, public roads induce stochastic vibrations to the vehicles. The intensity of these vibrations depends on the quality of the road and the velocity of the passing vehicle. In order to provide a realistic framework regarding the excitation signals considered in this Thesis, measurements of real road profiles are used for the simulations and for the experiments conducted at the designed test rigs. The road profiles have been recorded on German highways and country roads by a vehicle equipped with laser scanners and accelerometers to compensate for the test vehicle's chassis movements.

Two exemplary profiles (P1 and P2) are depicted in Figure 2.3, where y_d denotes the horizontal coordinate of the road in $[\mathrm{m}]$. A way to analyze the road roughness in terms of its spatial frequency components is the calculation of the spatial power spectral density (PSD) $\tilde{P}_{x_g x_g}(\tilde{f})$ in $[\mathrm{m}^3]$, where $\tilde{f}$ denotes the spatial frequency given in $[\frac{1}{\mathrm{m}}]$ (see Appendix A.3). The profiles P1 and P2 as well as their corresponding PSDs are shown in Figure 2.3. The broader spatial power spectrum of profile P2 (Figure 2.3 (b)) indicates its high frequency components and a higher roughness compared to profile P1.

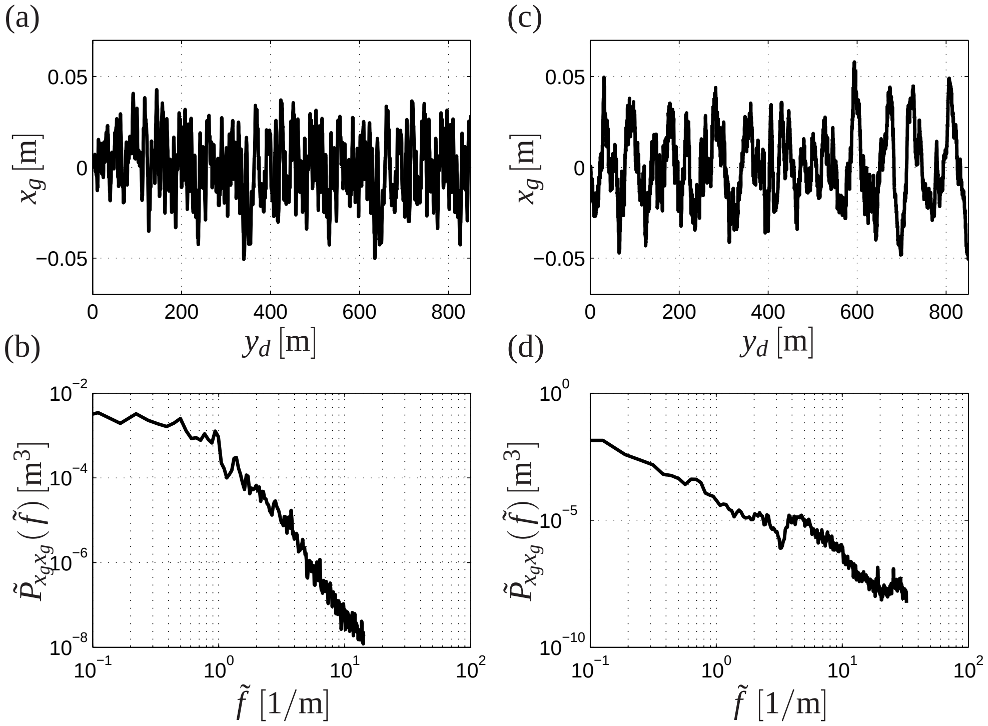

Figure 2.3: Measured road profiles and their spatial power spectral density (profile P1 (a) and (c) and profile P2 (b) and (d)).

For the description of road induced vibrations in terms of a disturbance model, different approaches exist in literature (see e.g. [55], [106]). Random road induced vibrations are frequently modeled by a stationary random process. A corresponding simple approximation of the power spectral density of stochastic road displacement signal $x_g(t)$ is given in [55] as

$$S_{x_g x_g}(f) = \frac{1}{v} A \left(\frac{2\pi f}{v} \right)^n , \tag{2.11}$$

where A is a constant roughness factor in $[\mathrm{m}]$, f is the excitation frequency in $[\mathrm{Hz}]$ and v is the constant vehicle velocity in $\left[\frac{\mathrm{m}}{\mathrm{sec}}\right]$. For the parameter n a value of -2 is assumed, which coincides with the commonly used assumption of white noise for the vertical ground velocity and hence a constant power spectrum

$$S_{\dot{x}_g \dot{x}_g}(f) = (2\pi f)^2 \cdot S_{x_g x_g}(f) = Av \tag{2.12}$$

depending on the road conditions and the driving speed. To characterize the stochastic properties of the road surface (without the dependence on v), the one-sided spatial PSD $\tilde{P}_{x_g}(\tilde{f})$ (see Appendix A.3) subject to the spatial frequency $\tilde{f} = \frac{f}{v}$ can be calculated from (2.11) by (see e.g. [169])

$$\tilde{P}_{x_g x_g}(\tilde{f}) = 2 \cdot v \cdot S_{x_g x_g}(v\tilde{f}) . \tag{2.13}$$

Figure 2.4 shows an approximation of the one-sided spatial PSD of a measured road profile by the model of the PSD given in (2.13). It can be seen that the approximation justifies the assumption of white noise for the vertical ground velocity for a certain class of stochastic road profiles. Due to its simple structure, this model is frequently used for the analysis of the performance potential of a suspension system, e.g. in [55], [75] and will also be employed for a similar analysis in Chapter 6.

A more detailed model of the road displacement is bandlimited white noise since it introduces one additional free parameter to describe the PSD of the road induced vibrations. The model is given by

$$S_{x_g x_g}(\omega) = \frac{\alpha v}{\beta^2 v^2 + \omega^2} , \tag{2.14}$$

where ω is the angular frequency, v is the vehicle velocity and α, β are parameters characterizing the road irregularities [106]. By this model, the nearly constant power spectral density of profile P1 (see Figure 2.3 (b)) can be better approximated in the low frequency range. The model is presented in more detail in Chapter 4.1.1 since it will be employed for the estimator design.

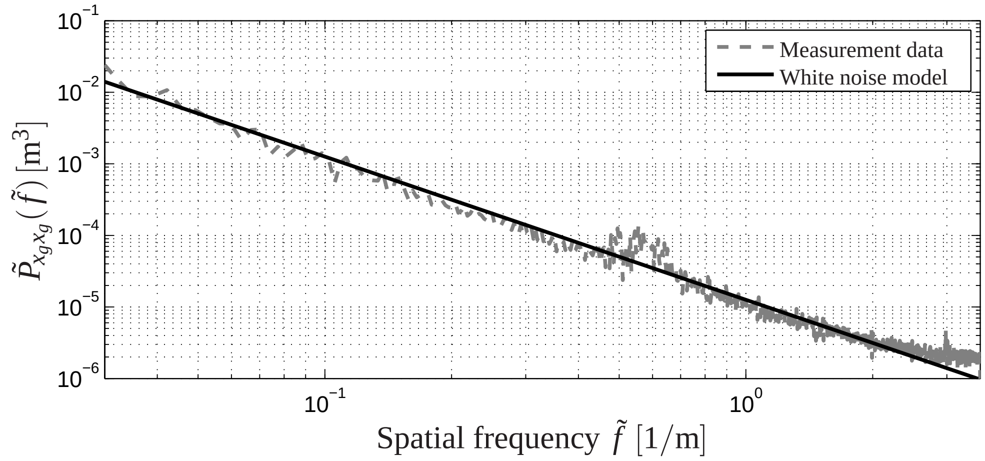

Figure 2.4: One-sided spatial spectral density $\tilde{P}_{x_g x_g}(\tilde{f})$ of a measured highway road profile and an approximation according to (2.11) with $n = -2$.

2.2.2 Singular disturbance events

Besides stochastic excitation signals, singular disturbance events are used in literature (e.g. in [30, 106]) to test the performance of suspension systems. A simple model of the vertical road displacement resulting from a singular disturbance event (a “bump”) is given in [106] as

$$x_g(y) = \begin{cases} h\left(1 - \cos\left(\frac{2\pi}{L} y_d\right)\right) & \text{for} \quad 0 \leq y_d \leq L \\ 0 & \text{else} \end{cases} , \tag{2.15}$$

where y_d marks the longitudinal distance in [m], the parameter h is half the bump height $\hat{h}$ and L is the length of the bump in [m]. Figure 2.5 shows an exemplary parametrization of this model for a singular disturbance event. If a vehicle passes the bump with the velocity v_b the corresponding signal

$$x_g(t) = \begin{cases} h\left(1 - \cos\left(\frac{2\pi v_b}{L} t\right)\right) & \text{for} \quad 0 \leq t \leq \frac{L}{v_b} \\ 0 & \text{else} \end{cases} \tag{2.16}$$

results.

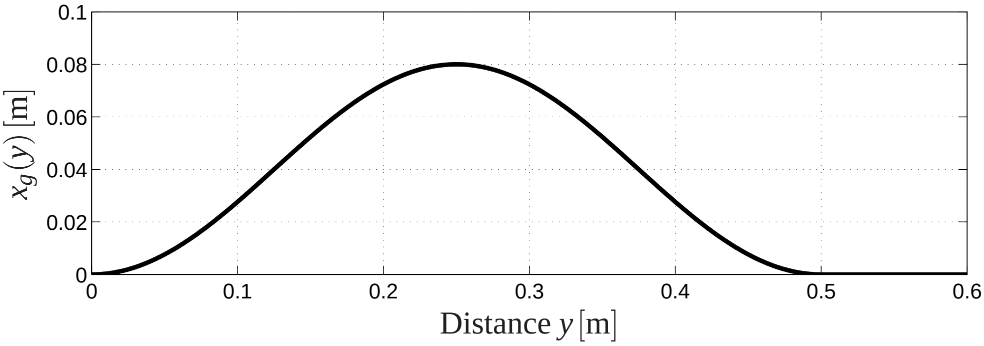

Figure 2.5: Singular disturbance event with $\hat{h} = 0.08\,\mathrm{m}$ and $L = 0.5\,\mathrm{m}$.

2.3 System requirements and performance evaluation

2.3.1 Ride comfort

A simple, yet frequently used measure for ride comfort is the root mean square (rms) value of the vertical chassis acceleration $||\ddot{x}_c||_{\mathrm{rms}}$, which should be minimized. A suspension system enhances ride comfort by isolating the chassis mass from the vibrations induced by the road or the dynamics of the vehicle. Thus, in terms of vertical translatory vibrations, ride comfort can be quantified by the acceleration of the chassis mass (if the suspensions of the seats are neglected [106]). However, to objectify ride comfort, the human sensitivity for vibrations, which is frequency dependent, must be taken into account. The most sensitive frequency range for vertical mechanical excitation is $4-8\,\mathrm{Hz}$ [59, 106, 163].

This fact is considered in the design of suspension configurations since the mass ratio of sprung and unsprung mass as well as the stiffnesses of the primary spring and the tire are chosen so that this frequency interval lies between the natural frequencies of the sprung and the unspung mass (see Table 2.1). Thereby, the resulting isolation effect of the sprung mass is utilized (see Figure 2.6 (upper)). In the frequency response of the disturbance transfer function $|G_{\ddot{x}_c\dot{x}_g}(j\omega)|$ from the vertical ground velocity $\dot{x}_g(t)$ to the chassis acceleration $\ddot{x}_c(t)$, the gain decreases between the two resonance peaks. However, the shape of the frequency response depends on the damping d_c, since low damping coefficients lead to good isolation properties of the chassis mass in the comfort relevant frequency range, but increase the resonance peaks. Hence, ride safety is deteriorated due to the low damping of the unsprung mass and high amplitudes of the chassis acceleration are caused in the range of the natural frequency of the sprung mass. This conflict for the choice of damping is called *damping-isolation conflict* (see e.g. [10, 119, 170]).

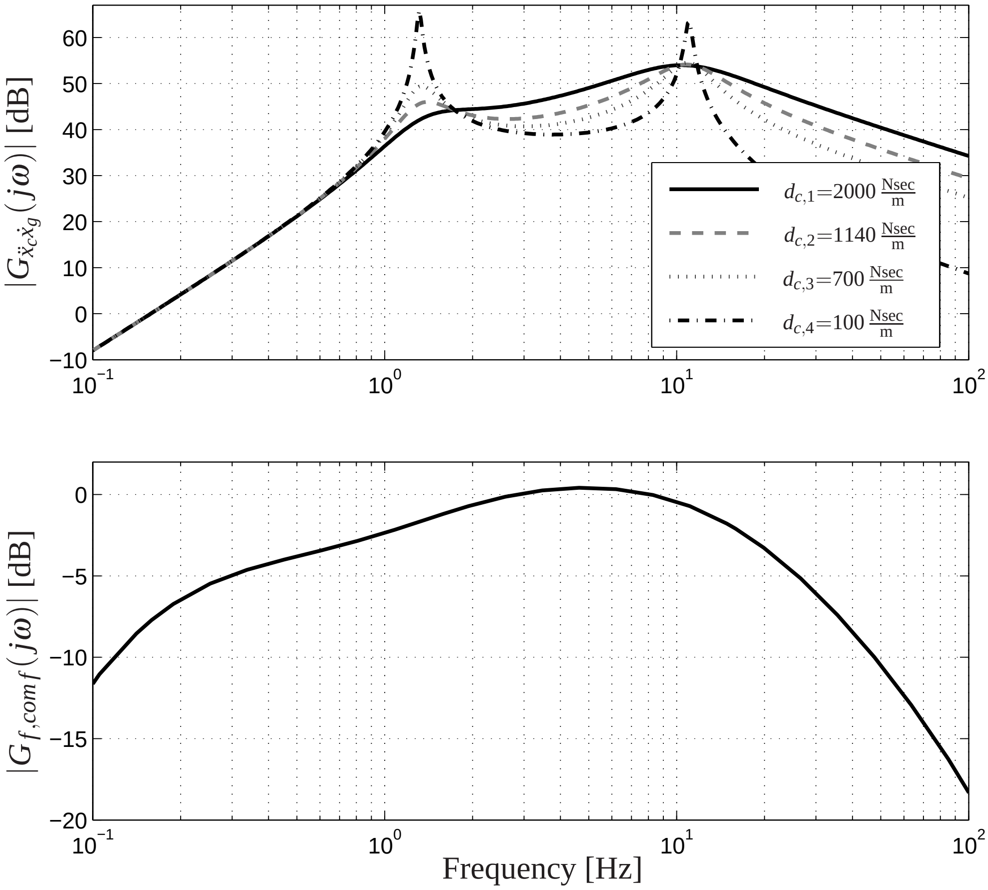

Figure 2.6: Damping isolation conflict (upper) and frequency response of the shaping filter $G_{f,comf}(s)$ (lower) [59, 163].

The shaping filter characteristic presented in [59, 163] can be approximated by a fifth-order linear transfer function $G_{f,comf}(s)$ with a frequency response as depicted in Figure 2.6 (lower) to emphasize the comfort relevant frequency range for the evaluation of ride comfort. Thus, the weighted chassis acceleration can be calculated by the convolution

$$\ddot{x}_{c,comf}(t) = g_{f,comf}(t) * \ddot{x}_c(t)\,, \tag{2.17}$$

where $g_{f,comf}(t)$ represents the impulse response of the system $G_{f,comf}(s)$. A measure for comfort is accordingly the rms-value of the weighted vertical chassis acceleration $\|x_{c,comf}(t)\|_{\text{rms}}$, since the frequency weighting is especially relevant for vibrations acting on the human body over a longer time period [59, 163].

Furthermore, the maximum of the absolute value of the chassis acceleration $\max(|\ddot{x}_c(t)|)$ is employed to evaluate ride comfort of a suspension which allows to consider peaks in the acceleration signal, especially occuring for singular disturbance events. Further criteria to evaluate ride comfort are formulated e.g. in [106, 171].

2.3.2 Safety requirements

As pointed out in Chapter 1, ride safety in terms of the vertical dynamic behavior of the vehicle is provided by the suspension if forces can be transferred between the tire and the road. This is the crucial requirement to provide that the driver has authority over the vehicle by steering, braking and throttle actions. A simplified criterion to provide ride safety is that the dynamic wheel load must not exceed the static wheel load, which can be achieved if the dynamic wheel load is bounded [106]. For the formulation of an appropriate bound, it is assumed that the vertical road displacement is stochastic and that the resulting dynamic wheel load F_{dyn} has a Gaussian probability density. A bound on F_{dyn} can then be formulated using the standard deviation (see Appendix A.3)

$$\sigma_{F_{dyn}} = \|F_{dyn}\|_{\text{std}} = \sqrt{\frac{1}{T}\int_0^T F_{dyn}^2(\tau)d\tau} \tag{2.18}$$

over a time period T. Since the mean of the dynamic wheel load is zero, $\sigma_{F_{dyn}} = \|F_{dyn}\|_{\text{rms}}$ holds (see Appendix A.3.1). The 3σ-rule for stochastic signals assures - assuming a normally distributed zero mean stochastic signal - that F_{dyn} remains within the bounds $\pm F_{stat}$ for approx. 99.7% of the time period T [106, 169].

Therefore, the bound for the dynamic wheel load's rms-value is formulated as

$$\|F_{dyn}\|_{\text{rms}} \leq \frac{F_{stat}}{3} , \tag{2.19}$$

where $F_{stat} = g\,(m_c + m_w)$ denotes the static wheel load with $g = 9.81\,\frac{\text{m}}{\text{sec}^2}$ being the gravitational constant. In Figure 2.7, a Gaussian approximation of the probability density of the dynamic wheel load of a passive suspension system resulting from the excitation by the measured road profile P1 (passed with the velocity $v_{p1} = 50\,\frac{\text{km}}{\text{h}}$) is depicted. It can be seen that the bound formulated in (2.19) is kept. It is noted that only negative dynamic wheel loads are safety critical since they can cause the wheel to lose ground contact. Hence, due to the symmetry of the Gaussian probability distribution, the bound (2.18) even ensures that the wheel keeps ground contact for approx. 99.88% of T (under the presented assumptions).

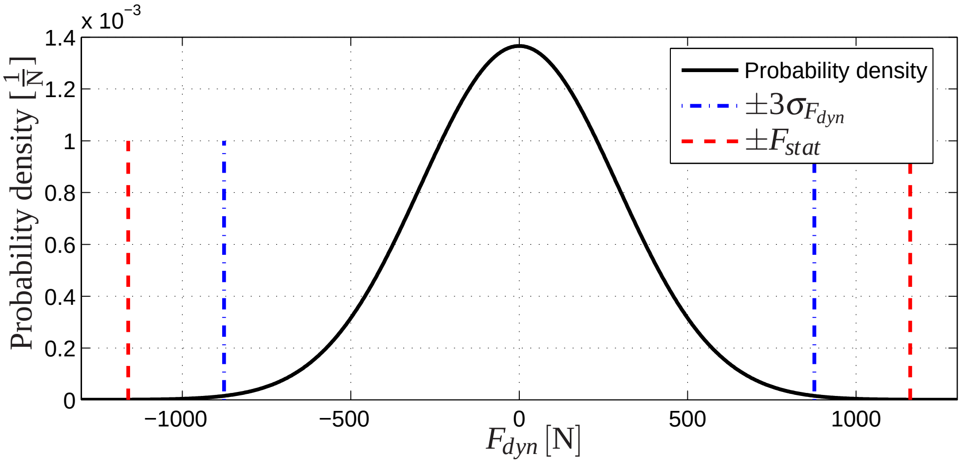

Figure 2.7: Approximation of the probability density of F_{dyn} for a stochastic road profile (passive suspension system).

2.3.3 Further requirements

Requirements on suspension deflection

The suspension deflection has to keep the constructionally given limits in order to prevent peak-like chassis accelerations and wear of components. Moreover, by keeping the suspension limits, the behavior of the suspension remains predictable for the driver which facilitates keeping the authority over the vehicle. Therefore, the suspension deflection $x_c - x_w$ should remain between its lower and upper bound, i.e.

$$\underline{x}_{cw} \leq x_c - x_w \leq \overline{x}_{cw}. \tag{2.20}$$

A violation of the compression limit $\underline{x}_{cw}$ of the suspension is frequently more critical than a violation of the rebound limit $\overline{x}_{cw}$ as by hitting the compression end stop the base valve of the damper may be damaged and the transferred energy can be higher if the kinetic energy of the heavier sprung mass must be dissipated by the compression end stop.

It is noted that due to the constructionally given asymmetry of the damper characteristic in compression and rebound direction, the equilibrium point of the suspension can shift slightly in the presence of a nonvanishing stochastic road excitation [106]. In this case, the suspension deflection exhibits a mean value, which differs from zero. To consider this fact, the standard deviation (see Appendix A.3.1) of the suspension deflection is frequently used to characterize the dynamic suspension behavior on different roads. To accordingly prevent the suspension deflection from being exceeded by means of a stochastic bound, the same approach as for the dynamic wheel load bound (2.19) can be employed using the 3σ-rule, i.e. the standard deviation of the suspension deflection should not exceed a third of the maximum suspension deflection, which can be expressed using the compression limit as

$$\|x_c - x_w\|_{\mathrm{std}} \leq \frac{1}{3}|\underline{x}_{cw}| \,. \tag{2.21}$$

Actuator power demand

A mechatronic suspension system should operate with a minimum amount of power. In order to classify the actuator power demand, the rms-value of the positive mechanical actuator power $\|P^+\|_{\mathrm{rms}}$ is considered (see also [116], [115]), which is calculated as

$$\|P^+\|_{\mathrm{rms}} = \sqrt{\frac{1}{T}\int_0^T (P^+)^2(\tau)d\tau}\,, \tag{2.22}$$

$$P^+(t) = \begin{cases} F(t)\Delta\dot{x}_{act}(t) & \text{for} \quad F(t)\Delta\dot{x}_{act}(t) > 0 \\ 0 & \text{else} \end{cases} \,, \tag{2.23}$$

where $\Delta\dot{x}_{act}(t)$ denotes the relative velocity of the actuator rod and $F(t)$ denotes the actuator force. It is noted that for a more realistic analysis of the absolute power demand, the efficiency factors of the actuator system (e.g. hydraulic and/or electrical efficiency factors) as well as potential recuperation effects have to be taken into account. However, since these factors are not exactly known for the actuators presented in this Thesis and primarily a relative comparison of power demand is intended (as in [81]), the described approach represents a suitable method for the power demand analysis.

Moreover, for the realization of a mechatronic suspension system, further requirements especially regarding the actuators have to be taken into account for the design: Low friction of the actuators, compact packaging, low weight, low costs, few moving parts to minimize wear and low maintenance effort.

2.3.4 Performance evaluation

Besides the system requirements described in the last Section, the suspension performance relative to benchmark suspension systems is important to evaluate the suspension system. Consequently, for the performance evaluation of the suspension controllers presented in this Thesis, the performance gain of a mechatronic suspension is given with respect to a reference system as

$$P_{g,\mathrm{obj}} = 1 - \frac{\|\mathrm{obj}_{\mathrm{cont}}\|_i}{\|\mathrm{obj}_{\mathrm{ref}}\|_i}\,, \tag{2.24}$$

where $\|\mathrm{obj}_{\mathrm{cont}}\|_i$ denotes the absolute performance of the controlled suspension with respect to any of the criteria $\|\cdot\|_i$ (rms-value, peak values etc.) described in this Section and $\|\mathrm{obj}_{\mathrm{ref}}\|_i$ is the performance of a benchmark suspension, which represents the reference. A positive value of $P_{g,\mathrm{obj}}$ denotes a reduction of the absolute value of the corresponding quantity and thus a performance improvement. As an example, the ride comfort performance of a controlled mechatronic suspension with respect to the passive reference suspension is specified as

$$P_{g,\ddot{x}_{c,comf}} = 1 - \frac{\|\ddot{x}_{c,comf,reg}\|_{\mathrm{rms}}}{\|\ddot{x}_{c,comf,pass}\|_{\mathrm{rms}}}\,. \tag{2.25}$$

2.4 Mechatronic suspension systems: State of the art

Mechatronic suspension systems can be classified according to their actuator types including the actuator bandwidth, the power demand of the actuators and their controllability range (see [129]), i.e. the restrictions for the forces the actuators deliver. Accordingly, mechatronic suspension systems can be classified into five groups [106, 129]:

1. *Automatic level control systems* operate quasi-statically and keep the distance between the chassis and the road constant to compensate for different loading levels of the vehicle [50]. A level control system can be based on airsprings and compressors. Thus, a soft, comfort oriented suspension setup with sufficient suspension travel can be realized independent from the vehicle's load level. Their power demand is within the range of $100-200\,\mathrm{W}$ [129].

2. *Adaptive suspension systems* denote in the literature suspension systems, which realize a slow variation of the spring and the damper characteristics. The variation is scheduled e.g. according to the vehicle velocity in order to lower the center of gravity of

the vehicle to ensure a more sportive road holding. This is realized e.g. in the *Porsche Panamera* (model year 2009) via airsprings [22, 52]. *Citroën* introduced the adaptive suspension system *hydractive suspension* in 1989, which realizes a slow adjustment between different airspring characteristics and discrete settings of the damper characteristics [106, 121]. Their power demand depends mainly on the required energy for changing the spring stiffness. It is emphasized that in this Thesis, adaptive suspension control concepts are presented to achieve a highly dynamic adaptation to the current driving state.

3. Suspension systems with the possibility of a fast adjustment of the damper characteristics and/or spring stiffness are called *semi-active suspensions*. A main attribute of semi-active systems is that the force generated by the semi-active element depends on the direction of relative motion of the element (see Section 2.4.1). Semi-active dampers can change the level of energy dissipation but do not supply energy to the system. Accordingly, they have a very low power demand of approx. $20-40\,\mathrm{W}$ per damper. The bandwidth of the semi-active dampers ranges up to approx. $40\,\mathrm{Hz}$ [129]. Semi-active dampers are integrated amongst others in the current versions of the *Audi R8*, *BMW 7 series*, *Porsche 911* and *Mercedes Benz E-class*. An example for a semi-active spring element is an anti-roll bar with switchable additional springs, which is presented by *ZF Lemförder GmbH* in [50].

4. *Slow active systems* (also called *low bandwidth active system*) are a class of active suspension systems (see Section 2.4.2). They are characterized by an additional actuator (e.g. an electrical linear motor or hydraulic cylinder), that is integrated into the suspension and can generate suspension forces independent of the relative motion of the chassis and wheels. The bandwidth of slow active systems is in the range of approx. $5\,\mathrm{Hz}$. Slow active systems typically employ actuators, which are integrated in series to the primary spring and tend to "stiffen" if their bandwidths are exceeded [137]. Their energy demand is in the range of $1-5\,\mathrm{kW}$ [129].

5. In *fully active systems* (also called *high bandwidth active systems*) the passive damping element is replaced or supplemented by an actuator with a bandwidth of $20\,\mathrm{Hz}$ or higher [129]. The actuators of fully active systems are integrated in parallel to the primary spring and in some applications, the passive damper is omitted (although its consider-

ation in the quarter-vehicle model can be used to describe friction effects). The main drawback of fully active suspensions, however, is their high energy demand, which ranges from 4 – 20 kW [50].

Table 2.2 summarizes the main categories of mechatronic suspension systems. Semi-active and active suspension systems are described in more detail in the following Sections.

2.4.1 Semi-active suspension systems

Todays semi-active suspension systems are able to rapidly adjust the damper characteristics [68, 106] of the shock absorbers. Three physical principles of operation can be distinguished [19, 50]:

- *Hydraulic dampers* dissipate energy by throttling hydraulic oil between two or more chambers inside the damper. For the technical realization of a semi-active hydraulic damper, valves are used to vary the cross-section of the opening between the chambers and thus the level of dissipation is varied [43]. Exemplary applications for the widely used hydraulic damping principle for semi-active suspensions are presented in [133] and [60].

- In *magnetorheological dampers*, the viscosity of a magnetorheological fluid is changed by applying a magnetic field, which causes magnetic particles in the fluid to form chains [38, 129]. A magnetorheological damping system called *MagneRide* is presented by *Delphi* [2].

- *Electrorheological dampers* also operate based on varying flow properties of the contained electrorheological fluids except that an electrical field is used to cause the forming of particle chains in the fluid [19]. An advantage of electrorheological dampers over magnetorheological dampers is that the particles in the fluids are not abrasive so that the durability of the seals is less critical.

The fact that a semi-active damper is a passive element, which can not supply energy to the suspension system, is expressed by a passivity constraint (see e.g. [41, 129]) for the velocity

Table 2.2: Classification of suspension systems [32, 50, 121, 129].

Type	Model	Force restriction	Operating range	Energy demand
Passive	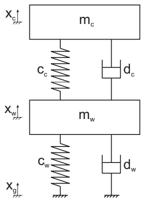	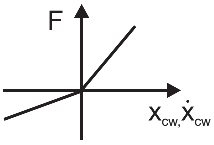	no actuators	0 W
Adaptive	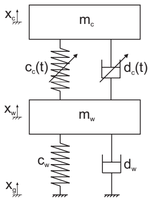	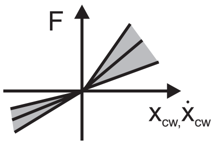	< 1 Hz	low
Semi-active	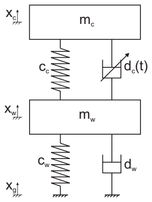	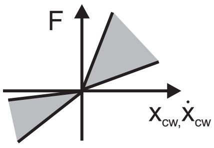	0 – 40 Hz	low
Slow active	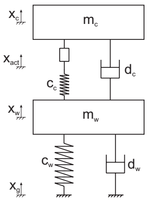	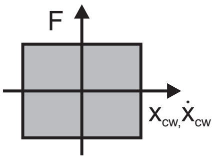	0 – 5 Hz	medium
Fully active	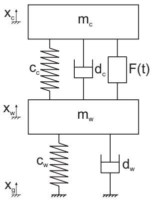	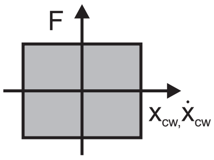	0 – 30 Hz	high

dependent damper force $F_d(t) = d_c\,(\dot{x}_c(t) - \dot{x}_w(t))$, i.e.

$$F_d(t)\,(\dot{x}_c(t) - \dot{x}_w(t)) \geq 0\,, \quad \forall t\,. \tag{2.26}$$

Important criteria for the achievable performance of semi-active suspensions are the spread of the damper, which denotes the range $d_{c,min} \leq d_c \leq d_{c,max}$ in which the damping coefficient can be varied, and the dynamics of the damper, which are determined by its electrical and fluid dynamical components (see also Section 2.5.1 and Chapter 8). Due to their comparatively low energy consumption (only for the positioning of the electromagnetical valves or the generation of electrical or magnetic fields respectively energy is required), their low costs and their simple structure, semi-active damping systems are significantly more prominent in modern mechatronic vehicle suspensions than active systems (see also [165]).

2.4.2 Active suspension systems

As described at the beginning of this Section, *high bandwidth* and *low bandwidth active systems* are classes of active suspension systems (Table 2.2). The company *BOSE* works on a concept for a high bandwidth active suspension system since 1980 (Figure 2.8) [61]. In this system, the conventional passive dampers are replaced by electrical linear motors and the static load of the vehicle is suspended by torsion bars. A reaction mass absorber is attached to each wheel (Figure 2.8 (right)) in order to reduce the resonance peak at the natural frequency of the unsprung mass (see Figures 2.6 (upper) and 2.2) without transferring the reaction forces directly to the chassis [3]. Although the system is able to recuperate energy by driving the linear motors in generator mode, and *BOSE* specifies the power demand of the system as being less than “one-third of the energy used by a car’s air conditioner” [61], the system has not yet been integrated into a production vehicle presumably due to packaging aspects, costs and power demand.

Mercedes Benz employs a low bandwidth active suspension system called *Active Body Control (ABC)* (see Figure 2.9 (left)), which is integrated since 1999 in the *Mercedes Benz S-class*, the coupe *CL-class* and since 2001 in the *SL roadster* [121]. It features a hydraulic cylinder that is mounted in series to the primary spring (Figure 2.9 (right)) and has a control bandwidth of 5 Hz. The system actively damps the translatory movement of the chassis mass as well as the roll and pitch motions and can also operate as a level control system [147]. The damping of the unsprung mass, however, is realized by a passive damper.

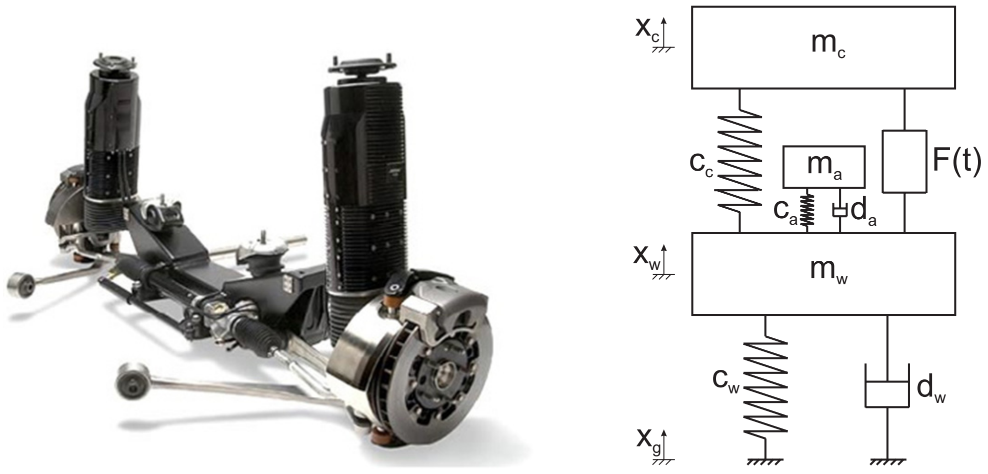

Figure 2.8: High bandwidth active suspension concept by *BOSE* [3, 61] (left) and its quarter-car model (right). The left image is reproduced with kind permission of *BOSE Automotive GmbH*.

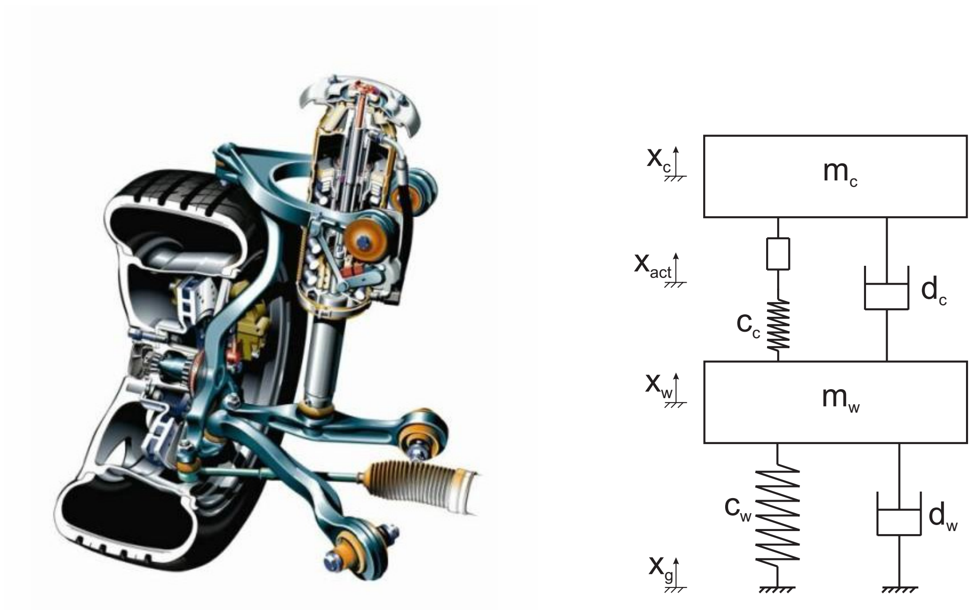

Figure 2.9: *Active Body Control (ABC)* low bandwidth active suspension system by *Mercedes Benz* [121] (left) and its quarter-car model (right). The left image is courtesy of *Daimler AG* and is reproduced with kind permission.

In 2008, an enhanced version of the *ABC-system* has been presented in the concept car *Mercedes Benz F700*, which features lidar-scanners in the vehicle's headlights to scan the road profile in front of the car. This preview-information is used in the control algorithm for disturbance feedforward compensation in order to be able to counteract the road induced vibration in advance [148, 164]. The actuators are based on the hydraulic *ABC*-actuators of the production vehicles.

In [109], a prototype of an electromechanical slow active suspension system integrated in series to the primary spring is presented, which is based on a spindle motor and can lower the energy consumption compared to the hydraulic *ABC-system* by up to $0.6\,\frac{\text{litres}}{100\,\text{km}}$. However, the system is not yet integrated into a production vehicle.

Moreover, *ZF Lemförder Fahrwerktechnik GmbH* has presented a concept of an active suspension system called *ASCA (Active suspension system with integrated body control and variable wheel damping)*. Therein, rotatory actuators are employed to introduce forces between the chassis and wheel mass via the wishbone struts [48]. The hydraulic actuator realizes also passive damping by a throttle and a cam ring inside the pump. The configuration primarily acts as an integrated roll and damping control system and has the advantage of comparably low power consumption due to the parallel placement of the efficient actuators to airsprings [50]. Further implementation studies on active suspensions are discussed in [130, 168].

Considerations on the design of electromagnetic actuators for active suspension systems are given in [100, 101] and for semi-active suspensions in [117]. Moreover, concepts for energy recuperation for low bandwidth suspension actuators and semi-active dampers exist. They preestimate that up to 50% of the energy demand of these suspension systems can be regained using appropriate electronics [131]. Further concepts for energy recuperation in suspension systems can be found in [42] and [28].

Slow active suspension systems for active roll damping are available in production vehicles (e.g. [160]) but are not within the scope of this Thesis. For the attenuation of the vehicles' roll movement, the combined application of semi-active dampers and active anti-rollbars is already available [22, 52, 160]. However, so far active and semi-active systems are not combined in vehicles for the attenuation of the vertical translatory movements of the chassis and wheel mass.

2.4.3 Suspensions with variable stiffness and damping

As pointed out at the beginning of this Chapter, slow adaptive suspension systems can also adjust the stiffness of their primary springs to adapt the suspension setting to the driving state of the vehicle, e.g. to different vehicle velocities [22, 52, 106, 121].

In the literature, the potential of suspensions with variable stiffness and damping and aspects of their technical realization are intensively discussed [46, 69, 126, 137, 139]. Exemplary suspension concepts with variable stiffness and damping, that can be adjusted with a higher bandwidth, are the following:

- Different approaches based on airhydraulic and mechanical suspension with variable dampers are studied in [69].
- In [50] a semi-active roll bar is presented. It is possible to switch between different spring elements manually in order to vary the stiffness of the anti-roll bar for special driving maneuvers (e.g. on offroad tracks).
- In [144] a concept is presented to approximate a suspension system with variable stiffness and damping by a *double suspension*, which is a series connection of two suspensions including a spring and a semi-active damper, respectively. By assuming a high spread of the damper, i.e. a large interval in which the damping coefficient can be varied, the spring stiffness resulting from the series connection of the springs can be controlled. However, in this concept the variation of the spring stiffness and the damping is coupled.

2.5 Suspension control: State of the art

A variety of suspension control concepts can be found in literature for active and semi-active vehicle suspension systems. Surveys of suspension control applications, algorithms and performance potentials are e.g. [32, 55, 110, 137, 141, 152]. Moreover, general limitations of mechatronic suspension concepts due to the actuator placement restrictions, passivity constraints as well as bandwidth and energy limits are discussed e.g. in [65, 66].

For the simultaneous increase of passenger comfort and safe driveability, suspension control is considered today in a global chassis control framework which fosters the interaction and combined optimization of mechatronic subsystems (like suspension systems, braking and steering systems) [21, 57, 135, 153]. Its potential is based on possible synergy effects by the interchange of data and interaction between mechatronic automotive subsystems. In Sections 2.5.1 and 2.5.2, an overview on selected literature on semi-active and active suspension control is given, respectively. This overview contains practical suspension control applications e.g. in production vehicles as well as suspension control concepts studied in simulations.

Adaptive control approaches for mechatronic suspension systems, which can quickly schedule the controller parametrization according to the road excitation or the driving state, are presented separately in more detail in Section 2.5.3 in order to ease the comparison and evaluation of the adaptive control approaches presented in this Thesis (Chapters 5 and 8).

2.5.1 Control of semi-active suspensions

An early semi-active suspension control approach is *skyhook-control*, which is still the most prominent control approach for mechatronic suspension systems. In this concept presented in 1974 by Karnopp [68], a force that is proportional to the absolute chassis velocity should be generated by the damper in order to reduce the motions of the chassis mass. Therefore, a so called skyhook damper is assumed to be integrated between a static inertial system (the sky) and the sprung mass (Figure 2.10 (right)). However, the desired skyhook force has to be provided by the semi-active damper, which is integrated between the unsprung and the sprung mass (Figure 2.10 (left)), and consequently its passivity restriction (2.26) and relative velocity has to be taken into account. The skyhook damping force acting on the chassis mass, which can be realized according to the passivity restriction of the damper (2.26), results from the skyhook-algorithm as

$$F_{d,sky} = \begin{cases} -d_{sky}\dot{x}_c & \text{for} \quad \dot{x}_c\,(\dot{x}_c - \dot{x}_w) \geq 0 \\ 0 & \text{for} \quad \dot{x}_c\,(\dot{x}_c - \dot{x}_w) < 0 \end{cases} \tag{2.27}$$

with $\dot{x}_c$ and $\dot{x}_w$ representing the velocities of the chassis and the wheel mass, respectively, according to the quarter-vehicle models in Section 2.1 [106]. If the damper force F_d would exceed the spread of the damper, the hardest or respectively softest damper setting is chosen. The skyhook control approach has been developed further and has found various implementations (e.g. in [45, 71, 93, 143, 174]).

One extension of the skyhook algorithm, which considers the aspect of ride safety, is the

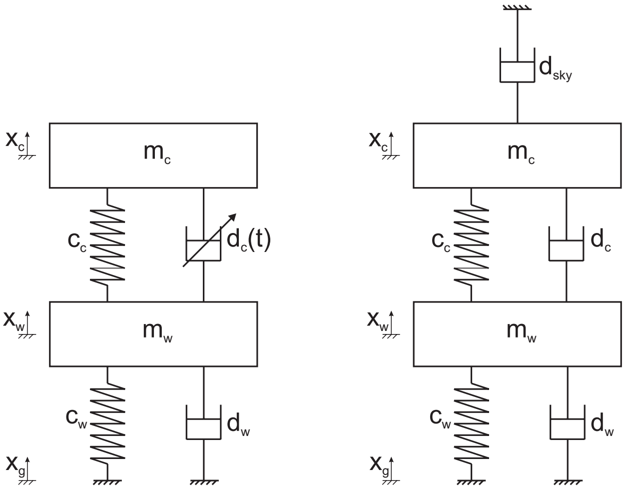

Figure 2.10: Semi-active suspension system (left) and the idea of the skyhook concept (right).

ground hook concept. It reduces the dynamic wheel load by introducing wheel damping with respect to a static inertial frame bound to the road [43, 158, 159, 162] analogously to the skyhook concept.

A different approach for the control of semi-active suspension systems is *clipped control* [158]. In the clipped control framework, the passivity restriction is neglected for the controller design, i.e. it is assumed that the damper can generate arbitrary forces $F_d = d_{act}(\dot{x}_c - \dot{x}_w)$ with $d_{act} \in \mathbb{R}$, so that control methods for active suspensions can be used for the design. By using this technique, primarily linear controller design methods are used in literature for the clipped control of semi-active suspension systems. However, for the implementation of the control law, the fractions of the damper force, which cannot be generated by the semi-active damper, are “clipped” by the real damper characteristic due to the passivity constraint (2.26) and the limited damper spread. Consequently, the damper coefficient $d_c \in [d_{min}, d_{max}]$ in a clipped control framework results as

$$d_c = \begin{cases} d_{max} & \text{for} \quad d_{max} < d_{act} \\ d_{act} & \text{for} \quad d_{min} \leq d_{act} \leq d_{max} \\ d_{min} & \text{for} \quad d_{act} < d_{min} \end{cases} . \tag{2.28}$$

If the method is combined with the design of an optimal controller (e.g. a linear quadratic regulator (LQR)), the method is called *clipped optimal control* [29, 157]. An alternative method to take into account the passivity constraint is described by Poussot-Vassal et al. in [120], who present a linear parameter-varying (LPV) control approach to deactivate the control law based on H_∞-controllers if the control force is outside the feasible sector of the damping characteristic.

In [40, 41], model-predictive control (MPC) is used to show that clipped optimal control, which is suboptimal due to the passivity constraint, for a semi-active suspension operates close to the real optimum. The aim of MPC is to minimize a cost functional by varying the control signal in a discrete time framework over a receding time horizon [14]. Exemplary applications of MPC for semi-active suspension range from optimal preview control [47] over the consideration of actuator time delays [44] to the implementation of a fast model predictive control algorithm in simulations [15]. The practical implementation of the MPC-algorithms is not realized in production vehicles for semi-active suspension control so far due to their significant online computational effort.

Robust H_∞- or μ-synthesis control approaches allow to take into account variations of the sprung mass or variations of the stiffness by aging or wear (see e.g. [86], [96]). In [175], a sliding-mode control approach (see also [24]) is presented for a magnetorheological semi-active suspension system that enables tracking of a skyhook-based reference model. A nonlinear control approach in a Hamiltonian framework that uses a passivity-based control approach is presented in [108].

In summary, a variety of control approaches have been studied for semi-active suspensions in the literature but the implemented controllers of these suspensions in production vehicles mainly employ skyhook-concepts. The main reasons for this are the limited computational power of the vehicles' electronic control units and the drawback of rather intransparent parametrizability of modern model-based controller designs (e.g. H_∞-optimal control, sliding mode control etc.) with respect to achieving an objectifiable vertical dynamic behavior of the vehicle. Furthermore, a semi-active damper represents a highly nonlinear dynamic system due to the involved fluid dynamics and electrical dynamics. Damper models that take these effects into account are presented in [25, 26, 118]. A discussion of the performance deterioration due to dynamic effects in the damper is given in [32]. However, in most works on semi-active suspension control, the damper is assumed to be a static, linear system.

2.5.2 Control of active suspensions

The controller structure of the *Mercedes Benz ABC* slow active suspension system consists of four primary parts [50]: Skyhook control, feedforward control using the lateral acceleration (in order to suppress the roll movement) and the longitudinal acceleration (in order to compensate pitch movement) as well as the *ABC*- (or *AKTAKON*) algorithm [9, 134]. The *ABC* algorithm suppresses pitch, roll and heave motions of the chassis by feedback control and also enables level control of the vehicle. The measured suspension deflections and chassis velocities of each suspension strut are used to calculate the modal quantities roll angle, pitch angle and heave motion [51]. Based on these quantities, the algorithm generates reference forces for the vehicle chassis motions and transforms them back to obtain the references for the local control forces at the suspension struts [9].

The controller design for the *Mercedes Benz* concept car *F700*, that is equipped with laser scanners to gather preview information on the road profile, is presented in [132] and it is shown that the preview approach can significantly enhance the suspension performance. Further control approaches for suspensions with preview information on the road profile ahead of the vehicle are given in [5, 105].

In [7], a skyhook control approach for an active suspension system that involves online estimation of parameters of the hydraulic actuator in order to account for nonlinear and time-varying actuator dynamics is presented. Also in [178] the dynamic behavior of a hydraulic actuator are considered for model reference adaptive and H_∞-control approaches of an active suspension system. A robust adaptive control approach involving parameter estimation of the chassis mass and the tire stiffness is presented in [123] and in [87] a pole-assignment controller, which also enables self-tuning of the controller parametrization, is discussed.

Multiobjective H_∞- or mixed H_2/H_∞-control approaches are used to employ frequency dependent shaping filters to shape the frequency response of the controlled system and to achieve robustness against parameter variations [39, 86, 96, 142, 179]. Further linear matrix inequality (LMI) based control approaches for active suspension systems are presented in [4, 87].

Further nonlinear control techniques studied for active suspension systems are state-dependent Riccati-equations [72] and a modified optimal control approach [73], which consider nonlinearities of the system and have been implemented by Kloiber, Koch and Lohmann at the test rig presented in Chapter 3. They promise excellent suspension performance of up to 42%

in terms of the performance index (2.25). A backstepping approach for a nonlinear full car model is presented in [173].

A frequently used assumption is that all state variables are measurable so that state feedback control strategies can be employed. This is not the case for production vehicles due to the costs and complex sensors, which would be required for this task. However, the performance degradation, which would result if an observer is used for the controller implementation is frequently neglected.

2.5.3 Driving state adaptive control

In the following, control concepts presented in literature, which adapt their controller parametrization according to the driving state and/or the road excitation, are summarized. The advantages of suspension systems that adaptively adjust their parameters in this manner have been pointed out in [46, 69, 137, 138]. In [46], it is stated that the controller adaptation to the driving state has the potential to improve the suspension performance more significantly than an adaptation due to varying plant parameters (as classical adaptive control methods strive for).

Venhovens has presented a wheel load adaptive control approach that schedules between a skyhook damping constant (d_{sky}) and a ride safety oriented passive damping configuration (d_c) [161, 162]. The structure of this adaptation logic serves as basis for the adaptation logic introduced in this Thesis since it takes into account variations of the rms-value of the dynamic wheel load as well as rapid singular wheel load increases, which could become critical for ride safety. For the quantification of ride safety, the same performance measure as presented in Section 2.3.2 is employed. A Kalman filter is used to estimate the dynamic wheel load for the adaptation and the concept has been evaluated using a linear quarter-car model. However, the simulation results could not be reproduced by Venhovens using a test vehicle on a hydraulic test rig [162]. In [161] the concept has also been considered for adaptive control of an active quarter-car model but no stability analysis of the switched system has been conducted.

In [89, 90, 91], an adaptive nonlinear controller for active suspension systems based on a backstepping design to compensate the nonlinearity of a hydraulic actuator, is presented. The regulated output variable is defined as the difference between the chassis displacement and the filtered wheel displacement. The bandwidth of this nonlinear filter is proportional to the suspension deflection. Thereby, the active suspension setting stiffens if the suspension deflection tends to reach its limits and focusses on ride comfort otherwise. In [90], the method is extended by an approach to adjust the shape of the filter's nonlinearity depending on the history of the suspension deflection with the aim of providing smoother transitions between the different controller settings. In order to preserve stability, the filter adaptation is realized slowly and only when the system trajectory is in regions of the state space where the nonlinearity is inactive. Although the performance achievements in terms of chassis acceleration reduction is specified in [89] to reach up to 70% in peak values occuring for singular disturbance events, it is noted that the suspension components are assumed to be linear except for the hydraulic actuator and no measurement results are given.

Tran and Hrovat motivate a driving state adaptive control approach, that is based on switching between state feedback controllers based on the dynamic wheel load and the suspension deflection in [156]. They propose a heuristic scheduling approach and briefly discuss a method to guarantee stability of the switched system by a dwell-time formulation, i.e. limitations for the switching frequency. A similar approach for the adjustment of controller weights if the suspension deflection becomes critical is presented in [46].

Linear parameter varying control

Fialho and Balas have presented a linear parameter varying (LPV) control approach to schedule between differently tuned H_∞-controllers depending on the suspension deflection [30]. The scheduling variable, which coordinates the adaptation of the controller parametrization is inferred from the measured suspension deflection signal by means of static look-up tables. By the controller adaptation process, the suspension is stiffened if the suspension deflection becomes critical. In [31], this approach is extended by a second scheduling variable, which quantifies the quality of the road although it is not specified, how this scheduling variable can be obtained from measurement data. The controller performance is analyzed in simulations using a linear time-invariant quarter-car model and the nonlinear dynamics of a hydraulic actuator are considered by a backstepping approach similar to the one described in [89].

A comparable H_∞-control based LPV methodology is applied in [179] to establish robustness against parameter variations of the component characteristics and nonlinearities in the suspension system. Thereby it is assumed that the scheduling signal to adapt the suspension with respect to the driving state is received from a higher level global chassis controller.

An LPV control approach that schedules between two H_∞-controllers according to the suspension deflection to suppress excessive suspension deflection for low-frequency road excitation is presented by Fritsch, Koch and Lohmann in [34, 35]. The approach achieves a comfort improvement of up to 43% in simulations considering the linear model presented in Section 2.1 and excitation with the measured road profiles P1 and P2.

Adaptation based on properties of the road excitation

In [53, 143], a modified skyhook control for semi-active suspensions is presented, which schedules a skyhook damping constant (d_{sky}) and the passive damping (d_c) depending on an estimate of the road excitation signal. The controller is designed for a McPherson suspension (see e.g. [50]) model and is tested in a hardware in the loop simulations with a continuously variable damper. The estimation of the road is realized by the inverse of the transfer function from road displacement to the chassis acceleration and an online discrete Fourier transform algorithm used for the calculation of a road index, that serves as a classification for the road quality according to ISO standards [58]. The optimal damper settings for five road classes have been determined by means of optimization and carpet plots and a scheduling logic adapts linearly between these settings. The damper velocity as well as the absolute velocity of the chassis mass, which are necessary for the proposed control algorithm, are estimated by a filter based estimation algorithm. The stability of the adaptive closed loop system is not analyzed in the paper. A similar road adaptive control approach has been presented by Yi and Song for semi-active suspension [174], by Sachs in [126] for a slow adaptive suspension system and by Tahboub for active suspensions in [151]. In [6] an idea to employ generalized predictive control for the suspension adaptation is briefly discussed. In [69], an adaptive control approach is proposed that slowly schedules different optimal controllers for active suspension systems according to the vehicle speed and to the rms-value of the chassis acceleration. The stability of the closed loop system is not analyzed due to the assumed slow variation of the controller parameters.

Model reference based adaptive suspension control approaches

In [150], a model reference adaptive control (MRAC) approach is presented, which enables an active suspension to track the behavior of a skyhook suspension model and thereby takes into account variations of the sprung mass and the spring and damper coefficients. The adaptivity in this approach refers to the involved self-tuning of the controller parameters to realize the tracking despite unknown or varying plant parameters. Stability of the controller structure is guaranteed by a Lyapunov function approach for the dynamics of the error between the actual suspension and the reference system. A model reaching adaptive control approach for general vibration isolation purposes is presented in [180, 181]. In both publications the tracking of the dynamics of a skyhook reference system is achieved by specifying a dynamic manifold for the target dynamics instead of employing a tracking error between the plant and the reference system. The important differences between the approaches in [150, 175, 180, 181] and the adaptive reference model presented in Chapter 8 in this Thesis are that in these works the reference models are time-invariant systems with skyhook damping and adaptivity refers to self-tuning in the case of variations of the plant parameters.

2.6 Vertical dynamic vehicle state estimation: State of the art

State feedback based control techniques for mechatronic suspension systems require the knowledge of the state vector. Moreover, for driving state adaptive control concepts, the signals that characterize the current driving state (e.g. the dynamic wheel load F_{dyn} or the damper relative velocity $\dot{x}_{cw}$) must be accessible. However, since the most complex available sensor configuration (in terms of the quarter-car framework) for vertical dynamic control in production vehicles involve only measurements of the chassis and wheel acceleration as well as the suspension deflection, the remaining quantities have to be estimated. In the following, a short overview on according estimator concepts is given based on two publications of the author ([78] and [77]).

For the estimation of the required suspension signals for suspension control, different techniques can be utilized. Conventional Kalman filters based on linear suspension models are presented e.g. in [136], [161] and [176]. In [122], the nonlinear behavior of the actuator is considered in the observer design while still assuming the suspension element characteristics to be linear. However, neglecting the nonlinearities of the suspension system, especially the nonlinear damper characteristic, deteriorates the estimation performance. This nonlinearity can be taken into account by using the nonlinear characteristic to calculate the damper force from the estimate of the damper velocity and considering the damper force as an additional input signal of the Kalman filter [111], [64]. This concept has been applied to semi-active suspension systems in [92] and [36] and it is used for the estimator design in this Thesis (Chapter 4).

Furthermore, nonlinear estimation concepts like Unscented Kalman filters [62] and Extended Kalman filters [104, 177] can be applied (see e.g. [36, 37]), which promise a good estimation performance but are computationally complex. Therefore, their implementation on electronic control units for suspension control applications is difficult.

As presented in this Chapter, in todays production vehicles mostly skyhook based suspension control approaches are employed, which do not require the full state information. Hence, simple linear filtering techniques (e.g. [36, 53], [81]) are employed frequently to estimate quantities like $\dot{x}_{cw}$ and F_{dyn}. However, their estimation performance deteriorates due to offsets in the measurement signals and phase delays resulting from the filters.

Moreover, for road adaptive suspension control or to study the possibility of additional disturbance feedforward control, the road profile has to be estimated because measuring it (e.g. by laser scanners in [148]) is very complex and expensive. Approaches for the estimation of road profiles for the purpose of road serviceability using sliding mode observers are presented e.g. in [56]. However, in these works the road unevenness has been assumed to be in the order of millimeters, which is unrealistic for vehicle suspension control. In [36], the estimation of the disturbance signal for suspension control applications is considered by Fröhlich in simulations, however, no experimental results for the estimation quality of the concept are given.

2.7 Benchmark systems

In order to evaluate the performance of the controllers presented in this Thesis (Chapters 5 and 8) benchmark systems are used. The parametrization of the controllers of the benchmark systems is adjusted to the considered suspension system/test rig by means of numerical optimization and the resulting parameters are given in Chapters 5.6 and 8.5.1).

The classes of benchmark systems used in this Thesis are:

- *Passive suspension system*: Most frequently, the performance gain of a control approach for a mechatronic suspension is specified with respect to the passive system. Therefore, for each suspension configuration in this Thesis the passive suspension is considered as a benchmark. Since for the control approach presented in Chapter 8, a semi-active damper is employed, a fixed damping ratio that represents the passive system is defined.

- *Skyhook control*: A skyhook concept with basic passive damping (Figure 2.10) is chosen as benchmark due to the popularity of the skyhook conrol approach in production vehicles. The resulting damper force F_d acting on the chassis mass results from

  $$F_d = -d_{sky}\dot{x}_c - d_c\left(\dot{x}_c - \dot{x}_w\right) . \tag{2.29}$$

  If the skyhook algorithm (2.29) is applied for a semi-active system, the force F_d as formulated in (2.29) can only be generated by the damper if the skyhook condition $\dot{x}_c(\dot{x}_c - \dot{x}_w) \geq 0$ is fulfilled and F_d is reachable by the damper's force velocity characteristic, otherwise the force F_d is clipped by the damper characteristic as presented in Section 2.4.1. For the implementation of the skyhook concepts estimates of the required velocities are employed.

- *Adaptation between two skyhook configurations including different passive damping coefficients*:

  In Chapters 5.2.1 and 8.2.1 adaptation algorithms, which determine scheduling signals that reflect the criticality of the current driving state, are presented. Let $0 \leq q_{adp}(t) \leq 1$ be a scheduling signal that indicates if the driving state becomes critical as $q_{adp}(t)$ approaches 1. This information is used in the following adaptive skyhook approach to schedule between two different passive damper settings with skyhook damping. The pair $(d_{sky,1}, d_{c,1})$ denotes a comfort oriented semi-active configuration and the pair $(d_{sky,2}, d_{c,2})$ a more safety oriented setting with a higher passive damping ($d_{c,1} < d_{c,2}$). The resulting adaptive damper force $F_{d,adp}$ acting on the chassis mass results from linear interpolation between these settings, i.e.

  $$F_{d,adp} = -\left(d_{sky,1} + q_{adp}(t)\left(d_{sky,2} - d_{sky,1}\right)\right)\dot{x}_c - \left(d_{c,1} + q_{adp}(t)\left(d_{c,2} - d_{c,1}\right)\right)\left(\dot{x}_c - \dot{x}_w\right) . \tag{2.30}$$

  The same restrictions for the damper force apply as for the conventional skyhook approach if the method is implemented for a semi-active system.

- *LQR*: A benchmark system employed for the fully active suspension configuration presented in Chapter 5 is a moderately tuned linear quadratic regulator. The tuning is accomplished by means of optimization in order to realize a comfort oriented active suspension system taking into account constraints on suspension deflection and dynamic wheel load (see Chapter 5.6).

Chapter 3

ACTIVE SUSPENSION TEST RIG

In Chapter 5 the performance potential of an adaptively controlled fully active suspension is studied, since this represents the most complex actuator configuration of mechatronic suspension systems. In order to conduct this analysis in a realistic framework, a quarter-vehicle test rig with a fully active suspension configuration has been designed, which is presented in this Chapter. An electrical linear motor is integrated in parallel to the passive suspension system on the test rig to control the motions of the chassis and the wheel mass.

To study the influence of nonlinearities on the dynamic behavior of the suspension system, identification experiments are conducted at the test rig to determine the main nonlinearities of the suspension components. Especially the nonlinearities of the damper and the tire as well as relevant friction effects are taken into account for the synthesis of a precise model of the suspension, that is utilized for the estimator and controller design in the next Chapters and provides a simulation platform for the controller performance before the implementation at the test rig is conducted. For these purposes the model should match the behavior of the system well within the control bandwidth ($0 - 25\,\mathrm{Hz}$) for realistic excitations.

First, the requirements for the test rig are summarized and the quadricycle suspension system is presented in Section 3.1. In Section 3.2 the sensors, actuators and digital signal processing hardware used in the test rig are described. Section 3.3 presents the modeling and identification of the suspension components, the identification of the actuator dynamics and the nonlinear component characteristics. Finally, the nonlinear model as well as a linear approximation are presented and short summary is given in Section 3.4. More details on the test rig, the identification and the modeling are given in [80].

3.1 Test rig requirements and quadricycle suspension

The requirements of the test rig can be summarized as follows:

- Similar dynamic behavior to an automotive suspension in terms of nonlinearities, damping and resonance frequencies of chassis and wheel mass (see e.g. [106]).
- Ideally frictionless vertical guidance of the chassis mass.
- Possibility to apply realistic excitation signals (with amplitudes of up to 5 cm) within the frequency range $0-25\,\mathrm{Hz}$.
- Realization of a fully active suspension configuration with an actuator integrated in parallel to the suspension strut and a control bandwidth of at least 25 Hz.

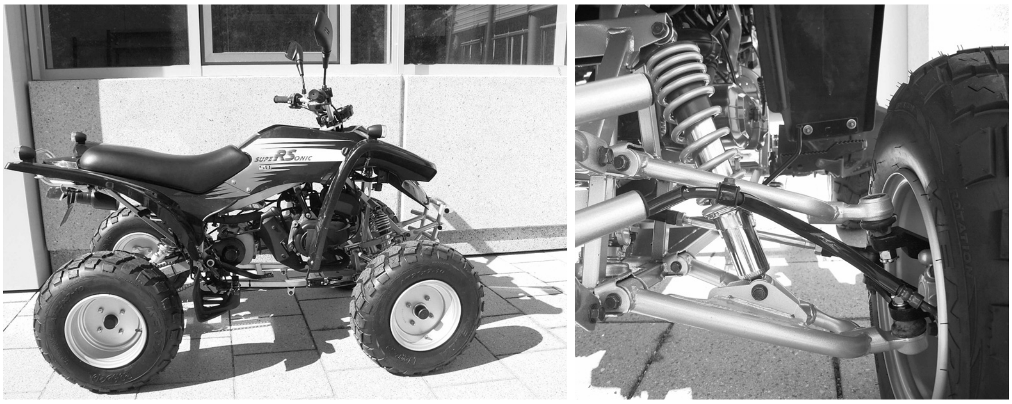

Figure 3.1: Experimental quadricycle vehicle (left), left front suspension (right).

A quadricycle (more precisely *all-terrain vehicle*, ATV) has been chosen as experimental vehicle (Figure 3.1 (left)) due to its lower masses compared to an automobile but its comparable suspension configuration. The suspension system (Figure 3.1) basically consists of the tire, the double wishbone elements, connected via two ball-joints to the wheel carrier, and the suspension strut with the primary spring and the damper. The suspension strut is linked between the lower wishbone and the chassis via slide bearings and it is inclined in the equilibrium position. Unlike a McPherson suspension (see e.g. [50]), the suspension strut at hand does not have a guidance function for the wheel.

The suspension kinematics determined by the double wishbone configuration and the tie rod result in camber and toe changes during compression and rebound operation of the spring. The wheel consists of an aluminium rim and a tire similar to that of an automobile is used for the test rig application instead of the original offroad tire.

The smaller sprung and unsprung masses of the quadricycle suspension correspond to smaller stiffnesses and a smaller damping coefficient compared to an automotive suspension system but its damping-isolation behavior is similar. The main differences can be summarized to:

- Lower masses, smaller primary spring and tire stiffness (tire air-pressure approx. 1.4 bar compared to approx. 2.2 bar), respectively.

- No rubber-mounts are integrated for the mounting of the double wishbones to the chassis. These are used in cars in order to enhance the performance of the vehicle suspension regarding acoustics and vibration-isolation [106]. In the quadricycle suspension, stiff slide bearings are integrated and therefore no elasto-kinematic effects are present at the wishbone attachments.

3.2 Test rig structure

The test rig (Figure 3.2) incorporates the left front suspension shown in Figure 3.1, which is mounted on a vertically guided steel plate via the double wishbone elements and the primary spring. The steel plate has a mass of 29 kg and represents in combination with the components attached to it approximately a quarter of the vehicle mass including a driver, i.e. approx. 94 kg for the active suspension. The plate is guided vertically by steel rolls on roller bearings. Due to remaining friction effects, low Coulomb friction forces counteract the movement of the chassis mass, which is not the case in the suspension assembly of a real vehicle and need to be considered in the test rig model (see Section 3.3.2).

Although no external steering command is applied to the wheel of the test rig, the tie rod is integrated on the test rig in order to appropriately simulate the kinematics (toe changes) of the wheel during compression of the suspension strut. Due to the toe changes during spring compression and rebound operation, the wheel rests on a mounted disc with a rotatory degree of freedom in order to also reduce the transmission of friction torques to the base plate.

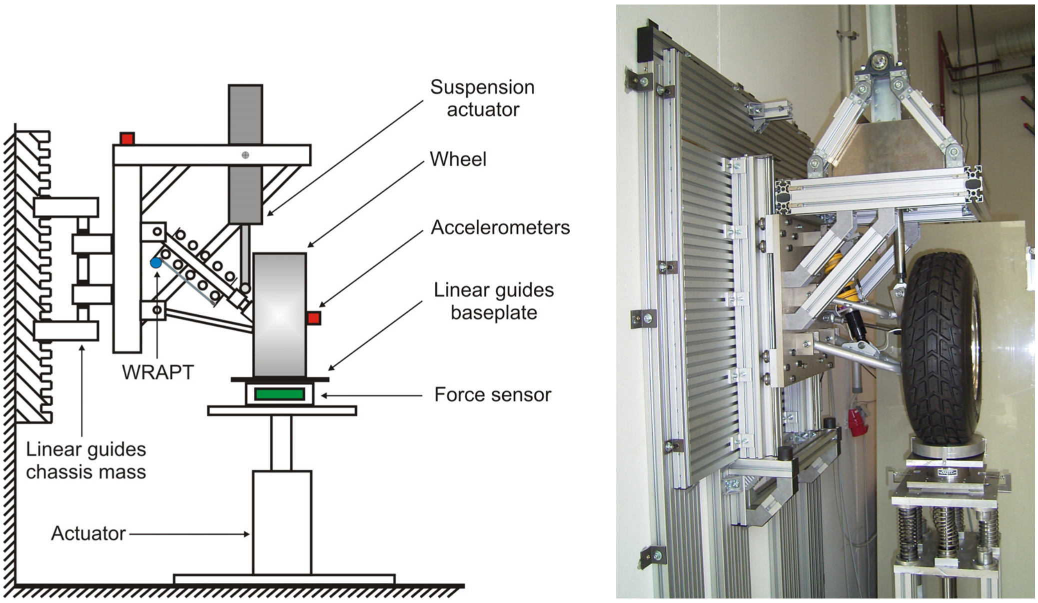

Figure 3.2: Test rig structure (left) and fully active suspension test rig (right).

Moreover, since the wheel cannot perform roll motions, its base plate is guided horizontally to reduce translational forces on the base plate below the wheel.

The tire is excited by an electrical linear motor that emulates the road induced vibrations. In order to compensate the gravitational force of the moving parts of the test rig, the static load is supported by four springs. The springs influence the excitation signals only marginally because the actuator position is controlled. In order to take the remaining alteration of the excitation signals into account, the movement of the wheel base plate (excitation signal) is measured by an incremental encoder of the linear motor. Hence, the measured signal can be used as disturbance input in simulations in order to ensure comparability of measurement and simulation results. The rod of the actuator is mounted to the base plate and is guided by an axial roller bearing in order to avoid lateral forces and torques on the actuator rod.

For the realization of the active suspension system, a second electrical linear motor is integrated between the tire and the wheel. Its rod is attached to the wheel carrier. In order to compensate for the additional unsprung mass of the rod, the original steel rim of the vehicle has been replaced by the aluminium light alloy rim.

3.2.1 Sensor configuration

The measurement signals and integrated sensors of the test rig are:

- Chassis acceleration: $\ddot{x}_c(t)$ is measured by a capacitive accelerometer with a measurement range of ±5g.
- Suspension deflection: The deflection of the suspension strut is recorded by a wire rope actuated position transducer (WRAPT) with a digital incremental encoder. From this measurement signal the suspension deflection $x_c(t) - x_w(t)$ in the coordinates of the quarter-vehicle model can be calculated taking into account the kinematic relations of the suspension system (see Section 3.3.2).
- Wheel acceleration: $\ddot{x}_w(t)$ is measured by a capacitive accelerometer (measurement range ±25g).
- Wheel load: $F_w(t) = F_{stat} + F_{dyn}(t)$ is measured by a resistance strain gauge based force sensor designed for high levels of cycling loads. The measurement signal is provided by a strain gauge amplifier.
- Road displacement: $x_g(t)$ is measured by an incremental encoder integrated in the test rig's lower actuator.
- Upper actuator current: $i_{act}(t)$, which is proportional to the actuator force $F(t)$, is provided by the actuator's inverter.

Detailed technical specifications of the sensors are given in [80].

3.2.2 Linear electromagnetic actuators

Because of the high bandwidth active suspension setup, the actuator is integrated in parallel to the vehicle suspension strut. Therefore, the operating principle of the actuator must allow that the rod of the actuator is movable as frictionless as possible in order to preserve the dynamic behavior of the passive suspension setup if the actuator does not operate. A custom-made ironless, permanently excited synchronous linear motor (see Figure 3.3 (left)) with maximum rms-force of $\max(\|F(t)\|_{\text{rms}}) = 800\,\text{N}$, peak force $\max(|F(t)|) = 4\,\text{kN}$ and maximum velocity $\max(v_{act}(t)) = 3.14\,\frac{\text{m}}{\text{sec}}$ is integrated in the setup. It is driven by a frequency converter, which has an internal PI current controller, that has been tuned to achieve an actuator bandwidth of approx. 29 Hz (see Section 3.3.1), i.e. the actuator satisfies the bandwidth requirement of the fully active suspension system. Due to the operating principle of the actuator, the actuator current is proportional to the actuator force, and the actuator operates in force control mode. More detailed information on the actuator, the inverter, the internal current and velocity control loops as well as further technical data is summarized in [80].

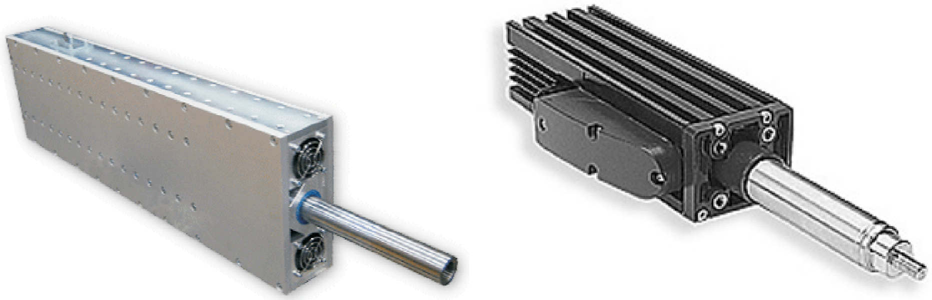

Figure 3.3: Linear actuators - Suspension actuator (left) and linear motor for the road excitation (right).

The linear motor to emulate the road excitation (Figure 3.3 (right)) can generate high peak forces of up to 1860 N but the maximum peak force is limited to 1 sec and the force rms-value cannot exceed 276 N.

3.2.3 Signal processing

The real time signal processing is performed by a *dSpace DS1104* controller board and the software *dSpace Control Desk*. A sampling time of $T_s = 1\,\text{msec}$ is employed for all experiments, which corresponds to a sampling frequency that is well above the bandwidth of interest for active suspension control (25 Hz). The real time controller board is integrated into a Host-PC (*AMD Athlon 64 X2 Dual Core Processor 5200+* (2.7 GHz) and 3.25 GB RAM) to evaluate the signals measured in the process.

In order to remove noise from the measurement signals, first order lowpass filter circuits with a cutoff frequency of $f_c = 380\,\text{Hz}$ are integrated into the test rig for the analog measurement signals. Additionally, first order (software) lowpass filters with a cutoff frequency of $f_{LP} = 60\,\text{Hz}$ are used for the measurement signals $\mathbf{y}_m$ as well as the actuator force $F(t)$ in order to reduce remaining high frequency measurement noise. The resulting low signal-to-noise ratios (SNR) and peak-to-peak noise values are given in [80].

3.3 Modeling and parameter identification

In this Section, the modeling and identification of the test rig is presented. The aim is a model that accurately matches the test rig's dynamic behavior in the frequency range $0-25\,\text{Hz}$. A detailed nonlinear model including actuator dynamics is desired for simulation purposes and a linear model is required for aspects of the estimator and the controller design presented in the Chapters 4 and 5.

3.3.1 Actuator model

The input signal of the actuator is a control voltage $u_v(t)$ and the measured output signal is the actuator current $i_{act}(t)$. The response of the actuator current to a 5V-step input of the control signal $u_v(t)$ is shown in Figure 3.4.

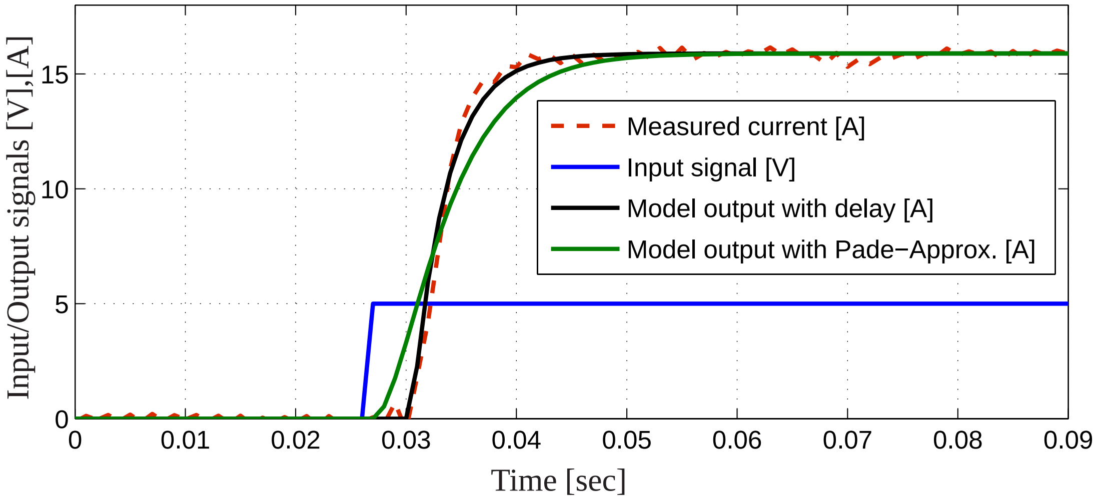

Figure 3.4: Response of the measured and modeled actuator current $i_{act}(t)$ to a $5\,\text{V}$ step input.

Based on the shape of the step response, the current's dynamic behavior can be modeled using a first order low pass and a time delay. The time delay of $T_d = 4\,\text{msec}$ has been included in the model using a first order Padé-Approximation (see e.g. [98]). The resulting model is

$$\begin{bmatrix} \dot{x}_{lm,1}(t) \\ \dot{x}_{lm,2}(t) \end{bmatrix} = \underbrace{\begin{bmatrix} a_{lm,11} & a_{lm,12} \\ a_{lm,21} & a_{lm,22} \end{bmatrix}}_{\mathbf{A}_{lm}} \begin{bmatrix} x_{lm,1}(t) \\ x_{lm,2}(t) \end{bmatrix} + \underbrace{\begin{bmatrix} b_{lm,11} \\ b_{lm,21} \end{bmatrix}}_{\mathbf{b}_{lm}} u_v(t), \tag{3.1}$$

$$i_{act}(t) = \underbrace{\begin{bmatrix} c_{lm,11} & c_{lm,21} \end{bmatrix}}_{\mathbf{c}_{lm}^T} \begin{bmatrix} x_{lm,1}(t) \\ x_{lm,2}(t) \end{bmatrix}, \tag{3.2}$$

$$F(t) = \tilde{\mathbf{c}}_{lm}^T \begin{bmatrix} x_{lm,1}(t) \\ x_{lm,2}(t) \end{bmatrix}, \tag{3.3}$$

$$\mathbf{A}_{lm} = \begin{bmatrix} -320.4019 & 0 \\ 250 & -250 \end{bmatrix}, \quad \mathbf{b}_{lm} = \begin{bmatrix} 1.2131 \\ 0 \end{bmatrix}, \quad \mathbf{c}_{lm} = \begin{bmatrix} 0 \\ 839.4076 \end{bmatrix} \tag{3.4}$$

with $x_{lm,1}(t)$ and $x_{lm,2}(t)$ being the actuator states and $i_{act}(t)$ being the actuator current proportional to the actuator force ($1\,\text{A} \sim 0.1\,\text{kN}$), i.e. $\tilde{\mathbf{c}}_{lm}^T = 100 \cdot \mathbf{c}_{lm}^T$. Figure 3.4 also shows the responses of the first order model with the time delay and the second order model including the Padé-Approximation to the step input signal. The transfer function from the input signal $u_v(t)$ to the current output $i_{act}(t)$ is $G_{act}(s) = \mathbf{c}_{lm}^T(s\mathbf{I} - \mathbf{A}_{lm})^{-1}\mathbf{b}_{lm}$ with $\mathbf{I} \in \mathbb{R}^{2\times 2}$ being the identity matrix. The bode diagram of $G_{act}(s)$ depicted in Figure 3.5 shows an actuator bandwidth (-3 dB cutoff frequency) of approx. $\omega_c = 2\pi \cdot 28.6\,\frac{\text{rad}}{\text{sec}}$, which is sufficient for the fully active suspension system.

3.3.2 Suspension component characteristics

For the identification of the suspension component characteristics, an appropriate design of experiments in terms of hardware setting and excitation signals has been conducted [80] and the results are presented in the following. The relevant component characteristics are:

- Force-displacement characteristic of the primary spring,
- Force-velocity characteristic of the damper,
- Stiffness characteristic and damping of the tire,

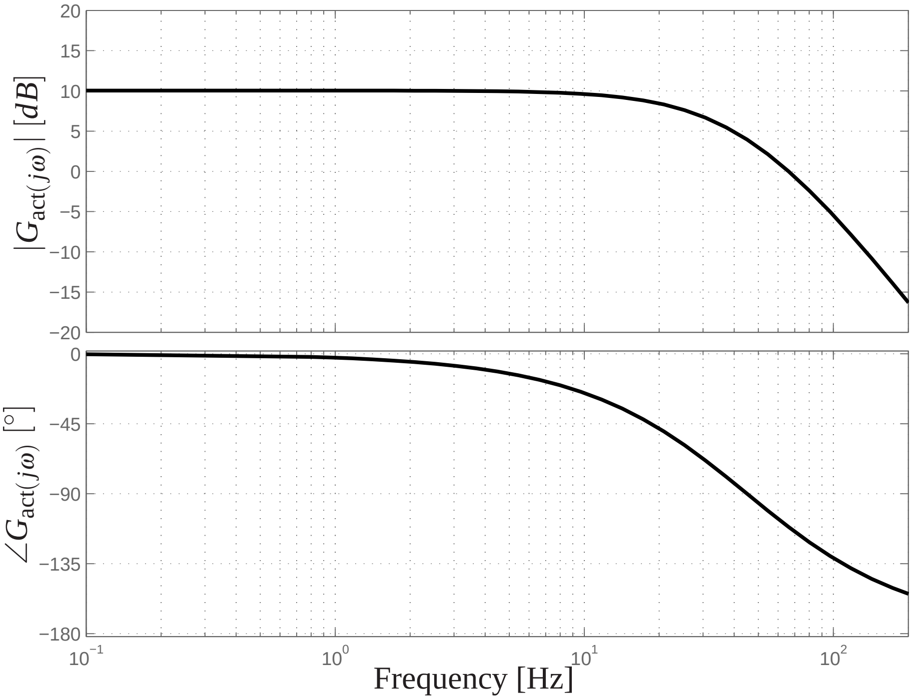

Figure 3.5: Bode diagram of the actuator model $G_{act}(s)$.

- Friction effects,
- Kinematic relations of the suspension system.

Note that the force-deflection characteristic of the spring has been identified in the assembled state of the suspension in the test rig. This has the advantage that all kinematic effects causing nonlinearities are included in the measured characteristic of the spring. All test rig parameters are summarized in Table B.1 in the Appendix.

Primary spring and damper

For the identification of the primary spring's stiffness characteristic the tire has been removed from the test rig and the sprung mass m_c representing the chassis mass has been clamped. The wheel carrier is moved vertically quasi-statically ($\dot{x}_w = 2\frac{\text{mm}}{\text{sec}}$) by the linear motor and the force, the position of the wheel carrier and the spring deflection at the suspension strut are measured.

The result is that the primary spring's stiffness is linear in the operating range of the test rig, which is determined by the suspension actuator's maximum stroke (±5 cm), i.e. the spring force is calculated by means of the linear spring stiffness c_c as

$$F_c = c_c(x_c - x_w) \ . \tag{3.5}$$

The degressive force-velocity characteristic of the damper has been supplied by the manufacturer of the damper (Figure 3.6 (left)), it is formulated in the coordinates of the quarter-vehicle model using the transmission factor described later in this Section. It is noted that a steeper damper characteristic occurs for rebound than for compression, which is conform with automotive dampers [106].

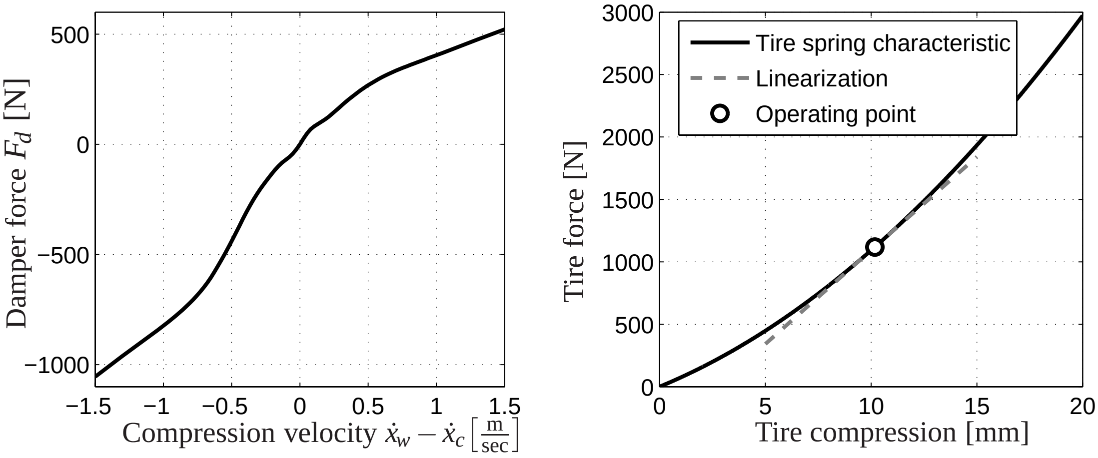

Figure 3.6: Nonlinear characteristics of the damper (left) and the tire (right).

Tire characteristic

For the determination of the tire properties, the primary spring has been replaced by a stiff steel rod and the chassis mass has been clamped. Therefore, the only relevant elasticity in the setup is the tire. Its spring characteristic has been measured by applying a quasi-static deflection by the linear motor with a tire pressure of 1.4 bar at room temperature.

The tire characteristic (Figure 3.6 (right)) can be approximated well by a second order polynomial. By relating the tire characteristic to the static equilibrium given by the operating point, the tire spring force can be formulated in coordinates of the quarter-vehicle model as

$$F_{t,c} = c_{w,lin}\left(x_g - x_w\right) + c_{w,quad}\left(x_g - x_w\right)^2 . \tag{3.6}$$

For a linear model, the tire characteristic can be linearized at the operating point characterized by the static wheel load. The tire damping has been identified in further experiments [80] and is comparably small ($d_w = 50\,\frac{\mathrm{Nsec}}{\mathrm{m}}$), which is coherent with literature stating that the tire damping can be neglected for a quarter-vehicle model (see also Chapter 2.1) [106].

Friction effects

Coulomb friction forces (see e.g. [112]) in the suspension ($F_{f,1}$) and in the vertical linear guides of the chassis mass ($F_{f,2}$) are taken into account for the modeling. The Coulomb friction forces are approximated by tanh-functions for smooth zero crossings (see e.g. [83]) and the resulting friction model (Figure 3.7) is

$$F_{f,i} = \hat{F}_{f,i}\tanh(\Delta v_i k_{f,i}) \tag{3.7}$$

with $\Delta v_1 = \dot{x}_c$, $\Delta v_2 = \dot{x}_c - \dot{x}_w$ and the scaling factors $k_{f,1} = k_{f,2}$. The numerical values have been identified experimentally (see [80]) and are given in Table B.1 of the Appendix.

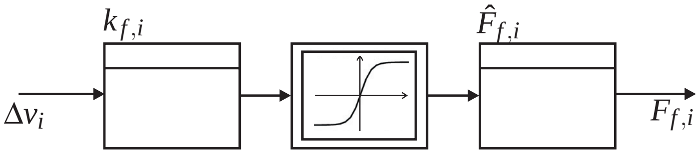

Figure 3.7: Friction model.

Suspension kinematics

The dynamic behavior of the suspension also depends on the kinematic relations between the deflection of the suspension strut and the vertical movement of the chassis and the wheel. The kinematics of the considered quadricycle suspension are mainly defined by the double wishbone configuration and the inclined assembly of the suspension strut. Although the spring stiffness is already formulated in the coordinates of the quarter-vehicle model, the kinematic relations are required to evaluate the measurement signals (the deflection of the inclined suspension strut and the vertical accelerations) in the same coordinates and for the formulation of the damper characteristic as depicted in Figure 3.6 (left).

The nonlinearities caused by the kinematics of the suspension system can be considered using a transmission factor

$$i_c = \frac{\dot{x}_{el}}{\dot{x}_c - \dot{x}_w} \tag{3.8}$$

with $\dot{x}_{el}$ being the relative velocity of the suspension strut in the direction of the element's center line [102]. The factor transforms the forces and kinematic relations at the elements (spring force $\bar{F}_{cc} = \bar{c}_c \Delta x_{el}$, damper force $\bar{F}_d$) to the corresponding quantities of the quarter-vehicle model (see Figure 2.1), i.e. the forces acting on the center of gravity of the wheel. According to [102] the primary spring stiffness results as

$$c_c = i_c^2 \bar{c}_c + \bar{F}_{cc} \frac{d i_c}{d(x_c - x_w)}\,. \tag{3.9}$$

The second term in (3.9) can be neglected in this suspension model because it has been identified to be small (see [80]). Due to the concentric configuration of the suspension strut the transmission ratio is the same for the spring and the damper so that $i_c = i_d = i = 0.392$ holds and for the damper force results $F_d = i\bar{F}_d$.

3.3.3 Nonlinear test rig model

Figure 3.8 depicts the basic structure of the nonlinear test rig model consisting of the sprung and unsprung masses of the suspension system, which are connected by the suspension components described in Section 3.3.2. The inputs of the system are the excitation signal $x_g(t)$, its time derivative $\dot{x}_g(t)$ and the actuator force $F(t)$. The output signals are the positions and velocities of the masses forming the state vector of the basic quarter-vehicle model. The resulting model is a nonlinear grey-box model (see e.g. [94]).

The quarter-vehicle test rig is used to record I/O-data of the suspension in order to identify the unknown parameters of the nonlinear model of the suspension system. These parameters are the mass distribution between sprung and unsprung mass, the parameters of the friction

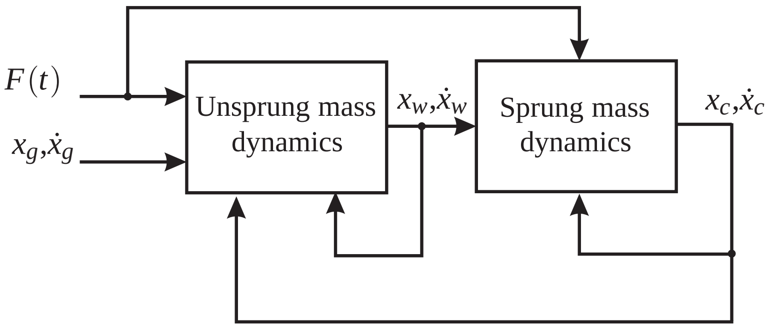

Figure 3.8: Structure of the nonlinear quarter-vehicle model.

models and the tire damping. The identification is accomplished in two steps, which are presented in detail in [80]:

1. The identified suspension component characteristics are embedded in the nonlinear model structure including the friction models. The remaining unknown parameters of this structure are optimized using least squares parameter identification routines.
2. The parametrized nonlinear model is validated by means of various measurement data sets.

The resulting model has order six (order four for the passive quarter-vehicle test rig and two for the suspension actuator described by (3.1), (3.3) and (3.4)). If the constraints for the signals (e.g. the end stops for the spring) are not considered the nonlinear model of the test rig can be represented by the state equation (3.12) with the state vector

$$\mathbf{x} = \left[\begin{array}{cccccc} x_c & \dot{x}_c & x_w & \dot{x}_w & x_{lm,1} & x_{lm,2} \end{array} \right]^T \tag{3.10}$$

and the output equation (3.13) with the output vector (gathering the measurement signals that can be employed for suspension control)

$$\mathbf{y} = \left[\begin{array}{ccc} \ddot{x}_c & \ddot{x}_w & x_c - x_w \end{array} \right]^T . \tag{3.11}$$

Note that the constraints are included in the corresponding *SIMULINK* model (see [80]), which is used for the simulations in this Thesis.

$$\dot{\mathbf{x}}(t) = \underbrace{\begin{bmatrix} \dot{x}_c \\ -\frac{c_c}{m_c}(x_c - x_w) - \frac{1}{m_c}F_d(\mathbf{x}) + \frac{1}{m_c}\tilde{c}_{lm,21}x_{lm,2}(t) - \frac{1}{m_c}\hat{F}_{f,1}\tanh(\dot{x}_c k_{f,1}) - \frac{1}{m_c}\hat{F}_{f,2}\tanh((\dot{x}_c - \dot{x}_w)k_{f,2}) \\ \dot{x}_w \\ \frac{1}{m_w}F_{c,t}(\mathbf{x}) + \frac{d_w}{m_w}(\dot{x}_g - \dot{x}_w) + \frac{c_c}{m_w}(x_c - x_w) + \frac{1}{m_w}F_d(\mathbf{x}) - \frac{1}{m_w}\tilde{c}_{lm,21}x_{lm,2}(t) + \frac{1}{m_w}\hat{F}_{f,2}\tanh((\dot{x}_c - \dot{x}_w)k_{f,2}) \\ a_{lm,11}x_{lm,1}(t) + b_{lm,1}u_v(t) \\ a_{lm,21}x_{lm,1}(t) + a_{lm,22}x_{lm,2}(t) \end{bmatrix}}_{\mathbf{f}(\mathbf{x}(t),u_v(t))} \tag{3.12}$$

$$\mathbf{y}(t) = \underbrace{\begin{bmatrix} -\frac{c_c}{m_c}(x_c - x_w) - \frac{1}{m_c}F_d(\mathbf{x}) + \frac{1}{m_c}\tilde{c}_{lm,21}x_{lm,2} - \frac{1}{m_c}\hat{F}_{f,1}\tanh(\dot{x}_c k_{f,1}) - \frac{1}{m_c}\hat{F}_{f,2}\tanh((\dot{x}_c - \dot{x}_w)k_{f,2}) \\ \frac{1}{m_w}F_{c,t}(\mathbf{x}) + \frac{d_w}{m_w}(\dot{x}_g - \dot{x}_w) + \frac{c_c}{m_w}(x_c - x_w) + \frac{1}{m_w}F_d(\mathbf{x}) - \frac{1}{m_w}\tilde{c}_{lm,21}x_{lm,2} + \frac{1}{m_w}\hat{F}_{f,2}\tanh((\dot{x}_c - \dot{x}_w)k_{f,2}) \\ x_c - x_w \end{bmatrix}}_{\mathbf{h}(\mathbf{x}(t),u_v(t))} \tag{3.13}$$

The matching of the nonlinear model is depicted in Figure 3.9 for the excitation of the test rig with a measured road profile. Note that the suspension actuator has been inactive for this measurement. As can be seen, the model matches the dynamic behavior of the test rig very well. The chassis position shows only small low-frequency deviations, while the other signals have primarily high-frequency errors well above the bandwidth of interest ($0-25$ Hz). The accuracy of the model is specified by the performance index

$$\Phi_i = 1 - \frac{\|e_i(t)\|_{\text{rms}}}{\|z_{i,meas}(t)\|_{\text{rms}}}, \tag{3.14}$$

where $e_i(t) = z_{i,\text{sim}}(t) - z_{i,\text{meas}}(t)$ denotes the error between the simulated $z_{i,\text{sim}}(t)$ and the measured quantity $z_{i,\text{meas}}(t)$. The resulting performance indices for the test rig model are given in Table 3.1. It is noted that for the validation, the absolute chassis position has been also measured by an incremental encoder to evaluate the model quality. All model parameters are summarized in Table B.1 of the Appendix. The natural frequencies of the sprung and the unsprung mass are $f_c = 1.5\,\text{Hz}$ and $f_w = 12.7\,\text{Hz}$ and the damping ratio of the sprung mass is $D_c = 0.397$. Thus, the suspension has a similar vertical dynamic behavior to an automotive suspension system.

Table 3.1: Performance indices of the nonlinear simulation for excitation by road profile P1 ($v_{p1} = 50\,\frac{\text{km}}{\text{h}}$).

Signal	Performance index Φ
Chassis position x_c	0.883
Chassis acceleration $\ddot{x}_c$	0.844
Dyn. wheel force F_{dyn}	0.793
Wheel acceleration $\ddot{x}_w$	0.608

3.3.4 Linear test rig model

The linear model is constructed from the linearization of the tire characteristic in the operating point, the omission of the friction models and the linearization of the damper characteristic (see Figure 3.6). For the linearization of the damper characteristic the mean value of the rebound and compression damper coefficients obtained between the velocities $0\,\frac{\text{m}}{\text{sec}}$ and

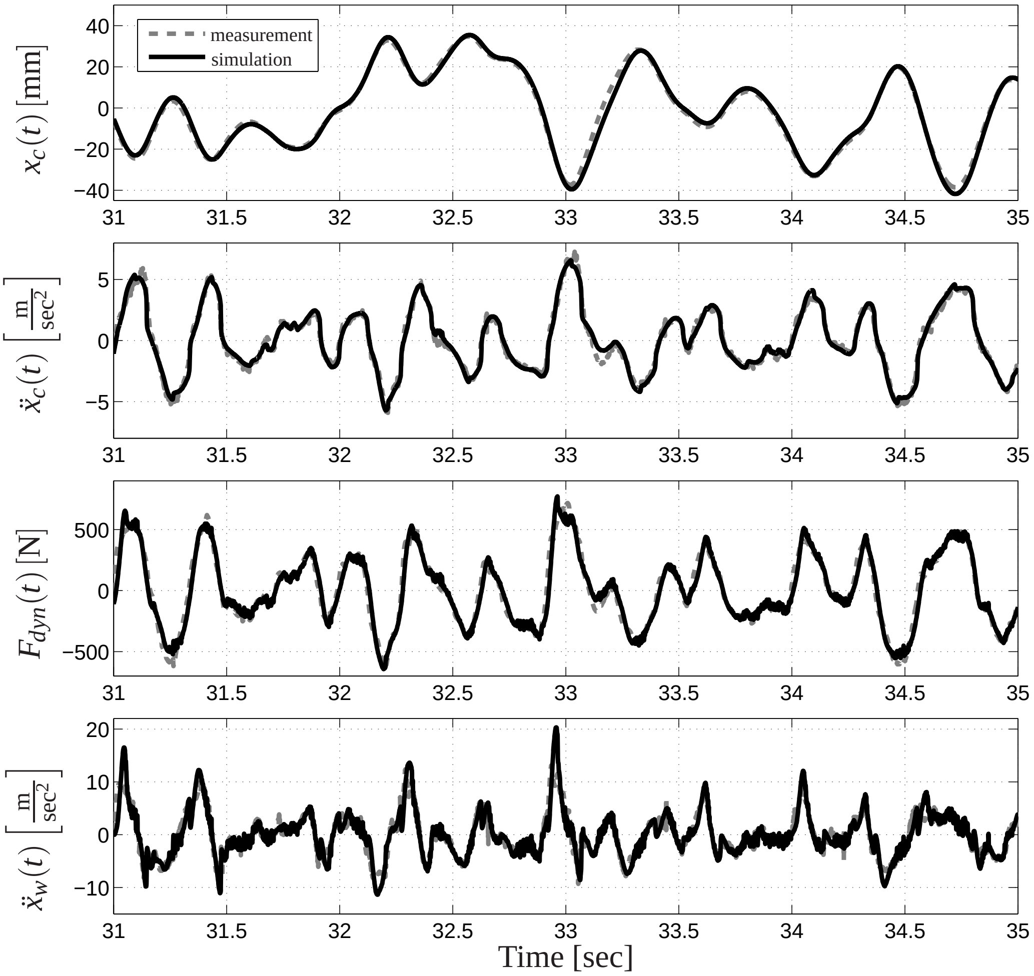

Figure 3.9: Model validation - Simulation and measurement data.

$\pm 0.4\,\frac{\text{m}}{\text{sec}}$, respectively, is taken for the linear damping coefficient as proposed in [106]. After the linearization operations, a further optimization run for the friction model parameters has led to an improvement of the simulation performance of the linear model. A detailed comparison between the nonlinear and the linear test rig model is presented in [80]. The parameters of the linear model are summarized in Table B.2 in the Appendix. For the controller design presented in Chapter 5, the linear model is represented using the same state variables, input and output signals as defined for the linear quarter-vehicle model in (2.3)-(2.6).

3.4 Summary

The quarter-vehicle test rig fulfills all requirements formulated at the beginning of this Section. With the electrical linear motor a high bandwidth active suspension system with a control bandwidth of more than 28 Hz has been realized. The active suspension system is equipped with a sensor configuration comparable to modern production-vehicles and can be excited by real measured road profile signals. Thus, a realistic framework for experimental validation of suspension controllers is guaranteed. The nonlinear model of the test rig has been obtained by system identification techniques using a physically motivated grey-box model structure and parameter identification by numerical optimization. The model matches the dynamic behavior of the test rig well and can be used for controller design and simulations.

Chapter 4

ESTIMATOR DESIGN

Adaptive mechatronic suspension systems require information about the driving state (e.g. the damper relative velocity $\dot{x}_{cw}$ or the dynamic wheel load F_{dyn} [106]) or - if state feedback control should be utilized - the complete vertical dynamic state vector of the vehicle (including the deflections of tire and primary spring as well as the tire and chassis velocities as defined in (2.3)). Since measuring all these quantities is unfeasible with reasonable economical effort, they have to be estimated from the available sensor signals, i.e. from the chassis and wheel acceleration and the suspension deflection in case of the test rig presented in Chapter 3. The trade-off for the estimator design for vehicle suspension control is to design an estimator that gives accurate estimations of the required quantities despite the nonlinearities of the suspension and that is also real-time capable.

In this Chapter new estimation concepts for adaptive suspension control are presented summarizing the results published in [78] and [77]: A new estimator structure based on three parallel Kalman filters that also take into account the nonlinearity of the damper and a signal based estimator concept, which is well implementable and computationally simple. The concepts are compared with the estimation results of an Extended Kalman filter, that represents a benchmark since it is a complex nonlinear estimation scheme that can take into account all nonlinearities of the suspension system. The performance of the estimators is analyzed and compared in simulations and experiments using the quarter-vehicle test rig described in the previous Chapter and excitation signals gained from measurements of real road profiles to provide a realistic framework.

4.1 Stochastic model for the Kalman filter design

For the design of the Kalman filter based estimator structures the test rig model presented in Section 3 is extended by a disturbance model for the road excitation. Moreover, the properties of the considered process noise and measurement noise, that are taken into account for the Kalman filter design, are presented.

4.1.1 Disturbance model

As described in Chapter 2.2.1, the power spectral density of a stochastic road profile $x_g(t)$ is frequently modeled by (2.14), i.e.

$$S_{x_g x_g}(\omega) = \frac{\alpha v}{\beta^2 v^2 + \omega^2}\,,$$

where ω is the angular frequency, v is the vehicle velocity and α, β are parameters characterizing the road irregularities [78, 106]. Assuming a Gaussian, zero-mean, white noise input $w_{x_g}(t)$ with a power spectral density of $S_{w_{x_g} w_{x_g}} = \alpha v$, a first order shaping filter with state space representation

$$\dot{x}_g(t) = -\beta v x_g(t) + w_{x_g}(t) \tag{4.1}$$

can be introduced as disturbance model. Its parameters are chosen according to [161] as $\beta = 0.2\,\frac{\mathrm{rad}}{\mathrm{m}}$ and $v = 30\,\frac{\mathrm{m}}{\mathrm{sec}}$. The parameter α results from the optimization routine for the Kalman filters' covariance matrices $\mathbf{Q}$ presented in Section 4.2.2.

For the simulations and the experiments (Section 4.5), measurements of real road profiles are utilized (see Section 2.2). The profiles are passed with the velocities $v_{p1} = 50\frac{\mathrm{km}}{\mathrm{h}}$ (profile P1) and $v_{p2} = 30\frac{\mathrm{km}}{\mathrm{h}}$ (profile P2), respectively. Figure 4.1 shows the resulting power spectral densities (PSD) of the road excitation signals in comparison with the disturbance model (with $\beta = 0.2\,\frac{\mathrm{rad}}{\mathrm{m}}$, $v = 30\,\frac{\mathrm{m}}{\mathrm{sec}}$ and $\alpha = 2.132 \cdot 10^{-3}$) indicating that the shaping filter describes the characteristic PSDs of the road profiles well, although its parametrization characterizes a rougher road.

4.1.2 Stochastic test rig model

The design of the Extended Kalman filter, which serves as a benchmark for the evaluation of the estimator performance, is designed using the nonlinear test rig model (3.12)- (3.13) without the actuator dynamics. The design of the new estimation concept based on parallel

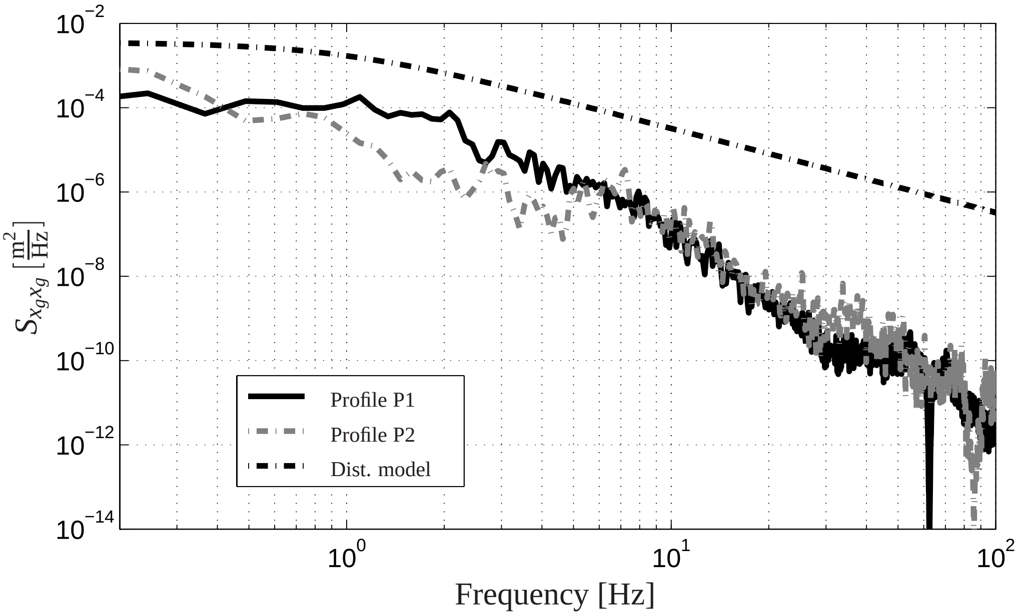

Figure 4.1: Power spectral densities (road profiles and disturbance model).

Kalman filters is accomplished by a model, which is linear except for the nonlinear damper characteristic. Both models are extended by process and measurement noise as well as the disturbance model, which is briefly described in the following for the latter model.

From the equations of motion and the disturbance model given in Section 4.1.1, a state space representation of the system can be derived with the state vector

$$\mathbf{x} = \begin{bmatrix} x_c & \dot{x}_c & x_w & \dot{x}_w & x_g \end{bmatrix}^T . \tag{4.2}$$

The state vector also contains the disturbance x_g in order to include the shaping filter (4.1) in the model. The nonlinear state equations are given as

$$\dot{\mathbf{x}}(t) = \underbrace{\begin{bmatrix} \dot{x}_c \\ \frac{c_c}{m_c}(x_w - x_c) - \frac{F_d(\mathbf{x})}{m_c} + \frac{1}{m_c}u(t) \\ \dot{x}_w \\ \frac{c_w}{m_w}(x_g - x_w) + \frac{d_w}{m_w}(-\beta v x_g - \dot{x}_w) - \frac{c_c}{m_w}(x_w - x_c) + \frac{F_d(\mathbf{x})}{m_w} - \frac{1}{m_w}u(t) \\ -\beta v x_g \end{bmatrix}}_{\mathbf{f}_{\mathrm{est}}(\mathbf{x}(t),u(t))} + \underbrace{\begin{bmatrix} w_{x_c} \\ w_{\dot{x}_c} \\ w_{x_w} \\ w_{\dot{x}_w} \\ w_{x_g} \end{bmatrix}}_{\mathbf{w}(t)} \tag{4.3}$$

The considered process noise $\mathbf{w}(t)$ is zero mean white Gaussian noise with covariance kernel $E\{\mathbf{w}(t)\mathbf{w}(t')\} = \mathbf{Q}\delta(t-t')$, where $\delta(t-t')$ denotes the Dirac delta and $\mathbf{Q}$ is symmetric and positive definite. While $w_{x_g}(t)$ is the input of the disturbance model (4.1), the first four elements of $\mathbf{w}$ represent model uncertainties.

The measurement signals are gathered in the measurement vector

$$\mathbf{y} = \begin{bmatrix} \ddot{x}_c & \ddot{x}_w & x_c - x_w \end{bmatrix}^T \tag{4.4}$$

and represent a sensor configuration of modern production vehicles. An analysis of Kalman filter based estimator configurations with only two sensors is presented in [36].

The equation of the measurement signals

$$\mathbf{y}(t_i) = \underbrace{\begin{bmatrix} \frac{c_c}{m_c}(x_c - x_w) - \frac{F_d(\mathbf{x})}{m_c} + \frac{1}{m_c}u \\ \frac{c_w}{m_w}(x_g - x_w) + \frac{d_w}{m_w}(-\beta v x_g - \dot{x}_w) - \frac{c_c}{m_w}(x_c - x_w) + \frac{F_d(\mathbf{x})}{m_w} - \frac{1}{m_w}u \\ x_c - x_w \end{bmatrix}}_{\mathbf{h}_{\text{est}}(\mathbf{x}(t_i), u(t_i))} + \underbrace{\begin{bmatrix} v_{\ddot{x}_c} \\ v_{\ddot{x}_w} \\ v_{x_c - x_w} \end{bmatrix}}_{\mathbf{v}(t_i)} \tag{4.5}$$

is given in discrete-time due to the discrete nature of the Kalman filter algorithm. In (4.5), $\mathbf{v}(t_i)$ represents discrete-time white Gaussian measurement noise with zero mean and covariance kernel

$$E\left\{\mathbf{v}(t_i)\mathbf{v}^T(t_j)\right\} = \begin{cases} \mathbf{R} & \text{for} \quad t_i = t_j \\ 0 & \text{for} \quad t_i \neq t_j \end{cases}, \tag{4.6}$$

where $\mathbf{R}$ is symmetric and positive definite. The initial condition $\mathbf{x}(t_0)$ is specified by the Gaussian random variable $\mathbf{x}_0$ with mean $\hat{\mathbf{x}}_0 = \mathbf{0}$ and covariance $\mathbf{P}_0 = \mathbf{0}$. Additionally, $\mathbf{x}(t_o)$, $\mathbf{w}$ and $\mathbf{v}$ are assumed to be stochastically independent.

For the nonlinear model utilized for the design of the Extended Kalman filter, measurement and process noise with the same properties as given above are considered. For the parameter optimization of the Kalman filter structures (Sections 4.2.2 and 4.3.2) and the simulation and measurement results presented in Section 4.5 the accurate nonlinear test rig model (see (3.12) and (3.13)) is used.

4.2 Parallel Kalman filter structure

Since the Kalman filter [63] is able to infer the state of a stochastically disturbed linear system in an optimal manner, it is selected as a basis for the estimation task at hand. In the following Section a short overview on the Kalman filter algorithm is given first and subsequently the new estimator structure for the quarter-vehicle system is presented including the handling of the damper nonlinearity.

4.2.1 Theoretical preliminaries

Let the system state $\mathbf{x} \in \mathbb{R}^n$ be modeled by the linear stochastic differential equation

$$\dot{\mathbf{x}}(t) = \mathbf{A}\mathbf{x}(t) + \mathbf{B}\mathbf{u}(t) + \mathbf{w}(t)\,, \tag{4.7}$$

where $\mathbf{u} \in \mathbb{R}^p$ is the deterministic control input, $\mathbf{w} \in \mathbb{R}^n$ is a zero mean white Gaussian noise process with covariance kernel according to Section 4.1.2 and $\mathbf{A}$, $\mathbf{B}$ are matrices of appropriate dimensions. The initial condition $\mathbf{x}(t_0)$ is specified by the Gaussian random variable $\mathbf{x}_0$ with mean $\hat{\mathbf{x}}_0$ and covariance $\mathbf{P}_0$. Assuming that a first order hold is applied for the control input, (4.7) can be represented equivalently by the stochastic difference equation

$$\mathbf{x}(t_i) = \mathbf{\Phi}(T_s)\mathbf{x}(t_{i-1}) + \mathbf{B}_d\mathbf{u}(t_{i-1}) + \mathbf{w}_d(t_{i-1})\,, \tag{4.8}$$

where $\Phi(\tau) = \exp(\mathbf{A}\tau)$ denotes the state transition matrix, $\mathbf{B}_d = \mathbf{A}^{-1}(\Phi(T_s) - \mathbf{I})\mathbf{B}$ is the discrete-time input matrix and $T_s = t_i - t_{i-1}$ denotes the sampling time [103]. The system noise $\mathbf{w}_d$ is a discrete-time white Gaussian process with mean zero and covariance kernel

$$\begin{aligned} E\left\{\mathbf{w}_d(t_i)\mathbf{w}_d^T(t_i)\right\} &= \mathbf{Q}_d = \int_0^{T_s} \Phi(\tau)\mathbf{Q}\Phi^T(\tau)\,d\tau\,, \\ E\left\{\mathbf{w}_d(t_i)\mathbf{w}_d^T(t_j)\right\} &= \mathbf{0}, \quad t_i \neq t_j\,. \end{aligned} \tag{4.9}$$

Moreover, let the discrete-time measurement process $\mathbf{y} \in \mathbb{R}^q$ be modeled by

$$\mathbf{y}(t_i) = \mathbf{C}\mathbf{x}(t_i) + \mathbf{v}(t_i)\,, \tag{4.10}$$

where $\mathbf{C} \in \mathbb{R}^{q\times n}$ is a constant matrix and $\mathbf{v} \in \mathbb{R}^q$ is a zero mean discrete-time white Gaussian noise process with covariance kernel given by (4.6). Additionally, $\mathbf{x}(t_o)$, $\mathbf{w}$ and $\mathbf{v}$ are assumed to be stochastically independent of each other.

The Kalman filter recursively determines the mean $\hat{\mathbf{x}}(t_i)$ and the covariance $\mathbf{P}(t_i)$ of the state vector $\mathbf{x}(t_i)$ at each sampling instant t_i, conditioned on the entire history of measurements taken. The calculation comprises two steps: According to [103], in the time update the two conditional moments are propagated forward from the point t_{i-1}^+ just after the measurement $\mathbf{y}_m(t_{i-1})$ has been processed to the time t_i^- just before the measurement $\mathbf{y}_m(t_i)$ becomes available as

$$\hat{\mathbf{x}}(t_i^-) = \Phi(T_s)\hat{\mathbf{x}}(t_{i-1}^+) + \mathbf{B}_d\mathbf{u}(t_{i-1}) \ , \tag{4.11}$$

$$\mathbf{P}(t_i^-) = \Phi(T_s)\mathbf{P}(t_{i-1}^+)\Phi^T(T_s) + \mathbf{Q}_d \ . \tag{4.12}$$

The measurement update incorporates the measurement $\mathbf{y}_m(t_i)$ by means of

$$\mathbf{L}(t_i) = \mathbf{P}(t_i^-)\mathbf{C}^T[\mathbf{C}\mathbf{P}(t_i^-)\mathbf{C}^T + \mathbf{R}]^{-1} \ , \tag{4.13}$$

$$\hat{\mathbf{x}}(t_i^+) = \hat{\mathbf{x}}(t_i^-) + \mathbf{L}(t_i)[\mathbf{y}_m(t_i) - \mathbf{C}\hat{\mathbf{x}}(t_i^-)] \ , \tag{4.14}$$

$$\mathbf{P}(t_i^+) = \mathbf{P}(t_i^-) - \mathbf{L}(t_i)\mathbf{C}\mathbf{P}(t_i^-) \ , \tag{4.15}$$

where $\mathbf{L}(t_i)$ is the Kalman filter gain [103]. Under the assumptions made, the conditional mean $\hat{\mathbf{x}}(t_i^+)$ can be shown to be the optimal state estimate. The conditional covariance $\mathbf{P}(t_i^+)$ of the state vector $\mathbf{x}(t_i^+)$ simultaneously characterizes the covariance of the error which results from using $\hat{\mathbf{x}}(t_i^+)$ as estimate [103].

4.2.2 Application to the quarter-vehicle model

As the suspension model in (4.3) and (4.5) contains the nonlinear damper characteristic, the standard Kalman filter algorithm cannot be applied directly. Obviously, (4.3) and (4.5) can be decomposed into a linear and a nonlinear part according to

$$\dot{\mathbf{x}}(t) = \mathbf{A}\mathbf{x}(t) + \mathbf{b}F(t) + \mathbf{b}_dF_d(\mathbf{x}(t)) + \mathbf{w}(t) \ , \tag{4.16}$$

$$\mathbf{y}(t_i) = \mathbf{C}\mathbf{x}(t_i) + \mathbf{d}F(t_i) + \mathbf{d}_dF_d(\mathbf{x}(t_i)) + \mathbf{v}(t_i) \ . \tag{4.17}$$

Considering the damper force as fictitious input signal as proposed by [111] and [64], one can define an augmented input vector $\mathbf{u}_a(t) = [F(t)\ F_d(t)]^T$ with associated matrices $\mathbf{B}_a = [\mathbf{b}\ \mathbf{b}_d]$ and $\mathbf{D}_a = [\mathbf{d}\ \mathbf{d}_d]$. The resulting linear system representation serves as basis for the Kalman filter design.

Since the damper force is unknown, an estimate is generated using the estimated damper velocity from the previous sampling instant and the damper characteristic displayed in Figure

3.6. The estimated damper force is fed back into the state estimator resulting in the Kalman filter structure depicted in Figure 4.2. If the damper characteristic of the damper element is used, the transmission factor i_d (see Chapter 3.3.2) must be employed to calculate the damper force in the coordinates of the quarter-vehicle model. Note that the characteristic depicted in Figure 3.6 (left) is already given in these coordinates, i.e. it represents the complete lower grey block in Figure 4.2.

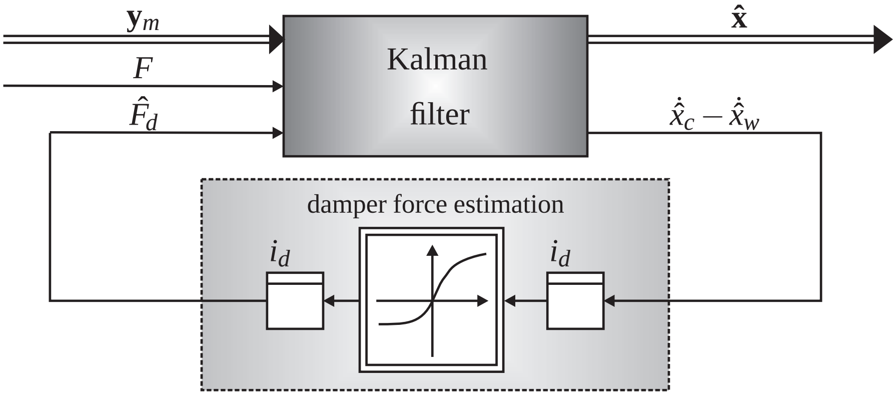

Figure 4.2: Kalman filter structure with nonlinear damper force estimation.

The tuning of the Kalman filter is accomplished by varying the diagonal entries of the covariance matrices **Q** and **R**, while all other elements are fixed at zero. In order to achieve the best possible estimation performance, a numerical optimization algorithm is employed to determine appropriate covariance values. Road profile P1 (see Chapter 2.2), being passed with a vehicle velocity of $v_{p1} = 50\ \frac{\text{km}}{\text{h}}$, serves as road excitation. In order to obtain realistic conditions, measurement noise derived from sensor signals recorded at the test rig is superimposed the simulated measurements. For the tuning process the passive test rig model (Section 4.1.2) is considered ($u(t) = u(t_i) = 0$), that includes all nonlinearities of the considered suspension system. It is noted that the resulting estimators are intensively tested in the active suspension case as well in order to validate their applicability for suspension control (see Section 4.5 and [78]).

To quantify the estimation accuracy of an arbitrary signal $z(t_i)$ in a time set $T_{\text{est}} = \{t_0, t_1, \ldots, t_N\}$

with equidistant t_i the performance measure

$$\Gamma_z = 1 - \frac{\sqrt{\frac{1}{N}\sum_{n=1}^{N}\left(z(t_n) - \hat{z}(t_n)\right)^2}}{\sqrt{\frac{1}{N}\sum_{n=1}^{N} z^2(t_n)}} = 1 - \Xi_z \tag{4.18}$$

is introduced, where $\hat{z}(t_i)$ denotes the estimated value of the quantity $z(t_i)$. Corresponding to the variables of primary interest (state variables and the dynamic wheel load), the objective function to be minimized is chosen as

$$\mathbf{J}(\eta) = \begin{bmatrix} \Xi_{x_c - x_w} & \Xi_{x_w - x_g} & \Xi_{\dot{x}_c} & \Xi_{\dot{x}_w} & \Xi_{F_{dyn}} \end{bmatrix}^T , \tag{4.19}$$

where $\Xi_z = \Xi_z(\eta)$ is defined as in (4.18) and η is a vector containing the diagonal elements of $\mathbf{Q}$ and $\mathbf{R}$ (all other elements are assumed to be zero, i.e. $\mathbf{Q}_{ij} = \mathbf{R}_{ij} = 0 \quad \text{for} \quad i \neq j$) as

$$\eta = \left[\mathrm{diag}(\mathbf{Q}), \mathrm{diag}(\mathbf{R})\right]^T . \tag{4.20}$$

Moreover, a constraint is introduced, which compares the actual estimation error of each state variable with its theoretical standard deviation $\sigma_j(t_i^+) = \sqrt{\mathbf{P}_{jj}(t_i^+)}$. Since the error process $\mathbf{e}(t_i^+)$ is Gaussian and has zero mean [103], it is demanded according to [177] that 68.3% of the error values are within the intervall $[-\sigma_j(t_i^+), \sigma_j(t_i^+)]$.

Hence, the resulting multiobjective optimization problem (see also [20] for a detailed presentation of this problem class) can be formulated as

$$\min_{\eta} \mathbf{J}(\eta) \tag{4.21}$$

$$\text{s.t.} \quad g_j = 0.683 - \frac{1}{N}\mathrm{card}\left\{t_i \,\middle|\, -\sigma_j(t_i^+) \leq e_j(t_i^+) \leq \sigma_j(t_i^+),\, t_i \in T_{\mathrm{est}}\right\} \leq 0 \tag{4.22}$$

with $j = 1, ..., 5$. In (4.22) $\mathrm{card}(M)$ denotes the cardinal number of a set M specifying the number of elements in M.

The optimization problem (4.21), (4.22) is solved by means of the *NSGA-II*, a multiobjective genetic algorithm proposed by Deb et al. in [23]. The results obtained from analyzing the received Pareto front in terms of the cost functional (4.18) are depicted as a spider chart in Figure 4.3. Therefore, a value of (4.18) close to one characterizes an excellent estimation performance for each quantity. The dashed line shows the performance measures Γ_z of the configuration, which minimizes the Euclidean norm $||\mathbf{J}||$ and thus is the best compromise for the parametrization of a single Kalman filter for the considered application. The dotted line

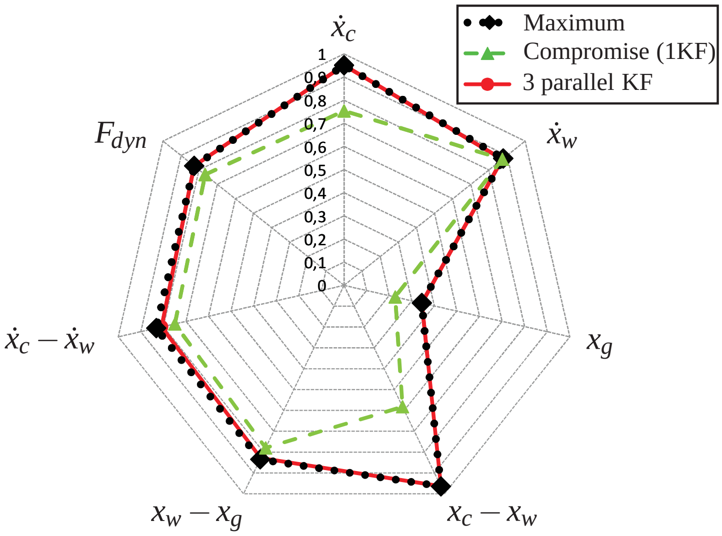

Figure 4.3: Maximum achievable performance measure for each quantity (dotted) in comparison with the best compromise (dashed) and a configuration of 3 parallel Kalman filters (solid).

represents the maximum Γ_z-value of each single quantity $z(t_i)$, individually determined over all configurations contained in the Pareto front. From the curves the conflict regarding the estimation performance of each signal becomes clear: By the use of a single Kalman filter not all required quantities can be estimated with maximum accuracy. One might argue that this contradicts the optimality of the Kalman filter, but it has to be noted that this optimality is based on the assumption, that the physical system is exactly modeled by the Kalman filter equations, a premise which is not met in the case at hand.

4.2.3 Resulting parallel Kalman filter structure

The conflict motivates the use of multiple parallel Kalman filters with damper force estimation, each of them supplying the signals, that are estimated with maximum quality. To choose the individual Kalman filter for the parallel structure, the configurations from the Pareto front are considered that maximize the estimation performance for each quantity. Thus, from the Pareto front the individuals η_i are chosen, that minimize each element of the cost function $\mathbf{J}(\eta)$, i.e.

$$\eta_i = \arg\min_{\eta} J_i \,. \tag{4.23}$$

By this approach, one individuum for each of the five performance objectives (see (4.19)) results. However, it is possible to discard two individuums since their advantage in estimation quality for the quantity they estimate most accurately is small compared to the other individuals and it is desirable to keep the number of parallel Kalman filters small to facilitate the implementation. As illustrated by the solid line in Figure 4.3, three Kalman filters are sufficient to approximate the maximum estimation accuracy sufficiently well. The first one provides the signals $\dot{x}_c$, $x_w - x_g$ and F_{dyn}, the second one $\dot{x}_w$ and $x_c - x_w$ and the third one is necessary only for the estimation of the road excitation x_g, which is considered to evaluate the estimation quality for a possible disturbance feedforward component of the suspension controller. A detailed comparison between the simulation and measurement results is given in Section 4.5.

A robustness analysis in [36] has shown that the main influence on the estimation performance of Kalman filters for suspension applications is a deviation of the chassis mass m_c from its nominal value. In order to consider this, the concept can be extended by a mass estimation, which can be accomplished by means of an Extended Kalman filter, that is presented in the next Section.

4.3 Extended Kalman filter

The Extended Kalman filter (EKF) is a concept that enables the application of linear Kalman filtering to nonlinear systems by linearizing the corresponding model in every time step [104]. Since all nonlinearities are considered in the design process, the EKF is used as a benchmark for the parallel Kalman filter concept and the filter based estimator presented in Section 4.4.

4.3.1 Theoretical preliminaries

For the estimator design, a system of the form

$$\dot{\mathbf{x}}(t) = \mathbf{f}(\mathbf{x}(t), \mathbf{u}(t), t) + \mathbf{w}(t) \tag{4.24}$$

is considered, where $\mathbf{w}(t)$ represents process noise with the properties described in Section 4.1.2. The initial condition $\mathbf{x}(t_0)$ is specified by the Gaussian random variable $\mathbf{x}_0$ with mean $\hat{\mathbf{x}}_0$ and covariance $\mathbf{P}_0$. The measurements are modeled as a discrete-time stochastic process

$$\mathbf{y}(t_i) = \mathbf{h}(\mathbf{x}(t_i), \mathbf{u}(t_i), t_i) + \mathbf{v}(t_i) \tag{4.25}$$

with $\mathbf{v}(t_i)$ being zero-mean white Gaussian measurement noise with covariance kernel as defined in (4.6).

For the linearization, the reference trajectories given by the undisturbed system

$$\begin{aligned}\dot{\mathbf{x}}_n(t) &= \mathbf{f}(\mathbf{x}_n(t),\mathbf{u}(t),t)\,, &(4.26)\\ \mathbf{y}_n(t_i) &= \mathbf{h}(\mathbf{x}_n(t_i),\mathbf{u}(t_i),t_i) &(4.27)\end{aligned}$$

are introduced with the initial condition $\mathbf{x}_n(t_0)=\hat{\mathbf{x}}_0$ and the same input vector as in (4.24). If the system is linearized along the reference trajectory $\mathbf{x}_n(t)$ given by (4.26) and $\delta\mathbf{x}(t)$ and $\delta\mathbf{y}(t)$ are introduced as first order approximations for the processes $\mathbf{x}(t)-\mathbf{x}_n(t)$ and $\mathbf{y}(t)-\mathbf{y}_n(t)$, respectively, the linear system representation

$$\begin{aligned}\delta\dot{\mathbf{x}}(t) &= \mathbf{A}(t,\mathbf{x}_n(t))\delta\mathbf{x}(t)+\mathbf{w}(t)\,, &(4.28)\\ \delta\mathbf{y}(t) &= \mathbf{C}(t,\mathbf{x}_n(t_i))\delta\mathbf{x}(t_i)+\mathbf{v}(t_i) &(4.29)\end{aligned}$$

results with the Jacobi matrices

$$\begin{aligned}\mathbf{A}(t,\mathbf{x}_n(t)) &= \left.\frac{\partial\mathbf{f}(\mathbf{x},\mathbf{u}(t),t)}{\partial\mathbf{x}}\right|_{\mathbf{x}=\mathbf{x}_n(t)}\,, &(4.30)\\ \mathbf{C}(t,\mathbf{x}_n(t_i)) &= \left.\frac{\partial\mathbf{h}(\mathbf{x},\mathbf{u}(t_i),t_i)}{\partial\mathbf{x}}\right|_{\mathbf{x}=\mathbf{x}_n(t_i)}\,, &(4.31)\end{aligned}$$

that are evaluated along the reference trajectory [104]. The initial condition is characterized by the Gaussian random variable $\delta\mathbf{x}(t_0)$ with $E\{\delta\mathbf{x}(t_0)\}=\mathbf{0}$ (due to $\mathbf{x}_n(t_0)=\hat{\mathbf{x}}_0$) and covariance $\mathbf{P}_0$. If linear estimation theory is applied to this model, the *linearized Kalman filter* is obtained [104]. The inputs of the Kalman filter are $\mathbf{u}(t)$ and $\mathbf{y}(t_i)-\mathbf{y}_n(t_i)$. The state estimate $\hat{\mathbf{x}}(t)$ can be calculated from the reference trajectory $\mathbf{x}_n(t)$ and the Kalman filter output $\delta\hat{\mathbf{x}}(t)$ as $\hat{\mathbf{x}}(t)=\mathbf{x}_n(t)+\delta\hat{\mathbf{x}}(t)$.

The main idea of the EKF is to perform this linearization in every time step using the estimate from the previous time step $\hat{\mathbf{x}}(t_{i-1}^+)$ as initial value in order to keep the deviations from the reference trajectory small and thus increase the estimation accuracy. Before the resulting equations (see e.g. [104]) are summarized, a few comments on the notation are given. The estimate of $\mathbf{x}(t)$ in the interval $t\in[t_{i-1},t_i[$ is referred to as $\hat{\mathbf{x}}(t/t_{i-1})$. Moreover, let $\Phi[t_i,t;\hat{\mathbf{x}}(\tau/t_{i-1})]$ denote the state transition matrix associated with the Jacobi matrix $\mathbf{A}(\tau;\hat{\mathbf{x}}(\tau/t_{i-1}))$ in the time interval $\tau\in[t_{i-1},t_i[$, propagating the state from t to t_i. As in the linear case, the state estimate $\hat{\mathbf{x}}(t_i)$ and its covariance $\mathbf{P}(t_i)$ are calculated in two steps: In the time update the estimate is propagated forward from the point t_{i-1}^{+}, just after the measurement $\mathbf{y}_m(t_{i-1})$ has been processed, to the time t_i^{-}, just before the measurement $\mathbf{y}_m(t_i)$ becomes available, i.e.

$$\begin{aligned}
\hat{\mathbf{x}}(t_i^-) &= \hat{\mathbf{x}}(t_{i-1}^+) + \int_{t_{i-1}}^{t_i} \mathbf{f}(\hat{\mathbf{x}}(t/t_{i-1}), \mathbf{u}(t), t)\,dt\,, && (4.32)\\
\mathbf{P}(t_i^-) &= \Phi[t_i, t_{i-1}; \hat{\mathbf{x}}(\tau/t_{i-1})]\mathbf{P}(t_{i-1}^+)\Phi^T[t_i, t_{i-1}; \hat{\mathbf{x}}(\tau/t_{i-1})] + \dots && (4.33)\\
&\quad + \int_{t_{i-1}}^{t_i} \Phi[t_i, t; \hat{\mathbf{x}}(\tau/t_{i-1})]\mathbf{Q}(t)\Phi^T[t_i, t; \hat{\mathbf{x}}(\tau/t_{i-1})]\,dt\,. && (4.34)
\end{aligned}$$

The measurement update incorporates the measurement $\mathbf{y}_m(t_i)$ by means of

$$\begin{aligned}
\mathbf{K}(t_i) &= \mathbf{P}(t_i^-)\mathbf{C}_{t_i,t_i^-}^T \left[\mathbf{C}_{t_i,t_i^-}\mathbf{P}(t_i^-)\mathbf{C}_{t_i,t_i^-}^T + \mathbf{R}(t_i)\right]^{-1}, && (4.35)\\
\hat{\mathbf{x}}(t_i^+) &= \hat{\mathbf{x}}(t_i^-) + \mathbf{K}(t_i)\left[\mathbf{y}_m(t_i) - \mathbf{h}(\hat{\mathbf{x}}(t_i^-), \mathbf{u}(t_i), t_i)\right], && (4.36)\\
\mathbf{P}(t_i^+) &= \mathbf{P}(t_i^-) - \mathbf{K}(t_i)\mathbf{C}_{t_i,t_i^-}\mathbf{P}(t_i^-) && (4.37)
\end{aligned}$$

with $\mathbf{C}_{t_i,t_i^-} = \mathbf{C}(t_i, \hat{\mathbf{x}}(t_i^-))$.

4.3.2 Application to the quarter-vehicle test rig model

For the implementation of the EKF, the integration in (4.32) is realized by a second order Runge-Kutta method (see e.g. [18]). The transition matrix in (4.34) is approximated by

$$\Phi[t_i, t; \hat{\mathbf{x}}(\tau/t_{i-1})] \approx \mathbf{I} + (t_i - t)\mathbf{A}(t_{i-1}; \hat{\mathbf{x}}(t_{i-1}^+))\,, \qquad (4.38)$$

which is sufficiently accurate for the application at hand (see [177] for a discussion of the approximation) and enables an analytic evaluation of the integral term in (4.34). The friction forces are not considered for the calculation of the Jacobi matrices (4.30), (4.31) and the transition matrix (4.38) as their gradient is approximately zero except for very low velocities (compare (3.7)). Although the Kalman filter algorithm could also consider time-variant covariance matrices $\mathbf{Q}(t)$ in (4.34) and $\mathbf{R}(t_i)$ (4.35), constant covariance matrices are chosen so that the tuning of the EKF can also be accomplished by means of numerical optimization as described in Section 4.2.2.

4.3.3 Mass estimation

The Extended Kalman filter can conveniently also be employed in the suspension application to estimate the chassis mass m_c, which varies during operation of a vehicle and thus influences the estimation performance. This can be accomplished by a simple extension of the estimator structure and is conducted to get insights on how accurate the mass can be estimated in the real suspension application at the quarter-vehicle test rig. Fröhlich has presented the theory of the concept in [36], which is only briefly reviewed.

The mass estimation is realized by including the parameter m_c in the nonlinear stochastic test rig model as a new state variable using a random walk approach (see e.g. [104]), i.e.

$$\dot{m}_c = w_{m_c}(t)\,, \tag{4.39}$$

where $w_{m_c}(t)$ represents zero-mean Gaussian white noise with appropriate intensity q_{m_c}. The initial value $m_c(t_0)$ is characterized by its mean $\hat{m}_{c,0} = m_{c,nom}$ (with $m_{c,nom} = 94.38\,\mathrm{kg}$ being the nominal value of the chassis mass, see Table B.1 in the Appendix) and the covariance $P_{m_c,0}$.

4.4 Filter based estimation

In production cars, filter based estimation concepts (see e.g. [36] for an overview of employed estimation concepts for suspension applications) are frequently preferred over Kalman filtering because the full state information is seldom necessary for the applied suspension control techniques (e.g. skyhook control described in Chapter 2.5). Therefore, besides the Kalman filters, a well applicable new filter based estimation concept (Figure 4.4) is presented for the states, the dynamic wheel load and the damper velocity in order to be compared to the more complex Kalman filter structures (Sections 4.2, 4.3).

In [154], a velocity estimation procedure without phase delay is presented calculating the velocity from filtered position and acceleration signals. In [81], this technique is employed to determine the damper velocity $\dot{x}_{cw}$ of a vehicle suspension system. The linear filters

$$G_1(s) = s - s^2 G_2(s) \;\text{ and }\; G_2(s) = \frac{T^2 s}{T^2 s^2 + 2kTs + 1} \tag{4.40}$$

are defined, where $G_1(s)$ is a highpass and $G_2(s)$ represents a bandpass filter. The estimated damper velocity results from the filter outputs as

$$\Delta\dot{\hat{x}}_{cw}(t) \circ\!\!-\!\!\bullet\, G_2(s)s^2\Delta X_{cw}(s) + G_1(s)\Delta X_{cw}(s) \tag{4.41}$$

with $\Delta X_{cw}(s)$ denoting the Laplace transform of the suspension deflection measurement signal and $s^2\Delta X_{cw}(s)$ resulting from the Laplace transform of the difference of the acceleration

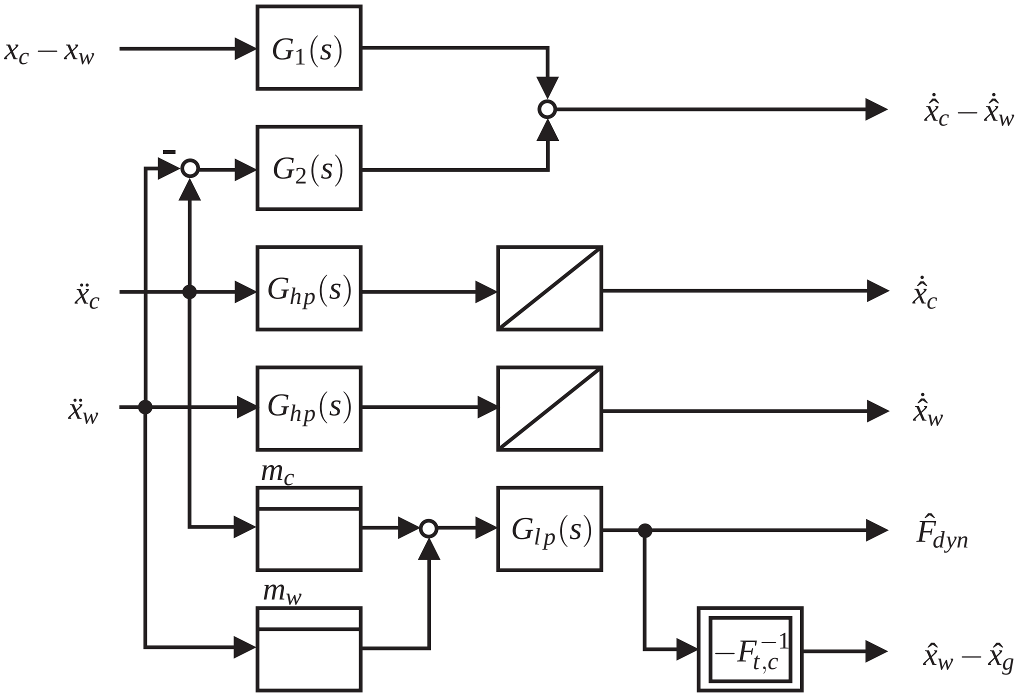

Figure 4.4: Filter based estimation scheme.

signals. The parameters of the filters in (4.40) are chosen as $k = 1$ and $T = 0.1$ for the application at hand. The absolute velocities of the chassis and the wheel mass ($\dot{x}_c$, $\dot{x}_w$) are gained from the corresponding acceleration measurements by integration after highpass filtering with first order filters $G_{hp}(s)$ (cutoff frequency 0.5 Hz) to remove offsets and drifts. A filter based estimate $\hat{F}_{dyn}$ for the dynamic wheel load can be gained from the accelerations of the chassis and wheel mass employing a first order lowpass filter $G_{lp}(s)$ with impulse response $g_{lp}(t)$ and cutoff frequency 60 Hz as

$$\hat{F}_{dyn}(t) = g_{lp}(t) * (m_c\ddot{x}_c(t) + m_w\ddot{x}_w(t)) \ . \tag{4.42}$$

The estimate of the tire deflection is calculated from (4.42) using the inverse of the tire's force-deflection characteristic (see Figure 3.6 (right) and the definition of $F_{t,c}$ given in (3.6), respectively), i.e.

$$\hat{x}_w(t) - \hat{x}_g(t) = -F_{t,c}^{-1}\left(\hat{F}_{dyn}(t)\right) \ . \tag{4.43}$$

The small tire damping of $d_w = 50\frac{\text{Nsec}}{\text{m}}$ is neglected for this calculation.

4.5 Simulation and measurement results

The nonlinear test rig model (Section 3.3.3) is used to analyze the performance of the estimator structure in simulations and the experimental validation is conducted at the fully active suspension test rig. Three different signals are used as excitations: Two of them are measurements of real road profiles (see Section 2.2.1), which are passed with the velocities $v_{p1} = 50\,\frac{\mathrm{km}}{\mathrm{h}}$ (profile P1) and $v_{p2} = 30\,\frac{\mathrm{km}}{\mathrm{h}}$ (profile P2), respectively. The other test-signal is a singular disturbance event (bump) (see Section 2.2.2) with $\hat{h} = 0.04\,\mathrm{m}$, $v_b = 10\,\frac{\mathrm{km}}{\mathrm{h}}$ and $L = 0.5\,\mathrm{m}$. The bump occurs after $0.41\,\mathrm{sec}$. The parameters have been chosen according to the test rig specifications. In order to ensure comparability between the simulation and the measurement results, the measured disturbance signals $x_g(t)$ of the test rig have been used for the simulations because the original road profile signals are slightly changed due to the dynamic behavior of the lower test rig actuator (see Chapter 3). Moreover, recorded sensor noise is superimposed the simulated measurement signals to emulate measurement noise in the simulations.

For the measurements, the reference signals for chassis and wheel velocity are calculated off-line from the acceleration signals by integration and high pass forward backward filtering (fourth order Butterworth filter with cutoff frequency $0.4\,\mathrm{Hz}$) to achieve zero-phase deviation and eliminate drifts. Because the tire did not loose ground contact during the experiments, the reference for the tire deflection is gained from the measured dynamic wheel load and the nonlinear tire force-deflection characteristic as in (4.43). The small tire damping is neglected for the calculation of the reference signal.

Figure 4.5 (left) shows the comparison of the simulation and measurement results of the parallel Kalman filter concept (3KF) and the respective performance of the Extended Kalman Filter (EKF) is shown in the right part of the Figure (both evaluated for road profile P1). The performance is quantified by the the cost functional (4.18). The simulation and measurement results are very similar, which underlines the accuracy of the nonlinear model of the test rig. The filter based estimator concept is only tested in experiments because its performance is primarily determined by the quality of the measurement signals.

The 3KF concept gives very accurate estimation results including the best estimation of the road profiles. Nevertheless, the estimation quality of the road excitation $x_g(t)$ is considerably lower than for the other quantities and it requires further analysis to determine if it is suitable for disturbance feedforward control. Note that if the estimation of the road profile is discarded,

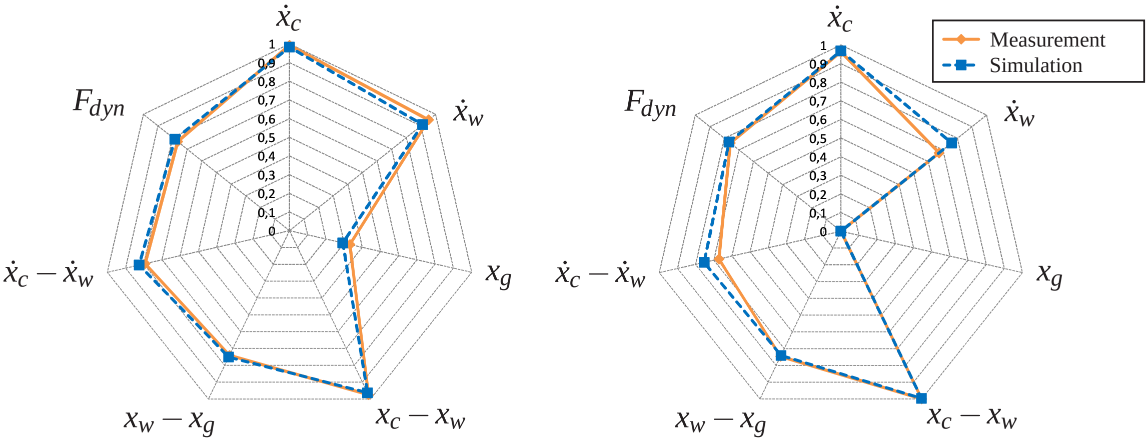

Figure 4.5: 3KF (left) and EKF (right) performance in simulation and measurement (profile P1).

since it is not necessary for state feedback control, the parallel Kalman filter concept can operate with only two parallel Kalman filters (2KF). The measurement results obtained with the 3KF concept for profile P1 are visualized in Figure 4.6 a) to e). Furthermore, exemplary results (estimates of the tire deflection and the wheel velocity) obtained for the excitation with the singular disturbance event with the 3KF concept are depicted in Figure 4.6 f) and g).

The EKF also achieves a high estimation performance (Figure 4.5 (right)) except for the road profile estimation. Although the 3KF concept shows better results than the EKF concept, it is noted that the EKF is superior to the application of only one conventional Kalman filter as presented in [78].

The comparison of the estimation performance of all three proposed estimator concepts is shown in the spider chart depicted in Figure 4.7. Furthermore, Table 4.1 summarizes the simulation and measurement results of the three estimator concepts for the excitation with the road profiles P1 and P2. It can be seen that the 3KF concept has the best overall performance. The filter based estimation (FB) of the damper's relative velocity is superior to the Kalman filter performance, which further motivates the well applicable phase-free filtering approach even if less accurate sensor signals are available in production cars. It is noted that the phase-free filtering approach (4.41) for the damper velocity gives better results ($\Gamma_{\dot{x}_c - \dot{x}_w} = 0.9$) than differentiating the suspension deflection measurement signal after lowpass filtering would ($\tilde{\Gamma}_{\dot{x}_c - \dot{x}_w} = 0.82$). The FB concept directly uses the suspension deflection measurement signal (scaled by i_d^{-1}) so that $\Gamma_{x_c-x_w} = 1$ results. The estimates of the states $\dot{x}_w(t)$ and $\dot{x}_c(t)$ of the computationally simple FB estimator, however, are less accurate than those of the 3KF concept, which indicates that the main application for the FB concept are semi-active damper control systems and wheel load estimations for the determination of the current driving state.

Table 4.1: Performance results of simulations and measurements (for road profiles P1 and P2).

Quantity		**Profile P1**		**Profile P2**	
		meas.	sim.	meas.	sim.
$\Gamma_{x_c-x_w}$	EKF	0.99	0.99	0.99	0.99
	3KF	0.97	0.96	0.95	0.93
	FB	1	-	1	-
$\Gamma_{\dot{x}_c}$	EKF	0.96	0.97	0.90	0.94
	3KF	0.99	0.98	0.98	0.96
	FB	0.70	-	0.71	-
$\Gamma_{x_w-x_g}$	EKF	0.75	0.74	0.63	0.75
	3KF	0.74	0.75	0.62	0.76
	FB	0.75	-	0.63	-
$\Gamma_{\dot{x}_w}$	EKF	0.67	0.76	0.64	0.78
	3KF	0.95	0.91	0.97	0.92
	FB	0.82	-	0.90	-
$\Gamma_{F_{dyn}}$	EKF	0.76	0.77	0.65	0.79
	3KF	0.77	0.78	0.65	0.81
	FB	0.76	-	0.64	-
Γ_{x_g}	EKF	-0.98	-0.06	-0.62	-0.07
	3KF	0.33	0.29	-0.02	-0.01
	FB	-	-	-	-
$\Gamma_{\dot{x}_c-\dot{x}_w}$	EKF	0.67	0.75	0.61	0.77
	3KF	0.79	0.83	0.73	0.84
	FB	0.90	-	0.82	-

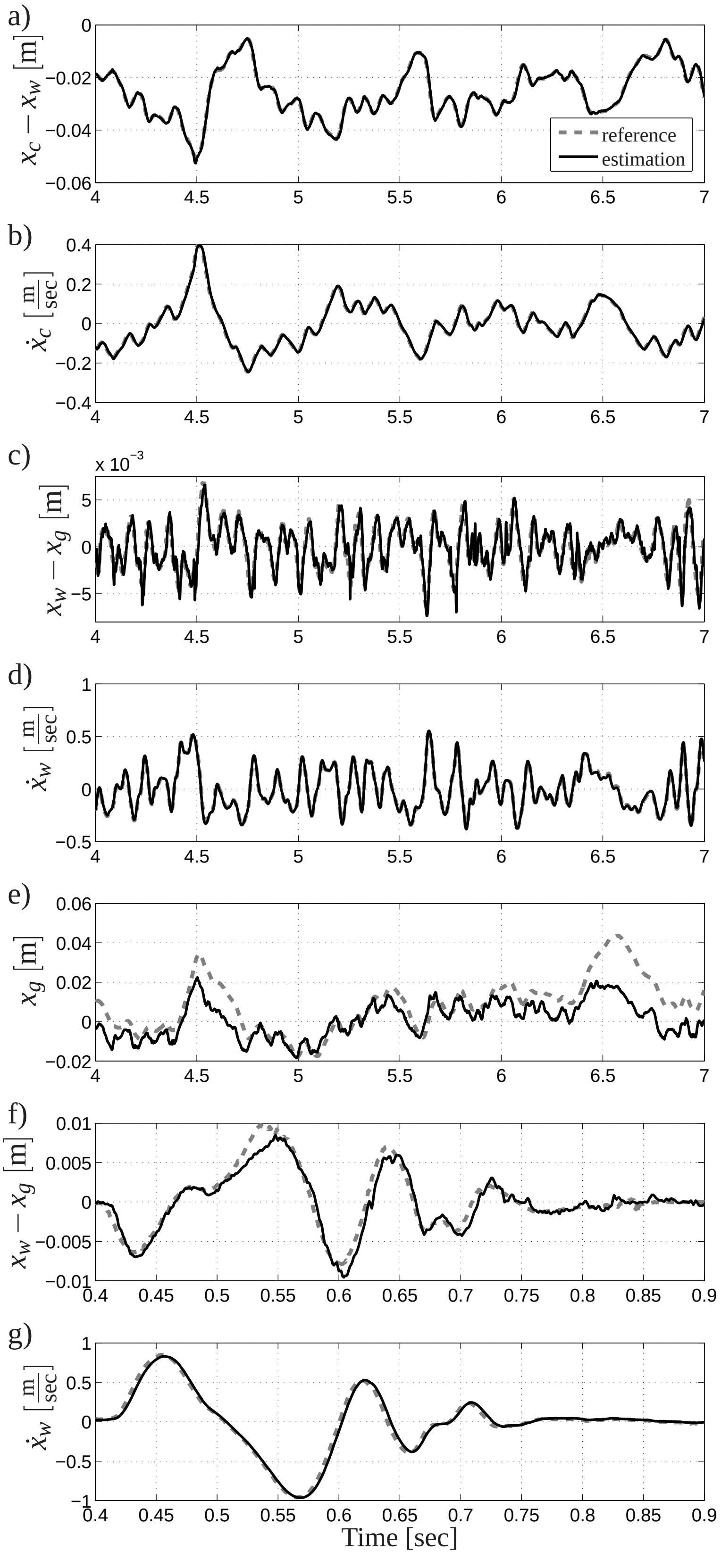

Figure 4.6: Exemplary measurement results for the active suspension system excited with the measured road profile P1 (a to e) and with the singular disturbance event (f to g).

Furthermore, it is noted that the application of two parallel Kalman filters (2KF) is sufficient for state feedback based control. In [78] the 3KF concept is also tested with a linear quadratic regulator that uses the estimated states for feedback, i.e. $u(t) \neq 0$. These results and further experiments at the test rig have shown that the estimator performance of all proposed estimator concepts does not significantly deteriorate in the active suspension case.

A comparison of the results given in Table 4.1 with estimator performance presented in the literature underlines the quality of the proposed estimator concepts: Venhovens presents in [161] results of $\Gamma_{\dot{x}_c}^{\text{ven}} = 0.67$ and $\Gamma_{F_{dyn}}^{\text{ven}} = 0.77$ in a linear simulation with a conventional Kalman filter. Using an Unscented Kalman filter, which is a computationally complex algorithm, Fröhlich gives measurement results of $\Gamma_{F_{dyn}}^{\text{fr}} = 0.73$, $\Gamma_{\dot{x}_c}^{\text{fr}} = 0.86$ in [37], which are outperformed by the presented estimator structures EKF and 3KF.

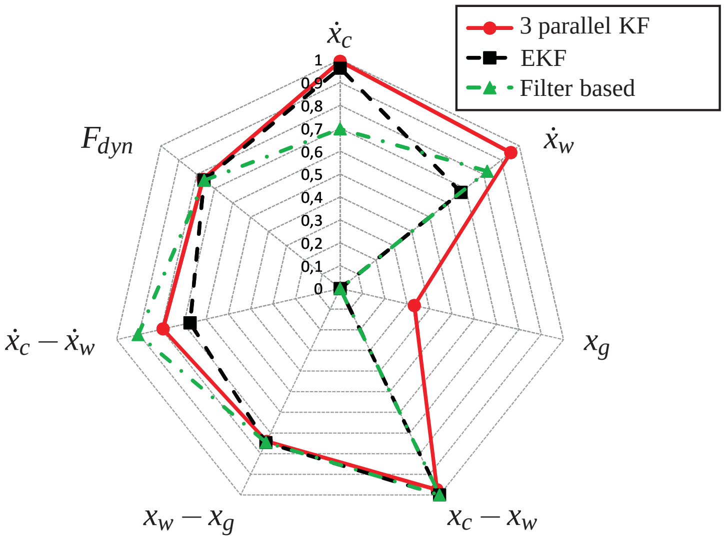

Figure 4.7: Measurement results of the estimation concepts EKF, 3KF, FB for road profile P1.

The computational complexity of the algorithms can be specified by the turnaround time of the real-time application. The turnaround time indicates the time the real-time system of the test rig (see Chapter 3.2.3) needs for the computation of one step of the sampled application. The resulting average turnaround times are $t_{ekf} = 0.327\,\text{msec}$, $t_{2kf} = 0.287\,\text{msec}$, $t_{3kf} = 0.409\,\text{msec}$, $t_{fb} = 0.081\,\text{msec}$. Although the average turnaround time of the 3KF concept is higher than the one for the EKF, in the case of the EKF algorithm parts of the real time application had to be removed from the software code since peaks in the EKF turnaround time have caused problems regarding real time capability. For all other algorithms this measure has not been necessary, which leads to the conclusion that the EKF is less appropriate for the considered real time application.

Mass estimation results

In order to experimentally validate the mass estimation, the EKF has been initialized with $\hat{m}_{c,0} = 30\,\text{kg}$. The result for the estimation of the chassis mass is shown in Figure 4.8. After a transient period of approx. 10 sec, the mass is estimated with sufficient accuracy (rms-error within $10\,\text{sec} \leq t \leq 25\,\text{sec}$ $\|\Delta m_c\|_{\text{rms}} \approx 3.1\,\text{kg}$, maximum peak error within this time-interval $\max(|\Delta m_c|) = 3.7\,\text{kg}$). Thus, the mass estimation performs well at the quarter-vehicle test rig and could also be used to adjust controller parameters to different load levels of the vehicle. However, due to the deficits of the EKF regarding real time capability a mass estimation e.g. by a filter based concept would be more appropriate for the considered application, which is an aspect of future work (see Chapter 9).

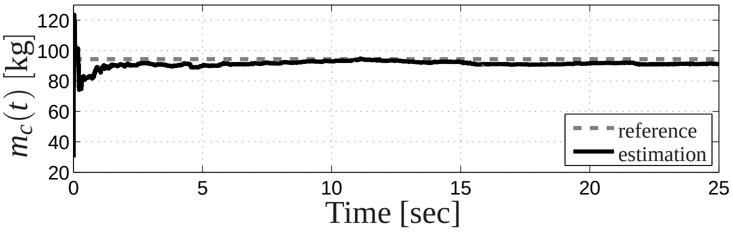

Figure 4.8: Measurement result of the mass estimation by the EKF.

4.6 Discussion

Three different estimator concepts for a quarter-vehicle suspension system have been presented: An Extended Kalman filter (EKF), which linearizes the nonlinear model in every time step, three parallel linear Kalman filters (3KF), differently tuned in order to maximize the estimation performance, and a filter based concept (FB), which gains the estimates for the variables of interest from filtered sensor signals. The comparison of the concepts has been conducted based on simulations as well as measurements on the quarter-vehicle test rig presented in Chapter 3. If the full state vector has to be estimated for suspension control, the concept 3KF represents a good compromise between estimation accuracy and real time capability. This estimator takes into account the nonlinear damper characteristic by considering the damper force as an additional input. Thus, the conventional Kalman filter algorithm can be used and computational effort is kept moderate. If the estimation of the road excitation is discarded due to its significantly lower quality compared to the other signals, two parallel Kalman filters are sufficient for the parallel Kalman filter concept, which reduces the computational load and facilitates the implementation of the concept.

The computationally complex benchmark estimator EKF achieves good estimations for the signals of interest and a very accurate estimate of the chassis mass. The well applicable FB concept gives accurate estimates of the damper velocity and the dynamic wheel load and is used for the control approach presented in Chapter 8. A possible extension of the filter based concept is a chassis mass estimation based on the suspension deflection measurement and the damper velocity estimate (such a concept has been proposed in [36]).

The overall evaluation of the estimation results and a comparison with results published in the literature confirm that the concept 3KF performs best. Consequently, it is used for the design of an adaptive controller structure presented in the next Chapter.

Chapter 5

ADAPTIVE SWITCHING CONTROL OF ACTIVE SUSPENSION SYSTEMS

As pointed out in Chapter 1, the conflict between ride comfort and ride safety can be ideally eased by mechatronic suspension systems if the controller parametrization can be adjusted according to the current driving state of the vehicle. The main idea of this driving state adaptive suspension control is to focus on ride comfort as long as the limits of the dynamic wheel load and suspension deflection are not violated. If the driving state tends to become critical, a more safety oriented controller parametrization is chosen. The benefit of this approach is that the flexibility, offered by modern mechatronic suspension components, is not limited by a time-invariant control law.

In this Chapter a corresponding adaptive control approach is presented for fully active suspension systems. The main questions addressed in this Chapter are:

- How is the criticality of the driving state detected and how is the controller adaptation realized?
- Which aspects must be considered to guarantee stability of the adaptively controlled active suspension system?
- What is the performance potential of a driving state adaptive suspension control approach?

Although the considered complex hardware structure of the fully active suspension system and the controller structure are both well beyond the state of the art of production vehicles, the Chapter focusses on the achievable performance of adaptively controlled mechatronic suspension systems in a very realistic framework. Consequently, the control approach is validated experimentally on the quarter-vehicle test rig presented in Chapter 3.

5.1 Motivation for adaptive suspension control

For the visualization of the controller performance regarding the conflicting objectives ride comfort and ride safety frequently *carpet plots*, which are also referred to as *conflict diagrams* in the literature, are used. The carpet plot concept has originally been introduced by Hrovat in [54]. Carpet plots thus provide a tool to tune a suspension setup in order to achieve a desired dynamic behavior of the suspension system. In this Thesis, the carpet plots are employed for the visualization of the rms-values of the weighted chassis acceleration, the rms-values of the dynamic wheel load and the standard deviation of the suspension deflection, respectively.

To get a first impression of the performance potential of an adaptively controlled fully active suspension system, the linear fully active test rig model (Chapter 3.3.4) is employed for the study and linear quadratic regulators (LQR) are chosen for the control of the active system (see Chapter 5.4 for a more detailed discussion on that choice and Appendix A.1 for theoretical preliminaries of LQR design). The carpet plot in Figure 5.1 shows the conflict between the objectives ride comfort and ride safety for different suspension configurations based on the considered linear fully active suspension model. The model is excited with the measurement data of road profile P1, passed with the velocity $v_{p1} = 50\,\frac{\mathrm{km}}{\mathrm{h}}$. The resulting rms-values $||\ddot{x}_{c,comf}||_{\mathrm{rms}}$ and $||F_{dyn}||_{\mathrm{rms}}$ are visualized for different suspension configurations in the plot. In order to optimally ease the conflict between ride comfort and ride safety, it is desired to lower the chassis acceleration and keep the dynamic wheel load below the limits depending on the static wheel load (see Chapter 2.3).

It can be seen in the carpet plot that the performance of semi-active systems depends on the damping coefficient d_c and that the comfort optimal configuration has a higher rms-value of the dynamic wheel load than the safety optimal configuration. The passive system is designed to primarily focus on ride safety due to the high damping, that results in low dynamic wheel loads at the expense of ride comfort. The conflict of the passive and the semi-active system, which is characterized by the fact that low damping result in higher rms-values of dynamic wheel load, can be eased by active suspension systems. The green markers denote the per-

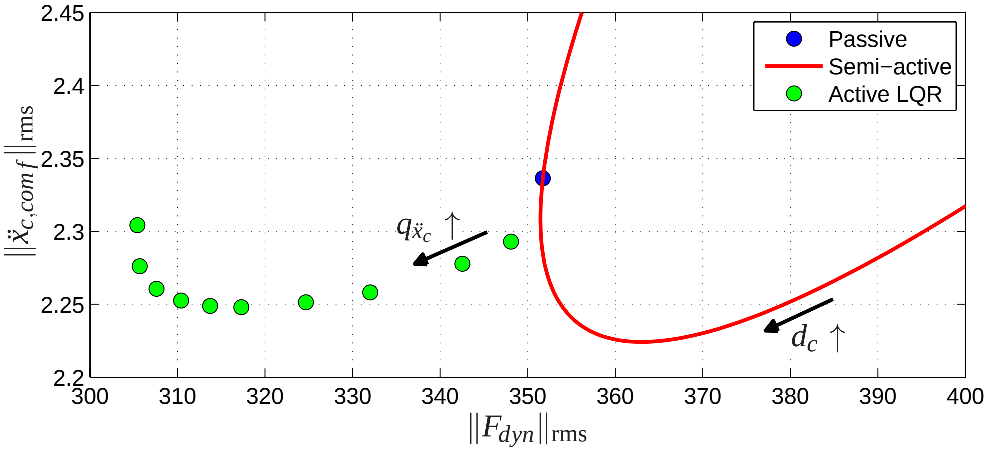

Figure 5.1: Carpet plot of the linear quadricycle quarter-vehicle model (see Chapter 3.3.4) to visualize the performance potential of an adaptively controlled suspension system.

formance of differently tuned linear quadratic regulators (LQR) for fully active suspension systems. The required theoretical preliminaries of linear quadratic regulators are described in Appendix A.1. The LQR tuning has been accomplished using the cost functional given in A.3

$$J_{LQR} = \int_0^\infty \left(\mathbf{y}^T \mathbf{Q}_y \mathbf{y} + R u^2\right) dt\,,$$

where the weighting for the control input $u(t) = F(t)$ has been fixed at $R = 10$ and the weighting matrix

$$\mathbf{Q}_y = \begin{bmatrix} q_{\ddot{x}_c} & 0 \\ 0 & q_{F_{dyn}} \end{bmatrix} \geq 0 \tag{5.1}$$

for the two output signals $\mathbf{y}(t) = \begin{bmatrix} \ddot{x}_c(t) & F_{dyn}(t) \end{bmatrix}^T$ has been varied in the interval $3 \cdot 10^5 \leq q_{\ddot{x}_c} \leq 2.5 \cdot 10^6$ with constant $q_{F_{dyn}} = 10$. Thus, for this first analysis only one tuning parameter ($q_{\ddot{x}_c}$) for the LQR design is employed. It is noted, that the given weights have been chosen heuristically and the suspension deflection is not considered for the LQR design at hand although the corresponding limits are not violated by any of the considered LQR. As can be seen, the first LQR configurations with the lower values for $q_{\ddot{x}_c}$ can simultaneously lower the dynamic wheel load and the body acceleration. However, for higher values of $q_{\ddot{x}_c}$ a similar conflict to the case of the semi-active suspension becomes apparent: In the fully active case the comfort and safety optimal weights in terms of the Pareto front also differ even though in the considered case the overall performance regarding ride safety is better than in the semi-active case.

This observation motivates the use of a controller structure, which can adapt its parametrization to the driving state. This could be realized by a comfort oriented controller parametrization (or damper setting), that is chosen if the limits on the dynamic wheel load ($\|F_{dyn}\|_{\mathrm{rms}} \leq \frac{1}{3}F_{stat}$) and the suspension deflection are not exceeded. A suitable safety oriented parametrization is activated otherwise. An important fact, which supports such an approach, is that the suspension performance depicted in carpet plots depends on the road excitation and on the vehicle's initial state when it passes the considered road profile. Thus, by a corresponding adaptive control approach, the vehicle is even enabled to pass road profiles with velocities, which would not be feasible without violating the limits for ride safety or suspension deflection otherwise.

Hence, to analyze the performance potential of the approach in more detail in the following Sections, a corresponding controller structure and an optimization based controller design using the nonlinear quarter-vehicle model (see Chapter 3.3.3 and the parameters given in Table B.1 in the Appendix) is presented.

5.2 Adaptive controller structure

A switching controller structure (see Figure 5.2 (left)) is chosen for the proposed adaptive control approach. Therein, an adaptation logic (switching logic) switches between n differently tuned state feedback controllers $\mathbf{k}_i^T$ depending on the dynamic wheel load and the suspension deflection, that characterize the vertical dynamic driving state of the vehicle in this framework. The term $\sigma(q_i)$ denotes a switching signal (see also Appendix A.2.2) depending on two scheduling signals $q_{fdyn}(t)$ and $q_{susp}(t)$ reflecting the vertical dynamic driving state of the vehicle. In order to prevent discontinuities in the control signal caused by discontinuous switching, in Section 5.4.2 the performance potential of a smooth interpolation approach for scheduling the controller gains is presented.

Since the structure of the control law is important for the stability considerations presented in Section 5.3, it is already presented at this point. From the analysis in Section 5.4.2 it will result that a remarkable performance can be achieved, if the number of controllers is chosen as $n=3$. Thus, one state feedback controller for each of the most important objectives for the active suspension system (ride comfort, ride safety, limited suspension deflection) is chosen, so that the resulting control law can be formulated using linear interpolation between the controllers as

$$u(t) = -\underbrace{\left((1-q_{susp}(t))\left((1-q_{fdyn}(t))\mathbf{k}_{comf}^{T}+q_{fdyn}(t)\mathbf{k}_{safe}^{T}\right)+q_{susp}(t)\mathbf{k}_{susp}^{T}\right)}_{\mathbf{k}_{adp}^{T}(t)}\mathbf{x}(t)\,. \qquad (5.2)$$

The design method of the adaptively controlled suspension system derived in this Chapter is applicable for a class of mechatronic suspension systems defined by the presented sensor configuration for the estimator design and an actuator being integrated between the chassis and the wheel. Since the design of the LQRs requires a linear model, parameters of the linear test rig model presented in Chapter 3.3.4 combined with a choice of linear damping that follows from stability considerations (see Section 5.3) are utilized. However, the tuning of the controller weights is accomplished using the nonlinear test rig model. The controller structure is then validated experimentally on the test rig described in Chapter 3. For the controller implementation the parallel Kalman filter structure (3KF) presented in Chapter 4 is employed. Furthermore, it must be considered that the actuator dynamics, that relate the voltage control input $u_v(t)$ to the actuator force $F(t)$, are present (Figure 5.2). Although the actuator force is not measured directly, it can be calculated from the measured actuator current (see Chapter 3.3.1) to be supplied to the Kalman filter.

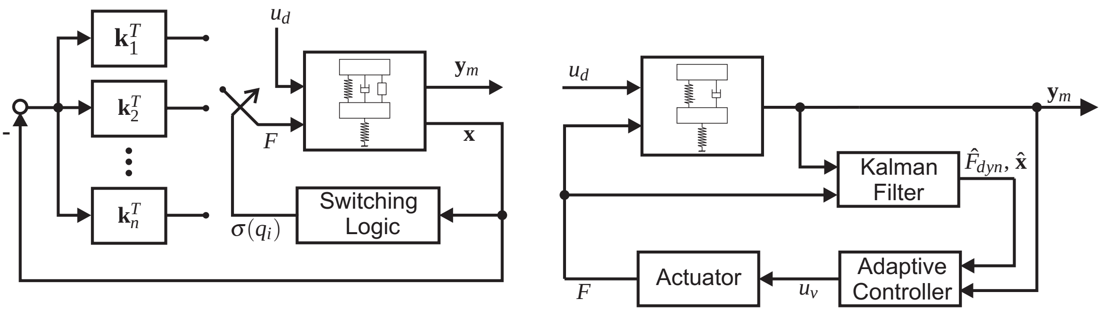

Figure 5.2: Adaptive controller structure (left) and realization of the approach at the test rig (right).

5.2.1 Adaptation logic

Since the adaptation should be performed in order to chose the optimal controller for the current driving state of the vehicle, information about the driving state must be processed from the measurement data. The driving state in the context of this Thesis is determined by the suspension deflection and the dynamic wheel load since these quantities should remain below the bounds presented in Chapter 2.3.

Dynamic wheel load based adaptation

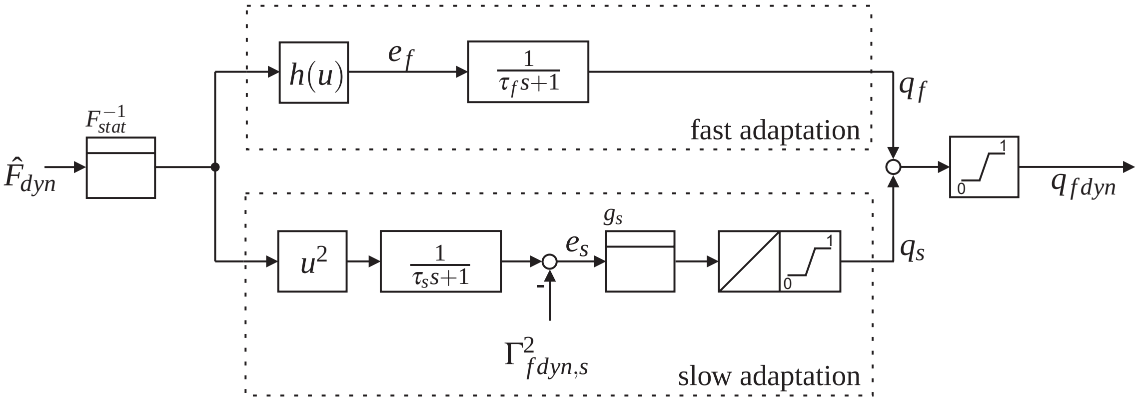

Figure 5.3: Wheel load adaptation structure.

An adaptation logic is designed based on an approach formulated by Venhovens in [161]. The approach has been modified by the author regarding important aspects (see e.g. [74, 79]), which will be pointed out in this Section. The adaptation logic calculates the scheduling signal $q_{fdyn}(t)$ from the estimate of the dynamic wheel load $\hat{F}_{dyn}(t)$ by taking into account slow variations of the dynamic wheel load, i.e. changes of its rms-value, as well as rapid increases. While the latter is realized by the upper branch (fast adaptation) in the block diagram shown in Figure 5.3, the variance of the dynamic wheel load is approximated by the slow adaptation part (lower branch).

To ensure safety for singular excitation events like potholes, which may not immediately be reflected in the rms-value of the dynamic wheel load, the primary control objective should change from comfort to safety, i.e. lowering the dynamic wheel load, if

$$\frac{|\hat{F}_{dyn}|}{F_{stat}} \geq \Gamma_{fdyn,f} = 0.8\,. \tag{5.3}$$

This is accomplished by means of the fast adaptation, which causes the scheduling signal $q_f(t)$ to rapidly increase if the limit defined in (5.3) is exceeded. The nonlinear scaling function $h\left(\frac{\hat{F}_{dyn}}{F_{stat}}\right)$ (Figure 5.4 (left)) for the realization is constructed from a fourth-order polynomial and a dead zone, so that $e_f(t)$ rises if (5.3) holds (see [90]). The time constant of the low pass filter τ_s, that is employed to avoid too rapid changes in the adaptation of the controller parameters, is chosen as

$$\tau_f = \frac{1}{2}\sqrt{\frac{m_w}{c_c + c_w}} \approx 0.006\,\text{sec}\,. \tag{5.4}$$

It is noted, that although only negative dynamic wheel loads are critical for the wheel to cause loss of ground contact, the scaling function $h\left(\frac{\hat{F}_{dyn}}{F_{stat}}\right)$ has been designed symmetrically because due to the elasticity of the tire and its low damping, positive dynamic wheel loads can be followed by safety critical negative wheel loads immediately.

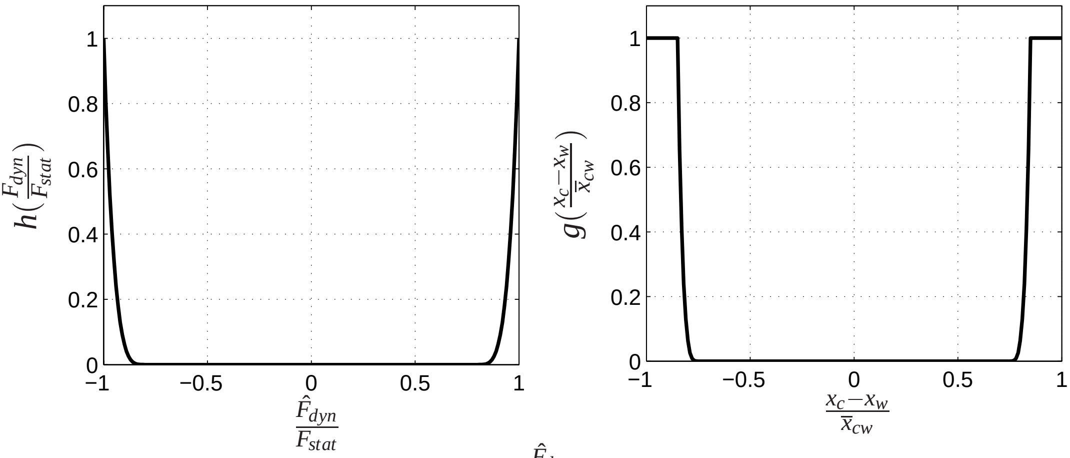

Figure 5.4: Nonlinear scaling function $h(\frac{\hat{F}_{dyn}}{F_{stat}})$ for the fast dynamic wheel load adaptation (left) and $g(\frac{x_c - x_w}{\bar{x}_{cw}})$ suspension deflection adaptation (right).

The slow adaptation rate $q_s(t)$ (illustrated in the lower branch in Figure 5.3) is used to adapt the suspension controller to different variances of the road excitation signal. Thereby slow changes of the stochastic properties of the road excitation are taken into account. The variance of the estimated dynamic wheel load is

$$\sigma^2_{F_{dyn}} = \lim_{T\to\infty} \frac{1}{T} \int_0^T \hat{F}^2_{dyn}(\tau) d\tau \,. \tag{5.5}$$

After Laplace transformation, the integral term $\frac{1}{s}$ is replaced by a first-order low pass filter as proposed in [161] in order to approximate the variance of the estimated dynamic wheel load by

$$\sigma^2_{F_{dyn}}(s) \approx \frac{1}{\tau_s s + 1} \hat{F}^2_{dyn}(s) \,. \tag{5.6}$$

The time constant of the low pass filter τ_s is chosen as

$$\tau_s = \frac{1}{2}\sqrt{\frac{m_c}{c_c}} \approx 0.053\,\mathrm{sec}\,. \tag{5.7}$$

The ratio of the dynamic wheel load filtered in this manner and the static wheel load is compared to the stochastic bound $\Gamma_{fdyn,s} = \frac{1}{3}$ according to the 3σ-rule formulated in (2.19). The deviation $e_s(t)$ is integrated by an output-limited integrator with an output signal range of $[0,1]$ resulting in $q_s(t)$. It is noted that output limitation in this context refers to the fact that the integral action is deactivated when the limit is reached to prevent wind-up. For the dynamic wheel load adaptation the integrator gain is $g_s = 1$. The resulting scheduling parameter is $q_{fdyn}(t) = \min\big(1, q_s(t) + q_f(t)\big)$. While $q_{fdyn}(t)$ remains close to zero, a comfort oriented controller can be activated. If $q_{fdyn}(t)$ rises, it indicates higher dynamic wheel loads and the urgency to activate a more safety oriented controller.

The main differences compared to Venhovens approach in [161] for the wheel load adaptation logic are the output-limiting of the integrator instead of the reset approach presented in [161], smaller time constants τ_f and τ_s to improve the response time of the logic and a higher gain value for g_s to ensure ride safety by the logic. Moreover, it is noted that in [161] a stability analysis of the gain scheduling based suspension control is missing.

Suspension deflection based adaptation

For the calculation of the scheduling signal $q_{susp}(t)$, which indicates if the suspension deflection becomes critical, the same structure of the adaptation logic as for the dynamic wheel load is considered. Although the absolute limit of the suspension deflection should be avoided, by also using an rms-constraint and the 3σ-rule, the probability of hitting the limits due to stochastic disturbances can be reduced as discussed in Chapter 2.3.

Consequently, the measured suspension deflection signal $x_{cw}(t) = x_c(t) - x_w(t)$ is divided by the absolute value of the maximum suspension deflection ($\bar{x}_{cw} = 5\,\mathrm{cm}$ at the test rig) and is supplied to the fast and the slow adaptation. In the fast adaptation the nonlinear scaling function $g(\frac{x_{cw}}{\bar{x}_{cw}})$ is also constructed from a dead zone and fourth-order polynomial such that its output $e_{susp}(t)$ rises in the interval $0.75 < \frac{x_{cw}(t)}{\bar{x}_{cw}} < 0.85$ from zero to one (Figure 5.4 (right)). The time constant of the low pass filter in the fast adaptation for the suspension deflection is chosen as

$$\tau_{f,susp} = \frac{1}{3}\sqrt{\frac{m_w}{c_c + c_w}} \approx 0.004\,\mathrm{sec} \tag{5.8}$$

to be able to quickly prevent the suspension from hitting the limits. The parameters of the slow adaptation are chosen as

$$\tau_{s,susp} = \sqrt{\frac{m_c}{c_c}} \approx 0.110\,\mathrm{sec} \tag{5.9}$$

and $g_{s,susp} = 1.5$.

5.3 Stability considerations

Before the controller design is described in the next Section some important preliminary considerations regarding the stability of the adaptively controlled active suspension system are presented. Guaranteeing stability for the proposed controller structure is challenging due to several aspects:

1. For the design of the linear quadratic regulators a linear model of the suspension is employed but the controllers are tested in simulations and measurements with the nonlinear system. Since the degressive damper characteristic represents the main nonlinearity of the system, it is desirable to take it into account for the controller design. If the characteristic is linearized at its origin (in the equilibrium the damper velocity is zero), a higher damping coefficient would result for the linearized system, which could cause instability of the controlled nonlinear system due to the missing damper forces.

2. The state feedback controller gains of the closed loop system can change rapidly due to the adaptation to the current driving state. Therefore, the stability of the switched system must be analyzed.

3. The suspension system is subject to nonvanishing perturbations by the road profile, i.e. strictly speaking, stability analysis methods, which are applicable for the stability of equilibrium points, are not sufficient to guarantee stability of the closed loop system.

4. Since state estimate feedback is used for control, the stability of the nonlinear closed loop system including the Kalman filters is not guaranteed.

Because the first and the second aspect are directly relevant for the LQR design, a method to guarantee stability of the adaptively controlled closed loop system including the nonlinear damper characteristic is presented in this Section. An approach to consider the third aspect is given in Section 5.3.3.

Regarding the fourth aspect, the stability of the Kalman filter structure has been experimentally verified in Chapter 4.5. The parallel Kalman filter structure has been tested for the passive suspension system and also with LQR suspension controllers for the active system. A stability analysis of the discrete time Kalman filter algorithm is given in [103] and the references therein. Since the adaptively controlled system including the Kalman filter structure has been stable in all simulations and experiments in the framework of this Thesis, the influence of the estimator on the stability of the closed loop system with the estimator is not analyzed in detail.

5.3.1 Stability analysis for the state feedback controlled quasilinear system

The first aspect is to evaluate, how stability of the closed loop system including the nonlinear damper characteristic can be guaranteed although the LQRs are designed based on a linear model. For the following stability analysis (see also [72]), a quasilinear system representation is required. This system representation is linear apart from the included nonlinear damper characteristic. Every nonlinear system

$$\dot{\mathbf{x}} = \mathbf{f}(\mathbf{x}) + \mathbf{B}(\mathbf{x})\mathbf{u} \tag{5.10}$$

with a continuously differentiable function $\mathbf{f}(\mathbf{x})$ can be represented in a quasi-linear form (see [127])

$$\dot{\mathbf{x}} = \mathbf{A}(\mathbf{x})\mathbf{x} + \mathbf{B}(\mathbf{x})\mathbf{u}\,. \tag{5.11}$$

To achieve continuous differentiability of $\mathbf{f}(\mathbf{x})$, the nonlinear damper characteristic (see Figure 3.6) is approximated by means of cubic spline interpolation. Then the state dependent damper coefficient

$$d_c(\mathbf{x}) = d_c(\dot{x}_{cw}) = \frac{F_d(\dot{x}_{cw})}{\dot{x}_{cw}} \tag{5.12}$$

is introduced so that $F_d(\dot{x}_{cw}) = d_c(\mathbf{x})\dot{x}_{cw}$ holds. The limit for $d_c(\mathbf{x})$ for $\dot{x}_{cw} \to 0$ exists and can be calculated using the rule of L'Hospital

$$\lim_{\dot{x}_{cw}\to 0} d_c(\dot{x}_{cw}) = \left.\frac{dF_d(\dot{x}_{cw})}{d\dot{x}_{cw}}\right|_{\dot{x}_{cw}=0} . \tag{5.13}$$

Using the state vector, control input and output signals defined in (2.3)-(2.6) the quasilinear system representation

$$\dot{\mathbf{x}} = \underbrace{\begin{bmatrix} 0 & 1 & 0 & -1 \\ -\frac{c_c}{m_c} & -\frac{d_c(\mathbf{x})}{m_c} & 0 & \frac{d_c(\mathbf{x})}{m_c} \\ 0 & 0 & 0 & 1 \\ \frac{c_c}{m_w} & \frac{d_c(\mathbf{x})}{m_w} & -\frac{c_w}{m_w} & -\frac{d_c(\mathbf{x})+d_w}{m_w} \end{bmatrix}}_{\mathbf{A}(\mathbf{x})} \mathbf{x} + \underbrace{\begin{bmatrix} 0 \\ \frac{1}{m_c} \\ 0 \\ -\frac{1}{m_w} \end{bmatrix}}_{\mathbf{b}} u \tag{5.14}$$

can be formulated for the linear quarter-vehicle model with (5.12). The measurement equation is

$$\mathbf{y} = \underbrace{\begin{bmatrix} -\frac{c_c}{m_c} & -\frac{d_c(\mathbf{x})}{m_c} & 0 & \frac{d_c(\mathbf{x})}{m_c} \\ 0 & 0 & -c_w & -d_w \\ 1 & 0 & 0 & 0 \end{bmatrix}}_{\mathbf{C}(\mathbf{x})} \mathbf{x} + \underbrace{\begin{bmatrix} \frac{1}{m_c} \\ 0 \\ 0 \end{bmatrix}}_{\mathbf{d}} u \,. \tag{5.15}$$

In Figure 5.5 different linear damping coefficients for the nonlinear damper characteristic are depicted including the nominal damping coefficient d_c of the linear quarter-vehicle model. The considered interval of the damper velocity for the following stability considerations is $\dot{x}_{cw} \in [-1.5\,\frac{\text{m}}{\text{sec}}, 1.5\,\frac{\text{m}}{\text{sec}}]$, which represents a conservative approximation of the realistic relative damper velocities based on the insights from simulations and measurements (see also [50]). As can be seen in Figure 5.5, the damping coefficient varies between $d_{c,min}$ and $d_{c,max}$. In the following, a method is shown to prove that the quasilinear system is stable when it is controlled by a time-invariant (nonadaptive) LQR designed for the linear system with the minimum damping constant resulting from the nonlinear damper characteristic. Thereby, it is

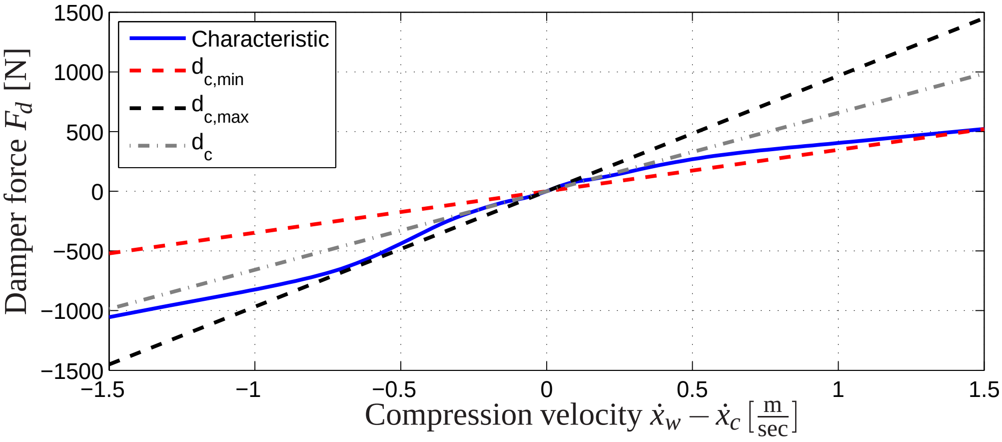

Figure 5.5: Damper characteristic (in coordinates of the quarter-vehicle) model and different linear approximations.

prevented that the real damper force resulting from the degressive nonlinear damper characteristic is lower than the damper force resulting for the current state for the linearized system. Consequently, for the LQR design the linear system representation with minimum damping and omitted Coulomb friction effects[1] is employed.

The method to guarantee stability of the LQR controlled nonlinear system is the circle criterion (see e.g. [70]), which is summarized for the relevant system class in Appendix A.2.3. For its applicability the system must be transformed into a feedback connection of a linear dynamical system and a nonlinear element (Figure A.1). The state equation of the controlled quasilinear quarter-vehicle model results from (5.14) and the control law resulting from the LQR $u = -\mathbf{k}^T\mathbf{x}$ (with the state feedback gain defined in (A.12)) as

$$\dot{\mathbf{x}} = \mathbf{A}(\mathbf{x})\mathbf{x} - \mathbf{b}\mathbf{k}^T\mathbf{x}\,. \tag{5.16}$$

---

[1] The friction effects are neglected since their gradient is zero except for very low velocities where it takes on very high values, which would deteriorate the accuracy of the linear model.

By splitting $\mathbf{A}(\mathbf{x})$ up into a linear and a nonlinear part as

$$\mathbf{A}(\mathbf{x}) = \mathbf{A}_{lin} - \underbrace{\begin{bmatrix} 0 \\ -\frac{1}{m_c} \\ 0 \\ \frac{1}{m_w} \end{bmatrix}}_{\mathbf{b}_{F_d}} \Delta d_c(\mathbf{x})(x_4 - x_2) \tag{5.17}$$

with

$$\Delta d_c(\mathbf{x}) = d_c(\mathbf{x}) - d_{c,min}\,, \tag{5.18}$$

(5.16) can be written as

$$\dot{\mathbf{x}} = \underbrace{\begin{bmatrix} 0 & 1 & 0 & -1 \\ -\frac{c_c}{m_c} & -\frac{d_{c,min}}{m_c} & 0 & \frac{d_{c,min}}{m_c} \\ 0 & 0 & 0 & 1 \\ \frac{c_c}{m_w} & \frac{d_{c,min}}{m_w} & -\frac{c_w}{m_w} & -\frac{d_{c,min}+d_w}{m_w} \end{bmatrix} \mathbf{x} - \mathbf{b}\mathbf{k}^T\mathbf{x}}_{\mathbf{A}_{reg}\mathbf{x}} - \underbrace{\begin{bmatrix} 0 \\ -\frac{1}{m_c} \\ 0 \\ \frac{1}{m_w} \end{bmatrix}}_{\mathbf{b}_{F_d}} \Delta d_c(\mathbf{x})(x_4 - x_2)\,, \tag{5.19}$$

which includes a linear and a nonlinear part. If the output signal

$$y = \underbrace{\begin{bmatrix} 0 & 1 & 0 & -1 \end{bmatrix}}_{\mathbf{c}^T} \mathbf{x} = x_4 - x_2 \tag{5.20}$$

and the nonlinear time-invariant control law

$$u(t) = \Psi(y) = \Delta d_c(y)y \tag{5.21}$$

are defined, the desired system representation

$$\dot{\mathbf{x}} = \mathbf{A}_{reg}\mathbf{x} - \mathbf{b}_{F_d}\Psi(y)\,, \tag{5.22}$$

can be formulated, where the pair $(\mathbf{A}_{reg}, \mathbf{b}_{F_d})$ is controllable and $(\mathbf{A}_{reg}, \mathbf{c}^T)$ is observable. Moreover, the sector condition

$$0 \leq y\Psi(y) \leq y^2 \Delta d_{c,max}\,, \quad \forall\, y \in \left[-1.5\,\frac{\text{m}}{\text{sec}}, 1.5\,\frac{\text{m}}{\text{sec}}\right] \tag{5.23}$$

with

$$\Delta d_{c,max} = \max_{\substack{y \\ y \in [-1.5\,\frac{\text{m}}{\text{sec}}, 1.5\,\frac{\text{m}}{\text{sec}}]}} \big(\Delta d_c(y)\big) \tag{5.24}$$

holds, which can be used to formulate the sector in the notation used in [70] as

$$\Psi(y) \in [0, \Delta d_{c,max}]\,. \tag{5.25}$$

The transfer function of the linear system is given by

$$G(s) = \mathbf{c}^T (s\mathbf{I} - \mathbf{A}_{reg})^{-1} \mathbf{b}_{F_d} \tag{5.26}$$

and $G(s)$ is Hurwitz. The conditions for absolute stability according to the circle criterion can be evaluated using the scalar transfer function (5.26) by means of the corresponding Nyquist-curve (see Appendix A.2.3).

When applying the circle criterion for $\Psi(y) \in [0, \Delta d_{c,max}]$, it is tested if

$$Re[G(j\omega)] > -\frac{1}{\Delta d_{c,max}} \tag{5.27}$$

holds, i.e. $1 + \Delta d_{c,max} G(s)$ is strictly positive real (see Appendix A.2.3). In Figure 5.6 a Nyquist curve is depicted for an exemplary LQR designed for the linear system with the minimum damping coefficient and since the curve remains in the right complex half-plane, the controlled system is absolutely stable within the sector $\Psi(y) \in [0, \infty[$ and hence also for the sector defined by (5.25). Because this result only holds for the considered LQR, the circle criterion is tested numerically for every LQR based suspension controller presented in this Chapter. It is noted that the criterion is tested only in the interval $[-1.5\,\frac{\mathrm{m}}{\mathrm{sec}}, 1.5\,\frac{\mathrm{m}}{\mathrm{sec}}]$ for the damper velocity, which, however, represents a conservative approximation as has been stated initially.

5.3.2 Common Lyapunov function approach

The second aspect (stability of the switched system) must be analyzed although every controller described in Section 5.4 results in an asymptotically stable control loop, because this does not imply asymptotic stability of the switched system (see e.g. [88]). The theoretical preliminaries for the utilized method are formulated in detail in Appendix A.2.

In the following, a common quadratic Lyapunov function (CQLF) approach is used to show stability of the switched system taking into account the nonlinear damper characteristic. The test to ensure that a CQLF exists for all closed loop subsystems involved in the switching controller structure is included in the controller design process (see Section 5.4). In Appendix A.2.2 it is also shown that fast interpolation between controllers does not destabilize a linear switched system if a CQLF for the switched system can be determined.

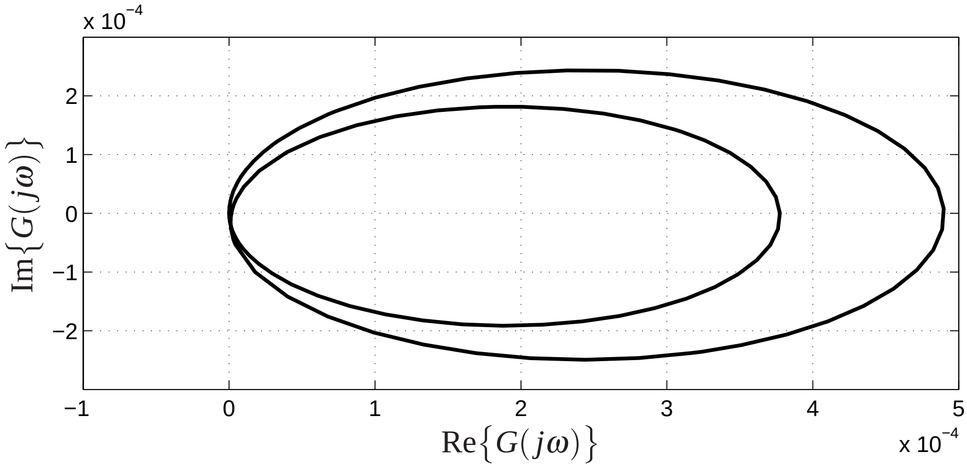

Figure 5.6: Nyquist-curve of $G(s)$ (defined in (5.26)) for an exemplary LQR.

CQLF approach for the switched quasilinear system

If the system matrix $\mathbf{A}(\mathbf{x})$ of the quasilinear system representation (5.14) is split up as in (5.17), the time derivative of the quadratic Lyapunov function candidate $V(\mathbf{x}) = \mathbf{x}^T\mathbf{P}\mathbf{x}$ can be formulated as

$$\dot{V}(\mathbf{x},t) = 2\mathbf{x}^T\mathbf{P}\left[\mathbf{A}_{lin} - \mathbf{b}\mathbf{k}^T_{adp} - \mathbf{b}_{F_d}\Delta d_c(\mathbf{x})\tilde{\mathbf{c}}^T\right]\mathbf{x} \tag{5.28}$$

using $\mathbf{k}^T_{adp}$ defined in the control law (5.2) and $\tilde{\mathbf{c}}^T = [\begin{array}{cccc} 0 & -1 & 0 & 1 \end{array}]$. Since $\dot{V}(\mathbf{x},t)$ is bilinear in the scheduling variables q_{susp} and q_{fdyn} and linear in the state dependent parameter $\Delta d_c(\mathbf{x})$ defined in (5.18), its maximum is located on the boundary of the region

$$H = \left\{ [\begin{array}{ccc} q_{susp} & q_{fdyn} & \Delta d_c \end{array}]^T \in \mathbb{R}^3 \,\middle|\, 0 \leq q_{susp} \leq 1,\ 0 \leq q_{fdyn} \leq 1,\ 0 \leq \Delta d_c \leq \Delta d_{c,max} \right\}. \tag{5.29}$$

Consequently, it can be stated that if a matrix

$$\mathbf{P} = \mathbf{P}^T > 0 \tag{5.30}$$

exists so that

$$\mathbf{P}\mathbf{A}^{(i)} + \left(\mathbf{A}^{(i)}\right)^T\mathbf{P} \leq -\varepsilon\mathbf{I}, \tag{5.31}$$

with a real parameter $\varepsilon > 0$ and $\mathbf{I}$ representing the unity matrix of appropriate dimension, holds for all matrices

$$\mathbf{A}^{(1)} = \mathbf{A}(d_{c,min}) - \mathbf{b}\mathbf{k}_{comf}^T\,, \qquad \mathbf{A}^{(2)} = \mathbf{A}(d_{c,max}) - \mathbf{b}\mathbf{k}_{comf}^T\,, \tag{5.32}$$

$$\mathbf{A}^{(3)} = \mathbf{A}(d_{c,min}) - \mathbf{b}\mathbf{k}_{safe}^T\,, \qquad \mathbf{A}^{(4)} = \mathbf{A}(d_{c,max}) - \mathbf{b}\mathbf{k}_{safe}^T\,, \tag{5.33}$$

$$\mathbf{A}^{(5)} = \mathbf{A}(d_{c,min}) - \mathbf{b}\mathbf{k}_{susp}^T\,, \qquad \mathbf{A}^{(6)} = \mathbf{A}(d_{c,max}) - \mathbf{b}\mathbf{k}_{susp}^T\,, \tag{5.34}$$

then $\dot{V}(\mathbf{x},t) \leq -\varepsilon \mathbf{x}^T \mathbf{x}$ holds and $V(\mathbf{x})$ is a CQLF of the closed loop switched system including all interpolations realized by the control law (5.2). In (5.32) - (5.34) $\mathbf{A}(d_{c,min})$ represents the system matrix with the minimum damping coefficient and $\mathbf{A}(d_{c,max})$ is the system matrix resulting from utilizing the maximum damping coefficient (see (5.17)).

If a corresponding CQLF exists, it can be calculated numerically, e.g. by using the *YALMIP* optimization toolbox (see e.g. [95]) and the *SeDuMi* solver (see [149]) for *Matlab*. To perform the test for the three controllers designed in Section 5.4, (5.31) has been formulated as a set of linear matrix inequalities (LMIs), which are solved with respect to the condition (5.30) and $\varepsilon = 1$. It is noted that the choice of $\varepsilon = 1$ does not impose restrictions for the feasibility of the problem, which is thoroughly discussed in [140].

5.3.3 Stability in the case of nonvanishing perturbation

Lyapunov-based stability analysis always considers stability of an equilibrium point assuming an initial perturbation of the system (see Appendix A.2.1). This assumption, however, does not exactly match the reality of a suspension system because in general, the vehicle suspension is subject to nonvanishing stochastic disturbances. In [70, 140] methods are described to guarantee stability of an asymptotically stable equilibrium point for this condition if certain constraints on the excitation signal are fulfilled.

The equilibrium point $\mathbf{x} = \mathbf{0}$ of the quasilinear suspension system (5.19) controlled by the adaptive state feedback controller (5.2) has been shown to be asymptotically stable by the CQLF approach presented in Section 5.3.2. Since the system (5.19) does not explicitly depend on time, it is an autonomous system (see e.g. [140]) and thus it can be concluded that the equilibrium point of the undisturbed system is uniformly asymptotically stable (see Propositions A.4 - A.5 in the Appendix). Taking into account Proposition A.5, the system is thereby also totally stable and thus preserves stability despite small disturbances, i.e. disturbances caused by realistic road excitations $\dot{x}_g$.

However, it is noted that in [140] an example is given, which illustrates that a nonlinear totally stable mechanical second-order system with a limited maximum damper force can be destabilized by a large periodic perturbation at the system's resonance frequency. Due to the degressive damper characteristic of the suspension system, i.e. a similar structure to the system in the example from [140], it becomes clear that for particular excitation signals even the nonlinear passive suspension system can be destabilized. However, since the disturbance signal caused by conventional roads (highways etc.) is stochastic and has small amplitudes, the suspension system under nonvanishing perturbation can presumably be considered to withstand realistic disturbance signals. A more detailed analysis of the stability under nonvanishing perturbation is, however, not within the scope of this Thesis.

5.4 Controller design

After the given preliminary considerations on the stability of the adaptive control approach, the controller design can be carried out accordingly. The involved controllers should be tuneable as transparently as possible. Since the system requirements for ride safety and ride comfort involve rms-formulations either in the performance index or in the formulation of the constraints, linear quadratic regulators (LQRs) are chosen to be implemented in the switching controller structure. They minimize a quadratic cost functional and have a fairly transparent tuning procedure using weighting matrices for the performance output signals and the control input. Moreover, LQR designs are frequently employed in the literature on performance potential studies of suspension systems (see e.g. [46, 55, 76, 137, 138]). The design procedure of LQRs is described in Appendix A.1.

The actuator model is not considered in the controller design, which is a justified approach since the bandwidth of the actuator is 28.6 Hz and thus below the frequency range of interest. In Figure 5.7 the power spectral density of the actuator force of a measurement with a time-invariant LQR is depicted. The actuator force thus contains primarily frequency components in the frequency range significantly below the actuator bandwidth. Moreover, for the controller design it is assumed that all states are available for feedback, which is also a reasonable assumption since the parallel Kalman filter concept described in Chapter 4 is used for the implementation.

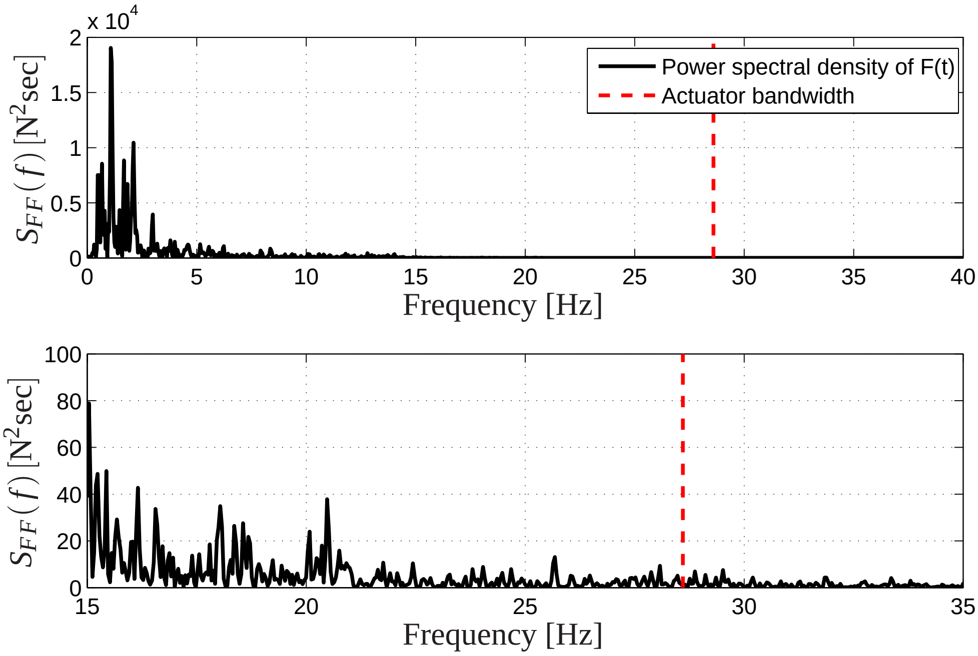

Figure 5.7: Power spectral density of the actuator force $F(t)$ for the LQR controlled active suspension system (with zoom (lower)).

5.4.1 Optimization based controller parametrization

In Section 5.1 the performance potential of differently tuned linear quadratic regulators have been shown by heuristically tuned weighting matrices for the controller design using the linear test rig model. In order to choose the weights for the controller design in a structured manner, optimization based controller parametrization is performed by employing the nonlinear quarter-vehicle model (Chapter 3.3.3) for the determination of the optimal controller parameters concerning the conflicting suspension objectives.

To add a further degree of freedom in the controller design, the suspension deflection is added as a performance output, i.e $\mathbf{y}(t) = \left[\begin{array}{ccc} \ddot{x}_c(t) & F_{dyn}(t) & x_c(t) - x_w(t) \end{array}\right]^T$. The control input is the actuator force $u(t) = F(t)$ and the performance index for the LQR design (see (A.3)) is

$$J_{LQR} = \int_0^\infty \left(\mathbf{y}^T \mathbf{Q}_y \mathbf{y} + R u^2\right) dt\,,$$

where R is fixed[2] at $R = 1$ and the weighting matrix

$$\mathbf{Q}_y = \begin{bmatrix} q_{\ddot{x}_c} & 0 & 0 \\ 0 & q_{F_{dyn}} & 0 \\ 0 & 0 & q_{x_{cw}} \end{bmatrix} . \tag{5.35}$$

The tuning parameters are the diagonal entries of $\mathbf{Q}_y$, which are summarized in the vector

$$\eta = \begin{bmatrix} q_{\ddot{x}_c} & q_{F_{dyn}} & q_{x_{cw}} \end{bmatrix}^T \tag{5.36}$$

and the vectorial cost functional for the optimization based controller tuning is chosen according to the control objectives as

$$\mathbf{J}_t(\eta) = \begin{bmatrix} \|\ddot{x}_{c,comf}\|_{\text{rms}} & \|F_{dyn}\|_{\text{rms}} \end{bmatrix}^T . \tag{5.37}$$

Since it should be prevented that the comfort oriented controller causes the suspension deflection limit to be violated frequently, for the optimization the maximum suspension deflection of the quarter-vehicle model is formulated as a constraint. Thus, it is arranged that for uncritical driving states the active controller parametrization is the most comfort oriented LQR. Afterwards, the suspension controller $\mathbf{k}_{susp}^T$ is designed separately.

Consequently, the resulting multiobjective optimization problem for the determination of Pareto optimal controller weights can be formulated as

$$\min_{\eta} \mathbf{J}_t(\eta) \tag{5.38}$$

$$\text{s.t.} \quad \max_{t\in[0,T_{sim}]} \left(|x_{cw}(t)|\right) \leq 0.05\,\text{m}, \tag{5.39}$$

where T_{sim} denotes the simulation time (see also [20] for a detailed presentation of this problem class).

For the optimization road profile P1 is used (passed with the velocity $v_{p1} = 50\,\frac{\text{km}}{\text{h}}$) because it represents a typical broad band stochastic road profile. The optimization problem (5.38) - (5.39) is also solved by means of the multiobjective genetic algorithm *NSGA-II* (see [23]), that has been used for the optimization of the Kalman filter structures presented in Chapter 4. The parameter space for η is discretized logarithmically and 200 individuals and 35 generations are chosen for the optimization.

---

[2] This procedure does not restrict the optimization since the state feedback gain, which minimizes the cost functional (A.3) with $\mathbf{Q}_y$ and $R = 1$ also minimizes the cost functional with $c\mathbf{Q}_y$ and $R = c$ for any $c > 0$.

The resulting Pareto front has a gap over an interval of $||F_{dyn}||_{\text{rms}}$, in which no Pareto-optimal configurations exist. The relevant part of the resulting Pareto front for suspension control is the part with low chassis accelerations $||\ddot{x}_{c,comf}||_{\text{rms}}$, which is depicted in Figure 5.8. From this Pareto front the comfort controller $\mathbf{k}_{comf}^{T}$ and the safety controller $\mathbf{k}_{safe}^{T}$ are chosen. Compared to the LQR designs for the linear system depicted in Figure 5.1 it can be seen that although the curve is shifted towards higher dynamic wheel load levels (the differences result from the use of the nonlinear suspension model), the comfort gain between the two chosen controllers is significant and for the considered road profile the controller $\mathbf{k}_{comf}^{T}$ does not violate the rms-limit for the dynamic wheel load ($\frac{F_{stat}}{3} \approx 387\,\text{N}$).

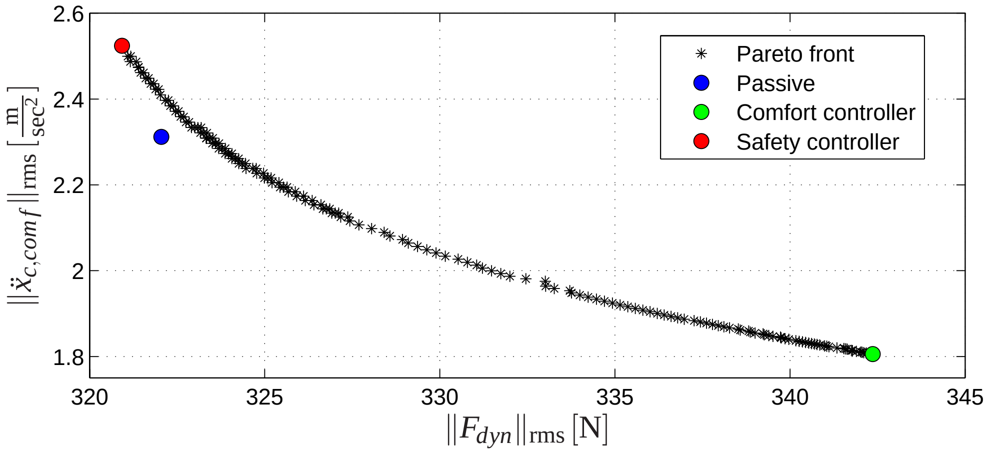

Figure 5.8: Pareto front for comfort and safety oriented LQR parametrizations.

Using the approach presented in Section 5.3.2 a CQLF has been calculated by (5.31) for the LMIs (5.32) - (5.33) and the condition (5.30). The result is that a solution for the LMIs can be obtained and the closed loop systems resulting from interpolation between $\mathbf{k}_{comf}^{T}$ and $\mathbf{k}_{safe}^{T}$ have a CQLF.

For the design of the suspension deflection controller, the weighting factors η_{safe} of the safety oriented controller $\mathbf{k}_{safe}^{T}$ are taken and the weighting term for the suspension deflection $q_{x_{cw}}$ is subsequently increased. For every increase the above mentioned conditions for the CQLF are tested including the LMIs formulated in (5.34). The suspension controller results from the set of weights with the highest value of $q_{x_{cw}}$, for which the switched system involving all three controllers possesses a CQLF. This procedure is motivated by the fact that driving states, which are critical for the dynamic wheel load, are frequently also critical for suspension deflection. By this procedure the suspension deflection weight has been increased from $q_{x_{cw}}^{safe} = 1.5849 \cdot 10^{10}$ to $q_{x_{cw}}^{susp} = 3.5413 \cdot 10^{10}$.

The numerical values for the three suspension controllers and the matrix **P** of the derived CQLF (rounded to multiples of 10^{-4}) are

$$\mathbf{k}_{comf}^{T} = \begin{bmatrix} -7605.4513 & 21.2489 & 789.3481 & 363.9968 \end{bmatrix}, \tag{5.40}$$

$$\mathbf{k}_{safe}^{T} = \begin{bmatrix} -7626.7206 & 41.9993 & -20578.3913 & -503.7479 \end{bmatrix}, \tag{5.41}$$

$$\mathbf{k}_{susp}^{T} = \begin{bmatrix} -7245.5240 & 132.8231 & -20923.9030 & -500.9276 \end{bmatrix}, \tag{5.42}$$

$$\mathbf{P} = \begin{bmatrix} 5.5024 & 0.8632 & -5.2069 & 0.0128 \\ 0.8632 & 0.8574 & -4.2785 & 0.0121 \\ -5.2069 & -4.2785 & 2060.9480 & 0.2039 \\ 0.0128 & 0.0121 & 0.2039 & 0.3257 \end{bmatrix}. \tag{5.43}$$

5.4.2 Interpolation

To accomplish the adaptation to the driving state without introducing discontinuous control inputs, that could cause deterioration of ride comfort, a continuous interpolation between controllers is preferable over a discontinuous switching function $\sigma(q_i)$. The proposed interpolation approach (see (5.2))

$$u(t) = -\underbrace{\left((1-q_{susp}(t))\left((1-q_{fdyn}(t))\mathbf{k}_{comf}^{T} + q_{fdyn}(t)\mathbf{k}_{safe}^{T}\right) + q_{susp}(t)\mathbf{k}_{susp}^{T}\right)}_{\mathbf{k}_{adp}^{T}(t)}\mathbf{x}(t)$$

offers this advantage and involves only a small number of state feedback controllers to be stored in an electronic control unit, which is attractive from an implementation point of view. The stability of the approach has been studied in the last Section, however, it must be analyzed how well the Pareto front (Figure 5.8) can be approximated by using this linear interpolation technique, i.e. which performance results from the control law (5.2).

An important fact is that the state feedback gain resulting from the interpolation of the LQRs is not necessarily an LQR in terms of the quadratic cost functional (A.3) with the quantities that have been defined in Section 5.4.1. However, if the resulting performance is comparable to the LQR performance given by the Pareto front in Figure 5.8 and the suspension deflection does not rise significantly, the interpolation method is suitable for the adaptive suspension control approach.

To verify the performance of the controller parametrizations resulting from the interpolation, the co-domains of $q_{fdyn}(t)$ and $q_{susp}(t)$ have been quantized and simulations with the nonlinear test rig model for the resulting controller configurations have been performed using profile P1 as excitation ($v_{p1} = 50\,\frac{\mathrm{km}}{\mathrm{h}}$). The results for the interpolation between each controller are depicted in Figure 5.9.

The Pareto front in terms of $||\ddot{x}_{c,comf}||_{\mathrm{rms}}$ and $||F_{dyn}||_{\mathrm{rms}}$ from Figure 5.8 as well as the passive suspension configuration are shown in each carpet plot. In order to study the performance for all three suspension objectives, the carpet plots are shown for relevant combinations of the quantities $||\ddot{x}_{c,comf}||_{\mathrm{rms}}$, $||F_{dyn}||_{\mathrm{rms}}$ and the standard deviation of the suspension deflection $||x_c - x_w||_{\mathrm{std}}$ (see Chapter 2.3.3). It is noted that due to the more transparent representation only the resulting performance from the interpolation between two controllers is depicted in each case. However, further simulations have shown that the performance resulting for combinations with $0 < q_{fdyn} < 1 \wedge 0 < q_{susp} < 1$ offer similar performance results.

As Figure 5.9 shows, the performance of the interpolated state feedback gains is even better with respect to most performance aspects than the performance of the LQRs from the Pareto front. The suspension deflection controller offers significant benefit in terms of $||x_c - x_w||_{\mathrm{std}}$ (Figure 5.9 (middle)), while it only marginally deteriorates ride comfort and ride safety (Figure 5.9 (upper)). None of the controllers resulting from the interpolation violates the bounds (Chapter 2.3) on the dynamic wheel load ($||F_{dyn}||_{\mathrm{rms}} \leq 387\,\mathrm{N}$ and $\min(F_{dyn}) \leq 1161\,\mathrm{N}$) or the suspension deflection ($||x_c - x_w||_{\mathrm{std}} \leq 1.67\,\mathrm{cm}$ and $\max(|x_c - x_w|) \leq 5\,\mathrm{cm}$).

By the results it becomes apparent that the LQR approach, which is also frequently employed in the literature due to its feasibility for the problem by its quadratic performance index and its fairly transparent tuning parameters, does not achieve the optimal overall performance for the considered suspension setting. However, by the considered interpolation approach no controller parametrization results, which dominates the comfort controller in terms of ride comfort. Since the interpolation based adaptive switching control outperforms the LQR configurations on the Pareto front regarding ride safety and suspension deflection, it represents a feasible suspension control approach, which promises excellent performance even compared to nonlinear control techniques (see e.g. [72, 73]).

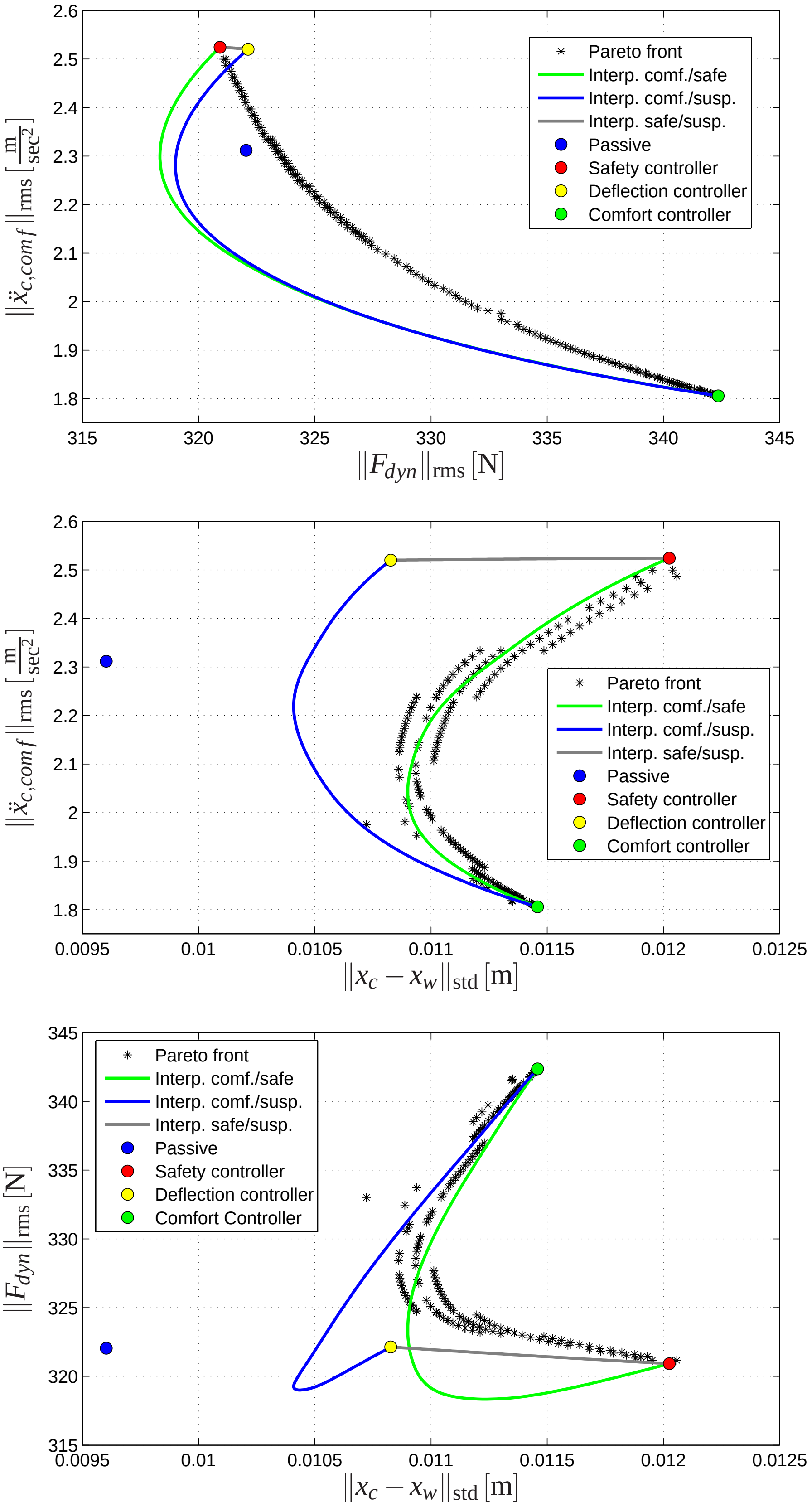

Figure 5.9: Performance results for the interpolation between the controllers $\mathbf{k}_{comf}^T$, $\mathbf{k}_{safe}^T$ and $\mathbf{k}_{susp}^T$ in comparison to the LQR configurations of the Pareto front of Figure 5.8.

5.5 Simulation results

The potential of the adaptive suspension control approach has been shown in the analysis of the controller performance for interpolation (Figure 5.9). In order to study the dynamic behavior of the controller adaptation, a simulation with a singular disturbance event as excitation is presented in the following.

The singular disturbance event involves two subsequent bumps with a height of $\hat{h} = 5.5\,\mathrm{cm}$, which corresponds to $h = \frac{\hat{h}}{2}$ in terms of (2.16) (Figure 5.10 (upper)). This amplitude of the disturbance signal can already become critical for comfort oriented controller designs at the test rig. The nonlinear test rig model presented in Chapter 3.3.3 is used for the simulations. It is noted that the state estimator is not employed in this simulation to focus on the dynamic behavior of the adaptive controller structure. In the simulation the adaptive suspension control approach is compared to the passive suspension system and to a time-invariant LQR (see (5.44) in Section 5.6). The simulation results are depicted in Figure 5.10.

The time-invariant LQR and the adaptive controller both provide better ride comfort than the passive suspension system as the peaks of the weighted chassis acceleration signal are lowered. The performance gains (see (2.24)) in terms of $\|\ddot{x}_{c,comf}\|_{\mathrm{rms}}$ with respect to the passive suspension system are $P^{LQR}_{g,\ddot{x}_{c,comf}} = 28\%$ and $P^{adp}_{g,\ddot{x}_{c,comf}} = 25\%$. However, the LQR violates the suspension deflection limit and also the peak limit on the dynamic wheel load (as does the passive system). The scheduling signals $q_{fdyn}(t)$ and $q_{susp}(t)$ rise as the driving state turns out to be critical and the controller parametrization is adjusted by the adaptive controller accordingly to prevent the limits from being exceeded. Due to the adaptation the focus is shifted from ride comfort to ride safety and suspension deflection. Considering the fact that the performance deterioration in terms of $\|\ddot{x}_{c,comf}\|_{\mathrm{rms}}$ with respect to the LQR is only 3% for the challenging singular disturbance event, the performance is remarkable. Moreover, the resulting control forces are well below the limits of the test rig actuator.

Based on further simulation results for profile P1 and P2, a comfort gain in terms of (2.25) of up to 36% can be achieved in simulations with the proposed adaptive control approach for the fully active suspension while keeping the limits for the suspension deflection and the dynamic wheel load. Thus, the concept resembles a very promising suspension control approach, which will be experimentally verified in Section 5.7. Further simulation results for a similar control concept for an automotive quarter-car model are presented by the author in [74].

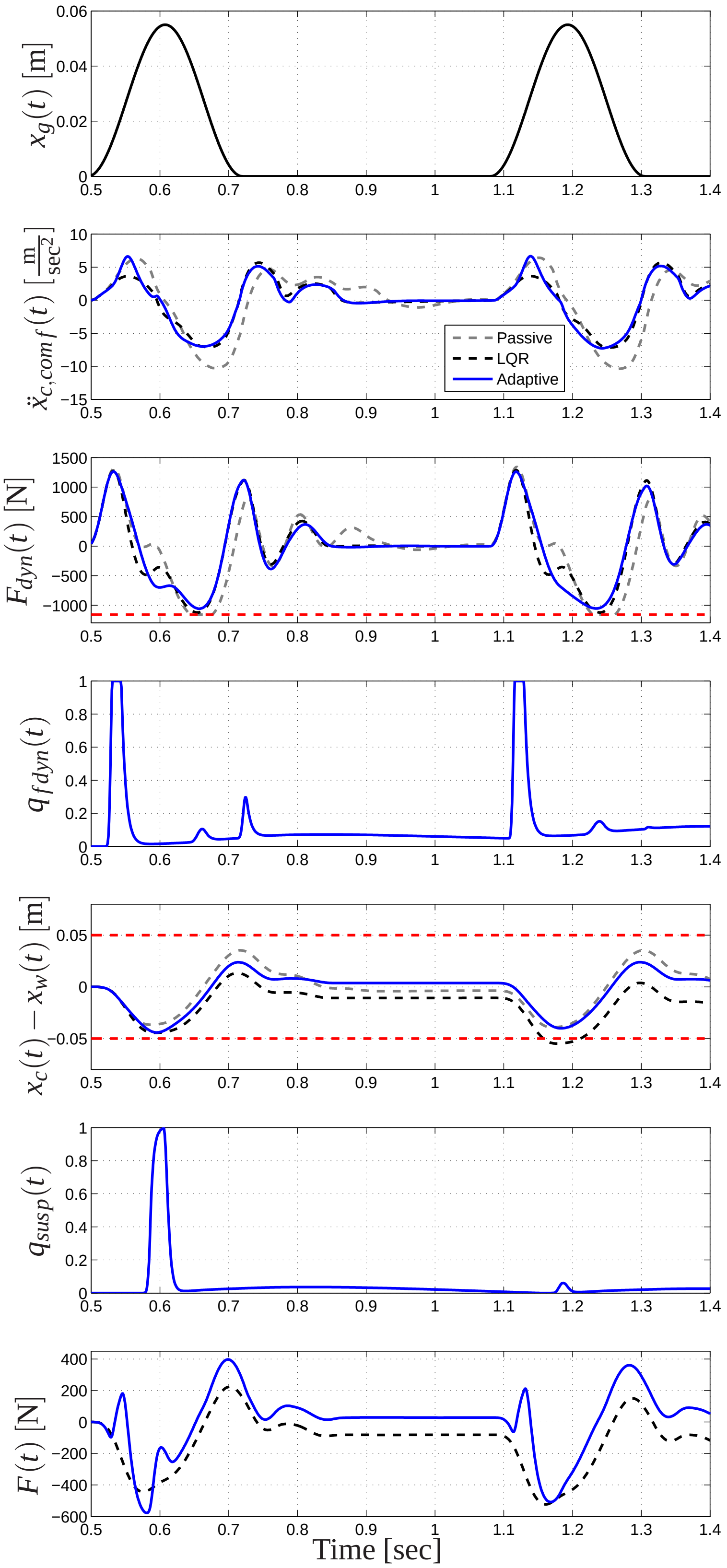

Figure 5.10: Simulation results of the adaptively controlled suspension versus the passive suspension and a time-invariant LQR for a singular disturbance event; the red lines indicate the limits for the peak value of F_{dyn} (i.e. $-F_{\text{stat}}$) and the suspension deflection limits.

5.6 Design of the benchmark controllers

In order to evaluate the performance of the new adaptive control approach in more detail, benchmark controllers are employed as presented in Chapter 2.7. Besides the benchmark controllers, the passive suspension configuration is considered in the comparison of the suspension concepts. In order to provide comparability of the approaches, the benchmark controller parametrizations are also determined by means of optimization.

1. Skyhook controller: The skyhook controller is employed for the active suspension configuration (Act.-Skyh.) and an emulation of a semi-active suspension (SA-Skyh.). Since the original passive damping ratio of the passive suspension system is tuned to represent a more safety oriented suspension configuration (see Figure 5.1), a damping compensation is realized by an actuator control logic to emulate a lower passive damping and superimpose skyhook damping (see (2.29)). If the compensation is not implemented, a semi-active skyhook control law cannot provide an increase of ride comfort for the considered quadricycle suspension setting. In the semi-active case (SA-Skyh.) the actuator control logic clips the skyhook control forces if they violate the passivity restriction (2.26) of a semi-active damper.

   The passive damping ratio has been lowered to $\tilde{D}_{c,p} = 0.28$ by emulating a damper coefficient of $d_c = 500\,\frac{\mathrm{Nsec}}{\mathrm{m}}$ and the skyhook damping is chosen as $d_{sky} = 2000\,\frac{\mathrm{Nsec}}{\mathrm{m}}$. Both values have been determined by carpet plot based optimization.

2. Adaptive Skyhook controller: The adaptation logic presented in Section 5.2.1 is used to interpolate between two semi-active controller settings according to the current driving state. The first setting is the comfort oriented skyhook setting described above. The second setting is more safety oriented with $d_c = 500\,\frac{\mathrm{Nsec}}{\mathrm{m}}$ and $d_{sky} = 0\,\frac{\mathrm{Nsec}}{\mathrm{m}}$. The adaptive skyhook controller (SA Ad.) is implemented for the emulated semi-active suspension configuration.

3. LQR: From the Pareto front depicted in Figure 5.8 an LQR is chosen, that exhibits a dynamic wheel load exactly between the passive configuration and the comfort controller, i.e. $||F_{dyn}||_{\mathrm{rms}} = 331\,\mathrm{N}$ for road profile P1, which has been used for the optimization based controller design. Thereby, the LQR benchmark resembles a moderately tuned

comfort oriented controller, which only slightly increases the dynamic wheel load. The corresponding state feedback gain vector is

$$\mathbf{k}_{bm}^{T} = \begin{bmatrix} -7649.8 & 12.5 & -955.4 & 190.1 \end{bmatrix}. \tag{5.44}$$

5.7 Experimental results

The adaptive controller has been tested for the measured road profiles P1 (passed with the velocity $v_{p1} = 50\,\frac{\mathrm{km}}{\mathrm{h}}$), P2 ($v_{p2} = 30\,\frac{\mathrm{km}}{\mathrm{h}}$) and the bump signal (singular disturbance event) that has been used in the simulations (Figure 5.10) but with a lower amplitude in order not to damage the hardware components of the test rig ($\hat{h} = 4.5\,\mathrm{cm}$). The performance gains according to (2.24) with respect to the passive suspension system of the corresponding measurement results are summarized in the spider charts in Figure 5.12. It is noted that in the spider diagrams the center represents performance gains $P_{g,\mathrm{obj}}$ (see (2.24)) of -40% or less.

In Figure 5.13 the relevant measurement signals of an exemplary interval of P1 are visualized in comparison to the passive system and it can be seen that the performance of the adaptive control approach is remarkable. The peaks of the filtered acceleration signal (see (2.17)) are significantly reduced and the scheduling parameters increase only mildly except for one peak in the dynamic wheel load. The slight increase of the suspension deflection parameter does not deteriorate ride comfort, which is coherent with the analysis conducted by means of Figure 5.9. The limits on the dynamic wheel load and the suspension deflection are kept and the actuator does not saturate. The numerical measurement results for this experiment including the results of the benchmark controllers are summarized in Table 5.1. To evaluate the performance benefit in the comfort relevant frequency range and to analyze the disturbance transfer behavior of the adaptively controlled system, the ratio of the power spectral densities of the weighted chassis acceleration $\ddot{x}_{c,comf}(t)$ and the road displacement signal $x_g(t)$ is visualized in Figure 5.11 including a zoom on the interval $4-8\,\mathrm{Hz}$. The adaptively controlled system shows a better isolation in the comfort relevant frequency interval compared to the passive system.

The semi-active skyhook controllers (SA-Skyh. and SA-Ad.) can only slightly enhance ride comfort and the adaptive skyhook approach offers only marginal advantages regarding suspension deflection. Especially for profile P2 (Figure 5.12 (middle)) the obvious reason is that

Table 5.1: Experimental results for profile P1 (passed with $v_{p1} = 50\,\frac{\mathrm{km}}{\mathrm{h}}$) for the passive suspension, the benchmark configurations and the adaptively controlled active suspension.

Quantity	Passive	SA-Skyh.	SA-Ad.	Act.-Skyh.	LQR	Adaptive
$\|\ddot{x}_c\|_{\mathrm{rms}}$ in $\frac{\mathrm{m}}{\mathrm{sec}^2}$	2.38	2.27	2.28	1.91	1.92	1.72
Benefit vs. passive	-	4.74%	4.24%	19.56%	19.44%	27.55%
$\|\ddot{x}_{c,\mathrm{comf}}\|_{\mathrm{rms}}$ in $\frac{\mathrm{m}}{\mathrm{sec}^2}$	2.28	2.16	2.17	1.79	1.83	1.62
Benefit vs. passive	-	5.2%	4.69%	21.32%	19.59%	28.78%
$\|F_{dyn}\|_{\mathrm{rms}}$ in N	331	332	333	392	341	356
Benefit vs. passive	-	-0.37%	-0.78%	-18.42%	-3.15%	-7.78%
$\min(F_{dyn})$ in N	-943	-975	-996	-1065	-981	-1076
Benefit vs. passive	-	-3.44%	-5.64%	-13.01%	-4.12%	-14.12%
$\min(x_c - x_w)$ in cm	-2.73	-2.49	-2.48	-2.62	2.72	-2.82
Benefit vs. passive	-	8.79%	9.16%	4.03%	0.37%	-3.30%
$\|P^+\|_{\mathrm{rms}}$ in W	0	0	0	46.9	17.0	24.8
Benefit vs. Act.-Skyh.	-	-	-	-	63.75%	47.12%

Table 5.2: Comparison of the actuator data of the active benchmark configurations and the adaptively controlled active suspension for profile P1 ($v_{p1} = 50\,\frac{\mathrm{km}}{\mathrm{h}}$), $\|P^+\|_{\mathrm{rms}}$ is calculated according to (2.23).

Quantity	Act.-Skyh.	LQR	Adaptive
$\|P^+\|_{\mathrm{rms}}$ in W	46.9	17.0	24.8
Benefit vs. Act.-Skyh.	-	63.75%	47.12%
$\|F\|_{\mathrm{rms}}$ in N	203	98	130
Benefit vs. Act.-Skyh.	-	51.7%	36.0%
$\max(\|F\|)$ in N	664	311	384
Benefit vs. Act.-Skyh.	-	53.2%	42.2%

the velocity of the chassis mass is too low due to the high frequency components included in profile P2 (Figure 2.3). Thus, the comfort advantages are mainly achieved by the lower emulated passive damping. The performance deterioration in terms of suspension deflection depicted in the spider diagram for profile P2 is uncritical for all controllers since the passive reference shows very low suspension deflections for this road profile ($\|x_c - x_w\|_{\mathrm{std}} = 0.25\,\mathrm{cm}$

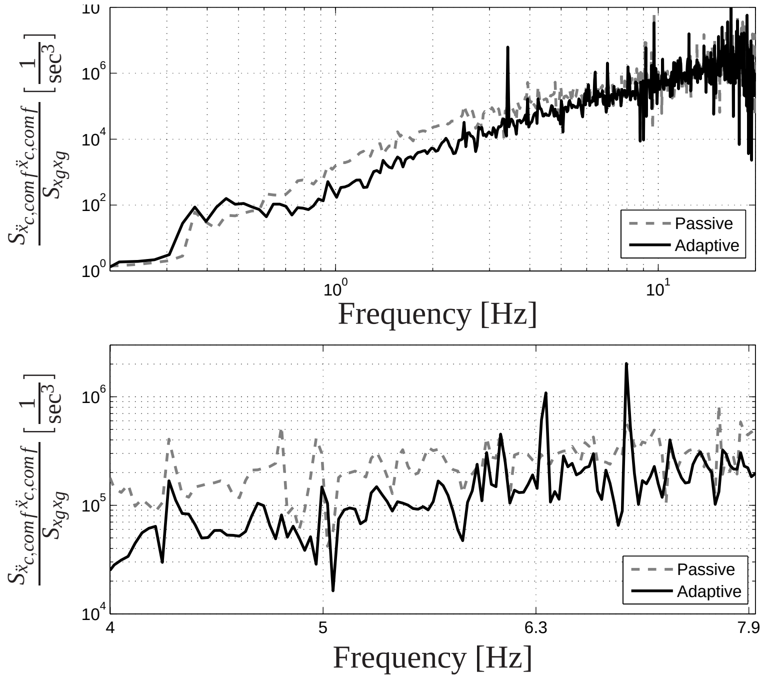

Figure 5.11: Power spectral density ratios for the measurement results of the adaptively controlled fully active system (P1 with $v_{p1} = 50\,\frac{\mathrm{km}}{\mathrm{h}}$) with zoom on the frequency range $4-8\,\mathrm{Hz}$.

and $\min(x_c - x_w) = -1.1\,\mathrm{cm}$). The active skyhook controller (Act.-Skyh.) achieves significantly better ride comfort for profile P1, which comes at the price of the violation of the rms-limit of the dynamic wheel load ($\frac{F_{stat}}{3} \approx 387\,\mathrm{N}$) and the highest power consumption of all considered active suspension configurations (Table 5.2). The conventional LQR performs well for all considered excitation signals. The adaptive control approach, however, offers by far the best ride comfort including 35% comfort increase for the singular disturbance event. It provides this comfort increase by activating the most comfort oriented controller and thus, shows higher suspension deflection for uncritical driving states to improve the isolation of the sprung mass.

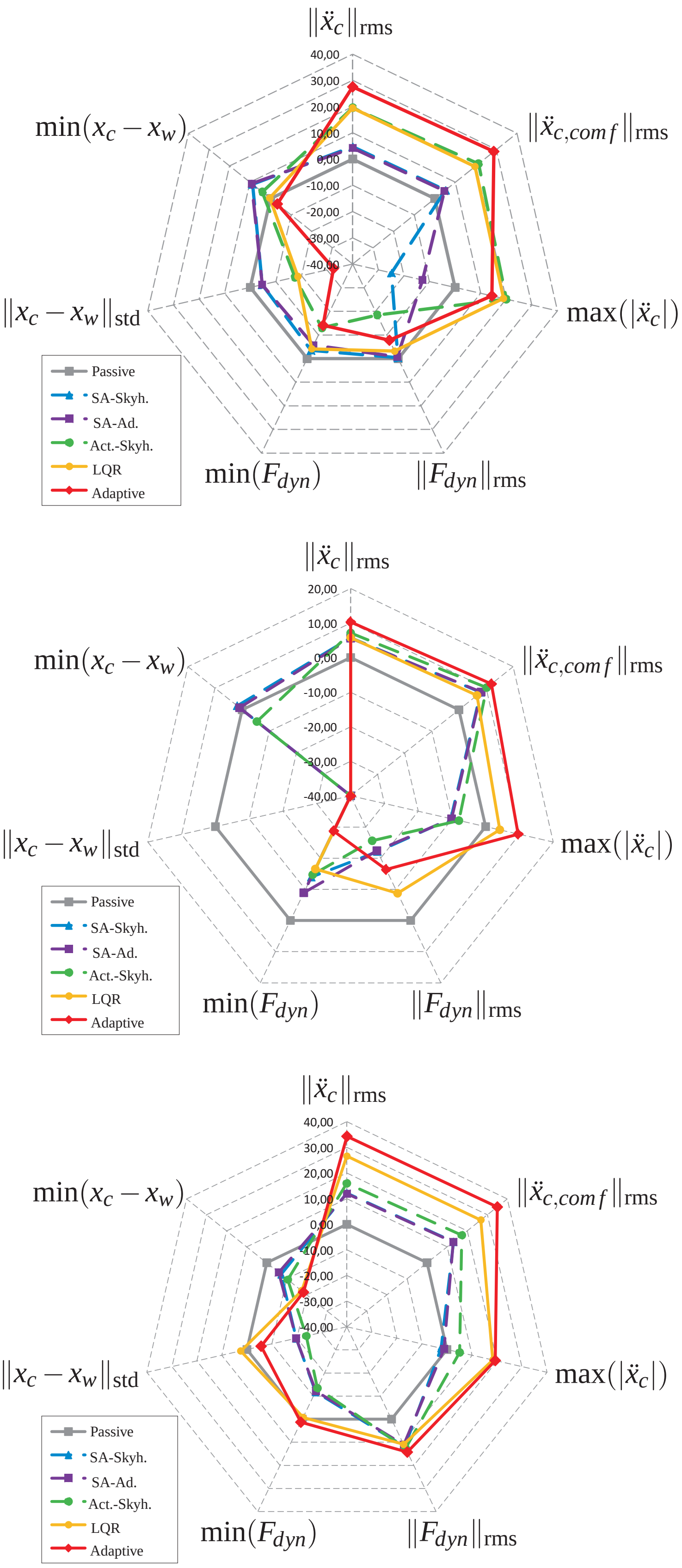

Figure 5.12: Measurement results of the controller performance for profile P1 with $v_{p1} = 50\,\frac{\text{km}}{\text{h}}$ (upper), profile P2 with $v_{p2} = 30\,\frac{\text{km}}{\text{h}}$ (middle) and the singular disturbance event (lower).

The performance advantage of the adaptive controller becomes even more apparent if the amplitude of profile P1 is increased by 25%: The adaptive controller can improve ride comfort even by 31.41% and still keeps the rms-limit for the dynamic wheel load as well as the suspension deflection limit while all considered benchmark systems including the passive system violate the dynamic wheel load and/or the suspension deflection limits. In summary, it can be stated that the new adaptive control approach outperforms all benchmark controllers regarding ride comfort improvement and fulfills the system requirements for all considered excitation signals.

Figure 5.14 shows the measurement signals of the singular disturbance event. Although the amplitude has been lowered it can be seen that the results are comparable to the simulations in spite of a slightly higher dynamic wheel load, which, however, still does not exceed the limit. The performance decrease between measurement and simulation for all profiles is less than 10% and is caused by the presence of the estimator, measurement noise, slight model inaccuracies and structural vibrations of the test rig.

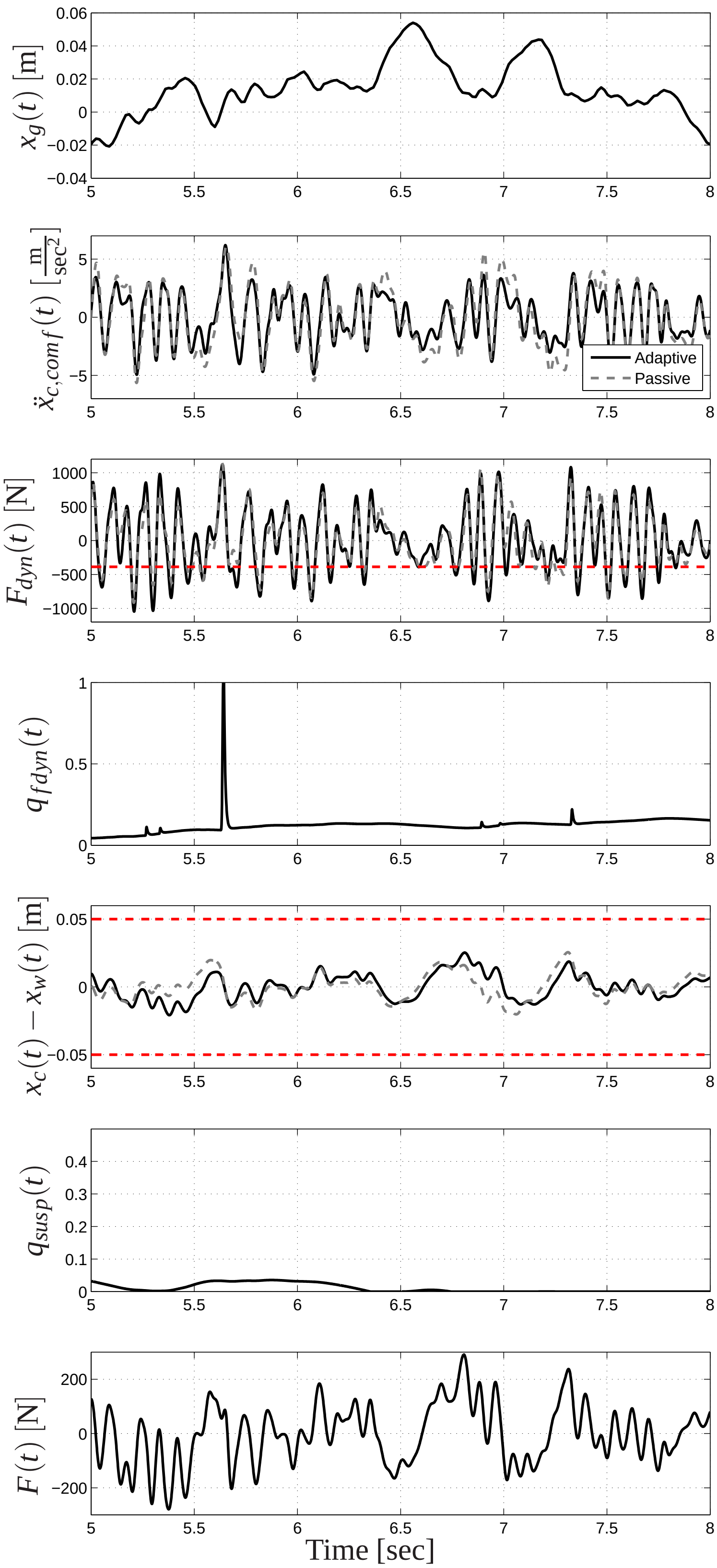

Figure 5.13: Measurement results of the adaptively controlled suspension versus the passive suspension (profile P1 with $v_{p1} = 50\,\frac{\mathrm{km}}{\mathrm{h}}$); the red lines indicate the limits for the rms-value of F_{dyn} (i.e. $\frac{F_{\mathrm{stat}}}{3}$) and the suspension deflection limits.

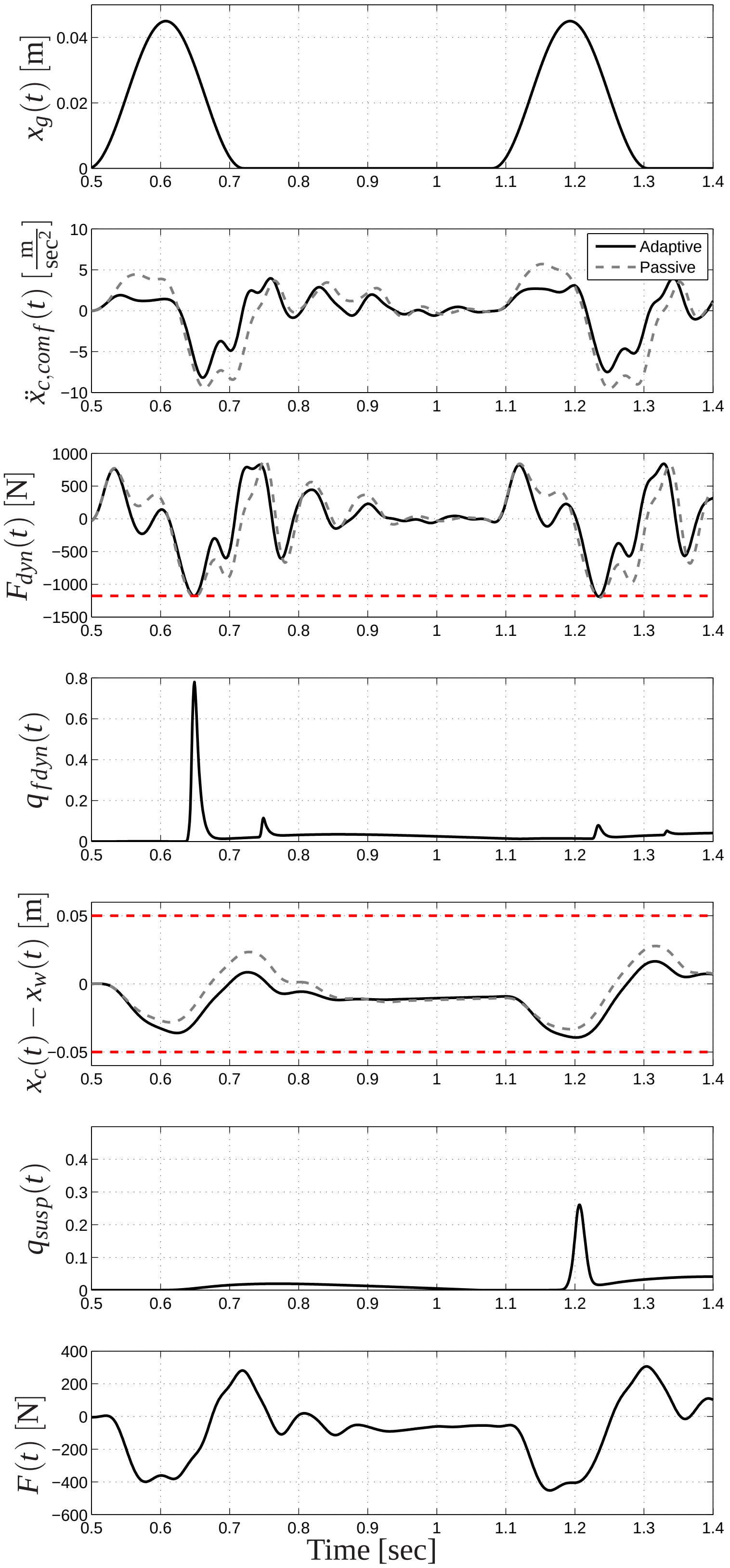

Figure 5.14: Measurement results of the adaptively controlled suspension versus the passive suspension (singular disturbance event); the red lines indicate the limits for the peak-value of F_{dyn} (i.e. $-F_{\text{stat}}$) and the suspension deflection limits.

5.8 Discussion

The proposed adaptive control approach has shown the performance of adaptively controlled suspensions and overcomes the conservatism frequently introduced by time-invariant suspension controllers. Although the controller structure is kept simple, the performance of the adaptive fully-active suspension system is remarkable: It outperforms all considered benchmark controllers, which partially (LQR, adaptive skyhook concept) even go beyond the state of the art of suspension controllers integrated in production vehicles, and keeps all limits defined in the system requirements for the considered road excitations. The approach offers ride comfort improvements of up to 35% in the conducted experiments, which is remarkably coherent with the simulation results.

However, remaining drawbacks of the fully active system with the proposed adaptive control approach can be summarized to:

1. **Complex stability analysis**: Although the nonlinear damper characteristic has been considered in the stability analysis, the existence of a CQLF is tested numerically for the quasilinear model, i.e. further minor nonlinearities (nonlinear tire stiffness and friction effects) have not been taken into account and thus the robustness of the stability requires further analysis. Furthermore it could be analyzed in more detail, how the Kalman filter influences the stability of the system, which has been discarded due to the excellent estimation performance of the estimator concept in the passive, active and adaptively controlled suspension cases.

2. **Actuator costs and energy demand:** The inherent problem of fully active suspension systems is their high energy demand. Although the energy demand is considerably lower than for the active skyhook controller, it is still significant, especially if it is considered that the power demand analysis is based on the average positive mechanical power (neglecting efficiency factors) and only in a quarter-vehicle setup. If it is furthermore considered that the required mechanical power scales linearly with the mass, that has to be accelerated by the actuator, it becomes clear that fully active suspension systems are not an option for production vehicles, especially if todays energy focussed vehicle design is taken into account. Other drawbacks are the costs and weight of the actuators.

3. **Tuning procedure of the controllers:** The adaptive switching controller structure is transparent from a control engineering point of view, however, the tuneability of the controller structure has drawbacks from the perspective of vehicle dynamics engineers. The tuning of the involved controllers is realized by the choice of the weighting matrices. However, the tuning procedure desired by the automotive industry is frequently based on tuning of the natural frequency and damping ratio of the sprung mass, which is one of the reasons for the frequent implementation of skyhook based control methods for mechatronic suspension systems. Especially since the stability of the closed loop system depends on the controller parametrization and must be verified after each change of the state feedback gains, the optimization based tuning process has deficits regarding its applicability.

In the next Chapters, concepts are presented to overcome these problems but to simultaneously maintain the advantages of adaptive suspension control, that have been shown in this Chapter.

Chapter 6

POTENTIAL OF A HYBRID SUSPENSION SYSTEM

The first task to be analyzed regarding the drawbacks of the fully active suspension system discussed in the last Chapter is the modification of the actuator structure. The aim is to find an actuator structure based on mechatronic suspension elements from production vehicles, which can potentially preserve the performance of the fully active system presented in Chapter 5.

The idea is to study the performance potential of the combination of a continuously variable semi-active damper and a low bandwidth actuator in series to the primary spring. The intuitive advantages of this new hardware configuration are that it is realizable from stock hardware, which offers a cost advantage over fully active systems, and that due to the application of a fast, continuously variable damper it potentially promises more energy efficient control of the vertical dynamic vehicle behavior. Since the actuator configuration includes semi-active (continuously variable damper) and active elements (actuator in series to primary spring), it is referred to as a *hybrid suspension system* in this Thesis.

In this Chapter, it is analyzed to what extent the performance of a high bandwidth active suspension system can be attained by a hybrid suspension system (see also [75] and [76]). Therefore, an iterative optimization procedure for the controller weights of linear quadratic regulators and damping ratios for a low bandwidth active suspension (LBAS), based on the methods and insights presented in [138] and [55], is utilized. Although a linear quarter-car model of an automotive suspension is considered, the analysis is conducted in a generalized framework, which involves the use of normalized signals to remove the dependency of the suspension performance on the road excitation signal.

6.1 The hybrid suspension concept

Before the potential analysis of the hybrid suspension system is conducted, the hardware structure is presented in more detail and some annotations regarding the term *hybrid suspension* are given. In Chapter 2.4 concepts and realizations of semi-active, slow active (LBAS, Figure 6.1 (left)) and high bandwidth/fully active suspension systems (HBAS, Figure 6.1 (middle)) have been presented. Only for the attenuation of roll movements, the combination of semi-active dampers and active anti-rollbars is already realized in production vehicles (see Chapter 2.4). The term *hybrid suspension* in this Thesis refers to a suspension system, which contains semi-active elements (e.g. a semi-active damper) and active elements (e.g. hydraulic or electrical actuators) employed to influence the heave dynamics of the sprung and unsprung mass[1].

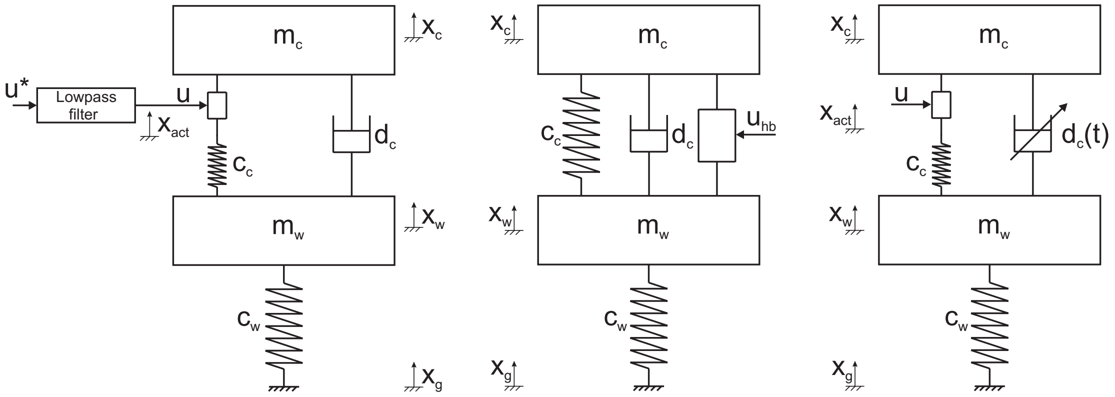

Figure 6.1: Low bandwidth active suspension (LBAS) model (left), high bandwidth active suspension (HBAS) (middle) and hybrid suspension model (right).

The *hybrid suspension* configuration analyzed in this Thesis is depicted in the right quarter-car model in Figure 6.1, i.e. it contains a continuously variable, fast semi-active damper and an actuator in series to the primary spring. In the literature ([138] and [137]) the combination of variable damping and a low bandwidth actuator has also been indicated, however, a slow variation of the damper has been considered so that the characteristic of the passive damper can be quasi-statically adjusted by a supervisor with respect to changes of the road conditions. The important difference of the hybrid suspension system is that it utilizes the higher bandwidth of the damper (compared to the actuator) to significantly improve the suspension performance

---

[1] Of course, a *hybrid suspension* configuration can also be used to attenuate pitch and roll movements of the car if a full-car model is considered.

by dynamic adaptation.

The proposed *hybrid suspension* concept should be clearly distinguished from a further suspension configuration presented in the literature. In [101] an *electromagnetic hybrid active-passive* vehicle suspension system has been presented. This suspension system resembles the combination of a new electromagnetic actuator integrated in parallel to a hydraulic damper with the purpose to reduce the actuator forces required by a fully active suspension system without a hydraulic damper. Thus, a smaller and lighter active suspension system can be designed based on an electromagnetic actuator principle. The suspension concept has been further developed including the design and realization of the actuator type and the consideration of recuperation possibilities [17, 100]. This concept proposed in the literature, however, does not consider semi-active damping and focusses on hardware aspects of the electromagnetic actuator rather than on suspension control concepts.

6.2 Suspension models for the potential analysis

In this Section, the considered quarter-car models for the analysis are described. The hybrid combination (Figure 6.1 (right)) results from the low bandwidth active suspension (LBAS) if the damper is continuously adjustable. Therefore, it is analyzed utilizing an iterative optimization process of the controller parameters and damping ratios, to what extend a hybrid suspension configuration can achieve the performance of the HBAS.

First the LBAS model is described. The displacement generating actuator integrated in series to the primary spring is considered to be ideal, i.e. the actuator instantly produces the displacements requested by the signal u. All bandwidth limitations of the actuator are represented by a second order low pass filter applied for the desired control input u^*. The cutoff frequency ω_f of the low pass filter and the damping ratio of the sprung mass $\omega_c = d_c/(2\sqrt{c_c m_c})$ are fixed for any particular set of performance calculations, which, however, are carried out for a wide range of these parameters. The definitions and values of the parameters used in this Chapter are given in Table B.3 in the Appendix. With the ideal actuator assumption $u = x_c - x_{act}$, the equations of motion can be written as

$$\begin{aligned} m_c\ddot{x}_c &= -c_c(x_c - x_w) + c_c u - d_c(\dot{x}_c - \dot{x}_w)\,, \\ m_w\ddot{x}_w &= c_c(x_c - x_w) - c_c u + d_c(\dot{x}_c - \dot{x}_w) - c_w(x_w - x_g)\,. \end{aligned} \tag{6.1}$$

In order to simplify the model representation and to analyze the influence of actuator bandwidth and variable damping in a more generalized framework, the model is represented by means of damping ratios and undamped natural frequencies of chassis and wheel mass. The parameters of the models used for the potential analysis (see Table B.3 in the Appendix) have been chosen as an estimate of the automotive test rig parameters (Chapter 7) since the analysis has been conducted before the test rig has been designed. Following approaches on suspension performance analysis from the literature (e.g. [138] and [55]), the tire damping is neglected and the tire deflection $x_{wg} = x_w - x_g$ is considered as an indicator for ride safety instead of the dynamic wheel load. Hence, with the state vector **x** and output vector **y**

$$\mathbf{x} = \begin{bmatrix} x_1 \\ x_2 \\ x_3 \\ x_4 \end{bmatrix} = \begin{bmatrix} x_c - x_w \\ \dot{x}_c \\ x_w - x_g \\ \dot{x}_w \end{bmatrix}, \quad \mathbf{y} = \begin{bmatrix} y_1 \\ y_2 \\ y_3 \end{bmatrix} = \begin{bmatrix} \ddot{x}_c \\ x_c - x_w \\ x_w - x_g \end{bmatrix}, \tag{6.2}$$

the state space representation becomes

$$\begin{aligned} \dot{\mathbf{x}} &= \mathbf{A}\mathbf{x} + \mathbf{b}u + \mathbf{g}\dot{x}_g \,, \\ \mathbf{y} &= \mathbf{C}\mathbf{x} + \mathbf{d}u \,, \end{aligned} \tag{6.3}$$

where

$$\mathbf{A} = \begin{bmatrix} 0 & 1 & 0 & -1 \\ -\omega_c^2 & -2D_c\omega_c & 0 & 2D_c\omega_c \\ 0 & 0 & 0 & 1 \\ \frac{\omega_c^2}{\rho} & \frac{2D_c\omega_c}{\rho} & -\omega_w^2 & -\frac{2D_c\omega_c}{\rho} \end{bmatrix}, \quad \mathbf{b} = \begin{bmatrix} 0 \\ \omega_c^2 \\ 0 \\ -\frac{\omega_c^2}{\rho} \end{bmatrix}, \quad \mathbf{g} = \begin{bmatrix} 0 \\ 0 \\ -1 \\ 0 \end{bmatrix}$$

$$\mathbf{C} = \begin{bmatrix} -\omega_c^2 & -2D_c\omega_c & 0 & 2D_c\omega_c \\ 1 & 0 & 0 & 0 \\ 0 & 0 & 1 & 0 \end{bmatrix}, \quad \mathbf{d} = \begin{bmatrix} \omega_c^2 \\ 0 \\ 0 \end{bmatrix}$$

parametrize the state space model utilizing the chassis damping ratio $D_c = \frac{d_c}{2\sqrt{c_c m_c}}$, the natural frequency of the sprung mass ($\omega_c = \sqrt{\frac{c_c}{m_c}}$), the tirehop frequency ($\omega_w = \sqrt{\frac{c_w}{m_w}}$) and the mass ratio $\rho = \frac{m_w}{m_c}$ (see Table B.3). The state space model (6.3) describes the system dynamics without the bandwidth limitation. The inputs of the system are the actual displacement of the actuator u and the state disturbance $\dot{x}_g$, which is the vertical ground velocity. The outputs of the system are the vertical body acceleration y_1, the suspension deflection y_2, and the tire deflection y_3. The low pass filter is described following an approach by [138] by

$$\ddot{u}+2D_f\omega_f\dot{u}+\omega_f^2u=\omega_f^2u^*\,, \tag{6.4}$$

where the cutoff frequency ω_f incorporates the bandwidth of the actuator. By augmenting (6.3) with the additional states $x_5 = u$ and $x_6 = \dot{u}$ of (6.4), a sixth-order state space representation, that describes the whole system shown in Figure 6.1 (left), including the filter can be derived. The resulting system matrices are

$$\mathbf{A}_{lb} = \begin{bmatrix} 0 & 1 & 0 & -1 & 0 & 0 \\ -\omega_c^2 & -2D_c\omega_c & 0 & 2D_c\omega_c & \omega_c^2 & 0 \\ 0 & 0 & 0 & 1 & 0 & 0 \\ \frac{\omega_c^2}{\rho} & \frac{2D_c\omega_c}{\rho} & -\omega_w^2 & -\frac{2D_c\omega_c}{\rho} & -\frac{\omega_c^2}{\rho} & 0 \\ 0 & 0 & 0 & 0 & 0 & 1 \\ 0 & 0 & 0 & 0 & -\omega_f^2 & -2D_f\omega_f \end{bmatrix}, \tag{6.5}$$

$$\mathbf{b}_{lb} = \begin{bmatrix} 0 & 0 & 0 & 0 & 0 & \omega_f^2 \end{bmatrix}^T, \tag{6.6}$$

$$\mathbf{g}_{lb} = \begin{bmatrix} 0 & 0 & -1 & 0 & 0 & 0 \end{bmatrix}^T, \tag{6.7}$$

$$\mathbf{C}_{lb} = \begin{bmatrix} -\omega_c^2 & -2D_c\omega_c & 0 & 2D_c\omega_c & \omega_c^2 & 0 \\ 1 & 0 & 0 & 0 & 0 & 0 \\ 0 & 0 & 1 & 0 & 0 & 0 \end{bmatrix}, \tag{6.8}$$

$$\mathbf{d}_{lb} = \begin{bmatrix} 0 & 0 & 0 \end{bmatrix}^T. \tag{6.9}$$

The new control input to the system is now the desired actuator deflection u^*.

The high bandwidth active suspension system (HBAS, Figure 6.1 (middle)) has a force generating actuator mounted in parallel to the spring and the damper. In the following description, no bandlimit is considered for the HBAS, which makes it possible to treat it as a performance benchmark for the LBAS in the analysis presented in Sections 6.4 and 6.5. With u_{hb} being the actuator force, the equations of motion can be derived as formulated in (2.1) and (2.2). By using the states defined in (6.2), one can transfer (2.1)-(2.2) into a state space representation, where the matrix **A** and the vector **g** are identical to those of (6.3). The relationship between the vector $\mathbf{b}_{hb}$ of the HBAS model and the vector $\mathbf{b}$ of the LBAS model can be expressed as

$$\mathbf{b} = \begin{bmatrix} 0 \\ \omega_c^2 \\ 0 \\ -\frac{\omega_c^2}{\rho} \end{bmatrix} = c_c \begin{bmatrix} 0 \\ \frac{1}{m_c} \\ 0 \\ -\frac{1}{m_w} \end{bmatrix} = c_c \mathbf{b}_{hb} \, . \tag{6.10}$$

Thus, if all model parameters are chosen identically, the HBAS and the LBAS *without* the low pass filter behave equivalently if

$$c_c u = u_{hb} \, , \qquad \forall t \geq t_0 \tag{6.11}$$

holds. This means that despite of the different mechanical structure, both systems offer the same performance potential. Taking the bandlimit into account, the performance of the LBAS tends towards the performance of the HBAS, when the filter cutoff frequency is increased. For the performance analysis, the passive suspension is also used as a benchmark system. The model of the passive system results from the HBAS model if the actuator force vanishes, i.e. $u_{hb} = 0$.

6.3 Suspension controller design

Since the focus of this Chapter is the determination of the potential of LBAS systems with variable damping, a transparent linear controller structure that provides good insight in the closed loop system behavior is used. Therefore, as in Chapter 5 and in numerous studies on performance capabilities of different suspension configurations presented in the literature (see e.g. [138], [55], [161]), linear quadratic regulators (LQR) are utilized as controllers.

The controllers are designed for the fourth-order system (6.3). For the LQR design it is assumed that all states are available for feedback (e.g. by using state estimation techniques as proposed in Chapter 4). Due to this assumption and the linear models, the resulting system performance can be regarded as an upper bound on what is achievable in practical applications. For the controller design the quadratic performance index

$$J = \int_0^\infty \mathbf{y}^T \mathbf{Q}_y \mathbf{y} dt \quad \text{with } \mathbf{Q}_y = \begin{bmatrix} q_{\ddot{x}_c} & 0 & 0 \\ 0 & q_{x_{cw}} & 0 \\ 0 & 0 & q_{x_{wg}} \end{bmatrix} \quad \text{and } \mathbf{r} = \begin{bmatrix} r_1 \\ r_2 \\ r_3 \end{bmatrix} = \begin{bmatrix} q_{\ddot{x}_c} \\ q_{x_{cw}} \\ q_{x_{wg}} \end{bmatrix} \tag{6.12}$$

is chosen. It contains the three performance criteria: Body acceleration y_1, suspension deflection y_2 and tire deflection y_3. While the weight for the body acceleration is fixed at $q_{\ddot{x}_c} = 1$, the weights $q_{x_{cw}} = r_2$ and $q_{x_{wg}} = r_3$ are varied to influence the optimal tradeoff between ride comfort, suspension travel and ride safety (see also [138] and [55]). The resulting state feedback control law is

$$u^* = -\mathbf{k}^T \mathbf{x}. \tag{6.13}$$

The state feedback gain $\mathbf{k}^T$ is calculated according to the LQR design procedure described in Appendix A.1. It is noted that to provide comparability with the results presented in [138], explicit weighting of the control input is omitted and in (6.13) the computed feedback is applied to the *augmented* LBAS model including the filter (see also [76] for a discussion of this aspect).

6.4 System analysis

The influence of bandwidth and damping on the performance of an LBAS is analyzed in a similar way as presented in [138] but with a more detailed analysis of the resulting carpet plots. The results are then used in Section 6.5 to evaluate the potential of LBAS systems including a dynamically adjustable semi-active damper by means of an iterative optimization procedure.

6.4.1 Disturbance model and normalization

The disturbance model presented in (2.11) is employed for the analysis. By assuming white noise for the vertical ground velocity and the simple model structure it is a very general disturbance model, which is frequently employed for studies on suspension performance potential in the literature (e.g. [55], [106]).

In order to ensure comparability of the performance, independent of the road excitation, normalized rms-values $||\tilde{y}_i||_{\text{rms}}$ of the outputs $\mathbf{y}$ are used. Therefore, the rms-values $||y_i||_{\text{rms}}$ are divided by the square root of the white noise intensity $V_{\dot{x}_g} = 2\pi A v$ of the disturbance model (see also [76]). For instance, the normalized rms-value of the chassis acceleration is

$$||\tilde{y}_1||_{\text{rms}} = \frac{||y_1||_{\text{rms}}}{\sqrt{2\pi A v}}. \tag{6.14}$$

The maximum acceptable suspension travel is assumed in this study as $y_{2,max} = \pm 0.08\,\mathrm{m}$ and the tire deflection is limited to $y_{3,max} = \pm 0.023\,\mathrm{m}$ to ensure ride safety. Using the 3σ-rule approach described in Chapter 2.3, these constraints are normalized accordingly to $\|\tilde{y}_{2,max}\|_{\mathrm{rms}} = 0.961\,\mathrm{s}^{1/2}$ and $\|\tilde{y}_{3,max}\|_{\mathrm{rms}} = 0.276\,\mathrm{s}^{1/2}$ with respect to the disturbance model parametrization given in Section 6.4.2.

6.4.2 Benchmark systems

Three suspension systems are used as performance benchmarks for the LBAS with variable damping: The two HBAS designs H and H_1 and a typical passive suspension system P. System H is designed to be optimal in terms of ride comfort (thus lowering the comfort measure[2] $\|\tilde{y}_1\|_{\mathrm{rms}}$), while not exceeding the suspension stroke or the tire deflection of the passive system P. The controller weights for the design H_1 result from an optimization process, which is performed with respect to the operating conditions characterized by the parameters $A = 4.9 \cdot 10^{-6}\,\mathrm{m}$ and $v = 25\,\frac{\mathrm{m}}{\mathrm{sec}}$ (as used in [55]) of the disturbance model. Thus, the design H_1 gives minimum chassis acceleration for the high bandwidth suspension system while not violating the constraints for tire and suspension deflection (see Section 6.4.1) for this specific disturbance model parametrization and thus represents the benchmark for ride comfort. Table 6.1 summarizes the properties of all benchmark systems. The system parameters of all listed designs are chosen according to Table B.3 in the Appendix.

Table 6.1: Benchmark systems.

Design	D_c	$\|\tilde{y}_1\|_{\mathrm{rms}}$	$\|\tilde{y}_2\|_{\mathrm{rms}}$	$\|\tilde{y}_3\|_{\mathrm{rms}}$	$r_2 = q_{x_{cw}}$	$r_3 = q_{x_{wg}}$
H	0.30	$26.50\,\mathrm{s}^{-3/2}$	$0.36\,\mathrm{s}^{1/2}$	$0.13\,\mathrm{s}^{1/2}$	1162	53509
H_1	0.30	$11.70\,\mathrm{s}^{-3/2}$	$0.59\,\mathrm{s}^{1/2}$	$0.28\,\mathrm{s}^{1/2}$	96	1531
P	0.30	$31.56\,\mathrm{s}^{-3/2}$	$0.38\,\mathrm{s}^{1/2}$	$0.13\,\mathrm{s}^{1/2}$	–	–

---

[2] As in [55], for this performance study the shaping filter presented in Chapter 2.3.1 is not employed.

6.4.3 Influence of bandwidth

To study the influence of bandwidth, the controller weights of design H are applied to the LBAS in order to compare the performance of both systems. The actuator bandwidth $f_f = \frac{1}{2\pi}\omega_f$ is varied from 0.1 Hz – 40 Hz and five different values of chassis damping ratio D_c are assumed. For the disturbance (2.12), Figure 6.2 shows the normalized rms-values of all outputs. The graphs approximately start at the values of the associated passive systems and asymptotically reach the performance of the HBAS system H.

Figure 6.2(a) shows remarkably low normalized rms chassis accelerations obtained with $f_f \approx$ 3Hz for lightly damped systems, which is coherent with the results presented in [138]. In terms of suspension deflection (Figure 6.2(b)), this actuator bandwidth leads to very good performance, especially for systems with low and medium damping. The ride safety performance is shown in Figure 6.2(c). With $f_f \geq 15\,\text{Hz}$ normalized rms tire deflections comparable to those of the HBAS benchmark system H (except for very strongly damped suspensions) can be obtained. A cutoff frequency of $f_f \approx 25\,\text{Hz}$ is roughly the threshold, which enables an LBAS to perform similarly to the HBAS, particularly if the damping is adjustable. As presented in Chapter 2.4.2, an actuator bandwidth of approximately 5 Hz is already realized in a low bandwidth hydraulic active suspension system of production vehicles, the *Mercedes Benz ABC-system* [121].

6.4.4 Influence of damping

As pointed out by [138], the graphs in Figure 6.2 clearly show that damping has a significant influence on the performance, especially for low filter cutoff frequencies. Therefore, the right choice of the damping ratio is essential for the design of an LBAS.

The significant influence of the damping ratio is further illustrated in Figure 6.3 for an LBAS with a filter cutoff frequency of 3 Hz. The two graphs correspond to two different sets of controller weights $r_2 = q_{x_{cw}}$ and $r_3 = q_{x_{wg}}$ applied to the bandlimited system. These weights were originally computed for the designs H and H_1. Even though the weights differ strongly, the influence on the normalized rms-values is marginal for a wide range of damping ratios. The influence of the controller weights becomes more significant only for very low damping ratios.

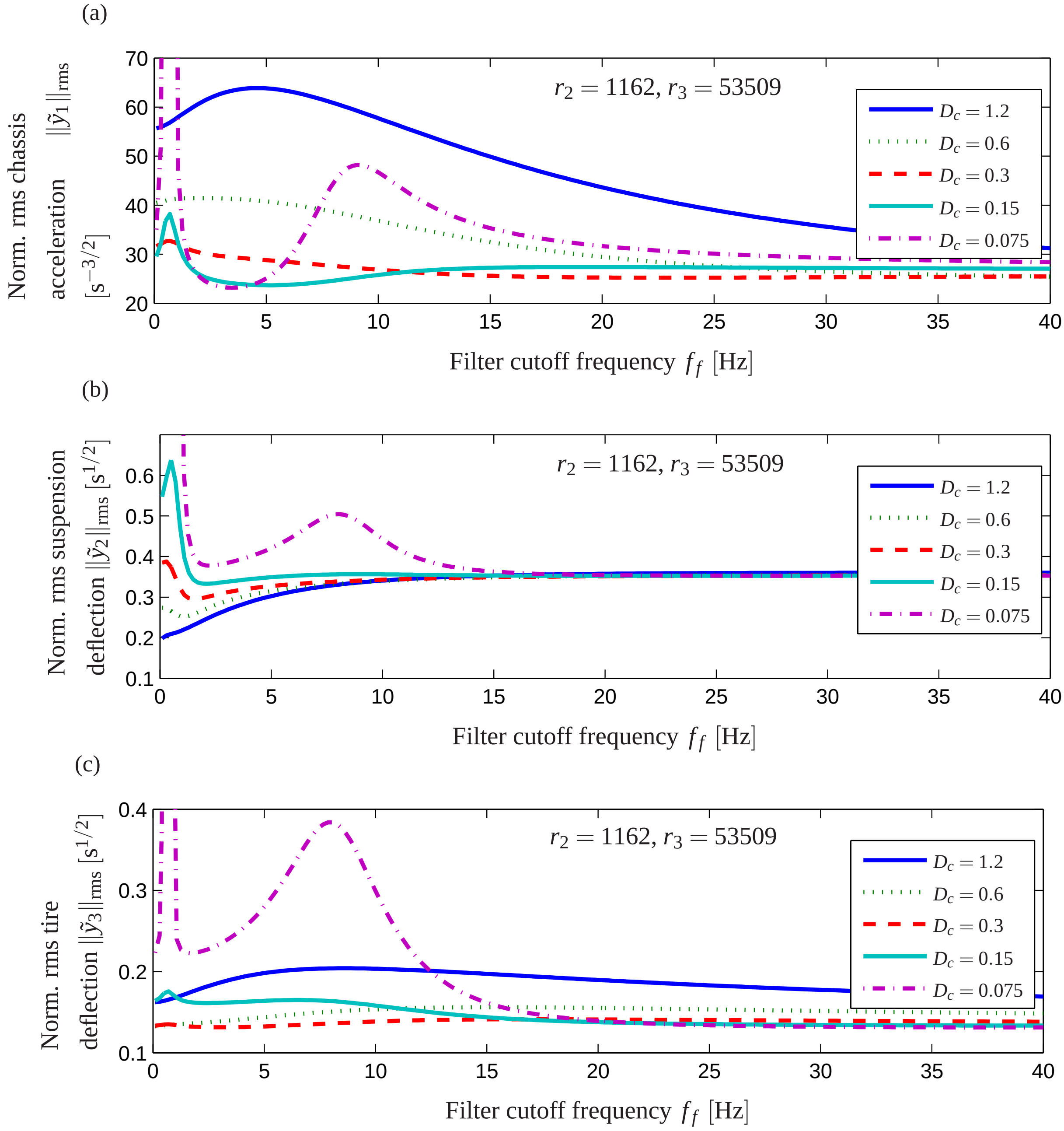

Figure 6.2: LBAS performance depending on f_c. (a) Chassis acceleration, (b) suspension deflection, (c) tire deflection.

6.5 Evaluation of achievable performance

In order to point out the potential of the hybrid suspension system by considering LBAS systems with continuously variable dampers, the results of Section 6.4 are now combined

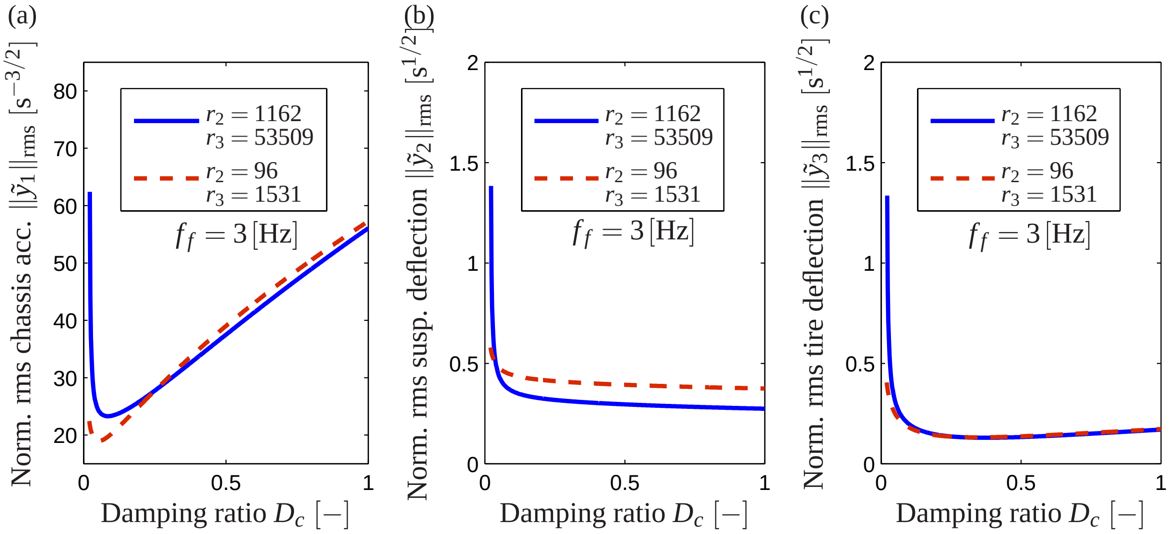

Figure 6.3: LBAS performance depending on D_c. (a) Chassis acceleration, (b) suspension deflection, (c) tire deflection.

in an iterative optimization of controller weights and damping ratio for the road excitation resulting from the disturbance model (see Section 6.4.1). The adaptation of the damping helps to increase suspension and tire deflection within tolerable bounds for the benefit of lower chassis acceleration.

6.5.1 Carpet plot based performance analysis

To find the optimal configuration for the considered road excitation, carpet plots in combination with damping plots like those of Figure 6.3 are used in an iterative optimization procedure. The considered carpet plots show the normalized rms chassis acceleration versus the normalized rms suspension deflection and the tire deflection, respectively. In order to systematically analyze the influence of the weights, one of the two weights (r_2 and r_3) is fixed at a constant value and the other one is varied over a wide range. By the resulting weighting net, a point in the carpet plot representing a specific suspension performance is assigned to a certain pair of weights. Figure 6.4 shows the carpet plots in their original form as they are obtained for the HBAS model shown in Figure 6.1 (right). The boundary of the weighting nets formed by the curves for $r_2 = 10^{-3}$ and $r_3 = 10^{-2}$ encloses the area of potential suspension performance achievable by varying the controller weights.

Because of the equivalence of the LBAS without the low pass filter and the HBAS derived in Section 6.2, very similar carpet plots are obtained for LBAS systems with very high filter cutoff frequencies. For lower actuator bandwidths, the parts of the weighting nets with low rms chassis acceleration and high rms tire and suspension deflection respectively (Figure 6.4) begin to ”fold upwards”, i.e. a performance degradation occurs (Figure 6.5). Parts of the weighting nets even tend to infinity. These instabilities occur because the control law is applied to the LBAS model including the low pass filter while it has been designed for the model without the filter (see also [138]). Figure 6.5 shows the carpet plots for an LBAS with a filter cutoff frequency of 3 Hz and a chassis damping ratio of $D_c = 0.30$. The plots still give good insights on the achievable performance of the LBAS in the relevant operating ranges where the limits on suspension and tire deflection are kept.

The carpet plots can be used to specify a target performance within the achievable area with respect to one of the constraints, i.e. maximum acceptable normalized rms tire deflection or suspension deflection. Then, an optimization process can be started to vary r_2 and r_3 until the specified performance is achieved within a predefined tolerance radius ε. Since it is only possible to specify a target performance in *one* of the plots, it is subsequently necessary to verify that the other constraint is not violated.

6.6 Performance results of the hybrid suspension system

The challenge is to find a setting for damping ratio and controller weights that minimizes the normalized rms chassis acceleration $||\tilde{y}_1||_{\mathrm{rms}}$ without violating the constraints $||\tilde{y}_{2,max}||_{\mathrm{rms}}$ and $||\tilde{y}_{3,max}||_{\mathrm{rms}}$ formulated in Section 6.4.1. This optimization usually is an iterative procedure because changing the damping ratio results in modified carpet plots and changing the controller weights results in new damping plots. Thus, the damping and the controller weights are optimized alternately until no further improvement can be obtained. Standard gradient based and direct search methods (see e.g. [12, 114]) are used for the optimization. The iterative optimization approach ensures performance improvement in each iteration step and is illustrated in the following for the considered road excitation.

A vehicle with parameters according to Table B.3 in the Appendix is equipped with an LBAS ($f_f = 3\,\mathrm{Hz}$) and a continuously variable damper. The vehicle speed is $v = 25\,\frac{\mathrm{m}}{\mathrm{sec}}$ and the road roughness coefficient is $A = 4.9 \cdot 10^{-6}\,\mathrm{m}$, which corresponds to a medium quality road [55].

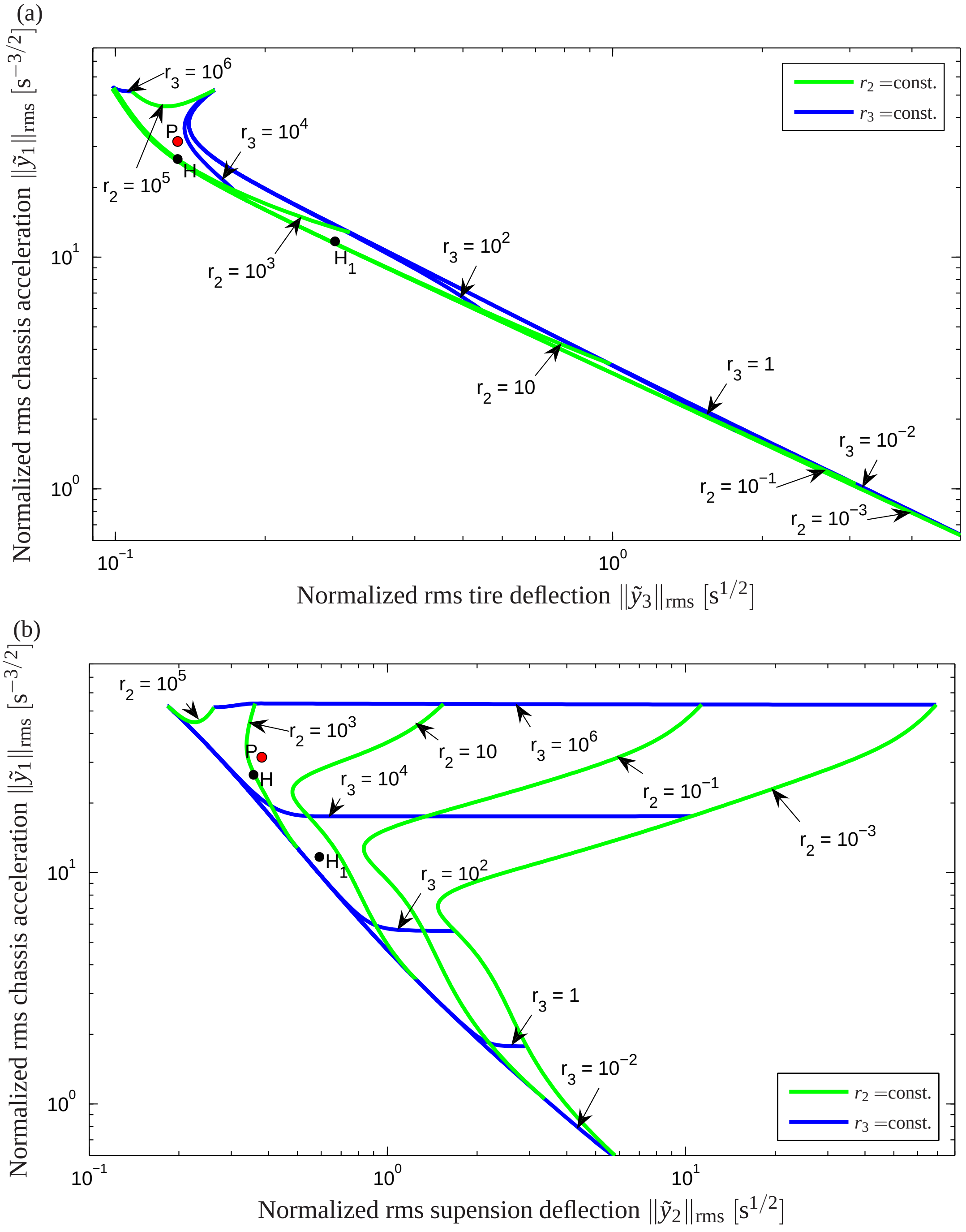

Figure 6.4: Carpet plots for an HBAS (with $r_2 = q_{x_{cw}}$ and $r_3 = q_{x_{wg}}$).

These are the road conditions, the controller parameters of the comfort benchmark system H_1 has been optimized for in Section 6.4.2. Moreover, the normalized constraints formulated

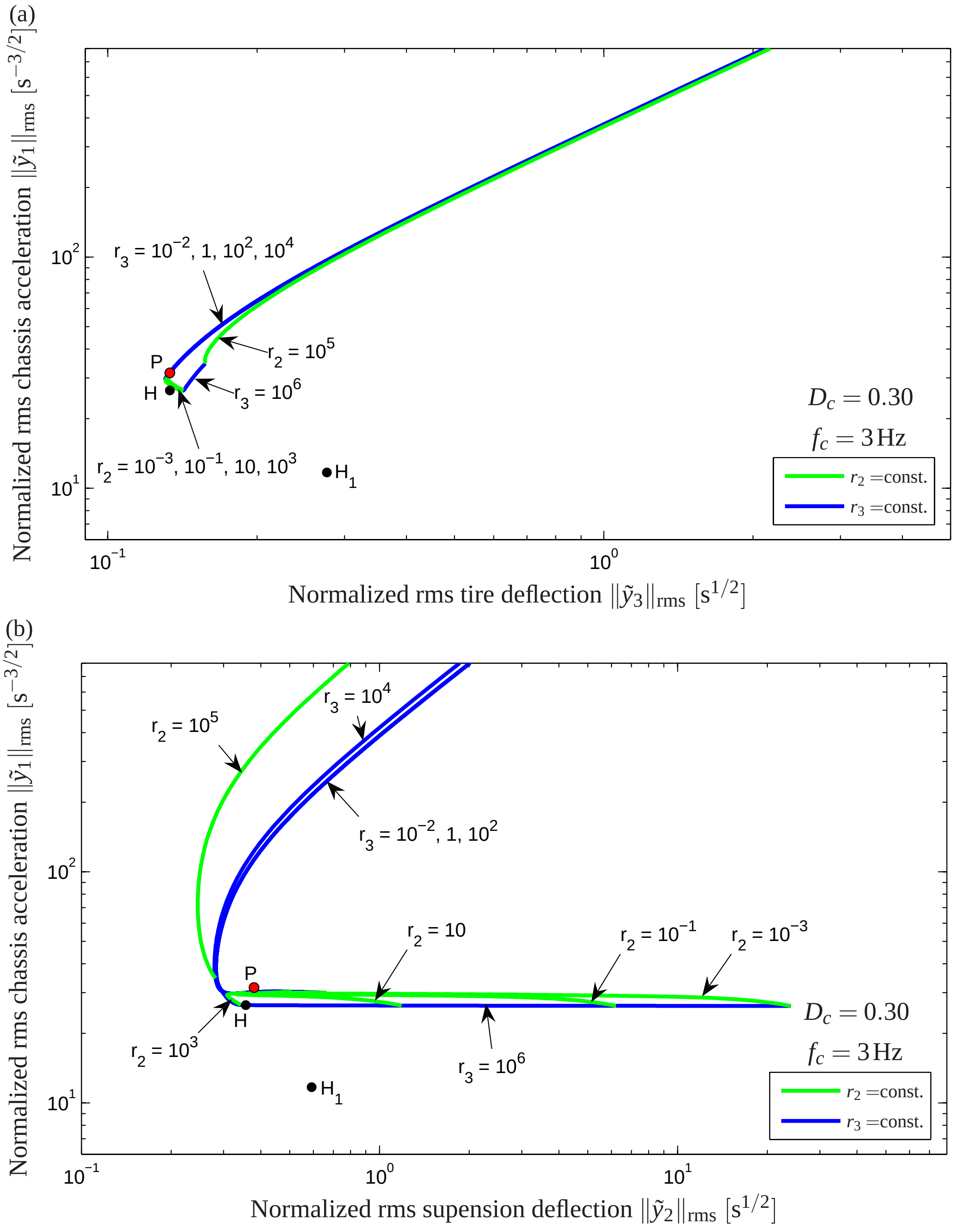

Figure 6.5: Carpet plots for an LBAS ($f_f = 3\,\text{Hz}$, $D_c = 0.30$ and $r_2 = q_{x_{cw}}$, $r_3 = q_{x_{wg}}$).

in Section 6.4.1 are considered. In Figure 6.6, 6.7 and 6.8 these limits are represented by a dashed line. The iterative optimization of controller weights and damping ratio for this driving

Table 6.2: Optimization results.

		I	$\xrightarrow{\text{DA1}} L_{1,a}$	$\xrightarrow{\text{CA1}} L_{1,b}$	$\xrightarrow{\text{DA2}} L_{1}$	
LQR-weights	$r_2 = q_{x_{cw}}$	1162	1162	0.0016	0.0016	
	$r_3 = q_{x_{wg}}$	53509	53509	241	241	
Damping ratio	D_c	0.3	0.085	0.085	0.048	
Performance objectives	$\|\|\tilde{y}_1\|\|_{\text{rms}}$	29.62	23.29	19.09	18.04	$\left[\text{s}^{-3/2}\right]$
	$\|\|\tilde{y}_2\|\|_{\text{rms}}$	0.31	0.37	0.44	0.48	$\left[\text{s}^{1/2}\right]$
	$\|\|\tilde{y}_3\|\|_{\text{rms}}$	0.13	0.22	0.19	0.25	$\left[\text{s}^{1/2}\right]$
Control Input	$\|\|\tilde{u}\|\|_{\text{rms}}$	0.27	0.35	0.39	0.39	$\left[\text{s}^{1/2}\right]$
Comf. gain vs. initial (I)		0%	21.37%	35.55%	39.10%	
Comf. gain vs. passive (P)		6.15%	26.21%	39.51%	42.85%	

condition is shown in Table 6.2. As an initial setting, denoted by I, the controller weights and the damping ratio $D_c = 0.30$ of the benchmark system H are chosen. This design represents a feasible ”allround” setting, since it offers lower chassis acceleration than the passive system P at comparable levels of suspension and tire deflection (see Figure 6.5).

However, by introducing variable damping better adaptation to the driving conditions described above is possible. Thus, in the first iteration step DA1 (first damping adjustment) the damping ratio can be lowered to the acceleration minimum ($D_c = 0.085$) according to Figure 6.3. Without violating the constraints this results in design $L_{1,a}$. The new carpet plots for this setup (see Figure 6.6) clearly show that it is possible to further improve ride comfort by adapting the controller weights. Since all acceleration optimal controller weights result in the same tire deflection (see Figure 6.6(a)), the target performance for iteration step CA1 (controller adjustment) is specified in Figure 6.6(b) to assure that the constraint for the suspension deflection is not violated. The target performance corresponds to the minimum of the normalized rms chassis acceleration, which is $||\tilde{y}_1^*||_{\text{rms}} = 19.09\,\text{s}^{-3/2}$, and a normalized rms suspension deflection of $||\tilde{y}_2^*||_{\text{rms}} = 0.444\,\text{s}^{1/2}$. To reach this performance within a tolerance radius of $\varepsilon = 2 \cdot 10^{-4}$ in the logarithmical plot, the weights are calculated as shown in Table 6.2. The new intermediate design is denoted by $L_{1,b}$.

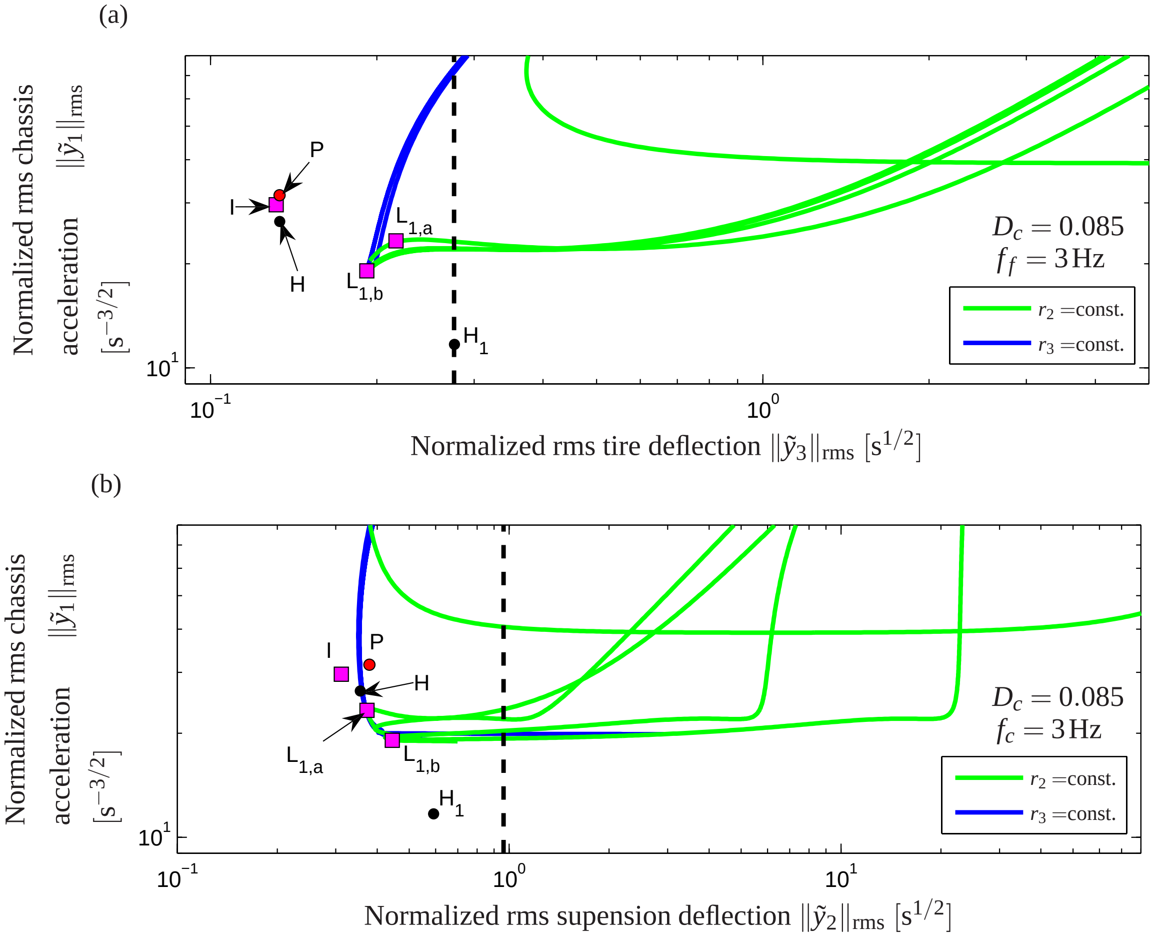

Figure 6.6: Carpet plots for an LBAS ($f_f = 3\,\text{Hz}$, $D_c = 0.085$).

In order to further improve the performance by adapting the damping in the next iteration step DA2 (second damping adjustment), the damping plots in Figure 6.7 are used. The acceleration optimal damping ratio $D_c = 0.048$ can be chosen and the new design L_1 results. As the new modified carpet plots in Figure 6.8 show, no further improvement is possible and hence L_1 is the final design.

To evaluate the ride comfort performance, the comfort gain

$$P_{g,\ddot{x}_c} = 1 - \frac{\|\tilde{y}_1\|_{\text{rms}}}{\|\tilde{y}_{ref,1}\|_{\text{rms}}} \tag{6.15}$$

is used (compare (2.24)). Therein, $\|\tilde{y}_1\|_{\text{rms}}$ is the normalized rms chassis acceleration of the hardware combination to be evaluated and $\|\tilde{y}_{ref,1}\|_{\text{rms}}$ is the rms chassis acceleration of a reference system (e.g. the passive system $\|\tilde{y}_{P,1}\|_{\text{rms}}$ or the initial LBAS setting $\|\tilde{y}_{I,1}\|_{\text{rms}}$).

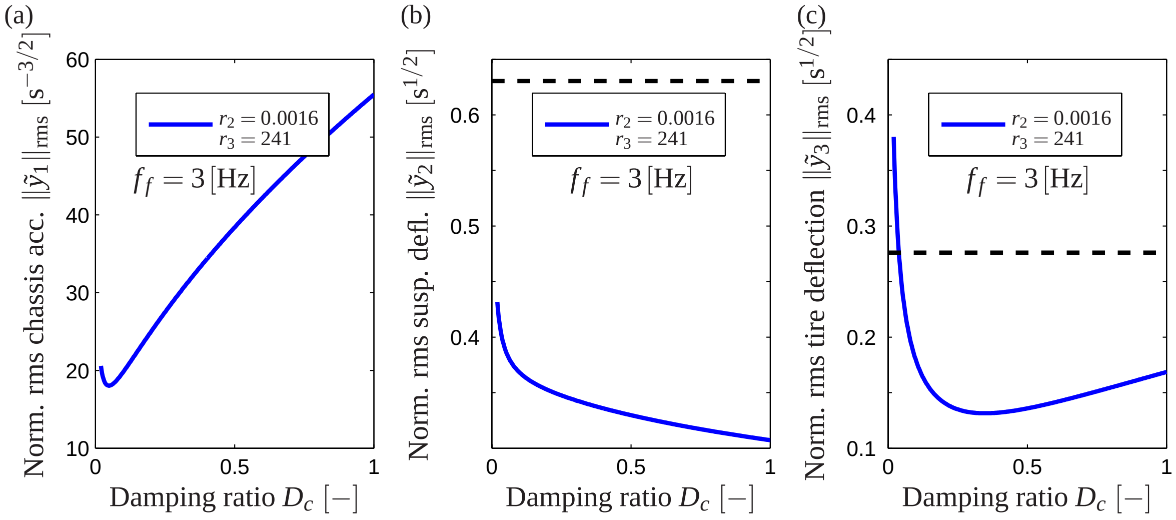

Figure 6.7: Damping plot for an LBAS ($f_f = 3\,\mathrm{Hz}$).

Applying this comfort gain definition, the iterative adaptation leads to a reduction of normalized rms chassis acceleration of more than 39% compared to the ”allround” LBAS I and approx. 43% with respect to the passive suspension P (see Table 6.2). The required damper spread is realizable with modern continuously variable dampers (see e.g. [16, 76]) and the actuator bandwidth of 3 Hz is realistic as well. Under the assumed operating conditions ($v = 25\,\frac{\mathrm{m}}{\mathrm{sec}}$ and $A = 4.9 \cdot 10^{-6}\,\mathrm{m}$), the rms-value of the actuator displacement is $\|u\|_{\mathrm{rms}} = \sqrt{2\pi A v} \cdot \|\tilde{u}\|_{\mathrm{rms}} = 0.0109$ m (see Section 6.4.1). Transforming it into a force value by multiplying with the suspension spring stiffness c_c yields an rms force value of 141.86 N, which is a feasible actuator force requirement.

For comparison, the performance of all benchmark systems is also marked in the carpet plots. As expected, the HBAS configuration H_1 can fully exploit one of the normalized rms-constraints (the rms tire deflection constraint) for the benefit of lower chassis accelerations. In contrast, a limit exists for the LBAS where increasing the suspension or tire deflection does no longer imply lower chassis accelerations (see Figure 6.8). The comfort gains of the benchmark systems H, H_1 and the LBAS with continuously variable damper L_1 compared to the

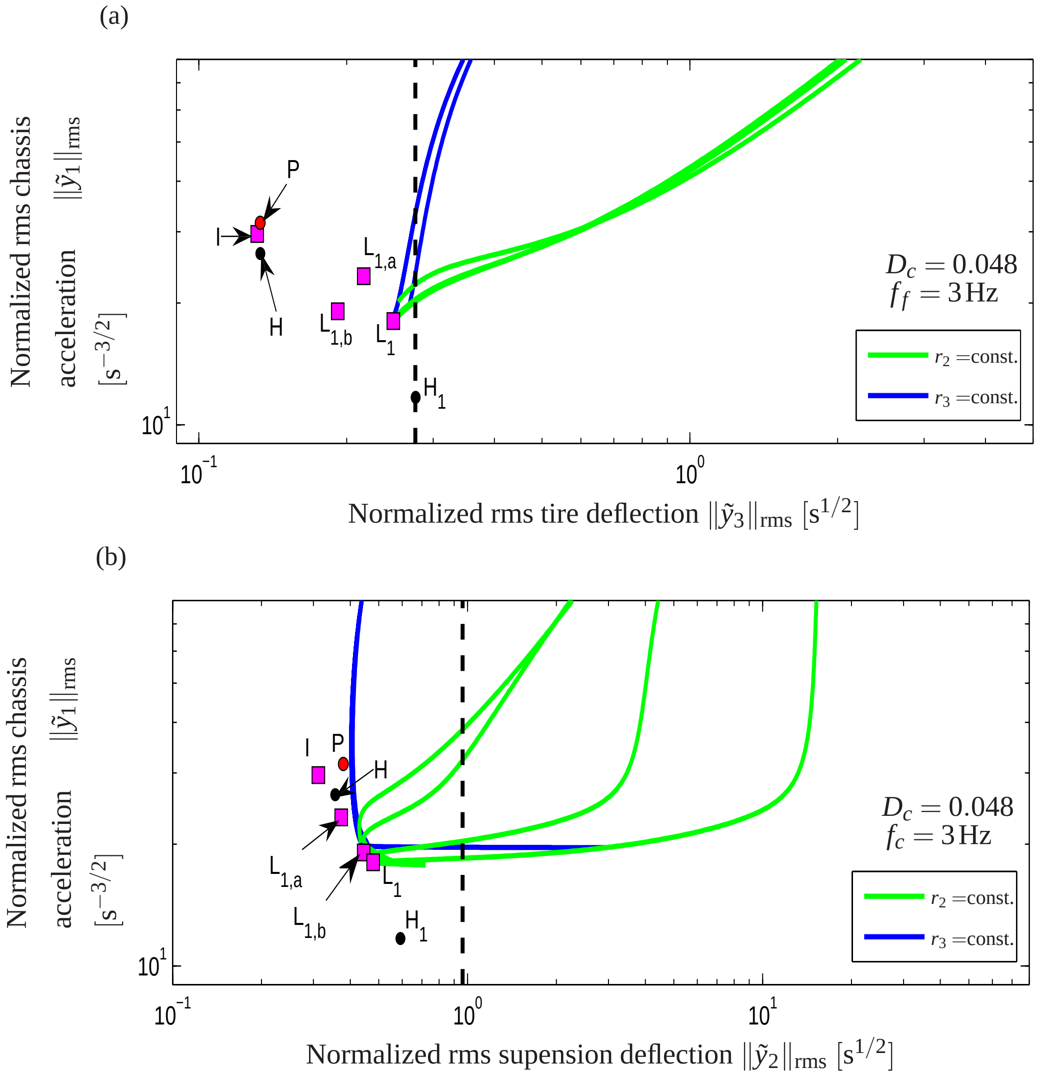

Figure 6.8: Carpet plots for an LBAS ($f_f = 3\,\mathrm{Hz}$, $D_c = 0.048$).

passive suspension are

$$P^{H}_{g,\ddot{x}_c} = 1 - \frac{\|\tilde{y}_{H,1}\|_{\mathrm{rms}}}{\|\tilde{y}_{P,1}\|_{\mathrm{rms}}} = 16\,\%\,, \tag{6.16}$$

$$P^{H_1}_{g,\ddot{x}_c} = 1 - \frac{\|\tilde{y}_{H_1,1}\|_{\mathrm{rms}}}{\|\tilde{y}_{P,1}\|_{\mathrm{rms}}} = 63\,\% \quad \text{and} \tag{6.17}$$

$$P^{L_1}_{g,\ddot{x}_c} = 1 - \frac{\|\tilde{y}_{L_1,1}\|_{\mathrm{rms}}}{\|\tilde{y}_{P,1}\|_{\mathrm{rms}}} = 43\,\%\,. \tag{6.18}$$

To achieve a performance similar to H_1 with an LBAS including a continuously variable damper (hybrid suspension system), a bandwidth of at least 25 Hz is required. Considering the lower hardware complexity, costs and energy demand of a hybrid suspension system, the achievable performance in ride comfort is nevertheless significant.

6.7 Discussion

It has been shown in a generalized framework in terms of the disturbance model and the consideration of normalized quantities, that the performance of a hybrid suspension configuration (low bandwidth active suspension systems with continuously variable damper) can be optimized by adapting the controller tuning and the damping ratio to the current driving state induced by the road excitation. Thereby, safety emphasizing settings improving the performance of passive systems as well as comfort oriented settings, located in performance regions otherwise only accessible to high bandwidth active suspensions, can be offered. In this context, the performance potential of the proposed hardware combination can be considered to be competitive to high bandwidth active systems. For the considered road excitation, a significant comfort increase of approx. 43% compared to the passive suspension has been reached by the hybrid suspension system with an actuator bandwidth of 3 Hz. Although the performance capabilities of low bandwidth active suspension systems with slowly adjustable damping have been indicated in [137] and [138], by the iterative optimization procedure presented in this Chapter and the comparison to benchmark systems it has been shown that even the performance of fully active suspensions can be approximated if a modern, fast semi-active damper is utilized in the hybrid suspension configuration. Moreover, todays availability of the actuator hardware proposed for the hybrid suspension configuration in modern vehicles guarantees feasibility of the concept.

In order to evaluate the performance in experiments, the realization of a hybrid suspension configuration is presented in the next Chapter. In Chapter 8 an appropriate adaptive control approach is introduced, that also utilizes carpet plots to infer the driving state optimal settings of the hybrid suspension.

Chapter 7

HYBRID SUSPENSION TEST RIG

In Chapter 6 it has been shown that a *hybrid suspension* system based on a continuously variable semi-active damper and a low bandwidth actuator integrated in series to the primary spring, offers significant performance potential. Moreover, it provides several advantages over fully active suspension concepts, e.g. lower costs due to the already available actuator components for production vehicles, a lower power demand due to the combined use of semi-active and active elements as well as packaging and weight advantages.

In order to validate the performance potential experimentally and to emphasize the realizability of the concept, a hybrid suspension is designed based on components from production vehicles (Section 7.1). Furthermore, a quarter-car test rig for the hybrid suspension is constructed (see Section 7.2), which is based on an automotive suspension of a modern upperclass vehicle, the *BMW 7 series* (model year 2009). A corresponding suspension model is presented in Section 7.3.

The hybrid suspension strut is used for identification experiments to derive models of the two integrated actuators and adequate actuator control approaches (Section 7.4). Based on the resulting realistic model of a hybrid quarter-car setup, a new adaptive suspension control technique is presented in Chapter 8.

7.1 Design of a hybrid suspension system

To emphasize the realizability of the hybrid suspension system, a realistic framework regarding the actuators and the sensor architecture is desired. Therefore, primarily stock components from the production vehicles are used for the design of the hybrid suspension.

The actuator components of the hybrid suspension system are depicted in Figure 7.1. A modern continuously variable hydraulic damper from the *BMW 7 series* (model year 2009) is used as semi-active damper and a hydraulic suspension actuator from a *Mercedes SL roadster* (model year 2003) is integrated in series to the primary spring.

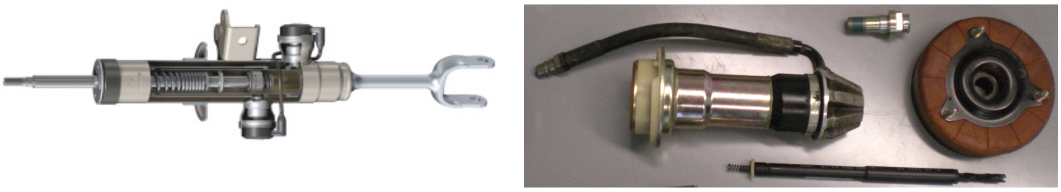

Figure 7.1: Continuously variable damper (*BMW 7 series*, see also [1]) and actuator components from the hydraulic *Mercedes Benz - Active Body Control* suspension system. The left image is courtesy of *ZF Friedrichshafen AG* and is reproduced with kind permission.

7.1.1 Hydraulic suspension actuator

A pump, which also supplies the hydraulic cylinder driving the test rig, is used as power supply for the actuator. Since one aspect for the experiments is to study the effect of the actuator bandwidth (see also Chapter 6.4.3), an external valve block (Figure 7.2) with an industrial servovalve is employed for the control of the hydraulic suspension actuator. Thus, also experiments with a higher bandwidth than the original bandwidth of the *ABC-system* (5 Hz) can be realized (see also Section 7.4.1).

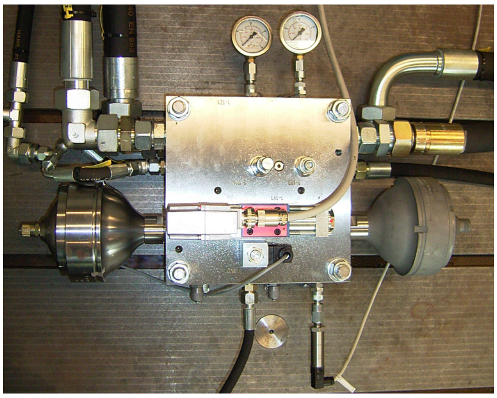

Figure 7.2: Valve block with pressure accumulators and servovalve.

The valve block has integrated pressure accumulators for the supply and the return lines as well as a pressure sensor in the supply line of the actuator (the original *ABC-system* also uses a pressure sensor for the control of the hydraulic actuator [121]). The supply pressure of the valve block has a nominal value of 200 bar, however, the pressure is adjustable by a pressure reduction valve. The -3dB-cutoff frequency of the servovalve is approx. 105 Hz considering a valve pressure drop of 140 bar and $\pm 25\,\%$ valve opening [107].

7.1.2 Continuously variable damper

The semi-active damper is a continuously variable hydraulic damper with separate valves for compression and rebound direction. In the vehicle the damper is controlled via a *FlexRay* bus (see [60]). In the considered application of the hybrid suspension system, the damper control is realized by an external power electronic unit, that offers BNC connectors for two analog input voltage signals ($\mathbf{u}_{v,cvd} = [\ u_{v,cvd,c} \quad u_{v,cvd,r}\ ]^T$ proportional to the setpoints of the two valve currents $\mathbf{i}_d^* = [\ i_{d,c}^* \quad i_{d,r}^*\ ]^T$ for compression and rebound of the damper strut) and provides as output signals the actual currents in the two valves. More details of the damper characteristics are given in Section 7.4.2.

7.1.3 Setup of the hybrid suspension strut

The further mechanical components for the automotive quarter-car test rig (double wishbone struts, steering rod, wheel) are taken from the *BMW 7 series*. Consequently, the parameters of the chassis mass are chosen accordingly so that the suspension concept reflects an upperclass limousine (see Table B.4 in the Appendix). For the realization of the hybrid suspension strut (Figure 7.3), it must be considered that the kinematic relations of the suspension as well as the suspension characteristic of the *BMW 7 series* are maintained. This is realized by using computer aided design (CAD) tools for the design of the hybrid suspension strut and the test rig.

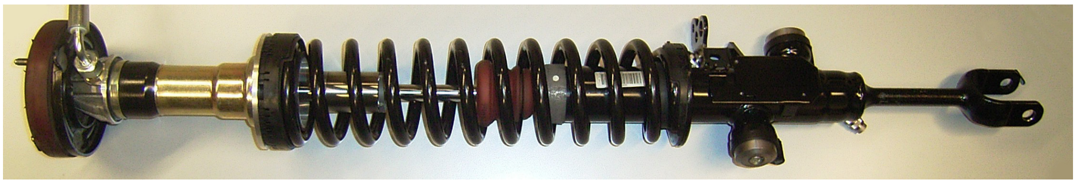

Figure 7.3: Realization of the hybrid suspension.

The hydraulic actuator strut (Figure 7.1 (right)) is fixed on the semi-active damper by a connection element. Since the original suspension of the *Mercedes SL roadster* has a lower transmission ratio i than the *BMW 7 series* suspension and a stiffer spring (due the more sportive vehicle characteristic and the transmission ratio), the original *Mercedes Benz* primary spring is not suitable for the hybrid suspension configuration. The *BMW* spring does not offer sufficient suspension deflection to preserve the kinematics of the original suspension for the maximum actuator displacement of $\pm 4\,\text{cm}$. Therefore, a new spring is integrated, which exhibits the same stiffness characteristic and resulting suspension deflection limits as the original *BMW* spring so that the suspension tuning and the relevant kinematic relations are equivalent to the original configuration.

7.2 Automotive quarter-car test rig

The quarter-car test rig (Figure 7.4) is designed using parameters of the *BMW 7 series* (model year 2009), which represents an upperclass vehicle. The sprung mass is $m_c = 507\,\text{kg}$ and the unsprung mass is $m_w = 68\,\text{kg}$ resulting in a static wheel load of $F_{stat} = 5641\,\text{N}$. The test rig is mounted on a steel plate, which rests on 16 airsprings in order to isolate the building from the test rig vibrations. The sprung mass is guided vertically by a parallel kinematics mounting to reduce friction forces. A highly dynamic hydraulic actuator is used to excite the tire vertically and thus simulates the road excitation.

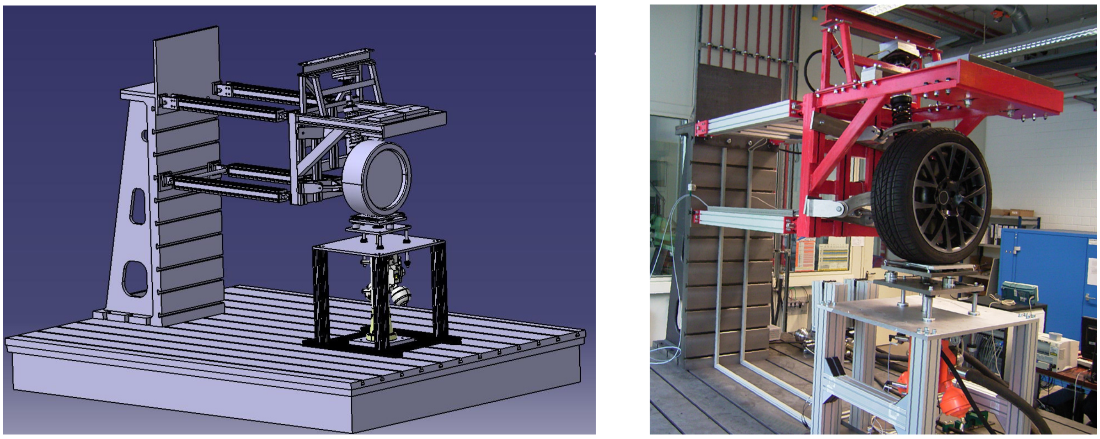

Figure 7.4: CAD-concept (left) und realization (right) of the hybrid suspension test rig.

In order to minimize structural vibrations of the chassis mass within the frequency range of interest, finite element methods (FEM) and a modal analysis of the steel construction have been employed already in the design phase of the test rig and the design of the structure has been optimized accordingly [113]. As a result, the first relevant eigenmodes (vertical bending of the front struts) of the chassis mass structure appear at approx. 51 Hz, which is well above the frequency range of interest for suspension control ($0 - 25\,\mathrm{Hz}$). The integration of the hybrid suspension into the quarter-car test rig is shown in Figure 7.5. The kinematic relations of the original *BMW 7 series* suspension configuration including the deflection depending transmission factor (see [102]) are preserved.

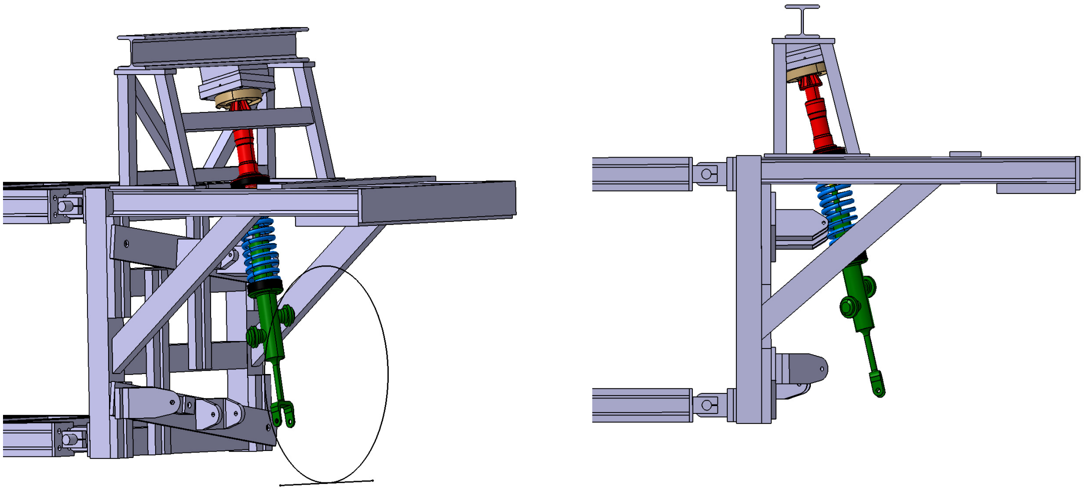

Figure 7.5: Integration of the hybrid suspension strut into the test rig.

7.2.1 Sensor architecture

The following measurement signals are provided at the test rig:

1. Chassis acceleration: $\ddot{x}_c(t)$ is measured by a capacitive accelerometer with a measurement range of ±10g.

2. Wheel acceleration: $\ddot{x}_w(t)$ is measured by a capacitive accelerometer (measurement range ±50g).

3. Suspension deflection: $x_c(t) - x_w(t)$ is recorded by the original encoder from the *BMW 7 series*.

4. Deflection of the suspension actuator: $\Delta x_{hy}(t)$ is measured by the original encoder inside the hydraulic actuator of the *Mercedes Benz ABC-system*.

5. Pressure in the supply chamber of the suspension actuator: $p_c(t)$ is measured by a piezo-electric pressure transducer.

6. Damper current: The valve currents for rebound and compression $\mathbf{i}_d(t) = [\ i_{d,c}(t) \quad i_{d,r}(t)\ ]^T$ are provided by the power electronic unit of the damper.

7. Wheel load: $F_w(t) = F_{dyn}(t) + F_{stat}$ is measured by three resistance strain gauge based force sensors and a strain gauge amplifier unit summing their signals.

8. Road displacement: $x_g(t)$ is measured by an incremental encoder integrated in the hydraulic cylinder of the test rig.

The sensor architecture for the signals, which are used for suspension control (items 1-6 of the above enumeration), is similar to the configuration integrated in the considered vehicles[1].

7.2.2 Signal processing

The real-time application is controlled utilizing a *dSpace DS1103 PPC Controller Board* integrated into a PC (*Intel Core2 CPU 6420* (2.13 GHz) and 3.24 GB RAM) and the software *dSpace Control Desk*. The system operates with a sampling frequency of $f_s = 1\,\text{kHz}$ for the suspension control experiments. For the signal processing, similar filter configurations (hardware and software filters) to those described in Chapter 3.2.3 are used for the analog measurement signals.

---

[1] The original accelerometers of the *BMW 7 series* have been replaced since their electrical interface is designed for a *FlexRay* bus architecture, which is not used at the proposed test rig.

7.3 Nonlinear suspension model

The model structure is similar to the test rig model presented in Chapter 3.3 (see (3.12)-(3.13)). However, more detailed models for secondary spring effects by endstops, suspension kinematics and the characteristic of the tire are considered for the automotive suspension since the relevant data could be provided by an industry partner. However, it is noted that the scalings in the Figures 7.6, 7.8 and 7.11 are omitted due to a confidentiality agreement.

7.3.1 Component characteristics

Primary spring and secondary spring effects

The primary spring is a steel spring with a linear characteristic. Moreover, an additional elastomer buffer is integrated into the suspension strut to provide a softer compression endstop. A spring inside the damper accomplishes this task for the rebound endstop. Thus, the resulting suspension force deflection characteristic becomes progressive if the suspension operates in a range where the buffers are compressed. Figure 7.6 shows the resulting spring characteristic in the coordinates of the quarter-car model, i.e. including the kinematics of the suspension described later in this Section. The limits for the suspension deflection are $\underline{x}_{cw} = -10\,\text{cm}$ in compression and $\overline{x}_{cw} = 11\,\text{cm}$ in rebound direction.

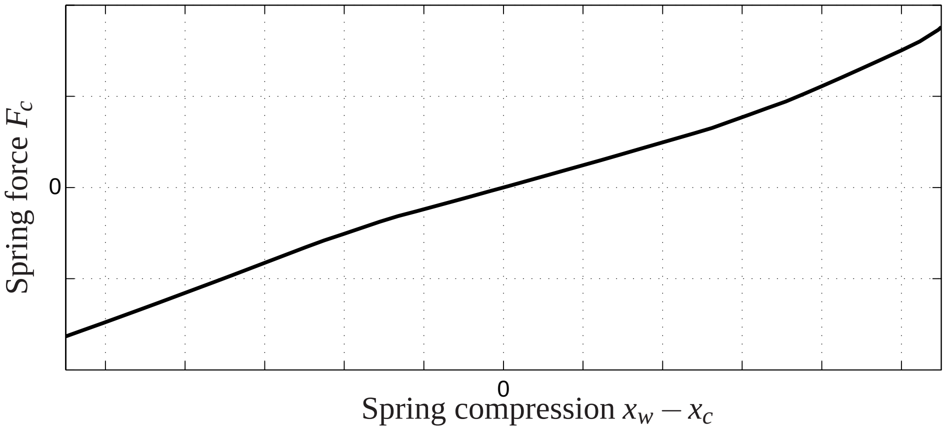

Figure 7.6: Suspension spring characteristic including primary and secondary spring effects and the suspension kinematics (visualized in the coordinates of the quarter-car model).

Suspension kinematics

The kinematics of the considered double wishbone suspension are mainly defined by the geometry of wishbone struts and the inclined assembly of the suspension strut (see also Chapter 3.3.2). Due to the change of the inclination of the suspension strut during suspension deflection, the kinematic transmission factor i_c defined in (3.8) of the considered suspension system changes depending on the suspension deflection according to

$$i_c(t) = \frac{\dot{x}_{el}(t)}{\dot{x}_c(t) - \dot{x}_w(t)} = i_0 - \frac{\Delta i}{\Delta x_{cw}}(x_c(t) - x_w(t)), \tag{7.1}$$

where x_{el} denotes the deflection of the damper, i_0 is a constant transmission factor and $\frac{\Delta i}{\Delta x_{cw}}$ denotes a constant term defining the linear change of the kinematic transmission factor (see also [102]). As a result of the concentric configuration of the suspension strut, the transmission ratio is the same for the spring and the damper.

Tire characteristics

Since more detailed measurement data describing the tire dynamics has been available, a more detailed tire model is employed for the simulation model of the hybrid suspension. Although in general the tire damping is small compared to the damping induced by the hydraulic damper (see Chapter 2.1), the tire has a complex dynamic behavior [106]: Its damping decreases with rising excitation frequencies and also the stiffness of the tire increases with the excitation frequency (the resulting stiffness is also known as “dynamic stiffness”). Figure 7.7 (left) shows this frequency dependent tire model. Another representation of this tire model is the Gehmann-Model depicted in Figure 7.7 (right) [106]. The Gehmann-Model represents the tire as a parallel connection of a spring (stiffness c'_w) and a series connection of a spring (stiffness c') and a damper (damping coefficient d'_w). To visualize the dynamic behavior of the Gehmann-Model with a linear stiffness c'_w, the resulting frequency dependent tire stiffness and damping are shown in Figure 7.8 (with $c_{w,max} = c'_w + c'$).

For the notation of the nonlinear quarter-car model in Section 7.3.2, the model representation involving $c_w(\omega)$ and $d_w(\omega)$ is used to keep the order $n = 4$ for the nonlinear quarter-car model of the hybrid suspension (without the actuator dynamics). For the implementation of the tire model an equivalent approach is employed that uses a first order lag element to express the

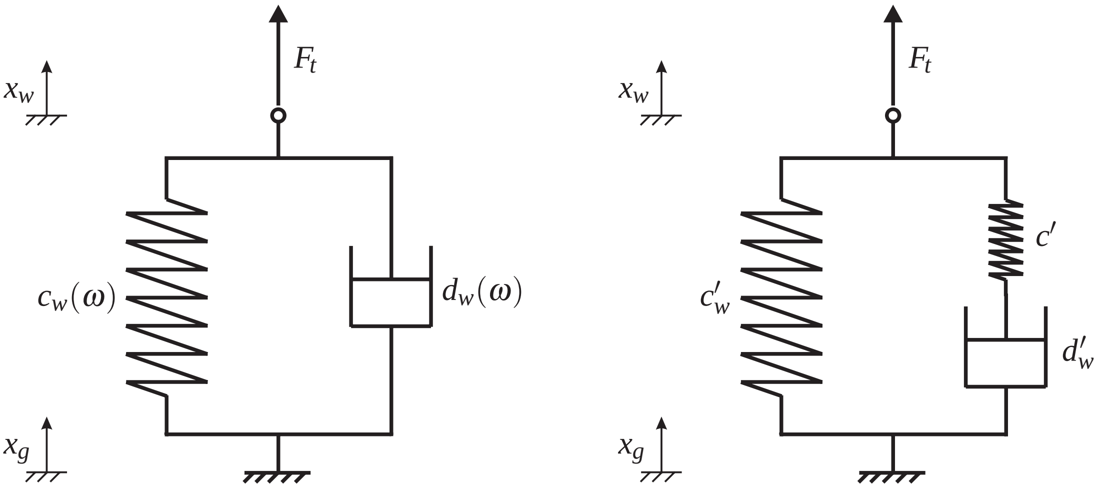

Figure 7.7: Frequency dependent tire stiffness and damping (left) and structure of the Gehmann-Model for the tire dynamics (right).

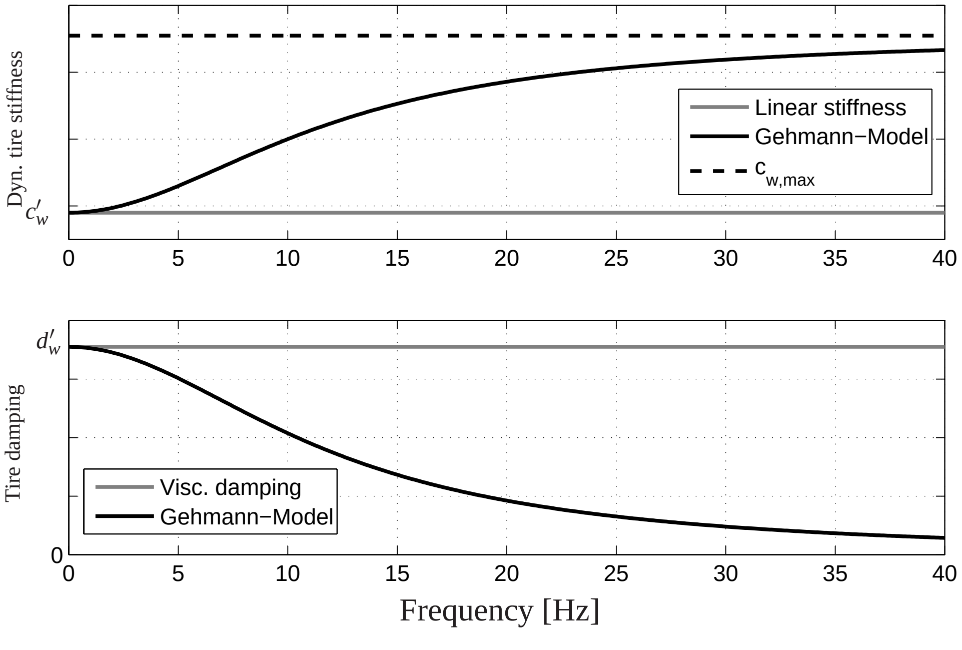

Figure 7.8: Frequency dependent tire stiffness and damping resulting from the Gehmann-Model (linear scaling).

frequency dependent damping force of the tire $F_{d,t}$, i.e.

$$\dot{F}_{d,t} + \frac{c'}{d'_w} F_{d,t} = c'(\dot{x}_g - \dot{x}_w) \,. \tag{7.2}$$

Moreover, for the considered tire the stiffness c'_w is not constant since the static force deflection characteristic is quadratic (similar to the tire force deflection characteristic of the quadricycle presented in Figure 3.6). Hence, the force resulting from this stiffness characteristic can be represented by the polynomial force

$$F_{c,t} = c_{w,lin}(x_g - x_w) + c_{w,quad}(x_g - x_w)^2 \,. \tag{7.3}$$

The resulting tire force is

$$F_t = F_{c,t} + F_{d,t} \,. \tag{7.4}$$

Friction effects

Coulomb friction effects in the suspension struts have been indentified experimentally and are taken into account for the modeling in the same manner as described in Section 3.3.2. The resulting friction model for the suspension friction is

$$F_f = \hat{F}_f \tanh\left(k_f\,(\dot{x}_c - \dot{x}_w)\right) \tag{7.5}$$

with the maximum friction force $\hat{F}_f = 65\,\mathrm{N}$ and the scaling factor $k_f = 1250\,\frac{\mathrm{sec}}{\mathrm{m}}$. The friction force of the parallel kinematic guides for the chassis mass has been identified to be less than 10 N and is thus neglected in the model.

7.3.2 Resulting suspension model

The described models of the tire, the kinematics and friction effects are integrated into a quarter-car model of the complete suspension setup (without the actuator dynamics). The state vector **x** and the output vector **y** are chosen correspondingly to (2.3) and (2.6) as

$$\mathbf{x} = \begin{bmatrix} x_c - x_w, & \dot{x}_c, & x_w - x_g, & \dot{x}_w \end{bmatrix}^T , \tag{7.6}$$

$$\mathbf{y} = \begin{bmatrix} \ddot{x}_c, & F_{dyn}, & x_c - x_w \end{bmatrix}^T . \tag{7.7}$$

With the control inputs actuator displacement $u_{hy}(t) = i_c(t)\,(x_c(t) - x_{act}(t)) = \Delta x_{hy}(t)$ and semi-active damper force $u_{cvd}(t) = F_d(t)$ as well as the disturbance input $u_d(t) = \dot{x}_g(t)$ defined in (2.5), the quarter-car model of the hybrid vehicle suspension system can be expressed as a fourth-order state space model in the form

$$\dot{\mathbf{x}}(t) = \mathbf{f}(\mathbf{x}(t), u_{hy}(t), u_{cvd}(t), u_d(t)) \,, \tag{7.8}$$

$$\mathbf{y}(t) = \mathbf{g}(\mathbf{x}(t), u_{hy}(t), u_{cvd}(t)) \tag{7.9}$$

with $\mathbf{f} \in \mathbb{R}^{4\times1}$ and $\mathbf{g} \in \mathbb{R}^{3\times1}$. It is noted that the model includes the frequency dependent tire stiffness and tire damping given by the Gehmann-Model. The model structure is similar to the model of the test rig described by (3.12) - (3.13) in Chapter 3. The differences can be summarized as follows:

1. The spring characteristic (in the coordinates of the quarter-car model) is nonlinear.
2. The tire damping and stiffness are frequency dependent.
3. The kinematic transmission factor $i_c(t)$ changes linearly with $x_{cw}(t)$ (see (7.1)).
4. The actuator dynamics are not integrated into the quarter-car model (7.8) - (7.9).
5. The small friction force due to the chassis mass guides is neglected.

The accuracy of the model is quantified by using the performance index defined in (3.14). The resulting values of the performance index for the excitation of the passive automotive quarter-car test rig with road profile P1 ($v_{p1} = 50\,\frac{\text{km}}{\text{h}}$) are summarized in Table 7.1 and the model matching is visualized for this road profile in Figure 7.9. The accuracy of the model is comparable to the model of the fully active suspension test rig (Chapter 3.3.3).

Table 7.1: Performance indices of the nonlinear model (for road profile P1, $v_{p1} = 50\,\frac{\text{km}}{\text{h}}$).

Signal	Performance index Φ
Suspension deflection x_{cw}	0.818
Chassis acceleration $\ddot{x}_c$	0.917
Dyn. wheel force F_{dyn}	0.930
Wheel acceleration $\ddot{x}_w$	0.831

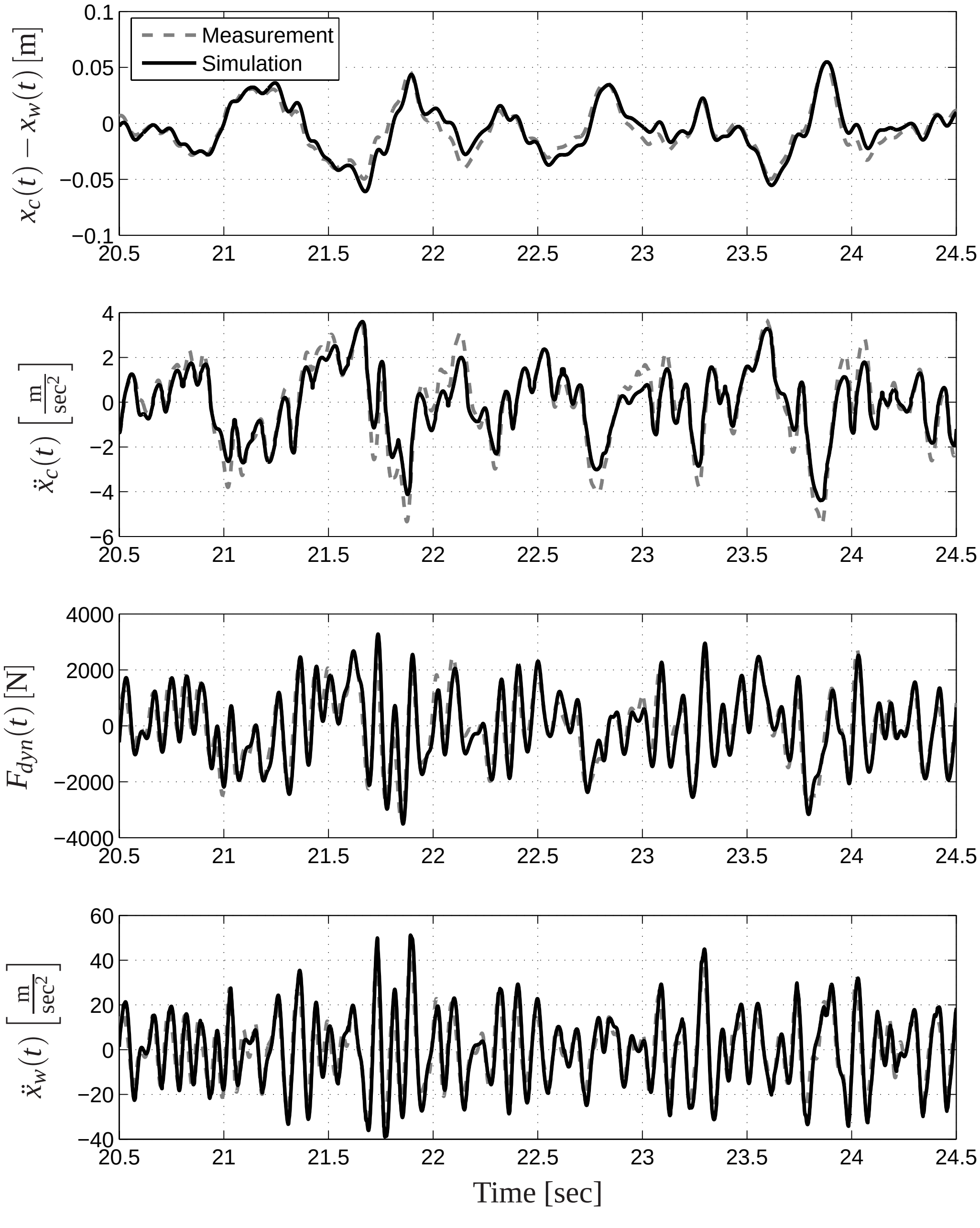

Figure 7.9: Model validation: Simulation and measurement data for excitation with road profile P1 ($v_{p1} = 50\,\frac{\text{km}}{\text{h}}$).

7.4 Actuator modeling and control

Actuator models are required for the simulation and for the design of the tracking controllers for $u_{hy}(t)$ and $u_{cvd}(t)$, respectively. The actuator dynamics are modeled by means of system identification and grey-box modeling techniques (see e.g. [94]). In the context of this Thesis, the closed loop dynamic behavior of the actuators is of primary interest for the simulations and performance evaluation of the higher level suspension controller presented in Chapter 8. Therefore, only the model of the controlled hydraulic actuator is presented in Section 7.4.1 and literature sources for the system identification procedures and the actuator controller design are given. For the modeling and control of the damper a simple but sufficiently accurate and well implementable approach is presented in Section 7.4.2.

7.4.1 Hydraulic actuator

A detailed nonlinear seventh-order model for the hydraulic actuator, similar to the one presented in [7], is employed for the design of the actuator controller. The model relates the pressure dynamics with the oil flow and also takes into account the influence of the tubes and the valve. Details of the system identification process and the nonlinear model of the actuator are given in [124].

The deflection $u_{hy}(t)$ of the hydraulic actuator is controlled by a voltage applied to the servovalve. In order to achieve the required minimum bandwidth of 5 Hz, which resembles the setting of the original *ABC-system*, the controller structure involves feedforward control for the actuator velocity as well as a PI-feedback controller for the actuator position. The control valve of the actuator offers a higher bandwidth (see Section 7.1.1) than the stock component of the vehicle. Thus, in order to be able to compare the influence of different bandwidths of the controlled actuator, a first-order low pass filter is used for the reference signals for the actuator position and velocity. The default cutoff frequency of the lowpass filter is $f_{hy} = 5\,\mathrm{Hz}$ as this represents the bandwidth of the original *ABC-system* [121]. Since the oil flow through the valve depends nonlinearly on the pressure drop, which in return depends on the spring force of the suspension, the measurement of the pressure p_c inside the actuator is used to compensate this nonlinearity of the servovalve's flow characteristic accordingly (see [124] for details on the actuator controller design). The PI-controller parameters are fine-tuned experimentally so that a well damped transient behavior is achieved.

The controlled actuator can be modeled as a second-order system (as proposed in [81], [82]). The dynamic behavior of the valve block (see Section 7.1.1) is considered in the model by a time delay of $T_d = 3\,\mathrm{msec}$, which is approximated by a first-order Padé-approximation. The resulting model is

$$\dot{\mathbf{x}}_{hy}(t) = \begin{bmatrix} -\omega_{hy} & 0 \\ \frac{1}{T_d} & -\frac{1}{T_d} \end{bmatrix} \mathbf{x}_{hy}(t) + \begin{bmatrix} \omega_{hy} \\ 0 \end{bmatrix} u^*_{hy}(t)\,, \tag{7.10}$$

$$u_{hy}(t) = \begin{bmatrix} 0 & 1 \end{bmatrix} \mathbf{x}_{hy}(t) \tag{7.11}$$

with the state vector of the controlled actuator $\mathbf{x}_{hy}(t)$, the reference actuator displacement $u^*_{hy}(t)$ and the filter bandwidth $\omega_{hy} = 2\pi f_{hy}$. As depicted in a comparison with measurement data (Figure 7.10), the model describes the dynamics of the closed loop system well for the default bandwidth of the reference signal filter ($\omega_{hy} = 2\pi \cdot 5\,\frac{\mathrm{rad}}{\mathrm{sec}}$). Hence, the model is employed in the simulation model of the test rig.

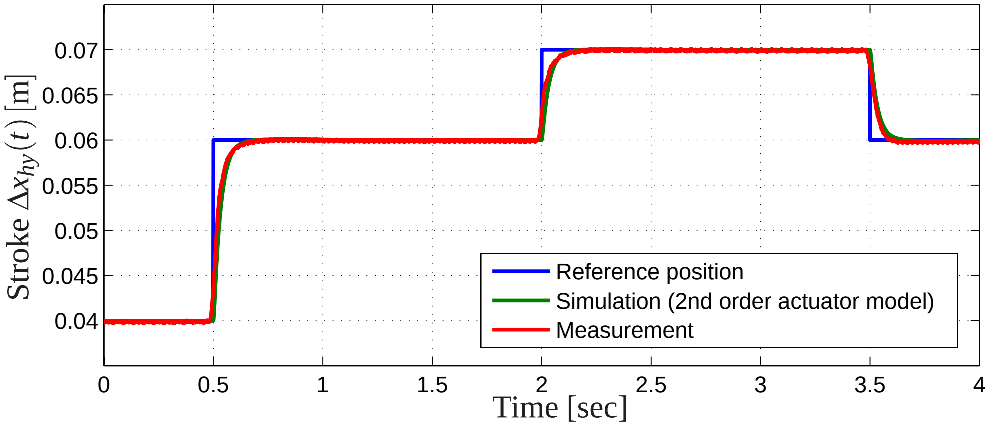

Figure 7.10: Comparison between measurement data and linear second order model for an actuator bandwidth of $\omega_{hy} = 2\pi \cdot 5\,\frac{\mathrm{rad}}{\mathrm{sec}}$.

7.4.2 Continuously variable damper

The characteristic of the semi-active damper can be adjusted by the valve currents $\mathbf{i}_d = [\begin{array}{cc} i_{d,c} & i_{d,r} \end{array}]^T$ for compression and rebound of the damper strut. If $\mathbf{i}_d = [\begin{array}{cc} 0\,\mathrm{A} & 0\,\mathrm{A} \end{array}]^T$, the hardest characteristic is activated, which represents a fail safe mode. The damper characteristic of the passive benchmark suspension is chosen to result from the damper currents

$\mathbf{i}_d = [\ 1.2\,\mathrm{A} \quad 1.2\,\mathrm{A}\ ]^T$ since the resulting damping ratio of $D_c = 0.21$ is representative for an upperclass vehicle [50, 106].

Although a complex modeling approach based on physical insight for the dynamic behavior of the semi-active dampers has been studied in [118], a more transparent, controller design oriented modeling approach for the damper is intended. The static characteristic (excluding hysteresis effects) of the semi-active damper has been obtained from measurements (Figure 7.11 (left)). It maps the damper velocity $\dot{x}_c - \dot{x}_w$ and the valve currents $\mathbf{i}_d$ to the static damper force $F_{d,s}$ (see also [26, 27]).

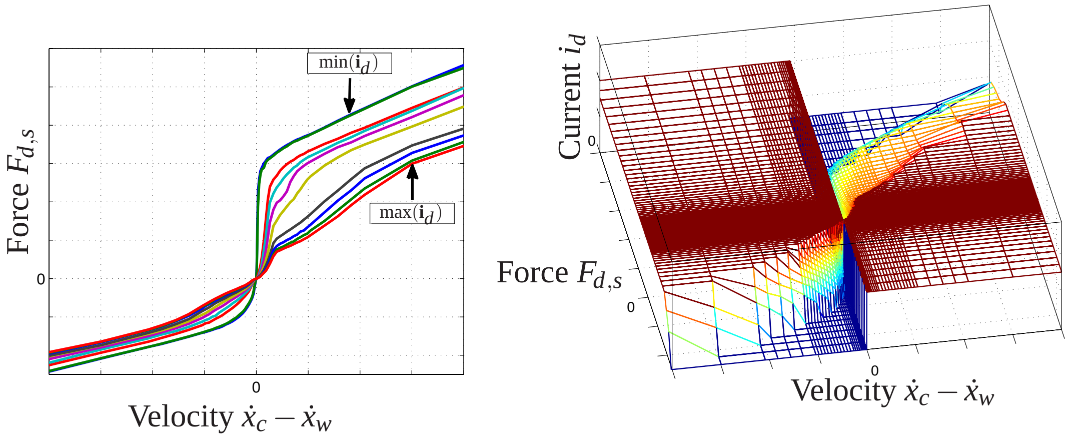

Figure 7.11: Semi-active damper characteristics (left) and its inverse as 3D-diagram (right).

The dynamic behavior of the semi-active damper is determined by two main aspects:

- Due to the hydraulic properties of the damper and the inertia of the oil, the measured damper force has a time lag compared to the damper force calculated from the static damper characteristic and the measured relative damper velocity [118]. Although the resulting mechanical time constant differs for distinct operating modes of the damper (see e.g. [118]), a first-order low pass filter with a mechanical time constant of 10 msec (obtained from averaging over different measurements) describes the dynamic behavior of the damper sufficiently accurate for the simulation model.
- Furthermore, the magnetic valves of the damper are actuated by the valve currents, which are influenced by the inductance of the valve and the properties of the power

electronic unit. The tracking control of the desired damper current is accomplished by an internal PI-controller of the power electronic unit. As can be seen in the step response of the valve current (Figure 7.12 (lower)), the resulting current dynamics can be approximated well by a first-order low pass filter with a small time constant of 1 msec.

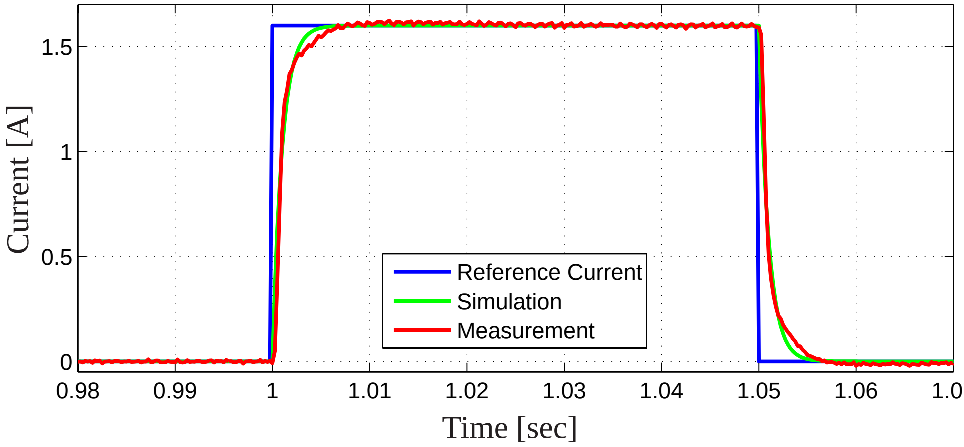

Figure 7.12: Damper current step response (measurement and simulation).

As a result, the damper dynamics are taken into account using the two transfer function formulations

$$G_m(s) = \frac{1}{10 \cdot 10^{-3} s + 1}, \tag{7.12}$$

$$\mathbf{G}_{el}(s) = \begin{bmatrix} G_{el,1}(s) & 0 \\ 0 & G_{el,2}(s) \end{bmatrix} \quad \text{with} \quad G_{el,1}(s) = G_{el,2}(s) = \frac{1}{1 \cdot 10^{-3} s + 1}. \tag{7.13}$$

The mechanical dynamics are described by $G_m(s)$ (input signal: static damper force $F_{d,s}$; output signal: actual damper force F_d). The electrical dynamics are characterized by the transfer matrix $\mathbf{G}_{el}(s)$ (input signals: voltage inputs of the power electronic unit $\mathbf{u}_{v,cvd}$; output signals: valve currents $\mathbf{i}_d$). The voltage inputs of the power electronic unit are proportional to the reference values $\mathbf{i}_d^*$ of the damper currents (see Section 7.1.2), which can be expressed as

$$\mathbf{i}_d^* = \alpha \mathbf{u}_{v,cvd} \tag{7.14}$$

with $\alpha > 0$. The transfer functions are parametrized by the identified time constants (see also [81]).

Since the damper force is not measured at the test rig and the electrical time constant is small, the model of the damper dynamics (7.12) - (7.13) is only used for the simulations. However, for the controller design a feedforward control based on the inverse of the static damper characteristic (Figure 7.11 (right)) is employed. For the control of the damper, an estimate of the relative damper velocity $\dot{\hat{x}}_{cw}$ provided by the filter based estimator structure (see Chapter 4.4) and the reference force F_d^* commanded by the high level suspension controller (presented in Chapter 8) are utilized to calculate the reference currents $\mathbf{i}_d^*$ from the inversion of the static damper characteristic (see Figure 7.11). The feedforward controller and the damper model are shown in Figure 7.13.

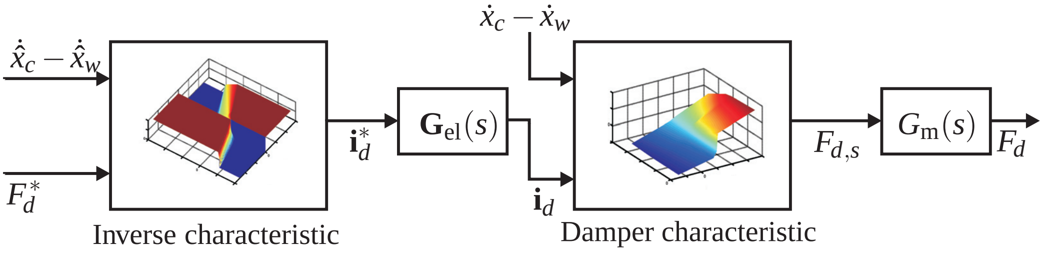

Figure 7.13: Damper model and feedforward control (see also [81]).

7.5 Summary

The proposed hybrid suspension system has been realized from suspension components of production vehicles. Moreover, a quarter-car test rig designed to evaluate the performance of the adaptively controlled hybrid suspension system has been presented. A precise model of the test rig dynamics including actuator models has been derived, that is used for the design of the adaptive suspension control concept for the hybrid suspension and for the simulations presented in the next Chapter.

Chapter 8

ADAPTIVE REFERENCE MODEL BASED CONTROL OF A HYBRID SUSPENSION SYSTEM

In Chapter 6 it has been shown that an adaptively controlled hybrid suspension system can theoretically almost achieve the same performance as a high bandwidth active suspension system. The realization of a hybrid suspension strut as well as an automotive quarter-car test rig has been presented in Chapter 7. Based on these preliminaries, a new adaptive suspension control approach, which is especially suitable for the hybrid suspension system, is presented in this Chapter. The main idea of this adaptive reference model based control concept is to emulate the behavior of a passive suspension system, that is optimally tuned for the current driving state in terms of ride comfort and safety. To realize this emulation, the suspension actuators vary the stiffness and the damping of the suspension if necessary to keep the limits for the dynamic wheel load and the suspension deflection. The new control approach overcomes the drawbacks of the adaptive suspension controller presented in Chapter 5.8, since the stability of the adaptive system can be guaranteed analytically and implementability as well as tuneability of the mechatronic suspension concept are supported.

The performance of the new adaptive controller structure is validated in simulations and in experiments at the automotive quarter-car test rig. The proposed control approach is compared with benchmark controllers in the experiments and it is analyzed, how the performance depends on the actuator bandwidth and on variations of the chassis mass. At the end of the Chapter, the two new adaptive suspension control techniques presented in this Thesis are compared and discussed.

8.1 Adaptive reference model based control approach

First, the motivation of the new control approach, that is based on an adaptive reference model, and its main idea are illustrated. Figure 8.1 (left) reviews the performance potential of fully active and semi-active suspension systems in a linear framework (see also Chapter 1). In Chapter 5 it has been pointed out that the significant performance potential of adaptive controllers for fully active suspension systems comes along with drawbacks regarding the transparent controller tuning and a complex stability analysis. Even besides their hardware complexity, these two aspects obviate the implementation of fully active systems in production vehicles.

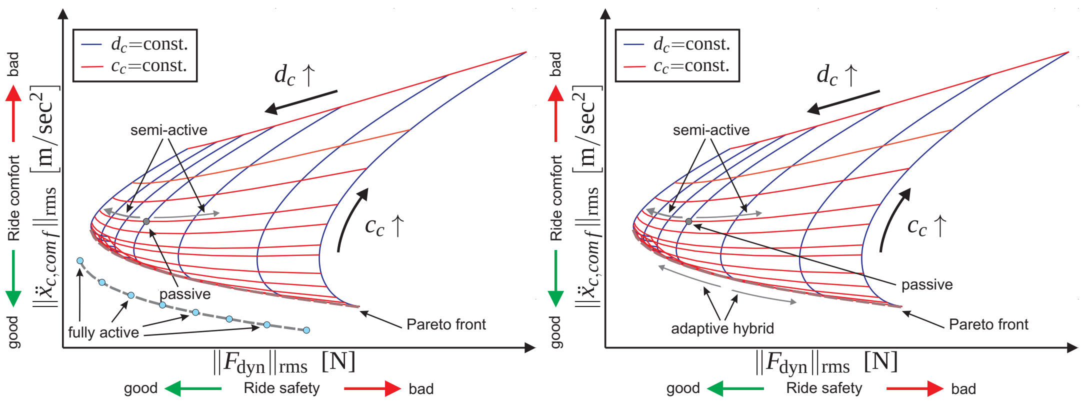

Figure 8.1: Motivation for the adaptive reference model based control approach - Achievable performance by fully active systems (left) and by a hybrid system controlled by an adaptive reference model based control approach (right).

Therefore, the idea of the new adaptive control approach is to employ the optimal passive suspension configuration for the current driving state as a reference model and track its dynamic behavior. If the driving state (determined by the estimate of the dynamic wheel load $\hat{F}_{dyn}(t)$ and the suspension deflection $x_c(t) - x_w(t)$) is not critical, a comfort oriented passive suspension configuration with low natural frequency and damping ratio of the sprung mass is emulated. If the driving state becomes critical, which is detected by an adaptation logic similar to the one presented in Chapter 5.2.1, the parametrization of the reference model is adapted acccordingly and the hybrid suspension uses the actuator combination to dynamically adjust the natural frequency of the chassis mass $\left(f_c(t) = \frac{1}{2\pi}\sqrt{\frac{c_c(t)}{m_c}}\right)$ and the damping ratio $\left(D_c(t) = \frac{d_c(t)}{2\sqrt{c_c(t)m_c}}\right)$ by varying the stiffness $c_c(t)$ and the damper coefficient $d_c(t)$ (Fig. 8.2).

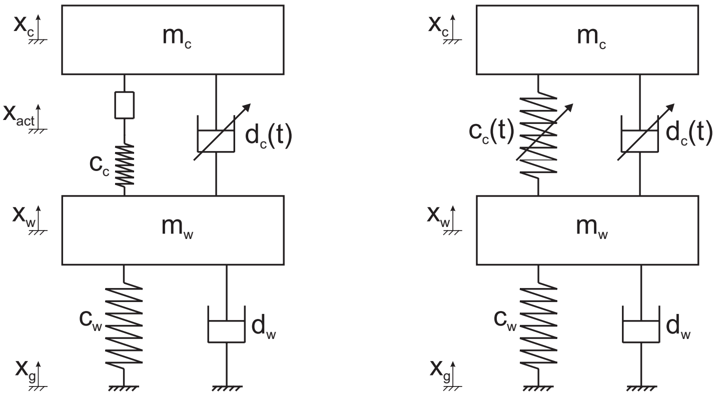

Figure 8.2: Hybrid suspension (left) and passive reference model with dynamically variable stiffness and damping (right).

Thus, as in Chapter 6, carpet plots are used to determine the optimal suspension configuration for the current driving state. However, the proposed approach offers the advantage that the well-known tuning parameters f_c and D_c of passive suspension systems are employed to adjust the dynamic behavior of the hybrid suspension instead of weighting terms of linear quadratic regulators. An important fact is, however, that by using a passive suspension configuration as reference model and for the calculation of the carpet plots, performance is potentially sacrificed since the Pareto front of the passive reference system is dominated by the Pareto front of the fully active suspension controller configurations (as can be seen when comparing the left and right part of Figure 8.1).

Utilizing the new control approach, the hybrid suspension "tracks" the Pareto front of the passive suspension system and the resulting forces of the spring $(F_c = c_c(t)(x_c - x_w))$ and the damper $(F_d = d_c(t)(\dot{x}_c - \dot{x}_w))$ satisfy the passivity constraints (see also Chapter 2.4.1)

$$F_c(x_c - x_w) \geq 0\,, \tag{8.1}$$

$$F_d(\dot{x}_c - \dot{x}_w) \geq 0\,, \tag{8.2}$$

that limit the achievable performance of the hybrid suspension if the proposed control approach is employed. However, in this Chapter it is shown that the achievable performance by this approach is remarkable.

8.1.1 Controller structure

The adaptive reference model based controller structure is shown in Figure 8.3 (see also [81], [82]). From the measurement signals, estimates of the damper velocity $\hat{\dot{x}}_{cw}(t)$ and the dynamic wheel load $\hat{F}_{dyn}(t)$ are obtained by the filter based estimation concept (FB) presented in Chapter 4.4, which is well suitable for this implementability focussed control concept. The measured suspension deflection and $\hat{F}_{dyn}(t)$ are supplied to an adaptation logic, that calculates the scheduling signals $q_{fdyn}(t)$ and $q_{susp}(t)$ in a similar manner to the one presented in Chapter 5.2.1. From the scheduling variables, the optimal values of $f_c(t)$ and $D_c(t)$ are determined from carpet plot based look-up tables, which are presented in detail in Section 8.2.1.

This optimal setting of the passive suspension in terms of $f_c(t)$ and $D_c(t)$ is supplied to the according passive reference model structure and by means of a control allocation scheme it is determined, which forces $F_d^*(t)$ and $F_{hy}^*(t)$ the actuators of the hybrid suspension have to generate to provide that the hybrid suspension system tracks the dynamic behavior of the reference model. To utilize the deflection controller of the hydraulic actuator (see Chapter 7.4.1), the reference deflection $u_{hy}^*(t)$ is calculated from the reference force $F_{hy}^*(t)$ using the kinematic relations and the spring stiffness (as will be explained in Section 8.2.2 in more detail). The resulting reference signals for the damper force and the actuator deflection are the input signals of the tracking controllers (with feedforward and feeback structures (FF/FB control)) for the actuators (continuously variable damper (CVD) and the hydraulic cylinder (SAC)), that have been presented in Chapter 7.4. The control inputs of the actuators $u_{cvd}(t) = F_d(t)$ and $u_{hy}(t) = i_c(t)\,(x_c(t) - x_{act}(t)) = \Delta x_{hy}(t)$ are applied to the suspension system.

The resulting control approach has a hierarchical structure: A high level suspension controller based on the adaptation logic, the adaptive reference model and the control allocation determines the reference signals for the lower level actuator controllers. This modular hierarchical architecture makes the approach well suitable for modern global chassis control concepts (see Chapter 2). It is noted that the adaptive reference model based control approach can be extended in order to take into account full-car dynamics and that the structure of the reference model does not necessarily have to be a passive suspension system with variable stiffness and damping although this choice provides several advantages as discussed in the next Sections.

Major differences of the proposed control approach compared to model reference adaptive control methods for vibration control proposed in the literature (e.g. [150], [181]) are that the

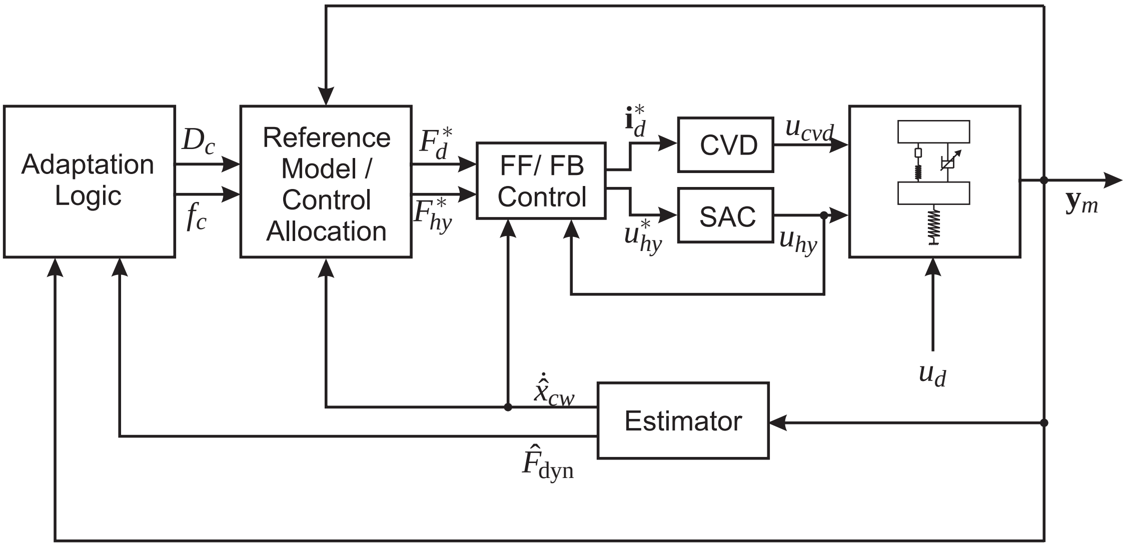

Figure 8.3: Adaptive reference model based controller structure for the hybrid suspension system.

reference model considered in this Thesis has time-varying parameters and it is based on the dynamics of passive suspension systems rather than skyhook concepts (see Chapter 2).

8.2 Adaptive reference model

In the following, the new components (adaptation logic, reference model and control allocation) of the controller structure depicted in Figure 8.3 are described in detail.

8.2.1 Adaptation logic

The driving state is determined by a similar adaptation logic to the one presented in Chapter 5. Thus, the rms-values of $\hat{F}_{dyn}$ and x_{cw} as well as rapid changes of these quantities are reflected by the two scheduling signals $q_{fdyn}(t)$ and $q_{susp}(t)$, which, however, range in this Chapter in the interval $0 \leq q_i \leq 2$. Moreover, slight modifications of the adaptation logic have been implemented, e.g. the asymmetric limits of the suspension deflection (see Chapter 7.3.1) are taken into account for the nonlinear function $g(\frac{x_c - x_w}{\bar{x}_{cw}})$ presented in Chapter 5.2.1 (see Figure 5.4). The details of the employed adaptation logic for the hybrid suspension system are summarized in [145]. The optimal values of the parameters f_c and D_c are gained from the

Pareto fronts of the carpet plots of the passive reference model structure (see Figure 8.4).

Adaptation laws derived from the passive reference model structure

The reference model and the adaptation laws are derived in simulations from carpet plots (relating $||\ddot{x}_{c,comf}||_{\text{rms}}$, $||F_{dyn}||_{\text{rms}}$ and $||x_c - x_w||_{\text{std}}$) of the passive suspension configuration with varying stiffness and damping. For the calculation of the carpet plots a simplified version of the passive quarter-car model presented in Chapter 7.3 is utilized. It includes the linearized primary spring characteristic (in the coordinates of the quarter-car model), the Gehmann-Model[1] of the tire and the friction effects. The damper characteristic has been linearized separately in compression and rebound direction (between $\dot{x}_{cw} = 0\,\frac{\text{m}}{\text{sec}}$ and $\dot{x}_{cw} = \pm 0.58\,\frac{\text{m}}{\text{sec}}$, respectively) using the damper current $\mathbf{i}_d = \begin{bmatrix} 1.2\,\text{A} & 1.2\,\text{A} \end{bmatrix}^T$ representing the passive reference. The damping ratio is calculated from the mean value of both linear damping coefficients [106]. To vary the damping ratio, the piecewise linear damping characteristic of the reference model is scaled accordingly. From the choice of the piecewise linear characteristics of the damper and the linear spring stiffness for the reference model, the effects resulting from the nonlinearities of the corresponding real suspension components will be cancelled by the actuators and the dynamic behavior of the controlled hybrid suspension becomes more transparent.

Figure 8.4 depicts the carpet plots of the reference model, that have been obtained from varying the natural frequency f_c and the damping ratio D_c of the sprung mass and using white noise for the road excitation's velocity as disturbance. The corresponding road model (2.11) is parametrized with $n = -2$, the vehicle velocity $v = 80\,\frac{\text{km}}{\text{h}}$ and the roughness factor $A = 1.8 \cdot 10^{-6}\,\text{m}^3$, which resembles a medium quality highway road profile [106]. In the carpet plots, the weighted chassis acceleration is employed using the shaping filter presented in Chapter 2.3.1. The original passive suspension setting has a damping ratio of the chassis mass of $D_{c,p} = \frac{d_{c,p}}{2\sqrt{c_{c,p}m_c}} = 0.21$ and a corresponding natural frequency of $f_{c,p} = \frac{1}{2\pi}\sqrt{\frac{c_{c,p}}{m_c}} = 1.1\,\text{Hz}$. The reference model, that is used for the adaptive controller, can vary these quantities in the ranges $0.18 \leq D_c(t) \leq 0.7$ and $0.8\,\text{Hz} \leq f_c(t) \leq 1.6\,\text{Hz}$, which represent meaningful ranges from comfort focussed upperclass-vehicles to sports cars [50, 106].

---

[1] The nonlinear effects of the tire are considered in the reference model but it is noted that the differences in the shape of the Pareto fronts compared to those generated with linear tire models are small.

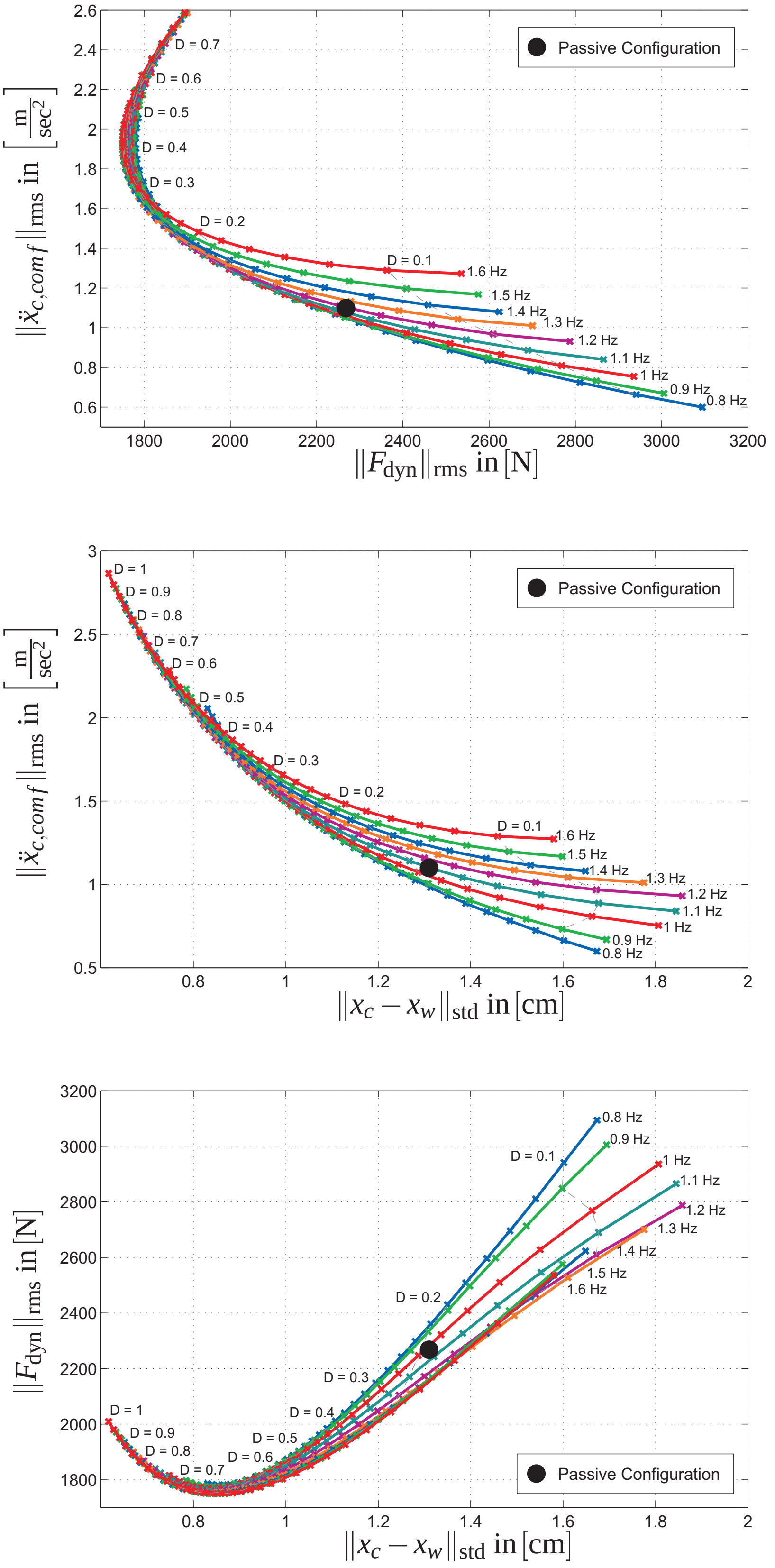

Figure 8.4: Carpet plots for the passive reference suspension model for different f_c and D_c.

The carpet plots of the reference model depicted in Figure 8.4 are used to formulate an appropriate adaptation strategy. Therefore, the Pareto front of the upper carpet plot is parametrized by the scheduling parameter $q_{fdyn}(t)$ so that adaptation laws for the desired values of $f_c(t)$ and $D_c(t)$ (within their admissible ranges) can be derived to provide ride safety for every driving state. The lower two carpet plots in Figure 8.4 are used to formulate adaptation laws based on $q_{susp}(t)$ in order to take into account the suspension deflection limits.

To improve ride comfort, a low natural frequency ($f_c = 0.8\,\mathrm{Hz}$) should be maintained as long as the driving state permits. Consequently, the adaptation is first realized by increasing the damping ratio (Figure 8.4 (upper)). Since an adjustment of the suspension setting influences the dynamic wheel load and the suspension deflection simultaneously, a minimum damping ratio $D_{c,min}$ is derived from the suspension deflection carpet plot depicted in Figure 8.4 (lower), which dominates the wheel load optimal damping ratio. Thereby, a suspension configuration is emulated, that simultaneously lowers the suspension deflection and the dynamic wheel load, if the suspension deflection becomes critical. Since the resulting suspension setting corresponding to the wheel load minimum in the lower carpet plot lies slightly above the Pareto front of the middle carpet plot, this setting is not optimal in terms of ride comfort, however, the comfort deterioration is moderate and enables a ride safety optimal setting. The rational behind this approach is to keep a predictable behavior of the suspension by preventing the violation of the suspension deflection limits and to simultaneously focus a wheel load optimal setting. Figure 8.5 shows the resulting adaptation laws:

- For an uncritical driving state ($q_i \approx 0$), $f_c = 0.8\,\mathrm{Hz}$ and $D_c = 0.18$ in order to focus on ride comfort (Figure 8.4 (upper)). This setting corresponds to point A in Figure 8.5 (c).

- If the dynamic wheel load increases, q_{fdyn} rises. Hence, f_c remains constant at first (Figure 8.5 (a)) and D_c rises (Figure 8.5 (c) between points *A* and *B*). Thus, the dynamic wheel load is lowered by emulating suspension settings, which constitute the middle part of the Pareto front shown in Figure 8.4 (upper). If F_{dyn} must be further reduced for $q_{fdyn} \geq 0.7$, f_c is increased (Figure 8.5 (a)). Simultaneously, D_c is adapted (Figure 8.5 (c) between points B and C) to minimize the dynamic wheel load along the Pareto front in Figure 8.4 (upper). Point C equals to the wheel load optimal point in the carpet plot shown in Figure 8.4 (upper), i.e. it resembles the suspension configuration activated for most critical dynamic wheel loads.

- If the suspension travel becomes critical, q_{susp} rises. The natural frequency f_c is first kept as low as possible (0.8 Hz, Figure 8.5 (b)) and the lower bound $D_{c,\text{min}}$ is increased (Figure 8.5 (d)). Thereby, $\|x_c - x_w\|_{\text{std}}$ is lowered. If q_{susp} exceeds the value 0.5, f_c is also increased and the minimum value of $\|F_{\text{dyn}}\|_{\text{rms}}$ is reached for $q_{susp} = 1.5$ (Figure 8.4 (lower)). For extreme suspension deflections corresponding to values of $q_{susp} \geq 1.5$, f_c and $D_{c,\text{min}}$ are increased further (Figure 8.5 (b), (c), (d) and Figure 8.4 (middle)). In this case, the minimum in terms of $\|x_c - x_w\|_{\text{std}}$ within the considered adaptation range is reached, however, $\|F_{\text{dyn}}\|_{\text{rms}}$ increases as shown in Figure 8.4 (lower).

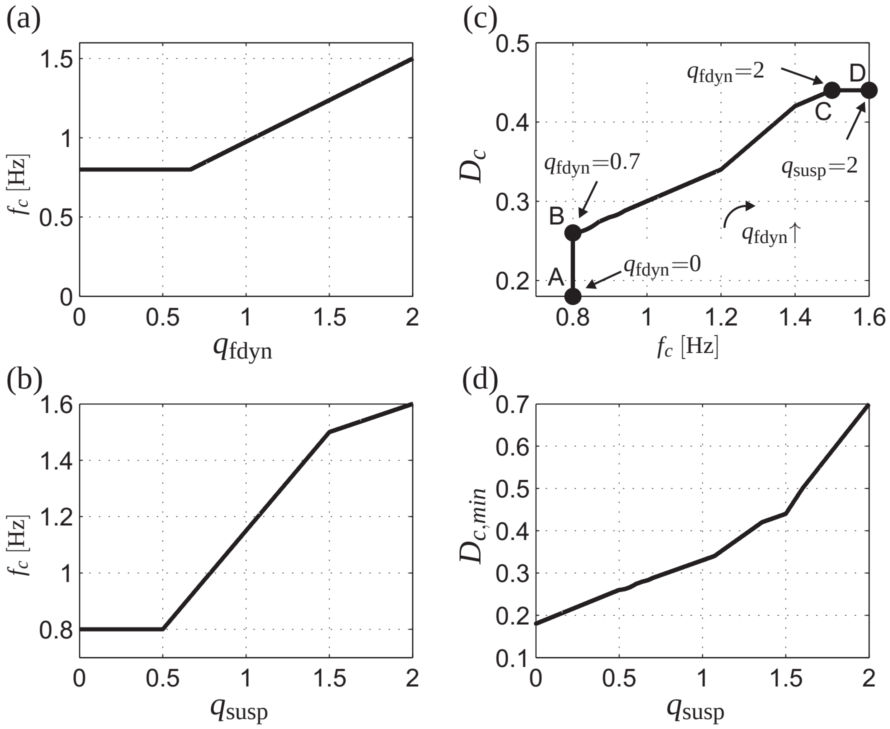

Figure 8.5: Reference model based adaptation laws.

8.2.2 Control allocation

From the optimal values of the damping ratio and the natural frequency calculated by means of the adaptation laws, the reference forces for the actuators of the hybrid suspension system have to be determined. This is accomplished in two steps as shown in Figure 8.6:

1. The resulting spring and damper forces ($F_{c,ref}$ and $F_{d,ref}$) of the passive reference model

(see Section 8.2.1), parametrized with the desired values of f_c and D_c are calculated for the current suspension deflection x_{cw} and estimated damper velocity $\hat{\dot{x}}_{cw}$.

2. The forces of the passive elements ($F_{c,pass}$ and $F_{d,pass}$) of the hybrid suspension setup are determined for x_{cw} and $\hat{\dot{x}}_{cw}$ using the nonlinear passive suspension model described in Chapter 7.3.2. They correspond to the forces acting between the sprung and the unsprung mass if no control action would be taken. The differences between the desired spring and damper forces from the reference model and the forces of the passive suspension model represent the reference forces for the actuators.

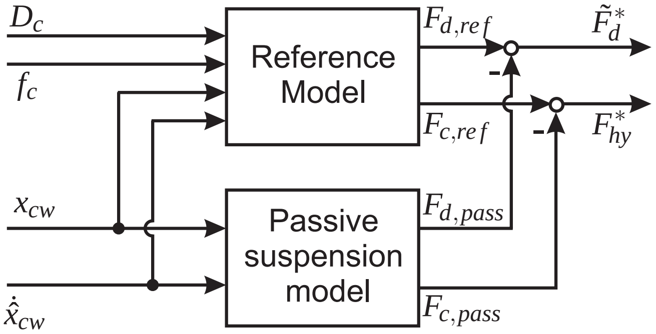

Figure 8.6: Reference model based control force calculation ($F_{c,j}$ represents a spring force, $F_{d,j}$ represents a damper force).

An increase of the natural frequency $f_c(t)$ by a change of the spring stiffness requires an active element, the damping ratio $D_c(t)$ can be adjusted by the semi-active damper. Consequently, the reference force for the hydraulic actuator $F_{hy}^*(t)$ is calculated from $f_c(t)$ and the damper force $F_d^*(t)$ results from the desired values of $D_c(t)$. Furthermore, the tracking error of the hydraulic actuator is added to the reference force of the damper in order to ease the effect of the bandwidth limitation of the hydraulic actuator. Accordingly, the force reference values are calculated as (see also Table B.5 in the Appendix)

$$F_{hy}^*(t) = \left(m_c(2\pi f_c(t))^2 - c_{c,\text{pass}}(\mathbf{x})\right) x_{cw}(t)\,, \tag{8.3}$$

$$F_d^*(t) = \underbrace{\left(4\pi f_c m_c D_c(t) - d_{c,\text{pass}}(\mathbf{x})\right) \hat{\dot{x}}_{cw}(t)}_{\tilde{F}_d^*(t)} + \left(F_{hy}^*(t) - F_{hy}(t)\right)\,. \tag{8.4}$$

In (8.4) $\tilde{F}_d^*(t)$ denotes the part of the reference force that does not include the tracking error compensation of the hydraulic actuator (see Figure 8.6). As noted in Section 8.1.1, for the implementation of the approach, the reference deflection is calculated from the reference force (given in the coordinates of the quarter-car model) of the hydraulic actuator as

$$u_{hy}^* = \frac{F_{hy}^*(t)}{\bar{c}_{c,lin} i_c(t)} \tag{8.5}$$

with the transmission factor defined in (7.1) and the linear spring stiffness $\bar{c}_{c,lin}$ of the steel spring without the endstops (compare (3.9)). This step is required since the displacement of the actuator is the controlled variable of the hydraulic actuator (see Chapter 7.4.1).

The effect of this control allocation approach is that the passive suspension forces are compensated if necessary and the reference force signals of the adaptive reference model can be tracked by the actuator controllers of the hybrid suspension system (see Chapter 7.4).

8.3 Stability analysis

The stability of the closed loop system has to be analyzed because the actuator force commanded by the reference model depends on the current vehicle state and as a consequence, feedback is introduced. Due to the passivity constraints of the spring and damper forces (8.1) - (8.2), the hybrid suspension with the proposed adaptive control approach can be considered as a passive suspension system with time-varying stiffness $c_c(t)$ and damping $d_c(t)$ (Figure 8.2 (right)). Although this fact leads to lower achievable performance compared to active suspension systems as pointed out in Section 8.1, it enables a considerably simpler, more transparent stability proof for the adaptively controlled hybrid suspension than the stability analysis presented in Chapter 5.3 for the adaptively controlled fully active suspension system.

It is noted that for the following energy based stability analysis the Gehmann-Model of the tire (see Chapter 7.3.1) is not considered since it primarily serves to increase the performance of the simulation model and the differences between constant and frequency dependent tire stiffness and damping are small in the considered suspension application. The tire is thus represented in the following by a spring with linear stiffness c_w as commonly proposed in the literature (see Chapter 2.1). It is emphasized that the omission of the tire damping ($d_w = 0$) leads to more conservative results in the following stability analysis due to the missing further dissipative element. This also applies for the omission of the suspension friction force F_f in the following analysis.

The system's energy gives a Lyapunov function (see also Appendix A.2)

$$V(\mathbf{x},t) = \frac{1}{2}\left(m_c x_2^2 + m_w x_4^2 + c_c(t) x_1^2 + c_w x_3^2\right) \tag{8.6}$$

with $V(\mathbf{x},t) > 0$ for $\mathbf{x} \neq \mathbf{0}$ and $V(\mathbf{0},t) = 0$. In the stability analysis, the stability of the equilibrium $\mathbf{x} = \mathbf{0}$ is considered first, i.e. the excitation by the road profile $u_d(t) = \dot{x}_g(t)$ is neglected and the derivative of the Lyapunov function is

$$\dot{V}(\mathbf{x},t) = -d_c(t)(x_2 - x_4)^2 + \frac{1}{2}\dot{c}_c(t) x_1^2, \tag{8.7}$$

which has to be negative definite for the closed loop system to be asymptotically stable. Because $d(t) > 0$ holds, only the second term of (8.7) must be further analyzed to guarantee stability.

By the hydraulic actuator energy is supplied to the system by compressing the spring. In order to ensure ride safety, an increase of the spring stiffness should always be possible but to prevent a switching sequence that continuously increases $V(\mathbf{x},t)$, switching back to a softer spring setting is only allowed if the energy increase from switching to a stiffer spring setting is dissipated. If the stiffness varies within the interval $c_{\min} \leq c_c(t) \leq c_{\max}$ with $c_{\min} > 0$ and $x_{1,\max}$ denoting the upper bound of suspension deflection, the maximum energy gain by a *single* stiffness increase without dissipation is

$$\int_{t_0}^{t} \frac{1}{2}\dot{c}_c(\tau) x_1^2 d\tau \leq \underbrace{\frac{1}{2}\left(c_{\max} - c_{\min}\right) x_{1,\max}^2}_{\Delta V_{\max}}. \tag{8.8}$$

If $\dot{c}_{c,d}(t)$ defines the desired change in stiffness commanded by the reference model, a lower bound for the stiffness c_{lb} is defined using

$$\Phi(t) = c_{\min} + \frac{2}{x_{1,\max}^2} \int_{t_0}^{t} \frac{1}{2}\dot{c}(\tau) x_1^2 - s d(\tau)(x_2 - x_4)^2 d\tau \tag{8.9}$$

as

$$c_{lb} = \begin{cases} \Phi(t) & \text{for} \quad c_{\min} \leq \Phi(t) \leq c_{\max} \\ c_{\min} & \text{for} \quad \Phi(t) < c_{\min} \\ c_{\max} & \text{for} \quad \Phi(t) > c_{\max} \end{cases} \tag{8.10}$$

with the parameter $0 < s < 1$, that is introduced to improve robustness regarding estimation errors in the damper velocity $\dot{\hat{x}}_{cw} = \hat{x}_2 - \hat{x}_4$ (here $s = 0.9$ is chosen). Moreover, an anti-windup structure is implemented for the integral in (8.9). The resulting switching restriction

$$\dot{c}_c(t) = \begin{cases} 0 & \text{for} \quad \dot{c}_{c,d}(t) < 0 \wedge c_c(t) \leq c_{lb} \\ \dot{c}_{c,d}(t) & \text{else} \end{cases} \tag{8.11}$$

guarantees that the system's energy increase by *multiple* switching with dissipation is bounded by

$$\int_{t_0}^{t} \dot{V}(\mathbf{x},\tau)d\tau \leq \Delta V_{\max} - \int_{t_0}^{t} (1-s)d_c(\tau)(x_2-x_4)^2 d\tau \tag{8.12}$$

such that

$$V(\mathbf{x},t) \leq \frac{c_{\max}}{c_{\min}} V(\mathbf{x}(t_0),t_0) \tag{8.13}$$

holds for all $t \geq t_0 \geq 0$ and for all $\|\mathbf{x}(t_0)\| < \gamma$ with $\gamma \in \mathbb{R}^+$. Consequently, the closed loop system is uniformly stable [70]. Due to the fact that in (8.12), $x_2 - x_4 = 0$ holds permanently only in the equilibrium of the system, $\lim_{t\to\infty} V(\mathbf{x},t) = 0$ holds such that the system is even uniformly asymptotically stable. Therefore, it can be concluded that the system is totally stable and withstands bounded disturbance signals using the same argumentation as presented in Chapter 5.3.3 (see also Appendix A.2.4).

The stability restriction is implemented in the control algorithm for all simulations and experiments.

8.4 Simulation results

To evaluate the controller performance, simulations with the adaptive reference model based controller are conducted using the nonlinear test rig model and the actuator models presented in Chapter 7. Figure 8.7 shows the performance of the hybrid suspension in comparison to the passive suspension system (the simulation results are shown in Figure B.1 in the Appendix). The performance gain in simulations with road profile P1 ($v_{p1} = 50\,\frac{\text{km}}{\text{h}}$) regarding ride comfort improvement is up to 30% in terms of $\|\ddot{x}_c\|_{\text{rms}}$ and 17% in terms of $\|\ddot{x}_{c,comf}\|_{\text{rms}}$ compared to the passive system. A remarkable observation is that the quantities related to the dynamic wheel load and the suspension deflection are also improved compared to the passive system. This indicates a significant performance potential of the proposed control approach. Further simulation results conducted with a similar nonlinear model from an earlier design stage of the test rig have been presented by the author in [81].

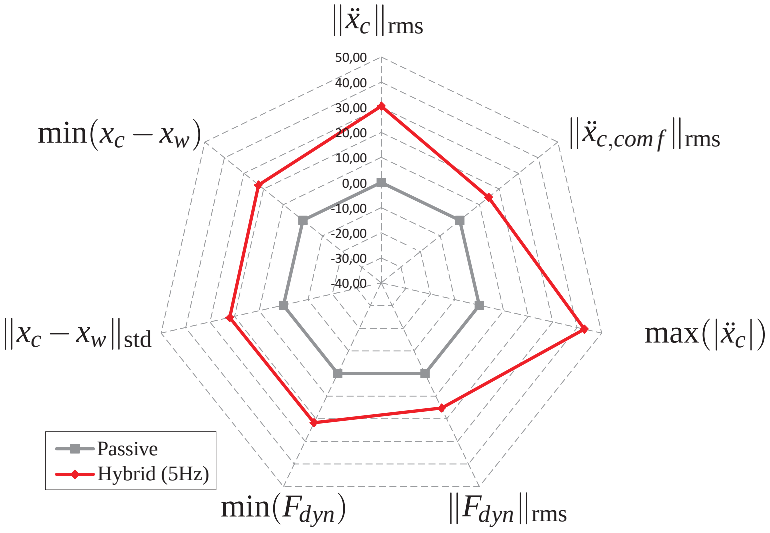

Figure 8.7: Controller performance in simulation for profile P1 with $v_{p1} = 50\,\frac{\mathrm{km}}{\mathrm{h}}$.

8.5 Experimental results

The experiments are conducted at the quarter-car test rig using the two measurements of real road profiles (profiles P1 and P2, see also Chapter 2.2). Further results for a singular disturbance event are presented in Section 8.6.1.

8.5.1 Benchmark systems

To evaluate the performance results of the hybrid suspension and the proposed control approach, the same benchmark controller structures as presented in Sections 2.7 and 5.6 except the LQR are employed (since it requires full state feedback, which is not envisaged at this point due to the focus on implementability). The comparison with skyhook based control concepts is of primary interest because skyhook suspension control techniques are also implemented in the vehicles, the actuator components are taken from [50]. The skyhook benchmark concepts are used for the semi-active suspension configuration (nonadaptive (SA-Skyh.) and adaptive (SA-Ad.)) and the active configuration (Act.-Skyh.), in this case with a fixed soft setting of the semi-active damper. The absolute velocity of the chassis mass for the skyhook benchmark controller (see Section 8.5.1) is gained from the filter based estimation approach described in Section 4.4.

The reference damping force in the adaptive case (SA-Ad.) is

$$F_{d,sky}(t) = -d_{sky}\dot{\hat{x}}_c(t) - \left(d_{c,c} + (d_{c,s} - d_{c,c})\frac{q_{fdyn}(t)}{2}\right)\left(\dot{\hat{x}}_c(t) - \dot{\hat{x}}_w(t)\right), \tag{8.14}$$

with the damping terms $d_{c,c} = 300\,\frac{\text{Nsec}}{\text{m}}$ (comfort damping), $d_{c,s} = 1416\,\frac{\text{Nsec}}{\text{m}}$ (safety damping) and $d_{sky} = 2000\,\frac{\text{Nsec}}{\text{m}}$ (see also Chapter 2.7 for the dissipativity conditions in the semi-active case). The damping parameters of the skyhook benchmark controllers are obtained by means of optimization to minimize the rms-values $||\ddot{x}_{c,comf}||_{\text{rms}}$ and lower $||F_{dyn}||_{\text{rms}}$ subject to the constraints given by the suspension deflection limits. For the nonadaptive skyhook control law, $q_{fdyn}(t) = 0$ holds in (8.14).

8.5.2 Power demand analysis

For the evaluation of power demand of the hybrid suspension, the approach based on the positive average mechanical power presented in Chapter 2.3 is used. In (2.23) the relative velocity of the hydraulic actuator $\Delta\dot{x}_{act}(t) = \Delta\dot{x}_{hy}(t) = \dot{u}_{hy}(t)$ is substituted. In [147] a different approach for the calculation of the power of a hydraulic actuator in series to the main spring is employed, i.e. it is calculated as 50% of the total rms-power. If the actuator stroke $\Delta x_{hy}(t)$ has zero mean, the two approaches are equal. However, the method of power quantification presented in Chapter 2.3.3 is a more general approach, which is also feasible for biased actuator stroke signals, and is further employed in order to ensure comparability with the results presented in Chapter 5.

In order to be able to compare the power demand of the hybrid suspension system with the fully active suspension system in Chapter 5, the power demand of the fully active system is scaled accordingly. Since mechanical power $P_m(t)$ scales linearly with the accelerated mass m as

$$P_m(t) = F(t)\dot{x}(t) = m\ddot{x}(t)\dot{x}(t) \tag{8.15}$$

($x(t)$ denotes the displacement of the mass), the average positive actuator power $||P^+_{m,full}||_{\text{rms}}$ required by the fully active system at the quadricycle quarter-vehicle test rig is scaled by the ratio of the chassis masses of the test rigs to calculate the equivalent power $||P^+_{m,c}||_{\text{rms}}$ as

$$||P^+_{m,c}||_{\text{rms}} = \frac{m_{c,car}}{m_{c,quad}}||P^+_{m,full}||_{\text{rms}}, \tag{8.16}$$

with $\frac{m_{c,car}}{m_{c,quad}} \approx 5.37$.

8.5.3 Measurement results

For the evaluation of the measurement results, spider charts are used to visualize the performance gain defined in (2.24) for each considered quantity with respect to the passive suspension. Figure 8.8 summarizes the performance results for the measurements of the benchmark systems and the hybrid suspension for both road profiles. The grey line denotes the performance of the passive suspension and the numerical values for profile P1 ($v_{p1} = 50\,\frac{\mathrm{km}}{\mathrm{h}}$) are summarized in Table 8.1 (with a 5 Hz bandwidth of the actuator). It is noted that the critical values for the considered suspension configuration according to the system requirements formulated in Chapter 2.3 are $\min(F_{dyn}) = -5641\,\mathrm{N}$, $\|F_{dyn}\|_{\mathrm{rms}} = 1880\,\mathrm{N}$ and $\min(x_c - x_w) = \underline{x}_{cw} = -10\,\mathrm{cm}$.

Table 8.1: Experimental results for profile P1 ($v_{p1} = 50\,\frac{\mathrm{km}}{\mathrm{h}}$).

Quantity	Passive	SA-Skyh.	SA-Ad.	Act-Skyh.	Hybrid
$\|\ddot{x}_c\|_{\mathrm{rms}}$ in $\frac{\mathrm{m}}{\mathrm{sec}^2}$	1.88	1.65	1.58	1.50	1.24
Benefit vs. passive	-	12%	16%	20%	34%
$\|\ddot{x}_{c,\mathrm{comf}}\|_{\mathrm{rms}}$ in $\frac{\mathrm{m}}{\mathrm{sec}^2}$	1.24	1.18	1.01	1.08	0.87
Benefit vs. passive	-	5%	19%	13%	30%
$\|F_{dyn}\|_{\mathrm{rms}}$ in N	1136	1027	1078	1009	1016
Benefit vs. passive	-	10%	5%	11%	11%
$\min(F_{dyn})$ in N	-3479	-2918	-3206	-2876	-2979
Benefit vs. passive	-	16%	8%	17%	14%
$\min(x_c - x_w)$ in cm	-7.7	-6.2	-6.6	-6.4	-7.6
Benefit vs. passive	-	19%	14%	18%	1%
$\|P^+\|_{\mathrm{rms}}$ in W	0	0	0	92	115

In order to study the influence of the bandwidth of the hydraulic actuator, the bandwidth ω_{hy} of the filter for the reference signal (see (7.10)) of the actuator controller is increased from 5 Hz to 12 Hz. The expected slightly higher performance is visualized in Figure 8.8. This comes, however, at the price of a higher power demand (for profile P1 the increase is $\Delta\|P^+\|_{\mathrm{rms}} = 60\,\mathrm{W}$). Consequently, $\omega_{hy} = 2\pi \cdot 5\,\frac{\mathrm{rad}}{\mathrm{sec}}$ (the original bandwidth of the *ABC-system*)

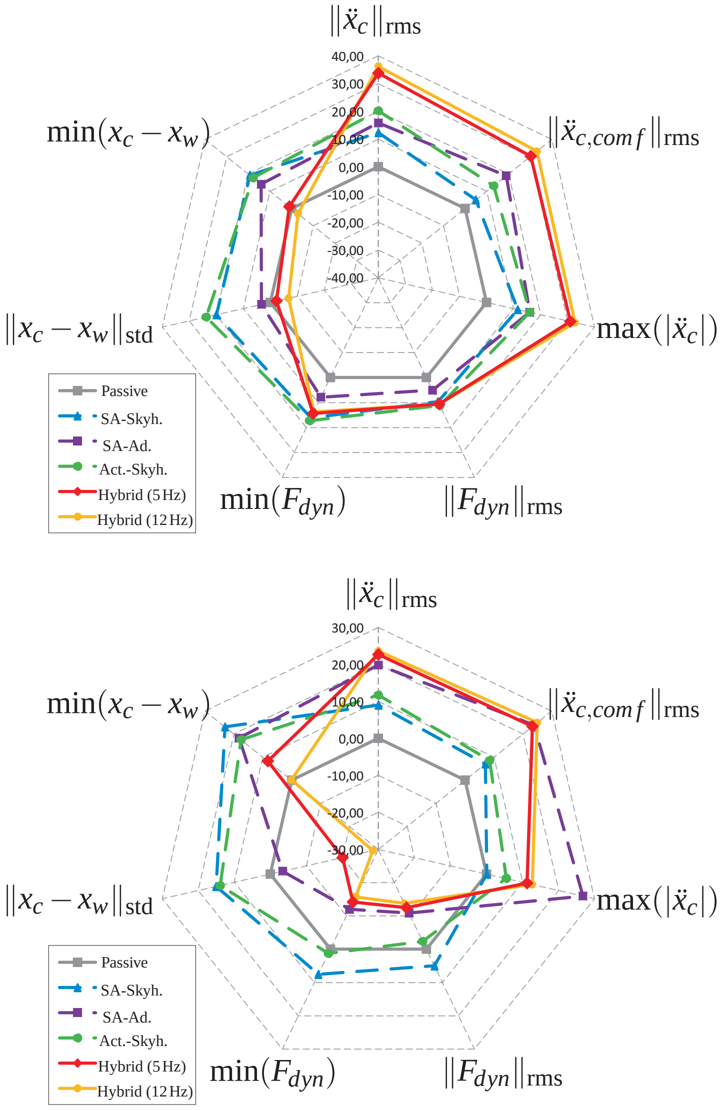

Figure 8.8: Controller performance for profile P1 with $v_{p1} = 50\,\frac{\text{km}}{\text{h}}$ (upper) and profile P2 with $v_{p2} = 30\,\frac{\text{km}}{\text{h}}$ (lower) for different actuator bandwidths $\omega_{hy} = 2\pi \cdot 5\,\frac{\text{rad}}{\text{sec}}$, $\omega_{hy} = 2\pi \cdot 12\,\frac{\text{rad}}{\text{sec}}$.

represents a good trade-off for the bandwidth of the hydraulic actuator.

As can be seen in Figure 8.8, the adaptive reference model based control approach in combination with the hybrid suspension configuration outperforms the benchmark controllers by far. The measurement results confirm that the presented approach offers significant performance improvements for ride comfort and in the case of road profile P1 ($v_{p1} = 50\,\frac{\text{km}}{\text{h}}$) even for ride safety. These performance gains of the hybrid suspension, however, come along with higher suspension deflections, which is not a drawback since the adaptation logic prevents hitting the suspension limits. It is noted that the switching restriction (8.11) has been triggered neither in simulations nor in the experiments. Consequently, it can be concluded that it does not imply performance limitations for the control approach.

For profile P2 ($v_{p2} = 30\,\frac{\text{km}}{\text{h}}$), which contains more high frequency components despite the lower velocity (see Figure 4.1), the performance can also be increased by the hybrid suspension, however, by permitting higher dynamic wheel loads and suspension deflection (both quantities are still well within the formulated limits). Due to this property of the road excitation signal, the actuator becomes less involved which reduces the actuator power to $\|P^+\|_{\text{rms}} = 60\,\text{W}$. Thus, the ride comfort for profile P2 can obviously also be increased considerably by the controlled semi-active damper using the proposed adaptive skyhook algorithm (see (8.14)).

Performance evaluation for a particularly challenging road profile

In order to show the full potential of the proposed new control approach, the velocity for passing profile P1 is increased to $75\,\frac{\text{km}}{\text{h}}$. Simulations have shown that the wheel would loose contact to the road with the conventional passive damping ratio ($D_{c,p} = 0.21$). Thus, the damping ratio of the passive system is increased to $D_{c,p} = 0.42$. Figure 8.9 shows the measurement results of this passive suspension configuration and the hybrid configuration with an actuator bandwidth of 5 Hz. Neither the dynamic wheel load nor the suspension deflection limits are violated by both configurations but the performance increase by the hybrid configuration is 36% regarding ride comfort while $\|F_{dyn}\|_{\text{rms}}$ remains almost unchanged. It can also be seen clearly from Figure 8.9 how the scheduling parameters $q_{fdyn}(t)$ and $q_{susp}(t)$ relate to the characteristics of the signals $F_{dyn}(t)$ and $x_c(t) - x_w(t)$. The ratio of the power spectral densities of the weighted chassis acceleration $\ddot{x}_{c,comf}(t)$ and the road excitation signal $x_g(t)$ is visualized in Figure 8.10 to compare the disturbance transmission behavior of the passive and the hybrid system. The Figures show that the hybrid configuration leads to a better vibration isolation in the important frequency range for ride comfort.

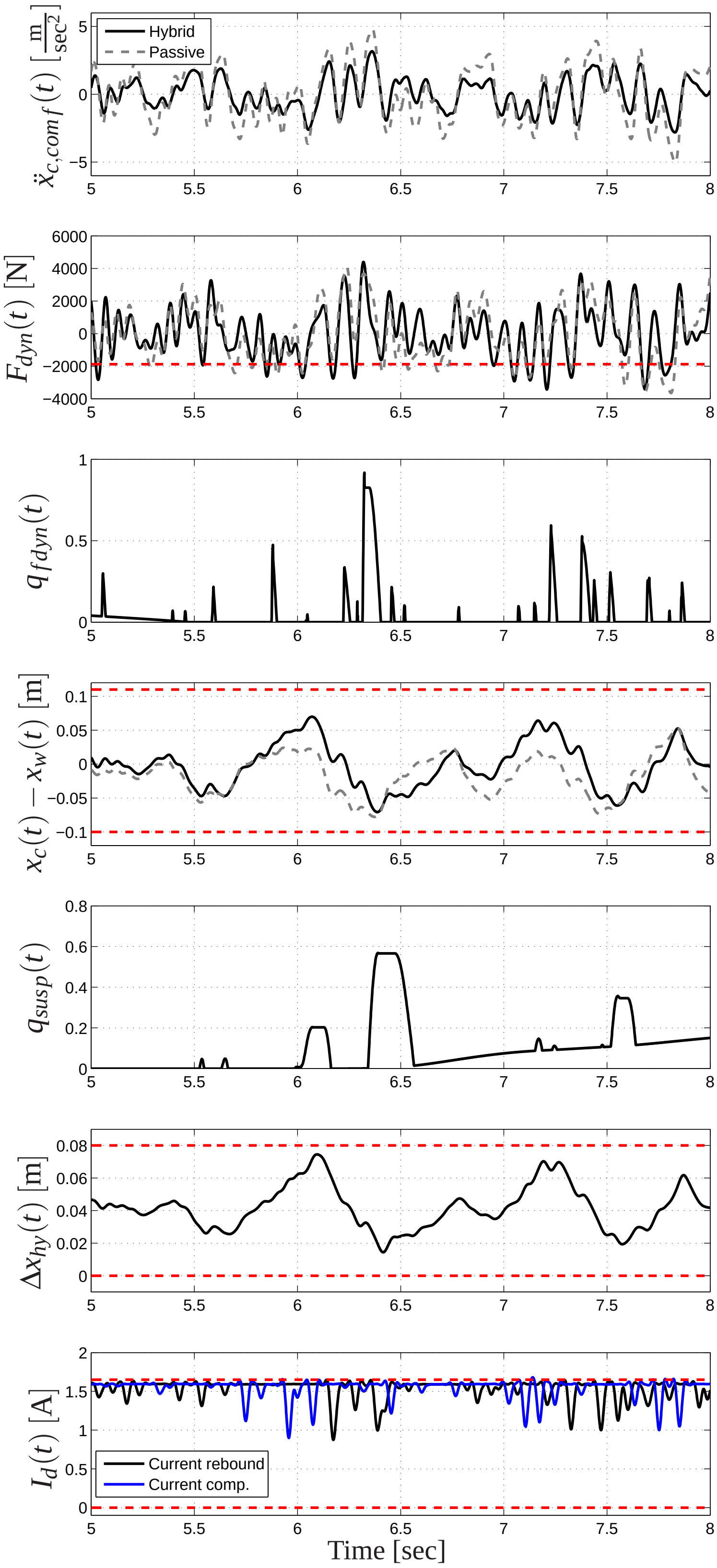

Figure 8.9: Measurement results of the hybrid versus the passive suspension (P1 with $v_{p1} = 75\,\frac{\text{km}}{\text{h}}$); the red lines indicate the limits for the rms-value of F_{dyn} (i.e. $\frac{F_{\text{stat}}}{3}$), the suspension deflection limits and the saturation limits of the control inputs.

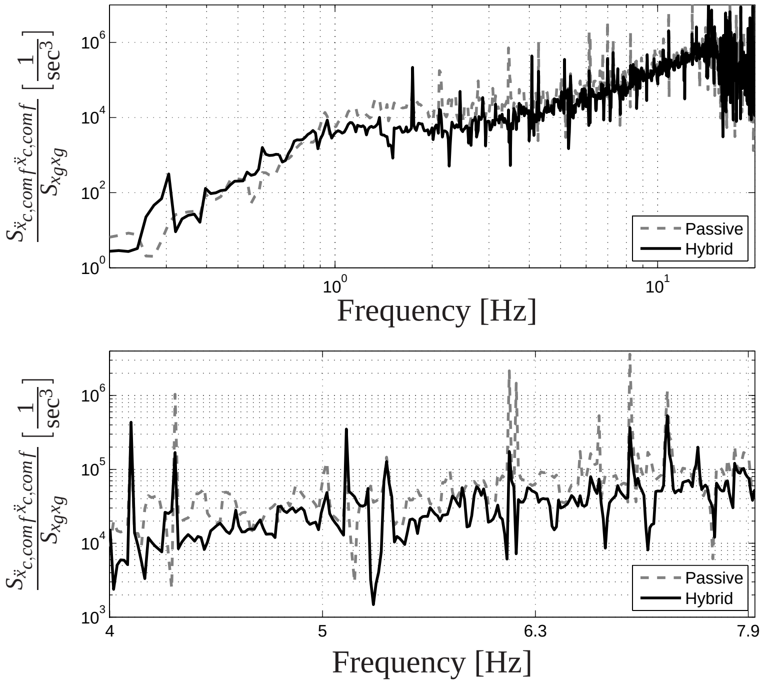

Figure 8.10: Power spectral density ratios for the measurement results of the hybrid versus the passive suspension (P1 with $v_{p1} = 75\,\frac{\mathrm{km}}{\mathrm{h}}$) with zoom on the frequency range $4-8\,\mathrm{Hz}$.

Experimental robustness study

Furthermore, the robustness of the proposed control approach is studied experimentally. Therefore, the chassis mass m_c is increased at the test rig by 10.55% in order to simulate a higher vehicle load[2]. The adaptive reference model based controller designed for the nominal chassis mass is then used for suspension control. The result is that the increase of the chassis mass even enhances the performance regarding ride comfort by approx 3% and ride safety by 2.3% due to the resulting lower natural frequency of the chassis mass. In this experiment, the hydraulic actuator has readjusted the equilibrium point as the load levelling system of the vehicle would do. Due to the higher chassis mass, the peak suspension deflection is approx. 32% higher.

These results underline the robustness of the control approach since it performs well despite

---

[2] A mass increase of approx. 10% has been envisaged, the realized slightly higher increase, however, has been better applicable due to hardware aspects.

the mass variation. However, to prevent estimation errors in the dynamic wheel load and to adjust the adaptation laws (Figure 8.5) for varying vehicle loads, a filter based sprung mass estimator (see e.g. [36]) would be an interesting extension of the concept.

8.6 Extensions of the controller structure

To further enhance the performance of the hybrid suspension system in combination with the proposed control approach, the controller structure could be extended by a feedforward component. A realistic, yet very effective feedforward approach is briefly discussed in the following Section.

8.6.1 Optimal control for suspension deflection

An inherent problem of the suspension deflection based adaptation presented in this Thesis is that the scheduling parameter $q_{susp}(t)$ only rises based on the suspension deflection itself. Thereby, the time left for the controller adaptation and the generation of actuator forces is short if peaks in the excitation signal cause critical suspension deflections. This issue becomes especially critical for the hardware if the vertical chassis velocity $\dot{x}_c$ is negative, i.e. the chassis mass moves towards the compression endstop of the suspension (see Chapter 2.3.3). Moreover, by the resulting peak-like actuator forces, which are generated to prevent hitting the suspension limit, high vertical accelerations can be caused, which deteriorate ride comfort.

One approach to overcome this problem is to take into account also the velocity of the suspension movement, which equals the damper velocity $\dot{x}_{cw}$ in the considered application. By means of an optimal feedforward control approach, the state space is discretized and for each point of the discretization an optimal control force $F_{oc}(t)$, which prevents the compression endstop to be reached, is computed offline in a manner similar to a dynamic programming approach [114]. To reduce the dimension of the problem for the calculation of the optimal solution, only the suspension deflection and the damper velocity are considered, i.e. the state vector of the reduced model is $\mathbf{x}_{red} = [\ x_{cw} \quad \dot{x}_{cw}\ ]^T$. Moreover, the only nonlinearities considered in the employed model are a piecewise linear approximation of the damper characteristic and the friction effects to further reduce the computational complexity of the optimization problem. The measured suspension deflection, the estimated damper velocity as well as the actual values of $f_c(t)$ and $D_c(t)$ are then supplied to the resulting 4-dimensional look-up table for the force component

$$F_{oc}(t) = f(x_{cw}(t), \dot{\hat{x}}_{cw}(t), D_c(t), f_c(t)), \tag{8.17}$$

which is superimposed the reference signal for the hydraulic cylinder $F_{hy}^*(t)$, i.e. the new force reference becomes $\tilde{F}_{hy}^*(t) = F_{hy}^*(t) + F_{oc}(t)$. The formulation of the optimal control approach and the corresponding optimization problem is presented in detail in [146]. The resulting look-up table for $f_c = 0.8\,\text{Hz}$ and $D_c = 0.2$ is depicted in Figure 8.11 and in Figure 8.12 measurement results for the hybrid system including the feedforward extension are shown. As specified in the design of the feedforward component, only for negative suspension velocities $\dot{x}_c - \dot{x}_w$ the additional control forces are generated (Figure 8.11). The forces have been limited to 4 kN, which is sufficient for realistic road excitations.

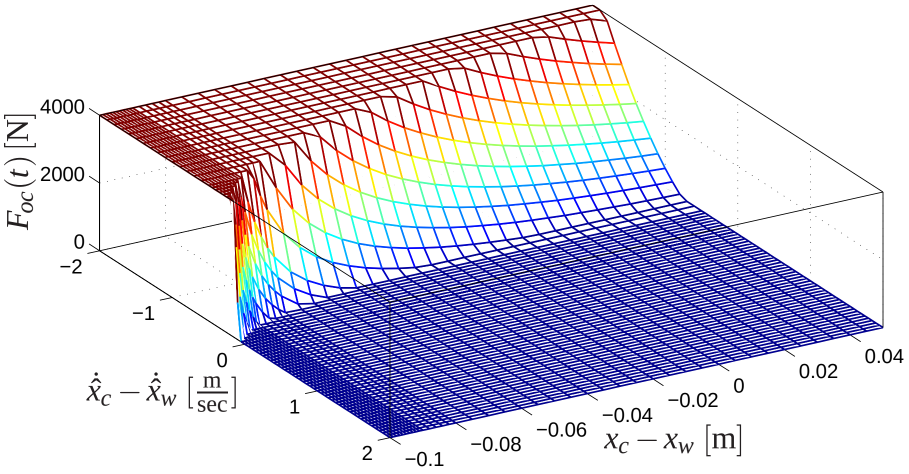

Figure 8.11: Look-up table for the force values for the optimal feedforward control component $F_{oc}(t)$ for $f_c = 0.8\,\text{Hz}$ and $D_c = 0.2$.

The singular disturbance excitation for the experimental validation of the concept has been chosen to match the natural frequency of the passive suspension's sprung mass. Thereby, the suspension deflection resulting from two bumps with a height of $\hat{h} = 12.8\,\text{cm}$ can become critical if it is applied for the low damped comfort oriented suspension configuration, that is emulated by the reference model based control approach for an otherwise uncritical driving state ($q_{fdyn}(t) = q_{susp}(t) = 0$). For the passive suspension configuration, that is used for the comparison in this experiment, the damping ratio has been increased to $D_{c,p} = 0.42$ to prevent excessive suspension deflection.

The effect of the optimal control component becomes clear in the comparison to the nonextended adaptive reference model based control approach (Figure 8.12): By the optimal control component one additional force peak is generated by the actuator, which prevents the suspension deflection limits from being reached in contrast to the hybrid suspension system without the optimal control component. Moreover, the weighted chassis acceleration is lowered by the optimal control component. The results are depicted in the spider chart in Figure 8.13 (upper).

Although both variants of the hybrid suspension show a lower performance for this particular road excitation signal than the strongly damped passive suspension, it can be clearly seen that the optimal control component compensates the discussed drawback of the adaptive control approach by a faster reaction to the disturbance. In the lower part of the spider chart, the measurement results for profile P1 ($v_{p1} = 75\,\frac{\mathrm{km}}{\mathrm{h}}$) are depicted to exemplarily study, how the disturbance feedforward term influences the performance on a challenging stochastic road profile (compare Section 8.5.3). The performance for profile P1 is, however, nearly identical to the regular adaptive reference model based controlled hybrid suspension so that it can be concluded that the extension leads to an overall improvement of the control concept.

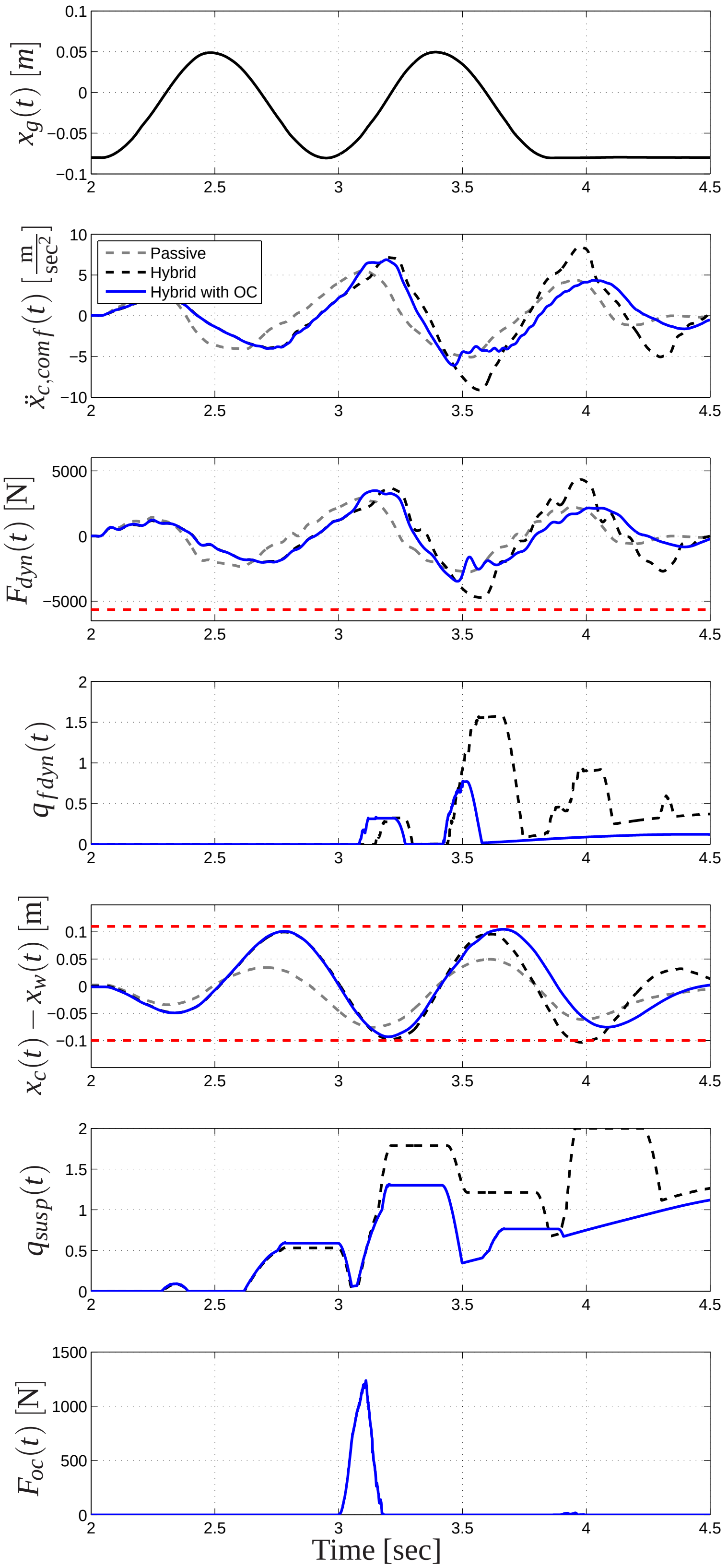

Figure 8.12: Measurement results of the hybrid suspension with optimal control (OC) component (excitation with bump in Figure 8.13); the red lines indicate the limits for the peak-value of F_{dyn} (i.e. $-F_{\text{stat}}$) and the suspension deflection limits.

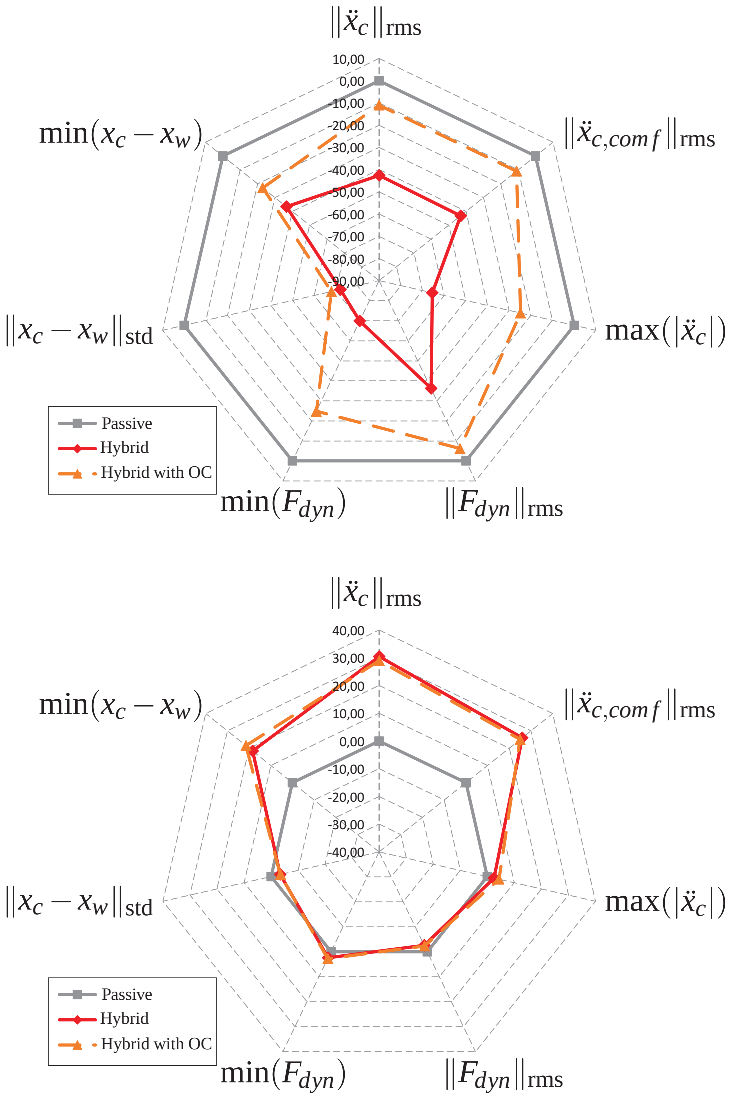

Figure 8.13: Measurement results to visualize the influence of the optimal control component for the excitation with the bump signal (Figure 8.12) (upper) and with profile P1 with $v_{p1} = 75\,\frac{\mathrm{km}}{\mathrm{h}}$ (lower).

8.7 Discussion and summary of results

The proposed reference model based control approach is a transparent and implementation oriented adaptive control concept for mechatronic suspension systems. Its performance potential in combination with the proposed hybrid suspension configuration has been validated in simulations and experiments utilizing a very realistic framework. The stability analysis has been conducted based on physical insights and the resulting switching restriction does not imply relevant performance limitations of the concept. From a study of the influence of actuator bandwidth it can be concluded that the performance benefit from increasing the actuator bandwidth above 5 Hz does not outweigh the significantly higher actuator power demand. The performance evaluation has been conducted with respect to established control concepts (skyhook based techniques) and the experimental results have underlined the performance potential of the proposed new adaptive suspension control concept. The concept has been experimentally proven to be robust against a sprung mass variation and its performance for highly critical singular disturbances for suspension deflection can be enhanced by a feedforward optimal control component.

8.7.1 Comparison to the adaptive switching control approach for the fully active suspension

When the performance improvements of the adaptively controlled hybrid suspension system are compared to the fully active suspension system controlled by the concept presented in Chapter 5, it must be considered that the suspension settings and test rigs employed for the validation of the concepts are different. Especially the fact that the hybrid suspension test rig, that is based on automotive components, has higher suspension deflection limits has supported the high performance of the hybrid suspension system and its even higher comfort improvement compared to the adaptive switching concept validated at the fully active suspension test rig (see Table 8.1 vs. Table 5.1 and the spider charts 5.12 vs. 8.8).

Simulations of the adaptive switching control approach applied to a model with a parametrization similar to the automotive quarter-car model presented in Chapter 7.3 have shown that comfort improvements of up to 47% (with respect to the passive suspension) are achievable for certain road profiles. This underlines the discussed performance restrictions of the proposed control approach for the hybrid suspension in Section 8.1 due to the passivity constraints of the underlying reference model. However, as pointed out in Chapter 6, the performance potential of the hybrid suspension system in combination with the proposed control approach is remarkable, which has been proven by the experimental comparison to the benchmark systems in Section 8.5. In [81] simulation results are presented for the adaptive reference model based control approach applied to a fully active suspension system and a hybrid suspension system with an actuator bandwidth of 5 Hz. The results show that although providing lower performance in terms of ride comfort, the considered hybrid system achieves a better overall performance regarding ride safety and power demand due to the fast semi-active damper. Moreover, besides the remarkable performance of the hybrid suspension system, its realizability and transparent tuneability have to be taken into account for a detailed evaluation.

The actuator power can be compared for the concepts presented in this Thesis if the scaling approach (8.16) presented in Section 8.5.2 is used. The equivalent power required for control by the fully active suspension for the considered excitation with profile P1 ($v_{p1} = 50\,\frac{\mathrm{km}}{\mathrm{h}}$) is $\|P^+_{m,c}\|_{\mathrm{rms}} = \frac{m_{c,car}}{m_{c,quad}} \cdot 24.8\,\mathrm{W} = 133.2\,\mathrm{W}$. Thus, the hybrid suspension requires approx. 14% less power ($\|P^+\|_{\mathrm{rms}} = 115\,\mathrm{W}$) despite its remarkable performance. It is noted that the presented control approach for the hybrid suspension system has been designed to focus on performance. To further reduce the power demand of the hydraulic actuator the control allocation concept and the adaptation laws of the control approach can be modified accordingly (see Chapter 9).

Implementation of the reference model based controller at the fully active suspension test rig

The reference model based adaptive control approach has also been implemented at the test rig for the fully active suspension system to directly compare the performance with the adaptive switching control approach presented in Chapter 5 [145]. In this case, the high bandwidth electrical linear motor (see Chapter 3.3.1) has to generate the complete force determined from the adaptive reference model based control approach since it has to emulate the change of f_c and D_c. The results for road profile P1 ($v_{p1} = 50\,\frac{\mathrm{km}}{\mathrm{h}}$) are summarized in the spider chart in Figure 8.14.

However, for this control approach an average positive mechanical power of $\|P^+\|_{\mathrm{rms}} = 58\,\mathrm{W}$ is necessary, which is more than twice as high as for the adaptive switching based control (see Table 5.2) at the quadricycle test rig. The required actuator forces are also higher for the adaptive reference model based approach ($\|F\|_{\mathrm{rms}} = 173\,\mathrm{N}$ vs. $\|F\|_{\mathrm{rms}} = 130\,\mathrm{N}$). This

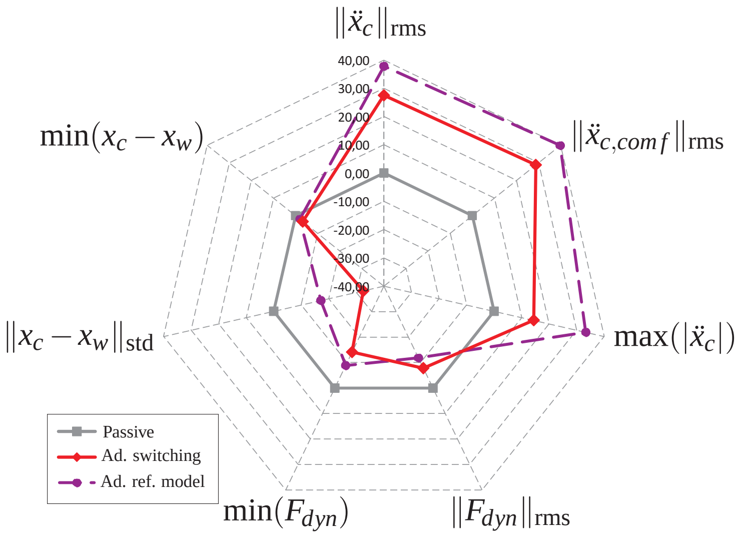

Figure 8.14: Reference model based controller performance at the fully active suspension system (profile P1 with $v_{p1} = 50\,\frac{\text{km}}{\text{h}}$): Measurement results in comparison to the adaptive switching controller (see Chapter 3).

higher controller effort results from the fact that in order to emulate the low damping ratio, the damping forces of the passive damper must be compensated such that a significant part of the actuator power has been dissipated by the damper. This further motivates the combination of the adaptive reference model based control approach and the hybrid suspension system, which provides excellent suspension performance at significantly lower required actuator power.

Thus, the adaptive reference model based controller structure overcomes the drawbacks of the adaptive controller structure for the fully active suspension system. It provides more transparent tuning parameters by means of the natural frequency and the damping ratio of the chassis mass. If a more handling oriented controller setting is desired, the adaptation laws given by Figure 8.5 can be modified accordingly without affecting the stability of the system. The stability proof itself has been less complex than for the fully active suspension by using the passivity restrictions induced by the structure of the adaptive reference model. However, the experimental results have shown that despite these restrictions the performance of the adaptively controlled hybrid system is remarkable, which underlines the feasibility of this new suspension control approach. Moreover, the hierarchical controller structure is well suitable to be integrated in a global chassis control architecture. For this purpose, the reference model structure can be extended towards a full-car model.

8.7.2 Realizability of the adaptively controlled hybrid suspension

To conclude, some brief remarks on the realizability of the hybrid suspension system are given. The approach has been motivated by the fact that the mechatronic suspension components, which are used for the realization of the hybrid suspension strut at the quarter-car test rig, are stock components from production vehicles. Hence, the realization of the hardware combination is primarily a matter of economical aspects. Moreover, of course the complexity of the hydraulic actuator system and the higher power demand compared to semi-active suspension concepts have to be taken into account.

However, the fact that also electromechanical approaches for the realization of low bandwidth suspension systems exist [109], which offer lower power demand, better integrability into modern electromobility focussed automotive concepts and potentially even the possibility of energy recuperation (see Chapter 2.4.2), fosters the realizability of the hybrid suspension concept.

Chapter 9

CONCLUSION AND FUTURE WORK

This Thesis has presented adaptive control concepts that enable to exploit the performance potential of mechatronic vehicle suspensions. The results range from new estimator concepts, new adaptive suspension control techniques to the proposal of a new mechatronic suspension system, the *hybrid suspension*. The proposed control concepts foster the flexibility of modern mechatronic suspension systems by adapting the dynamic behavior of the suspension to the driving state of the vehicle. Thereby, significant performance enhancements in terms of ride comfort and ride safety can be achieved without violating suspension travel limits.

Since for the determination of the vehicle's driving state and for the implementation of state feedback based suspension controllers an estimator concept is required, two different estimators have been presented and compared to an Extended Kalman filter representing a benchmark in terms of estimation quality. The first one is an estimator including parallel Kalman filters and a damper force estimation to take into account the nonlinearity of the damper characteristic. This eases the conflict of the parametrization of a single Kalman filter for the estimation of different signals in the presence of model uncertainties and measurement noise. The second estimator uses a simple filter based concept that is especially suited for the determination of the damper velocity and the dynamic wheel load. It has been shown that both concepts offer excellent estimation performance with respect to the Extended Kalman filter and to estimation approaches presented in the literature.

In order to study the potential of adaptively controlled fully active suspensions, a switching adaptive suspension control concept, that dynamically interpolates between different optimal controllers according to the dynamic wheel load and the suspension deflection, has been presented. The stability of the closed-loop system has been thoroughly analyzed and it has been shown that the adaptively controlled suspension system including the nonlinear damper characteristic is stable for arbitrary fast adaptation of the controller parameters. For the experimental validation, a quarter-vehicle test rig based on a quadricycle suspension, that includes a linear motor to realize the fully active suspension, has been designed. The new control approach achieves significant performance improvements in the simulations and experiments and enables the suspension to handle road profiles which would not be accessible with the considered velocities for passive or mechatronic suspension systems with ride comfort focussed time-invariant controllers.

Despite this performance potential of the fully active suspension system, the integration of these systems in production vehicles is obviated by their costs and actuator power demand. Therefore, an analysis has been presented showing that the adaptively controlled hardware combination of a low bandwidth actuator and a continuously variable damper can approximate the performance of a fully active suspension. This *hybrid suspension* configuration has been realized based on suspension actuators from production vehicles and has been integrated into an appropriately designed automotive quarter-car test rig.

To fulfill the requirement of transparent tuning parameters for adaptively controlled suspension systems, a new control method has been presented and applied for the hybrid suspension system: Adaptive reference model based control. Utilizing this control approach, the hybrid suspension emulates the dynamic behavior of passive suspensions in terms of natural frequency and damping ratio of the sprung mass. By an adaptation strategy it is specified, which passive suspension configuration is optimally suited for the current driving state of the vehicle to maximize ride comfort while considering the dynamic wheel load and suspension limits. Thereby, well-known tuning methods of passive suspensions, based on carpet plots, can be employed to shape the adaptation laws. Modifications of these adapation laws do not affect the stability of the system, which is preserved by a physically motivated switching restriction. The resulting hierarchical controller structure is well suited to be implemented in global chassis control architectures. Simulations and experiments have shown that remarkable comfort and safety improvements can be achieved by the proposed adaptively controlled hybrid suspension system.

All concepts have been analyzed and experimentally validated in a very realistic framework regarding the suspension nonlinearities, disturbance signals as well as sensor and actuator architectures. It has been shown that the performance of mechatronic suspension systems can be significantly improved by the proposed adaptive suspension control techniques and that the hybrid suspension system is a realizable configuration, which offers many advantages over fully active suspension systems.

The following areas of future research are proposed to further evaluate the concepts presented in this Thesis and to enhance their performance potential:

1. **Full-car vehicle dynamics:** Since the adaptive control concepts have been presented in a quarter-vehicle framework, the concepts can be extended for a full-car model. Thereby, the effect of additional disturbances, e.g. chassis accelerations and wheel load deviations induced by the pitch and roll movements of the car, can be analyzed. The reference model based control concept can be extended appropriately to take the further vertical dynamic degrees of freedom into account.

2. **Energy efficient adaptation:** Although the hybrid suspension configuration offers a significant advantage in terms of power demand over the fully active suspension system, the adaptive reference model based control approach has been designed to focus on performance. In further studies it could be investigated, how the adaptation laws can be modified in order to prevent control actions of the actuator, that only marginally enhance the performance but significantly increase the power demand.

3. **Control concept of the semi-active damper:** The presented control concept of the semi-active damper is based on feedforward control of the damper force utilizing the static damper characteristics. In order to improve the force tracking ability of the controlled semi-active damper, more complex control schemes can be used, e.g. those that also consider hysteresis effects. In this context it should be evaluated, if an additional sensor to measure the force between the suspension strut and the sprung mass is a feasible and worthwile approach to allow the implementation of feedback control for the damper force. Since the damper is a highly nonlinear dynamic system, the quality of more sophisticated control concepts, however, depend on the accuracy of the damper model. Therefore, in order to enhance the performance of semi-active and hybrid suspension control, model based control of the damper is recommended. Moreover, suspension control concepts involving frequency-dependent damping forces can be utilized.

4. **Signal based sprung mass estimation:** In order to increase the robustness of the reference model based controller structure and the estimator concepts (parallel Kalman filter structure and filter based estimation), an estimation algorithm for the sprung mass could be implemented. In this Thesis, the estimation of the vehicle mass by means of an Extended Kalman filter has been presented. A filter based mass estimator (see also [37]) is under current development, that can be used to change the parametrization of the adaptive reference model if the sprung mass deviates significantly from its nominal value.

BIBLIOGRAPHY

[1] www.zf.com. Status: 10/2010.

[2] www.delphi.com. Status: 10/2010.

[3] http://www.bose.de/de/de/learning-centre/suspension-problem/index.jsp. Status: 10/2010.

[4] M. O. Abdalla, N. Al Shabatat, and M. Al Quaisi. Linear matrix inequality based control of vehicle active suspension system. *Vehicle System Dynamics*, 47:121 – 134, 2009.

[5] A. Akbari. *Multi-Objective* H_∞/GH_2 *preview control of active vehicle suspensions*. PhD thesis, Technische Universität München, 2009.

[6] Y. Al-Assaf. Adaptive control for vehicle active suspension systems. In *Proceedings of the 1996 American Control Conference*, pages 1183 – 1185, 1996.

[7] A. Alleyne and J. K. Hedrick. Nonlinear Adaptive Control of Active Suspensions. *IEEE Transactions on Control Systems Technology*, 3:94 – 101, 1995.

[8] B. Anderson and J. B. Moore. *Optimal Control: Linear Quadratic Methods*. Dover Publications, 2007.

[9] M. Becker, K.-P. Jäker, F. Frühauf, and R. Rutz. Development of an active suspension system for a Mercedes-Benz coach (O404). In *Proceedings of the 1996 IEEE International Symposium on Computer-aided Control System Design*, pages 146 – 151, 1996.

[10] C. Bohn, H.-J. Karkosch, and F. Svaricek. Zustandsbeobachter für periodische Signale: Anwendungen zur aktiven Kompensation von motorerregten Karosserieschwingungen. *AT-Automatisierungstechnik*, 53:525 – 536, 2005.

[11] H.-H. Braess and U. Seiffert, editors. *Handbuch Kraftfahrzeugtechnik*. Vieweg Verlag, Wiesbaden, 2003.

[12] R. Brent. *Algorithms for Minimization without Derivatives*. Prentice Hall, Upper Saddle River, New Jersey, 1973.

[13] B. Buttkus. *Spectral analysis and filter theory in applied geophysics*. Springer, Berlin, 2000.

[14] E. F. Camacho and C. Bordons. *Model Predictive Control*. Springer, London, 2005.

[15] M. Canale, M. Milanese, and C. Novara. Semi-active suspension control using ”fast” model-predictive techniques. *IEEE Transactions on Control Systems Technology*, 14(6):1034–1046, 2006.

[16] P. Causemann. Moderne Schwingungsdämpfung. *Automobiltechnische Zeitung*, 105:1072 – 1079, 2003.

[17] M. Chaves, J. Maia, and J. Esteves. Analysis of an electromagnetic automobile suspension. In *Proceedings of the 2008 International Conference on Electrical machines*, pages 1 – 4, 2008.

[18] W. Cheney and D. Kincaid. *Numerical mathematics and computation*. Thomson Brooks/Cole, Belmont, 2008.

[19] S. K. Chung and H.-B. Shin. High-voltage power supply for semi-active suspension system with ER-fluid damper. *IEEE Transactions on Vehicular Technology*, 53:206 – 214, 2004.

[20] C. A. Coello Coello, G. B. Lamont, and D. A. Van Veldhuizen. *Evolutionary Algorithms for Solving Multi-Objective Problems*. Springer, London, 2007.

[21] Continental AG. Global chassis control is the future of the automobile. Online-Report, 2002.

[22] R. Danisch. Der Porsche Panamera. *Automobiltechnische Zeitung ATZ*, 10:726 – 736, 2009.

[23] K. Deb, A. Pratap, S. Agarwal, and T. Meyarivan. A fast and elitist multiobjective genetic algorithm: NSGA-II. *IEEE Transactions on Evolutionary Computation*, 6(2):182–197, 2000.

[24] R. K. Dixit and G. D. Bruckner. Sliding mode observation and control for semi-active vehicle suspensions. *Vehicle System Dynamics*, 43:83 – 105, 2005.

[25] S. Duym. Simulation tools, modelling and identification for an automotive shock absorber in the context of vehicle dynamics. *Vehicle System Dynamics*, 33:261–285, 2000.

[26] S. Duym and K. Reybrouck. Physical characterization of nonlinear shock absorber dynamics. *European Journal of Mechanical and Environmental Engineering*, 43(4):181–188, 1998.

[27] S. Duym, R. Stiens, and K. Reybrouck. Evaluation of shock absorber models. *Vehicle System Dynamics*, 27:109–127, 1997.

[28] K. Efatpenah, J. H. Beno, and S. P. Nichols. Energy requirements of a passive and an electromechanical active suspension system. *Vehicle System Dynamics*, 34:437 – 458, 2000.

[29] M. E. Elbeheiry. Suboptimal bilinear control methods applied to suppressing car vibrations. *Journal of Vibration and Control*, 7:279–306, 2001.

[30] I. J. Fialho and G. J. Balas. Design of nonlinear controllers for active vehicle suspensions using parameter-varying control synthesis. *Vehicle System Dynamics*, 33:351–370, 2000.

[31] I. J. Fialho and G. J. Balas. Road adaptive active suspension design using linear parameter-varying gain-scheduling. *IEEE Transactions on Control Systems Technology*, 10(1):43–54, 2002.

[32] D. Fischer and R. Isermann. Mechatronic semi-active and active vehicle suspensions. *Control Engineering Practice*, 12:1353 – 1367, 2004.

[33] O. Föllinger. *Regelungstechnik*. Hüthig, Heidelberg, 8. edition, 1994.

[34] O. Fritsch. Stabilitätssichernde LPV-Reglerentwurfsverfahren mit Applikationspotential in aktiven Fahrwerken. Master's thesis, Technische Universität München, 2008. Supervisor: G. Koch.

[35] O. Fritsch, G. Koch, and B. Lohmann. Deflection adaptive LPV control of an active suspension system. In *Proceedings of the 2009 European Control Conference*, pages 4404 – 4409, 2009.

[36] M. Fröhlich. *Ein robuster Zustandsbeobachter für ein semiaktives Fahrwerkregelsystem*. PhD thesis, Technische Universität München, 2007.

[37] M. Fröhlich and M. Nyenhuis. Entwicklung und Untersuchung eines Zustandsbeobachters für ein semiaktives Fahrwerkregelsystem. In *Tagungsband fahrwerk.tech*, 2005.

[38] G. S. Gao and S. P. Yang. Semi-active control performance of railway vehicle suspension featuring magnetorheological dampers. In *Proceedings 1st IEEE Conference on Industrial Electronics and Applications*, pages 1–5, 2006.

[39] H. Gao, J. Lam, and C. Wang. Multi-objective control of vehicle active suspension systems via load dependent controllers. *Journal of Sound and Vibration*, 290:654 – 675, 2006.

[40] N. Giorgetti, A. Bemporad, H. E. Tseng, and D. Hrovat. Hybrid model predictive control application towards optimal semi-active suspension. In *Proceedings IEEE International Symposium on Industrial Electronics ISIE 2005*, pages 391–398, 2005.

[41] N. Giorgetti, A. Bemporad, H. E. Tseng, and D. Hrovat. Hybrid model predictive control application towards optimal semi-active suspension. *International Journal of Control*, 79:521 – 533, 2006.

[42] K. E. Graves, P. G. lovenitti, and D. Toncich. Electromagnetic regenerative damping in vehicle suspension systems. *International Journal of Vehicle Design*, 24:182 – 197, 2000.

[43] E. Guglielmino, T. Sireteanu, C. T. Stammers, G. Ghita, and M. Giuclea. *Semi-active suspension control - Improved vehicle ride and road friendliness*. Springer, London, 2008.

[44] A. Guia, M. Melas, C. Seatzu, and G. Usai. Design of a predictive semiactive suspension system. *Vehicle System Dynamics*, 41:277–300, 2004.

[45] S. Guo, B. Xu, H. Xing, and C. Pan. Skyhook isolation with magnetorheological damper. In *Proceedings of the Sixth World Congress on Intelligent Control and Automation WCICA 2006*, volume 2, pages 7860–7863, 2006.

[46] A. Hać. Adaptive control of vehicle suspensions. *Vehicle System Dynamics*, 16:57 – 74, 1987.

[47] A. Hać. Optimal linear preview control of active vehicle suspension. *Vehicle System Dynamics*, 21:167–195, 1992.

[48] A. Hartmann and M. Ersoy. Aktives Fahrwerk zur integrierten Aufbaustabilisierung und variabler Raddämpfung - ASCA. In *15. Aachener Kolloquium*, 2006.

[49] J. K. Hedrick and T. Butsuen. Invariant properties of automotive suspensions. *Proceedings of the Institution of Mechanical Engineers, Part D: Journal of Automobile Engineering*, 240:21 – 27, 1990.

[50] B. Heißing. *Fahrwerkhandbuch*. Vieweg Verlag, Wiesbaden, 2007.

[51] T. Hestermeyer. *Strukturierte Entwicklung der Informationsverarbeitung für die aktive Federung eines Schienenfahrzeugs*. PhD thesis, University of Paderborn, 2006.

[52] C. Hilgers, J. Brandes, H. Ilias, H. Oldenettel, A. Stiller, and C. Treder. Aktives Luftfederfahrwerk für eine größere Bandbreite zwischen Komfort- und Dynamik-Abstimmung. *Automobiltechnische Zeitung ATZ*, 9:600 – 609, 2009.

[53] K.-S. Hong, H.-C. Sohn, and J. K. Hedrick. Modified skyhook control of semi-active suspensions: A new model, gain scheduling, and hardware-in-the-loop tuning. *Journal of Dynamic Systems, Measurement, and Control*, 124:158 – 167, 2002.

[54] D. Hrovat. Influence of unsprung weight on vehicle ride quality. *Journal of Sound and Vibration*, 145(1):497–516, 1987–1988.

[55] D. Hrovat. Survey of advanced suspension developments and related optimal control applications. *Automatica*, 33(10):1781–1817, 1997.

[56] H. Imine and Y. Delanne. Triangular observers for road profile inputs estimation and vehicle dynamics analysis. In *Proceedings of the 2005 IEEE International Conference on Robotics and Automation*, pages 4751 – 4756, 2005.

[57] R. Isermann. Automotive mechatronic systems - general developments and examples. *AT-Automatisierungstechnik*, 9:419 – 429, 2006.

[58] ISO. *ISO 8608:1995 - Mechanical vibration – Road surface profiles – Reporting of measurement data*. International Standard Organization, 1995.

[59] ISO. *ISO 2631-1:1997 - Mechanical vibration and shock – Evaluation of human exposure to whole-body vibration*. International Organization for Standardization, 1997.

[60] M. Jautze, A. Bogner, J. Eggendinger, G. Rekewitz, and A. Stumm. Das Verstelldämpfersystem Dynamische Dämpfer Control. *ATZ extra*, Sonderheft: Der neue BMW 7er:100–103, 2008.

[61] W. D. Jones. Easy ride - Bose corp. uses speaker technology to give cars adaptive suspension. *IEEE Spectrum*, 5:12 – 14, 2005.

[62] S. J. Julier and J. K. Uhlmann. A New Extension of the Kalman Filter to Nonlinear Systems. In *Proceedings of SPIE*, pages 182 – 193, 1997.

[63] R. E. Kalman. A new approach to linear filtering and prediction problems. *Transactions for the ASME–Journal of Basic Engineering*, 82 (Series D):35–45, 1960.

[64] H. Kamimae, M. Yamashita, K. Yoshida, and H. Nakai. Sprung- and unsprung-structure relative velocity computing apparatus for vehicle, 2007. Patent No. EP 1477342 B1.

[65] D. Karnopp. Active damping in road vehicle suspension systems. *Vehicle System Dynamics*, 12:291–316, 1983.

[66] D. Karnopp. Theoretical limitations in active vehicle suspensions. *Vehicle System Dynamics*, 15:41 – 54, 1986.

[67] D. Karnopp. How significant are transfer function relations and invariant points for a quarter car suspension model? *Vehicle System Dynamics*, 47:457 – 464, 2009.

[68] D. Karnopp, M. J. Crosby, and R. A. Harwood. Vibration control using semi-active force generators. *ASME Journal of Engineering for Industry*, 96:619–626, 1974.

[69] D. Karnopp and D. Margolis. Adaptive suspension concepts for road vehicles. *Vehicle System Dynamics*, 13:145 – 160, 1984.

[70] H. K. Khalil. *Nonlinear systems*. Pearson Education, Upper Saddle River, 2002.

[71] R.-K. Kim and K.-S. Hong. Skyhook control using a full-vehicle model and four relative displacement sensors. In *Proceedings of the International Conference on Control, Automation and Systems ICCAS '07*, pages 268–272, 2007.

[72] T. Kloiber. Beobachtergestützte Reglerstrukturen für die adaptive Regelung nichtlinearer aktiver Fahrwerke. Master's thesis, Technische Universität München, 2010. Supervisor: G. Koch.

[73] T. Kloiber, G. Koch, and B. Lohmann. Modified optimal control of a nonlinear active suspension system. In *Proceedings of the 49th IEEE Conference on Decision and Control*, 2010.

[74] G. Koch, K. J. Diepold, and B. Lohmann. Multi-objective road adaptive control of an active suspension system. In H. Ulbrich and L. Ginzinger, editors, *Motion and Vibration Control - Selected papers from MOVIC 2008*, pages 189 – 200. Springer, 2008.

[75] G. Koch, O. Fritsch, and B. Lohmann. Potential of low bandwidth active suspension control with continuously variable damper. In *Proceedings of the 17th IFAC World Congress*, pages 3392 – 3397, 2008.

[76] G. Koch, O. Fritsch, and B. Lohmann. Potential of low bandwidth active suspension control with continuously variable damper. *Control Engineering Practice*, 18:1251 – 1262, 2010.

[77] G. Koch, T. Kloiber, and B. Lohmann. Nonlinear and filter based estimation for vehicle suspension control. In *Proceedings of the 49th IEEE Conference on Decision and Control*, 2010.

[78] G. Koch, T. Kloiber, E. Pellegrini, and B. Lohmann. A nonlinear estimator concept for active vehicle suspension control. In *Proceedings of the 2010 American Control Conference*, pages 4576 – 4581, 2010.

[79] G. Koch, E. Pellegrini, and B. Lohmann. *Entwurf mechatronischer Systeme - 6. Paderborner Workshop*, chapter Zustandsadaptive Regelung eines aktiven Fahrwerks - Entwurf und Implementierung am Viertelfahrzeugprüfstand, pages 43 – 56. Heinz Nixdorf Schriftenreihe, 2009.

[80] G. Koch, E. Pellegrini, S. Spirk, and B. Lohmann. Design and modeling of a quarter-vehicle test rig for active suspension control. Technical Report on Automatic Control - TRAC-5 2, Institute of Automatic Control, Technische Universität München, July 2010.

[81] G. Koch, S. Spirk, and B. Lohmann. Reference model based adaptive control of a hybrid suspension system. *Proceedings of the IFAC Symposium Advances in Automotive Control*, 2010.

[82] G. Koch, S. Spirk, E. Pellegrini, N. Pletschen, and B. Lohmann. Experimental validation of a new adaptive control approach for a hybrid suspension system. In *Accepted and to be presented at the 2011 American Control Conference*, 2011.

[83] U. Kramer. *Kraftfahrzeugführung: Modelle, Simulation und Regelung*. Carl Hanser Verlag, München, 2007.

[84] H. Kwakernaak and R. Sivan. *Linear Optimal Control Systems*. John Wiley and Sons, Inc., New York, 1972.

[85] C. Lalanne. *Mechanical Vibration and Shock: Random Vibration*, volume 3. Taylor and Francis, New York, 2002.

[86] C. Lauwerys, J. Swevers, and P. Sas. Robust linear control of an active suspension on a quarter car test-rig. *Control Engineering Practice*, 13:577–586, 2005.

[87] V. Leite and P. L. D. Peres. Pole location control design of an active suspension system with uncertain parameters. *Vehicle System Dynamics*, 43:561 – 579, 2005.

[88] D. Liberzon. *Switching in systems and control*. Birkhäuser, Boston, 2003.

[89] J. Lin and I. Kanellakopoulos. Nonlinear design of active suspensions. *IEEE Control Systems Magazine*, 17:45 – 59, 1997.

[90] J. Lin and I. Kanellakopoulos. Road-adaptive nonlinear design of active suspensions. *Proceedings of the 1997 American Control Conference*, pages 714 – 718, 1997.

[91] S. Lin and I. Kanellakopoulos. Adaptive nonlinear control in active suspensions. In *Proceedings of the 13th IFAC World Congress*, pages 113 – 118, 1996.

[92] O. Lindgärde. Kalman filtering in semi-active suspension control. In *Proceedings of the 15th Triennial World Congress*, 2002.

[93] Y. Liu, T. P. Waters, and M. J. Brennan. A comparison of semi-active damping control strategies for vibration isolation of harmonic disturbance. *Journal of Sound and Vibration*, 208:21–39, 2005.

[94] L. Ljung. *System Identification - Theory for the user*. Prentice Hall, USA, 1999.

[95] J. Löfberg. Yalmip : A toolbox for modeling and optimization in MATLAB. In *Proceedings of the CACSD Conference*, pages 284 – 289, 2004.

[96] J. Lu and M. DePoyster. Multiobjective optimal suspension control to achieve integrated ride and handling performance. *IEEE Transactions on Control Systems Technology*, 10:807 – 821, 2002.

[97] G. Ludyk. *Theoretische Regelungstechnik 2*. Springer, Berlin, 1995.

[98] J. Lunze. *Regelungstechnik 1*. Springer, Berlin, 2001.

[99] J. Lunze. *Regelungstechnik 2*. Springer, Berlin, 2002.

[100] I. Martins, J. Esteves, G. D. Marques, and F. Pina da Silva. Permanent-magnets linear actuators applicability in automobile active suspensions. *IEEE Transactions on vehicular technology*, 55:89 – 94, 2006.

[101] I. Martins, J. Esteves, F. Pina da Silva, and P. Verdelho. Electromagnetic hybrid active-passive vehicle suspension system. In *Proc. of the 49th Vehicular Technology Conference*, volume 3, pages 2273 – 2277, 1999.

[102] W. Matschinsky. *Radführungen der Straßenfahrzeuge - Kinematik, Elasto-Kinematik und Konstruktion*. Springer, Berlin, 2007.

[103] P. S. Maybeck. *Stochastic Models, Estimation and Control*, volume 1. Academic Press, Inc, New York, 1st edition, 1979.

[104] P. S. Maybeck. *Stochastic Models, Estimation and Control*, volume 2. Academic Press, Inc, New York, 1st edition, 1982.

[105] R. K. Mehra, J. N. Amin, K. J. Hedrick, C. Osorio, and A. Gopalasany. Active suspension using preview information and model predictive control. In *Proceedings of the 1997 IEEE International Conference on Control Applications*, pages 860 – 865, 1997.

[106] M. Mitschke and H. Wallentowitz. *Dynamik der Kraftfahrzeuge*. Springer, Berlin, 2004.

[107] Moog. *Servoventile - Baureihe D636/638 (Valve datasheet)*, 2010.

[108] R. Morselli, R. Zanasi. Control of mechatronic systems by dissipative devices: Application to semi-active vehicle suspensions. In *Proceedings of the 2006 American Control Conference*, 2006.

[109] M. Münster, U. Mair, H.-J. Gilsdorf, A. Thomä, C. Mller, M. Hippe, and J. Hoffmann. Elektromechanische aktive Aufbaukontrolle. *Automobiltechnische Zeitung ATZ*, 9:644 – 649, 2009.

[110] M. Nagai. Recent researches on active suspensions for ground vehicles. *Japan Society of Mechanical Engineers - International Journal, Series C*, 36(2):161 – 170, 1993.

[111] S. Ohsaku. Vorrichtung und Verfahren zum Schätzen einer kinetischen Zustandsgröße für Kraftfahrzeuge. Offenlegungsschrift DE10016896A1, 2000. Patent No. DE 10016898A1.

[112] H. Olsson, K.J. Åström, C. C. de Wit, M. Gäfvert, and Lischinsky. P. Friction models and friction compensation. *European Journal of Control*, 4(3):176 – 195, 1998.

[113] A. Pahn. FEM Modellierung eines CATIA-Viertelfahrzeugprüfstandsmodells. Project Thesis, 2010. Supervisor: E. Pellegrini.

[114] M. Papageorgiou. *Optimierung: Statische, dynamische, stochastische Verfahren für die Anwendung*. Oldenbourg R. Verlag, München, 1996.

[115] J. Paschedag. *Aktive Schwingungsisolation in Kfz-Motoraufhängungen - Systemkonfiguration und Methoden*. PhD thesis, Technische Universität München, 2008.

[116] J. Paschedag and G. Koch. Energy saving actuator arrangements in an actively damped engine suspension system. In *Proceedings of the 17th IFAC World Congress*, pages 4701 – 4706, 2008.

[117] J. J. H. Paulides, L. Encica, E. A. Lomonova, and A. J. J. A. Vandenput. Design considerations for a semi-active electromagnetic suspension system. *IEEE Transactions on magnetics*, 42:3446 – 3448, 2006.

[118] E. Pellegrini, G. Koch, and B. Lohmann. Physical modeling of a nonlinear semi-active vehicle damper. In *Proceedings of the IFAC Symposium Advances in Automotive Control*, 2010.

[119] A. G. Piersol, C. M. Harris, and T. Paez. *Harris' shock and vibration handbook*. McGraw-Hill, 2009.

[120] C. Poussot-Vassal, O. Sename, L. Dugard, P. Gáspár, Z. Szabó, and J. Bokor. A new semi-active suspension control strategy through LPV technique. *Control Engineering Practice*, 16:1519 – 1534, 2008.

[121] M. Pyper, W. Schiffer, and W. Schneider. *ABC - Active Body Control*. Verlag Moderne Industrie, Augsburg, 2003.

[122] R. Rajamani and J. K. Hedrick. Adaptive observers for active automotive suspensions: Theory and experiment. *IEEE Transactions on Control Systems Technology*, 3(1):86 – 93, 1995.

[123] M. Ramsbottom and D. A. Crolla. Simulation of an adaptive controller for a limited-bandwidth active suspension. *International Journal of Vehicle Design*, 21(4/5):355 – 371, 1999.

[124] C. Rathgeber. Modellbildung und Regelung eines hydraulischen Aktuators für ein aktives Fahrwerk. Project Thesis, 2010. Supervisor: G. Koch.

[125] J. Reimpell and H. Stoll. *Fahrwerktechnik: Stoß- und Schwingungsdämpfer*. Vogel Buchverlag, Würzburg, 1989.

[126] H. K. Sachs. An adaptive control for vehicle suspensions. *Vehicle System Dynamics*, 8:201 – 206, 1979.

[127] M. Sackmann. *Modifizierte optimale Regelung: Nichtlinearer Reglerentwurf unter Verwendung der Hyperstabilitätstheorie*. PhD thesis, Universität Karlsruhe, 2001.

[128] S. Savaresi and C. Spelta. Improving the performance of a semi-active suspension at the damping-invariant point. In *Proceedings of the 2006 IEEE Intelligent Transportation Systems Conference*, pages 1394 – 1399, 2009.

[129] S. M. Savaresi, C. Poussot-Vassal, C. Spelta, O. Sename, and L. Dugard. *Semi-active suspension control design for vehicles*. Butterworth-Heinemann, Amsterdam, 2010.

[130] E. Schäfer, K.-P. Jäker, and A. Wielenberg. Entwicklung und Inbetriebnahme einer aktiven Federung für ein geländegängiges Nutzfahrzeug. In *3. VDI/VDE-Fachtagung zur Steuerung und Regelung von Fahrzeugen und Motoren (AUTOREG 2006)*, 2006.

[131] R. Schedel. Fahrwerk gewinnt Energie zurück und spart CO_2. www.atzonline.de, 03/2009.

[132] A. Schindler. *Neue Konzeption und erstmalige Realisierung eines aktiven Fahrwerks mit Preview-Strategie*. PhD thesis, Universität Karlsruhe, 2009.

[133] A. Schöpfel, H. Stingl, R. Schwarz, W. Dick, and A. Biesalski. Audi Drive Select. *ATZ extra*, Sonderheft: Der neue Audi A4:124–138, 2007.

[134] R. Schüssler and B. Acker. Aktives Federungssystem, 1988. Patent No. DE 3818188 C2.

[135] R. Schwarz and P. Rieth. Global Chassis Control - Systemvernetzung im Fahrwerk. *AT-Automatisierungstechnik*, 51:300–312, 2003.

[136] K. Sharma, D. A. Crolla, and D. A. Wilson. The design of a fully active suspension system incorporating a Kalman filter for state estimation. In *Proceedings of the International Conference on Control*, pages 344 – 349, 1994.

[137] R. S. Sharp and D. A. Crolla. Road Vehicle System Design – a review. *Vehicle System Dynamics*, 16:167–192, 1987.

[138] R. S. Sharp and S. A. Hassan. On the Performance of Active Automobile Suspension Systems of Limited Bandwidth. *Vehicle System Dynamics*, 16:213–225, 1987.

[139] R.S. Sharp and S. A. Hassan. An evaluation of passive automotive suspension systems with variable stiffness and damping. *Vehicle System Dynamics*, 15:335 – 350, 1986.

[140] J. J. E. Slotine and W. Li. *Applied Nonlinear Control*. Prentice Hall, Englewood Cliffs, New Jersey, 1991.

[141] M. C. Smith and G. W. Walker. Performance limitations and constraints for active and passive suspensions: A mechanical multi-port approach. *Vehicle System Dynamics*, 33:137 – 168, 2000.

[142] M. C. Smith and F.-C. Wang. Controller parametrization for disturbance response decoupling: Application to vehicle active suspension control. *IEEE Transactions on control systems technology*, 10:393 – 407, 2002.

[143] H. Sohn, K. Hong, and J. K. Hedrick. Semi-active control of the Macpherson suspension system: Hardware-in-the-loop simulations. In *Proceedings of the 2000 IEEE International Conference on Control Applications*, pages 982 – 987, 2000.

[144] C. Spelta, F. Previdi, S. M. Savaresi, P. Bolzern, M. Cutini, and C. Bisaglia. A novel control strategy for semi-active suspensions with variable damping and stiffness. In *Proceedings of the 2010 American Control Conference*, pages 4582 – 4587, 2010.

[145] S. Spirk. Adaptive Regelung aktiver Fahrwerke. Master's thesis, Technische Universität München, 2010. Supervisor: G. Koch.

[146] S. Spirk, G. Koch, and B. Lohmann. Improving suspension control by an optimal control component and disturbance compensation. In *Accepted and to be presented at the 18th IFAC World Congress*, 2011.

[147] R. Streiter. *Entwicklung und Realisierung eines analytischen Regelkonzeptes für eine aktive Federung*. PhD thesis, Technische Universität Berlin, 1996.

[148] R. Streiter. ABC-Pre-Scan im F700 - Das vorausschauende aktive Fahrwerk von Mercedes-Benz. *Automobiltechnische Zeitung*, 110:388 – 397, 2008.

[149] J. F. Sturm. *Using SEDUMI 1.02, a MATLAB Toolbox for Optimization over Symmetric Cones*. Department of Econometrics, Tillburg University, 2001. Manual.

[150] M. Sunwoo, K. C. Cheok, and N. J. Huang. Model reference adaptive control for vehicle active suspension systems. *IEEE Transactions on industrial electronics*, 38(3):217 – 222, 1991.

[151] K. A. Tahboub. Active nonlinear vehicle-suspension variable-gain control. In *Proceedings of the 13th Mediterranean Conference on Control and Automation*, pages 569 – 574, 2005.

[152] M. Tomizuka and J. K. Hedrick. Advanced control methods for automotive applications. *Vehicle System Dynamics*, 24:449 – 468, 1995.

[153] A. Trächtler. Integrierte Fahrdynamikregelung mit ESP, aktiver Lenkung und aktivem Fahrwerk. *AT-Automatisierungstechnik*, 53:11–19, 2005.

[154] A. Trächtler. Phasenfreie Messung. In *Lecture Notes "Echtzeitsimulation"*. University of Paderborn, 2007.

[155] A. Trächtler. *Entwurf mechatronischer Systeme - 6. Paderborner Workshop*, chapter Entwurf intelligenter mechatronischer Systeme - Regelungstechnische Konzepte für selbstoptimierendes Verhalten, pages 3 – 13. Heinz Nixdorf Institut Verlagsschriftenreihe, 2009.

[156] M. N. Tran and D. Hrovat. Application of gain-scheduling to design of active suspensions. In *Proceedings of the 32nd Conference on Decision and Control*, pages 1030 – 1035, 1993.

[157] H. E. Tseng and J. K. Hedrick. Semi-active control laws - optimal and sub-optimal. *Vehicle System Dynamics*, 23:545 – 569, 1993.

[158] M. Valášek and W. Kortüm. Semi-active suspension systems II. In O. D. I. Nwokah and Y. Hurmuzlu, editors, *The Mechanical Systems Design Handbook: Modelling, Measurement, and Control*. CRC Press Inc., 2002.

[159] M. Valášek, M. Novák, Z. Šika, and O. Vaculín. Extended ground-hook - new concept of semi-active control of truck's suspension. *Vehicle System Dynamics*, 27:289–303, 1997.

[160] R. van Basshuysen, editor. *Automobiltechnische Zeitung extra - Der neue BMW 7er*. Springer Automotive Media, GWV Fachverlage GmbH, 2008.

[161] P. J. Th. Venhovens. *Optimal Control of Vehicle Suspensions*. PhD thesis, Delft University of Technology, Faculty of Mechanical Engineering, 1993.

[162] P. J. Th. Venhovens. The development and implementation of adaptive semi-active suspension control. *Vehicle System Dynamics*, 23:211–235, 1994.

[163] Verein Deutscher Ingenieure. *VDI guideline 2057 - Human exposure to mechanical vibrations*, 09.2002.

[164] J. Voelcker. The Soul of a new Mercedes. *IEEE Spectrum*, 45:32 – 37, 2008.

[165] H. Wallentowitz, A. Freialdenhoven, and I. Olschewski. *Strategien in der Automobilindustrie - Technologietrends und Marktentwicklungen*. Vieweg + Teubner, Wiesbaden, 2009.

[166] WHO. Global status report on road safety - Time for action. Technical report, World Health Organization, Geneva, 2009.

[167] B. Widrow and S. D. Stearns. *Adaptive Signal Processing*. Prentice Hall, Englewood Cliffs, 1985.

[168] R. A. Williams and A. Best. Control of a low frequency active suspension. In *Proceedings of the International Conference on Control*, 1994.

[169] P. H. Wirsching, T. L. Paez, and K. Ortiz. *Random Vibrations – Theory and Practice*. John Wiley and Sons, Inc., New York, 1995.

[170] C. Woernle. Fahrmechanik. Lecture Notes: Institute of Technical Mechanics/Dynamics, University of Rostock, 2005.

[171] J. Y. Wong. *Theory of Ground Vehicles*. John Wiley & Sons, New York, 2001.

[172] K. Wulff. *Quadratic and non-quadratic stability criteria for switched linear systems*. PhD thesis, National University of Ireland, 2004.

[173] N. Yagiz and Y. Hacioglu. Backstepping control of a vehicle with active suspensions. *Control Engineering Practice*, 16:1457 – 1467, 2008.

[174] K. Yi and B. S. Song. A new adaptive sky-hook control of vehicle semi-active suspensions. *Proceedings of the Institution of Mechanical Engineers, Part D: Journal of Automobile Engineering*, 213:293 – 303, 1999.

[175] M Yokoyama, J.K. Hedrick, and S. Toyoma. A model following sliding mode controller for semi-active suspension systems with MR dampers. *Proceedings of the American Control Conference*, pages 2652–2657, 2001.

[176] F. Yu and D.A. Crolla. An optimal self-tuning controller for an active suspension. *Vehicle System Dynamics*, 29:51 – 65, 1998.

[177] P. Zarchan and H. Musoff. *Fundamentals of Kalman Filtering: A Practical Approach*. American Institute of Aeronautics and Astronautics, Inc., 1st edition, 2000.

[178] Y. Zhang and A. Alleyne. A practical and effective approach to active suspension control. *Vehicle System Dynamics*, 43:3005 – 330, 2005.

[179] A. Zin, O. Sename, P. Gaspar, L. Dugard, and J. Bokor. Robust LPV-H_∞ control for active suspensions with performance adaptation in view of global chassis control. *Vehicle System Dynamics*, 46(10):889–912, 2008.

[180] L. Zuo, J.-J. E. Slotine, and S. A. Nayfeh. Experimental study of a novel adaptive controller for active vibration isolation. In *Proceedings of the 2004 American Control Conference*, pages 3863 – 3868, 2004.

[181] L. Zuo, J.-J. E. Slotine, and S. A. Nayfeh. Model reaching adaptive control for vibration isolation. *IEEE Transactions on Control Systems Technology*, 13(4):611 – 617, 2005.

Appendix A

THEORETICAL PRELIMINARIES

A.1 Linear quadratic regulator design

A linear quadratic regulator (LQR) is a linear state feedback controller, that minimizes a quadratic cost functional. The cost functional includes weighting matrices for the states and input signals of a linear system in state space representation to balance dynamic performance and control effort in the controller design. The design procedure of linear quadratic regulators is presented in detail e.g. in [8, 33, 84, 97, 99].

In the following, the design of LQRs for improper SISO-systems with output weighting in the cost functional is presented, since this is the system class the LQR is designed for in Chapter 5. The state space description of the n-th order linear system is

$$\begin{aligned} \dot{\mathbf{x}} &= \mathbf{A}\mathbf{x} + \mathbf{b}u\,, && \text{(A.1)} \\ \mathbf{y} &= \mathbf{C}\mathbf{x} + \mathbf{d}u && \text{(A.2)} \end{aligned}$$

with a scalar control input $u \in \mathbb{R}$, the state vector $\mathbf{x} \in \mathbb{R}^n$, an output vector $\mathbf{y} \in \mathbb{R}^p$ and matrices $\mathbf{A}$, $\mathbf{b}$, $\mathbf{C}$, $\mathbf{d}$ of appropriate dimensions. The cost functional for the LQR design with output weighting is

$$J_{LQR} = \int_0^\infty \left(\mathbf{y}^T \mathbf{Q}_y \mathbf{y} + Ru^2 \right) dt \tag{A.3}$$

with the matrix $\mathbf{Q}_y = \mathbf{Q}_y^T \geq 0$ and the scalar $R > 0$ for the weighting of the outputs and the control input, respectively. Substituting the state space model (A.1), (A.2) in (A.3) results in the cost functional

$$J_{LQR} = \int_0^\infty \left(\mathbf{x}^T \mathbf{Q} \mathbf{x} + 2\mathbf{x}^T \mathbf{s} u + \tilde{R} u^2 \right) dt \tag{A.4}$$

with

$$\begin{aligned}\mathbf{Q} &= \mathbf{C}^T\mathbf{Q}_y\mathbf{C}\,, && \text{(A.5)}\\ \mathbf{s} &= \mathbf{C}^T\mathbf{Q}_y\mathbf{d}\,, && \text{(A.6)}\\ \tilde{R} &= \mathbf{d}^T\mathbf{Q}_y\mathbf{d}+R\,. && \text{(A.7)}\end{aligned}$$

In the cost functional (A.4) the mixed term $2\mathbf{x}^T\mathbf{s}u$ is contained due to the direct feedthrough term $\mathbf{d}$ present in (A.2). However, the classical LQR design formalism (see e.g. [8]) does not consider direct feedthrough.

Following an approach presented in [8, 97, 99], the control input in (A.4) is substituted by

$$\tilde{u} = u + \tilde{R}^{-1}\mathbf{s}^T\mathbf{x} \tag{A.8}$$

to remove the mixed term so that the classical LQR design formalism can be applied. By this procedure the system matrix becomes $\tilde{\mathbf{A}} = \mathbf{A} - \mathbf{b}\tilde{R}^{-1}\mathbf{s}^T$ and the weighting matrix $\mathbf{Q}$ becomes $\tilde{\mathbf{Q}} = \mathbf{Q} - \mathbf{s}\tilde{R}^{-1}\mathbf{s}^T$ (note that $\tilde{\mathbf{Q}} \geq 0$ must hold). The LQR problem without the mixed term can be solved for the new control (A.8) by the classical LQR design formalism yielding the state feedback control law

$$\tilde{u} = -\tilde{R}\mathbf{b}^T\mathbf{P}\mathbf{x} \tag{A.9}$$

with $\mathbf{P}$ being the symmetric, positive definite solution of the algebraic Riccati-equation

$$\tilde{\mathbf{A}}^T\mathbf{P} + \mathbf{P}\tilde{\mathbf{A}} - \mathbf{P}\mathbf{b}\tilde{R}^{-1}\mathbf{b}^T\mathbf{P} + \tilde{\mathbf{Q}} = \mathbf{0}\,. \tag{A.10}$$

The resulting optimal solution for the linear quadratic regulator with control input u can be obtained from (A.8) and (A.9) as

$$\begin{aligned}u &= -\mathbf{k}^T\mathbf{x}\,, && \text{(A.11)}\\ \mathbf{k}^T &= \tilde{R}^{-1}\left(\mathbf{b}^T\mathbf{P}+\mathbf{s}^T\right)\,. && \text{(A.12)}\end{aligned}$$

A.2 Preliminaries on stability

A.2.1 Lyapunov stability

Let the autonomous system of the form

$$\dot{\mathbf{x}} = \mathbf{f}(\mathbf{x}) \tag{A.13}$$

with $\mathbf{f} \in \mathbb{R}^n$ have an equilibrium point in $\mathbf{x} = \mathbf{0}$. The stability of this equilibrium can be analyzed by means of Lyapunov's direct method, which is presented in detail e.g. in [70, 140], as follows:

Proposition A.1. [1] *Let* $\mathbf{x} = \mathbf{0}$ *be an equilibrium point for* (A.13) *and* $D \subset \mathbb{R}^n$ *be a domain containing the equilibrium. Let* $V : D \to \mathbb{R}$ *be a continuously differentiable function such that*

- $V(\mathbf{0}) = 0$
- $V(\mathbf{x}) > 0 \quad \textit{for} \quad \mathbf{x} \neq \mathbf{0}$
- $\dot{V}(\mathbf{x}) \leq 0 \quad \textit{for} \quad \mathbf{x} \in D,$

then $\mathbf{x} = \mathbf{0}$ *is stable. Moreover, if*

- $\dot{V}(\mathbf{x}) < 0 \quad \textit{for} \quad \mathbf{x} \neq \mathbf{0}$

the equilibrium $\mathbf{x} = \mathbf{0}$ *is asymptotically stable. If furthermore* $D \equiv \mathbb{R}^n$*, the system is asymptotically stable and*

- $\|\mathbf{x}\| \to \infty \;\Rightarrow\; V(\mathbf{x}) \to \infty$

then $\mathbf{x} = \mathbf{0}$ *is globally asymptotically stable (*$\|\mathbf{x}\|$ *denotes any* $p-$*norm [70]).*

Moreover, it is noted that every (stable) / asymptotically stable autonomous system is (uniformly stable) / uniformly asymptotically stable since stability and asymptotic stability are uniform with respect to the initial time t_0 [70].

The linear time-invariant (LTI) system (A.1) with $\mathbf{A} \in \mathbb{R}^{n \times n}$, $\mathbf{b} \in \mathbb{R}^{n \times 1}$ and a scalar control input $u(t)$ is asymptotically stable if and only if the eigenvalues of $\mathbf{A}$ have negative real parts (see e.g. [33, 98]).

---

[1] See [70] Theorem 4.1.

A.2.2 Common Lyapunov functions for switched systems

In the following, a method to guarantee stability of a switched system is presented. In the context of this Thesis this method is applied to switched linear systems of the form

$$\dot{\mathbf{x}}(t) = \mathbf{A}_i \mathbf{x}(t) \quad \text{with} \quad i \in \mathcal{P} \tag{A.14}$$

with $\mathbf{f} \in \mathbb{R}^n$ and a finite index set $\mathcal{P} = \{1, ..., m\}$. The system (A.14) constitutes from m subsystems and a piecewise constant switching function $\sigma(q_{adp}(t)) : [0,1] \to \mathcal{P}$ (with $0 \leq q_{adp}(t) \leq 1$ denoting a parameter that controls the switching) with the properties described in [88]. The switching function specifies at each time instant the index $i(t) = \sigma(q_{adp}(t))$ of the active subsystem in (A.14). Regarding the asymptotic stability of (A.14), it is not sufficient that each of the subsystems is asymptotically stable. Various methods to prove asymptotic stability for switched systems are given e.g. in [88, 172].

One method to guarantee stability for systems subject to arbitrary switching is a common Lyapunov function, which is valid for each subsystem of (A.14) [88]. In the following, the stability of the switched linear system (A.14) is studied and a class of common Lyapunov function candidates, i.e. common quadratic Lyapunov-functions (CQLFs), is considered for this purpose. A CQLF for the system (A.14) is given by

$$V(\mathbf{x}) = \mathbf{x}^T \mathbf{P} \mathbf{x} \tag{A.15}$$

$$\text{with} \quad \mathbf{P} = \mathbf{P}^T > \mathbf{0} \tag{A.16}$$

if

$$\left(\mathbf{A}_i^T \mathbf{P} + \mathbf{P}\mathbf{A}_i\right) \leq -\mathbf{Q} \qquad \forall \quad i \in \mathcal{P}, \tag{A.17}$$

with $\mathbf{Q} \in \mathbb{R}^{n \times n}$ being a positive definite symmetric matrix, holds for all m subsystems [88].

If it is assumed that the subsystems result from state feedback control by m controllers $\mathbf{k}_i^T$ designed for the linear system (A.1), the subsystems are given by the closed loop system matrices $\mathbf{A}_i = \mathbf{A} - \mathbf{b}\mathbf{k}_i^T$. Thus, if a corresponding matrix $\mathbf{P}$ can be found so that (A.16)-(A.17) are fulfilled for all subsystems, the equilibrium $\mathbf{x} = \mathbf{0}$ of the switched closed loop system is uniformly asymptotically stable for arbitrary switching between the controllers $\mathbf{k}_i^T$ [88].

Numerical methods can be employed to solve the set of LMIs (A.16) - (A.17) and determine $\mathbf{P}$ if a feasible solution exists (see e.g. [95] and [149]).

Stability analysis for soft switching by interpolation

Switching between a set of controllers with a discontinuous switching function $\sigma\left(q_{adp}(t)\right)$ can cause discontinuities in the control signal. To avoid these discontinuities, "soft" switching by interpolating between the controllers via the continuous scheduling signal $q_{adp}(t)$ can be desirable instead. The stability for linear interpolation between state feedback controllers for a linear system is analyzed as follows:

Theorem 1. If a system of the form (A.14) *with* $m = 2$, *that is characterized by the closed loop system matrices* $\mathbf{A}_1$ *and* $\mathbf{A}_2$ *resulting from the two distinct stabilizing state feedback controllers* $\mathbf{k}_1^T$ *and* $\mathbf{k}_2^T$ *for the open loop system matrix* $\mathbf{A}$ *defined in* (A.1)*, has a CQLF characterized by* (A.16) - (A.17)*, the closed loop system resulting from a linear interpolation between* $\mathbf{k}_1^T$ *and* $\mathbf{k}_2^T$*, i.e.*

$$\tilde{\mathbf{k}}^T = q_{adp}(t)\mathbf{k}_1^T + \left(1 - q_{adp}(t)\right)\mathbf{k}_2^T \tag{A.18}$$

with $0 \leq q_{adp}(t) \leq 1\ \forall t$, *has the same CQLF characterized by* $\mathbf{P}$.

From (A.18) a convex combination of the closed-loop subsystems results. It can be shown that convex combinations possess the same CQLF [88, 172]. The proof for the considered example is:

Proof. If the two closed-loop systems have a CQLF, then there exists a matrix $\mathbf{P} = \mathbf{P}^T > \mathbf{0}$ such that

$$\mathbf{A}_i^T\mathbf{P} + \mathbf{P}\mathbf{A}_i \leq -\mathbf{Q} \qquad \forall i \in \{1, 2\} \tag{A.19}$$

with $\mathbf{Q} = \mathbf{Q}^T > 0$. A linear combination of the Lyapunov inequalities (A.19) with the scheduling signal $q_{adp}(t) : 0 \leq q_{adp}(t) \leq 1 \quad \forall t$ is

$$q_{adp}(t)\underbrace{\left(\mathbf{A}_1^T\mathbf{P} + \mathbf{P}\mathbf{A}_1\right)}_{\leq -\mathbf{Q}} + \left(1 - q_{adp}(t)\right)\underbrace{\left(\mathbf{A}_2^T\mathbf{P} + \mathbf{P}\mathbf{A}_2\right)}_{\leq -\mathbf{Q}} \leq -\mathbf{Q}\,. \tag{A.20}$$

Considering the stabilizing state feedback control laws $u_i = -\mathbf{k}_i^T\mathbf{x}$, $i \in \{1, 2\}$, (A.20) can be rewritten as

$$\mathbf{A}^T\mathbf{P} - \left(q_{adp}(t)\mathbf{k}_1^T + \left(1 - q_{adp}(t)\right)\mathbf{k}_2^T\right)^T\mathbf{b}^T\mathbf{P} + \mathbf{P}\mathbf{A} - \mathbf{P}\mathbf{b}\left(q_{adp}(t)\mathbf{k}_1^T + \left(1 - q_{adp}(t)\right)\mathbf{k}_2^T\right) \leq -\mathbf{Q}\,. \tag{A.21}$$

Linear interpolation between the controllers $\mathbf{k}_i^T$ results in the state feedback gain vector given in (A.18), i.e. (A.21) can be transformed into

$$\left[\mathbf{A}-\mathbf{b}\tilde{\mathbf{k}}^T\right]^T \mathbf{P}+\mathbf{P}\left[\mathbf{A}-\mathbf{b}\tilde{\mathbf{k}}^T\right] \leq -\mathbf{Q}\,. \tag{A.22}$$

□

Thus, **P** is a CQLF for all subsystems resulting from the interpolation between the state feedback controllers $\mathbf{k}_1^T$ and $\mathbf{k}_2^T$, which implies that the resulting closed loop system is asymptotically stable for arbitrary fast linear interpolation between the two stabilizing state feedback controllers by the scheduling signal $q_{adp}(t)$.

A.2.3 Absolute stability and the circle criterion

The circle criterion gives a sufficient condition for a nonlinear system that can be represented by a feedback connection of a linear dynamical system and a nonlinear element (Figure A.1) to be absolutely stable.

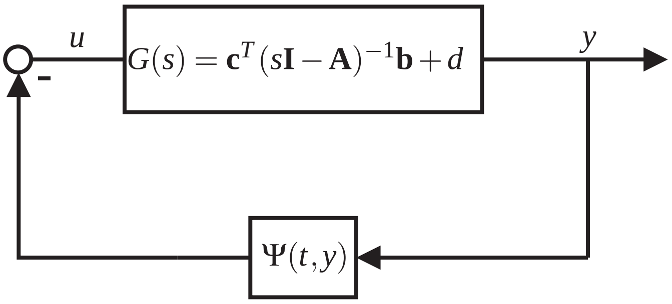

Figure A.1: Feedback connection of a linear dynamical SISO system and a nonlinear element

Although the circle criterion can be used for MIMO systems, it is formulated here for the SISO case. The feedback connection depicted in Figure A.1 is represented by

$$\dot{\mathbf{x}} = \mathbf{A}\mathbf{x}+\mathbf{b}u\,, \tag{A.23}$$

$$y = \mathbf{c}^T\mathbf{x}+du\,, \tag{A.24}$$

$$u = -\Psi(t,y)\,, \tag{A.25}$$

with $\mathbf{A} \in \mathbb{R}^{n\times n}$, $\mathbf{b} \in \mathbb{R}^{n\times 1}$, $\mathbf{c}^T \in \mathbb{R}^{1\times n}$, $d \in \mathbb{R}$ and a scalar control input $u(t)$. The pair $(\mathbf{A}, \mathbf{b})$ is controllable and $(\mathbf{A}, \mathbf{c}^T)$ is observable, thus $(\mathbf{A}, \mathbf{b}, \mathbf{c}^T, d)$ is a minimal realization of $G(s)$. Moreover, the sector condition

$$K_1 y^2 \leq y\Psi(t,y) \leq K_2 y^2 \tag{A.26}$$

holds for the scalar function $\Psi(t,y)$ for all (t,y) with $K_2 \geq K_1$ being real parameters. The function $\Psi(t,y)$ is then said to belong to the sector $[K_1, K_2]$, which can be written as $\Psi(t,y) \in [K_1, K_2]$.

A nonlinear system, that can be represented by a feedback connection, with a globally uniformly asymptotically stable equilibrium point at the origin for all nonlinearities in a given sector is called absolutely stable [70]

Before the circle criterion is formulated the definition of a strictly positive real transfer function for a SISO system is given as formulated in [70]:

Strictly positive real scalar transfer function

Proposition A.2. [2] *A proper rational SISO transfer function $G(s)$ is strictly positive real if and only if*

- *all poles of $G(s)$ have negative real parts,*
- *$Re[G(j\omega)] > 0$ for all $\omega \in \mathbb{R}$, and*
- *either $G(\infty) > 0$ or $G(\infty) = 0$ and $\lim_{\omega\to\infty} \omega^2 Re[G(j\omega)] > 0$.*

The circle criterion

Proposition A.3. [3] *According to the circle criterion (see e.g. [70]), the system* (A.23) - (A.25) *is absolutely stable if*

- $\Psi(t,y) \in [K_1, \infty]$ *and $G(s)[1 + K_1 G(s)]^{-1}$ is strictly positive real, or*

---

[2] See [70] Lemma 6.1.

[3] See [70] Theorem 7.1.

- $\Psi(t,y) \in [K_1, K_2]$, *with* $K = K_2 - K_1 > 0$, *and* $[1 + K_2 G(s)][1 + K_1 G(s)]^{-1}$ *is strictly positive real.*

In the SISO case and for $G(s)$ being Hurwitz, the circle criterion can be evaluated for a sector defined as $\Psi(t,y) \in [K_1, K_2]$ with $K_1 = 0$ and $K_2 > 0$ by means of the Nyquist curve of $G(s)$, i.e.

$$Re[G(j\omega)] > -\frac{1}{K_2} \tag{A.27}$$

must hold for the feedback connection from $G(s)$ and the given sector to be absolutely stable [70].

A.2.4 Total stability

Let

$$\dot{\mathbf{x}} = \mathbf{f}(\mathbf{x},t) + \mathbf{g}(\mathbf{x},t) \tag{A.28}$$

be a nonlinear dynamic system of order n with $\mathbf{f}(\mathbf{x},t) \in \mathbb{R}^n$ and $\mathbf{g}(\mathbf{x},t) \in \mathbb{R}^n$ being a perturbation term. An approach to derive a boundedness condition to guarantee stability for the perturbed system based on stability properties of the unperturbed system

$$\dot{\mathbf{x}} = \mathbf{f}(\mathbf{x},t) \tag{A.29}$$

is presented in [140].

Proposition A.4. [4] *The equilibrium point* $\mathbf{x} = \mathbf{0}$ *for the unperturbed system* (A.29) *is said to be totally stable if for every* $\varepsilon \geq 0$, *two parameters* δ_1 *and* δ_2 *exist such that* $||\mathbf{x}(t_0)|| < \delta_1$ *and* $||\mathbf{g}(\mathbf{x},t)|| < \delta_2$ *imply that every solution* $\mathbf{x}(t)$ *of the perturbed system* (A.28) *satisfies the condition* $||\mathbf{x}(t)|| < \varepsilon$.

Proposition A.5. [5] *If the equilibrium point of* (A.29) *is uniformly asymptotically stable, then it is totally stable.*

Hence, total stability can be considered a local version of bounded input bounded output stability [140].

---

[4] See [140] Definition 4.13.

[5] See [140] Theorem 4.14.

A.3 Signal processing

A.3.1 Properties of random vibration

A detailed presentation of the following aspects is given e.g. in [119, 169]. Let $x(t)$ be a stochastic signal with $x(t) = 0$ for all $t < 0$. The variance σ_x^2 over a time interval T of a stochastic signal is defined as

$$\sigma_x^2 = \frac{1}{T}\int_0^T \left(x(\tau) - x_{m,T}\right)^2 d\tau \tag{A.30}$$

with the mean value

$$x_{m,T} = \frac{1}{T}\int_0^T x(\tau)d\tau\,. \tag{A.31}$$

For the standard deviation σ_x, which is the square root of the variance (A.30), in this Thesis the notation $||x||_{\mathrm{std}}$ is used.

To characterize the intensity of vibrations, a frequently used measure is the root mean square value (rms-value)

$$||x||_{\mathrm{rms}} = \sqrt{\frac{1}{T}\int_0^T x^2(\tau)d\tau}\,, \tag{A.32}$$

which equals $||x||_{\mathrm{std}}$ if $x_{m,T} = 0$.

The average power of the signal $x(t)$ can be calculated as

$$P = \lim_{T\to\infty}\frac{1}{T}\int_0^T x^2(\tau)d\tau\,. \tag{A.33}$$

To compare the frequency contents of a stochastic signal or to describe, how stochastic vibrations are transferred through structures, the power spectral density (PSD) of the signal can be used [85]. The PSD of a random process is defined as the Fourier transform of the corresponding autocorrelation function of the random process [85].

In [13], a more graphical interpretation of the PSD is given: Let $x(t, f, \Delta f)$ be the fraction of the signal $x(t)$, that constitutes the spectrum of the signal in the frequency interval $[f, f + \Delta f]$ and

$$P(f,\Delta f) = \lim_{T\to\infty}\frac{1}{T}\int_0^T x^2(t, f, \Delta f)dt \tag{A.34}$$

be the power of that part of the signal $x(t)$. Then the one sided PSD of $x(t)$ is defined as

$$G_{xx}(f) = \lim_{\Delta f\to 0}\frac{P(f,\Delta f)}{\Delta f}\,. \tag{A.35}$$

The relation between the one sided PSD $G(f)$ and the two sided PSD $S_{xx}(f)$ is $G_{xx}(f) = 2S_{xx}(f)$ (see [169]).

A.3.2 Sampling data

While most physical signals are continuous, these signals can only be recorded by digital instruments in discrete time steps, which are typically multiples of a constant sampling time T_s. In order to be able to reconstruct the original data from the discrete time measurement data, the sampling frequency $f_s = \frac{1}{T_s}$ has to be chosen according to

$$f_s > 2 f_{max} \,, \tag{A.36}$$

where f_{max} denotes the maximum frequency contained in the continuous time signal (see e.g. [99]). The relationship (A.36) is known as *Shannon's sampling theorem*.

Appendix B

PARAMETERS AND FURTHER RESULTS

In this Chapter all parameters of the quarter-vehicle models and test rigs are given, which can be published with respect to the confidentiality agreement regarding the parameters of the hybrid test rig (see Chapters 7.3 and 7.4). Moreover, the simulation results discussed in Chapter 8.4 are presented in Section B.2.

B.1 Parameters of the quarter-vehicle models and test rigs

The parameter sets refer to the nomenclature of the quarter-vehicle model structure shown in Figure 2.1. In Table 2.1 parameters of an exemplary linear automotive quarter-car model for a compact-car are given. Furthermore, the parameters of the following quarter-vehicle models and test rigs are listed in this Section:

- Parameters of the nonlinear model of the active suspension test rig (Chapter 3) [72, 80],
- Parameters of the linear model of the active suspension test rig (Chapter 3.3.4) [72, 80],
- Pre-estimated parameters of the automotive quarter-car test rig for the performance analyis in Chapter 6 [75, 76],
- Selected parameters of the hybrid suspension test rig (Chapter 3) [82].

Furthermore, in Section B.1.1 the calculation of characteristic parameters of a suspension in a quarter-vehicle model (natural frequencies and damping ratios) framework are presented.

Parameters of the nonlinear model of the active suspension test rig

Table B.1: Optimized parameters of the nonlinear quarter-vehicle model (status 10/2010).

Model parameter	Symbol	Value	Unit
Sprung mass	m_c	94.38	$[\mathrm{kg}]$
Unsprung mass	m_w	23.92	$[\mathrm{kg}]$
Total mass	$m_c + m_w$	118.3	$[\mathrm{kg}]$
Primary spring stiffness	$c_c = i^2 \overline{c}_c$	8400	$[\mathrm{N/m}]$
Linear tire stiffness	$c_{w,lin}$	69790	$[\mathrm{N/m}]$
Quadratic tire stiffness	$c_{w,quad}$	3940000	$\left[\mathrm{N/m}^2\right]$
Friction force spring/damper	$F_{f,1}$	115	$[\mathrm{N}]$
Friction scaling spring/damper	$k_{f,1}$	125	$[\mathrm{sec/m}]$
Friction force chassis mass guides	$F_{f,2}$	20	$[\mathrm{N}]$
Friction scaling chassis mass guides	$k_{f,2}$	125	$[\mathrm{sec/m}]$
Transmission factor	i	0.392	$[-]$
Tire damping coefficient	d_w	50	$[\mathrm{Nsec/m}]$
Damping ratio sprung mass	D_c	0.397	$[-]$
Damping ratio unsprung mass	D_w	0.18	$[-]$
Undamped natural frequency of the sprung mass	f_c	1.5	$[\mathrm{Hz}]$
Undamped natural frequency of the unsprung mass	f_w	12.7	$[\mathrm{Hz}]$

Parameters of the linear model of the active suspension test rig

Table B.2: Parameters of the linear quarter-vehicle model (status 10/2010).

Model parameter	Symbol	Value	Unit
Sprung mass	m_c	94.38	[kg]
Unsprung mass	m_w	23.92	[kg]
Total mass	$m_c + m_w$	118.3	[kg]
Primary spring stiffness	$c_c = i^2 \overline{c_c}$	8400	[N/m]
Tire stiffness	c_w	152186	[N/m]
Damping coefficient (sprung mass)	d_c	666	[Nsec/m]
Transmission factor	i	0.392	$[-]$
Tire damping coefficient	d_w	50	[Nsec/m]
Damping ratio sprung mass	D_c	0.374	$[-]$
Damping ratio unsprung mass	D_w	0.09	$[-]$
Undamped natural frequency of the sprung mass	f_c	1.5	[Hz]
Undamped natural frequency of the unsprung mass	f_w	13.0	[Hz]

Parameters for the performance analyis in Chapter 6

Table B.3: Notation and parameter values used in Chapter 6.

Model parameter	Symbol	Value	Unit
Sprung mass	m_c	320	[kg]
Unsprung mass	m_w	32	[kg]
Mass ratio	$\rho = \frac{m_w}{m_c}$	0.10	$[-]$
Suspension spring stiffness	c_c	13000	[N/m]
Tire stiffness	c_w	127000	[N/m]
Sprung mass damping ratio	$D_c = \frac{d_c}{2\sqrt{c_c m_c}}$	varying	$[-]$
Low pass filter damping ratio	D_f	$\frac{1}{\sqrt{2}} \approx 0.707$	$[-]$
Undamped natural frequency of the sprung mass	ω_c	6.37	[rad/sec]
Tirehop frequency	$\omega_w = \sqrt{\frac{c_w}{m_w}}$	63	[rad/sec]
Low pass filter cutoff frequency	ω_c	varying	[rad/sec]

Parameters of the hybrid suspension test rig

Table B.4: Selected parameters of the hybrid suspension test rig (status 10/2010).

Model parameter	Symbol	Value	Unit
Sprung mass	m_c	507	[kg]
Unsprung mass	m_w	68	[kg]
Total mass	$m_c + m_w$	575	[kg]
Damping ratio of the sprung mass (passive)	$D_{c,p}$	0.21	$[-]$
Undamped natural frequency of the sprung mass (passive)	$f_{c,p}$	1.1	[Hz]

B.1.1 Characteristic parameters of suspension systems

For a quarter-vehicle model (see Figure 2.1 (le.)) the natural frequencies and damping ratios are calculated as given in Table B.5 [50, 106].

Table B.5: Characteristic parameters of quarter-vehicle models [50, 106]

Parameter	Calculation	Unit
Undamped (uncoupled) natural frequency (sprung mass)	$f_c = \frac{1}{2\pi}\sqrt{\frac{c_c}{m_c}}$	[Hz]
Undamped (uncoupled) natural frequency (unsprung mass)	$f_w = \frac{1}{2\pi}\sqrt{\frac{c_c+c_w}{m_w}}$	[Hz]
Tirehop frequency	$f_t = \frac{1}{2\pi}\sqrt{\frac{c_w}{m_w}}$	[Hz]
Damping ratio (sprung mass)	$D_c = \frac{d_c}{2\sqrt{m_c c_c}}$	[-]
Damping ratio (unsprung mass)	$D_w = \frac{d_c+d_w}{2\sqrt{m_w(c_c+c_w)}}$	[-]

B.2 Further results

The relevant signals of the simulations described in Chapter 8.4 are given in Figure B.1. The resulting performance is summarized in the spider chart 8.7.

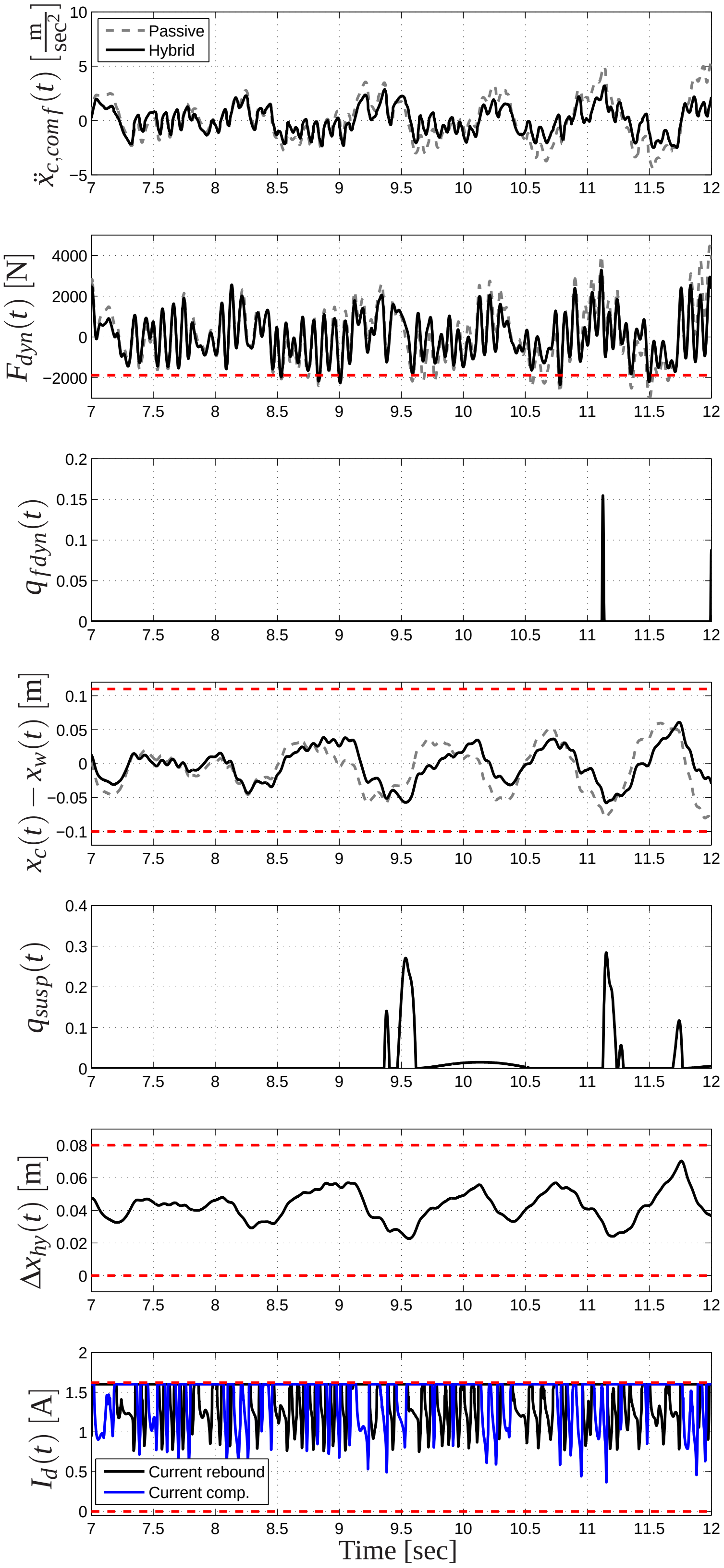

Figure B.1: Simulation results of the hybrid versus the passive suspension (P1 with $v_{p1} = 50\,\frac{\text{km}}{\text{h}}$); the red lines indicate the limits for the rms-value of F_{dyn} (i.e. $\frac{F_{\text{stat}}}{3}$), the suspension deflection limits and the saturation limits of the control inputs.